Multipolar Analysis of Ordered and Disordered Metasurfaces

—

Zur Erlangung des akademischen Grades eines
Doktors der Naturwissenschaften
(Dr. rer. nat.)

von der KIT-Fakultät für Physik
des Karlsruher Instituts für Technologie (KIT)

angenommene Dissertation

von

M.Sc. Aso Rahimzadegan

am Institut für Theoretische Festkörperphysik

Referent: Prof. Dr. Carsten Rockstuhl
Korreferentin: Prof. Dr. Isabelle Staude

Tag der mündlichen Prüfung: 29.10.2021
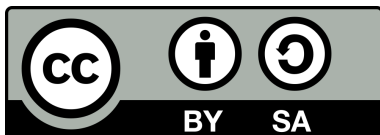
Selbstständigkeitserklärung

Eidesstattliche Versicherung gemäß § 13 Absatz 2 Ziffer 3 der Promotionsordnung des Karlsruher Instituts für Technologie (KIT) für die KIT-Fakultät für Physik:

1. Bei der eingereichten Dissertation zu dem Thema
   "Multipolar Analysis of Ordered and Disordered Metasurfaces"
   handelt es sich um meine eigenständig erbrachte Leistung.

2. Ich habe nur die angegebenen Quellen und Hilfsmittel benutzt und mich keiner unzulässigen Hilfe Dritter bedient. Insbesondere habe ich wörtlich oder sinngemäß aus anderen Werken übernommene Inhalte als solche kenntlich gemacht.

3. Die Arbeit oder Teile davon habe ich wie folgt/ bislang nicht[1] an einer Hochschule des In- oder Auslands als Bestandteil einer Prüfungs- oder Qualifikationsleistung vorgelegt.

Titel der Arbeit:
"Multipolar Analysis of Ordered and Disordered Metasurfaces",
Hochschule und Jahr:
KIT-Fakultät für Physik des Karlsruher Instituts für Technologie (KIT),
2021,
Art der Prüfungs- oder Qualifikationsleistung:
Dissertation.

4. Die Richtigkeit der vorstehenden Erklärungen bestätige ich.

5. Die Bedeutung der eidesstattlichen Versicherung und die strafrechtlichen Folgen einer unrichtigen oder unvollständigen eidesstattlichen Versicherung sind mir bekannt. Ich versichere an Eides statt, dass ich nach bestem Wissen die reine Wahrheit erklärt und nichts verschwiegen habe.

Ort und Datum   Unterschrift

---

[1]Nicht Zutreffendes streichen. Bei Bejahung sind anzugeben: der Titel der andernorts vorgelegten Arbeit, die Hochschule, das Jahr der Vorlage und die Art der Prüfungs- oder Qualifikationsleistung.

Abstract

Optical metasurfaces are 2D arrangements of nanoparticles that enable abrupt modulation of an impinging light wavefront within an ultra-thin surface. They are promising candidates to replace bulky conventional optical components such as mirrors, lenses, diffusers, etc. The rapid growth of nanofabrication and a constantly increasing demand for miniaturization have made metasurface's design with desired optical functionalities an ever-growing necessity. Analytical tools that can provide physical insights and improved design capabilities are crucial for that aim, and are the center of attention in this thesis. Based on a local-coordinate transition matrix (T-matrix) method, we aim at providing analytical insights to both ordered and disordered metasurfaces. The local-coordinate T-matrix method provides a comprehensive analytical tool to monitor the changes in the effective response of the nanoparticles inside a lattice.

For periodic metasurface made from identical nanoparticles, despite their abundance and importance, closed-form analytical expressions describing their optical response have not been reported, and most attempts have been predominantly approximations. In this thesis, we provide a comprehensive and unifying multipolar theory for periodic metasurfaces that describes the scattering analytically and enables the derivation of a closed-form expression for the optical response. Our analytical expressions are valid for diffraction orders under oblique and normal incidences up to an octupolar order. In this formalism, we link the macroscopic optical response of the metasurface to the optical response of the individual nanoparticles (via their T or polarizability matrix) and the lattice coupling matrix. Furthermore, we extensively explore the symmetries of the optical response of the nanoparticles inside and outside different lattices. Moreover, we propose several designs based on the insights from these expressions throughout the thesis.

In particular, we study Huygens' metasurfaces and their limits and capabilities. They are made from non-absorbing and equally induced electric and magnetic moments and are reflection-less. The reflection suppression enables efficient modulation of an optical wavefront without absorption losses.

To investigate disordered metasurfaces, we have resorted to statistical measures such as configurational entropy, structure factor, and pair correlation function. We introduce multiple disordered point configurations in metasurfaces, and study the optical response in correlation to their statistical measures. In particular, we have identified critical disorder regimes where the zeroth-order transmission and reflection go to zero, and the light is diffused to all non-specular directions. Driven from the insights, we have investigated metasurface-based optical diffusers.

The thesis follows a systematic and step-by-step approach. It seeks to provide a solid and comprehensive reference for future research on the topic.

Abstract in Kurdish

مێتا-ڕووه ئۆپتیکییەکان بریتین لە کۆمەڵێک نانۆتەنۆلکەی ڕیزکراو لەسەر ڕووبەرێکی دوو ڕەهەندی کە دەتوانن گۆڕانکاری کتوپڕ لە شەپۆلی ئەو ڕووناکییەدا دروووست بکەن کە لێیان دراوە. ئەم ڕووانە جێگرەوەیەکی هیوابەخشن بۆ پێکهاتە ئۆپتیکییە باو بەڵام قەبەکانی وەک ئاوێنە، لێنز، پرژێنەر و هتد. پێشکەوتنی خێرای تەکنەلۆجیای نانۆ و داواکاری ڕوولەگەشە بۆ چکۆلەترکردنەوەی ئامێرەکان، بووەتە هۆی ئەوەی کە دارشتنی مێتا-ڕووەکان بە جۆرێک کە ئەنجامی دلخواز لەسەر شەپۆلی ڕووناک دروووست بکەن، پێویستییەکی بەردەوام ڕوو لە زیادبوون بێت. بۆ ئەم مەبەستە، ئەو ئامرازە شیکاریانەی کە بتوانن تێگەیشتنی فیزیکی دەستەبەر بکەن و توانای دارشتن بەهێز بکەن، گرنگن، و بابەتی سەرەکی ئەم تێزی دکتۆرایەن. لەسەر بنەمای میتۆدی T ماتریکسی خۆجێیی، هەوڵ دەدەین تێگەیشتنێکی شیکاریانە بۆ مێتا-ڕووە ڕێک و نارێکەکان دەستەبەر بکەین (ڕێکی و نارێکی دەگەڕێتەوە بۆ ئەو تۆڕەی کە نانۆتەنۆلکەکانی لەسەر ڕیزکراون). میتۆدی ماتریکسی T ئامرازێکی شیکاریانەی گشتگیر بۆ چاودێریکردنی گۆڕانکارییەکان لە کاردانەوە کاریگەرەکەی نانۆتەنۆلکەکان لەناو مێتا-ڕووەکەدا دابین دەکات.

بۆ ئەو مێتا-ڕووە خولییانەی کە لە نانۆتەنۆلکەی هاوشێوە دروووست کراون، سەرەڕای گرنگی و فرەییان، هاوکێشەگەلێکی داخراوی شیکاریانە کە باسی کاردانەوەکانی ئۆپتیکییە ڕووەکان بکات بوونیان نییه. زۆربەی ئەو هەوڵانەی کە بۆ ئەو مەبەستە دراون تەنیا نزیکەیی بوون. لەم تێزەدا، ئێمە تیۆرییەکی فرەجەمسەری یەکانگیر و گشتگیر بۆ مێتا-ڕووە خولییەکان دەخەینە ڕوو کە بە شێوەیەکی شیکاریانە باس لە پەرشبوونەوەی ڕووناکییەکەیان دەکات و داتاشینی هاوکێشەیەکی شێوه-داخراو بۆ کاردانەوە ئۆپتیکییەکە دابین دەکات. هاوکێشە شیکاریانەکانمان دەتوانن هەموو پلەکانی لادان لەژێر ڕووناکی ئەستوون و لاردا، تا پلەی هەشتجەمسەری، بەدروووستی هەژمار بکەن. لەم هاوکێشانەدا، ئێمە کاردانەوەی ماکرۆسکۆپیکی ڕووەکە بەرامبەر ڕووناکی بە کاردانەوەی تاک بە تاکی نانۆتەنۆلکەکان (لە ڕێی ماتریکسی T یان ماتریکسی جەمسەرگری) و ماتریکسی جووتبوونی تۆڕی ڕووەکە دەبەستینەوە. جگە لەوە، هاوتایی کاردانەوەی نانۆتەنۆلکەکان بۆ ڕووناکیی لەناو یان دەرەوەی چەندین تۆڕی جیاوازی ڕێک بە چڕی دەخەینە بەرباس. دواتر، لەسەر بنەمای ئایدیاکانی ئەو هاوکێشانە چەند دیزاینێک/گەڵاڵەیەک پێشنیار دەکەین.

بەتایبەت، تیشک دەخەینە سەر مێتا-ڕووەکانی هۆیگێنس و توانایی و سنوورەکانیان پیشان دەدەین. ئەم ڕووانە لە کۆمەڵێک نانۆتەنۆلکەی وزە-هەڵنەمڕی وەک یەک پێک هاتوون کە زەبری کارەبایی و موگناتیسی یەکسانیان هەیە و هیچ ڕووناکییەک نادەنەوە. ئەم نەدانەوەی ڕووناکییە توانایی گۆڕینی شەپۆلی ڕووناکی دەبەخشێت بەم ڕووانە بەبێ ئەوەی وزە لە ڕووانە وزە بە فیڕۆ بدەن.

بۆ لێکۆڵینەوە لە مێتا-ڕووە نارێکەکان (شپرزەکان)، یارمەتی لە پێوانە ئاماریەکانی وەک ئینترۆپی، فاکتەری پێکهاتە، و نەخشەی هاوپەیوەندیی دووانە وەردەگرین. چەندین جۆر تۆڕی نارێک دەناسێنین و کاردانەوەی ڕووناکیی ئەو مێتا-ڕووانەی کە نانۆتەنۆلکەکانیان بەپێی ئەو تۆڕانە ڕیز کراون شی دەکەینەوە. بەتایبەت، خاڵێکی قەیرانیمان لە نارێکیدا دەستنیشان کردووە کە تێیدا ڕووناکیی تێپەڕیو و دراوەی ڕاستەوخۆی ڕووەکە ون دەبێت و ڕووناکییەکە بۆ هەموو لایەک دەپرژێت. بەپێی ئەم تێگەیشتنانە، لێکۆڵینەوەمان لەسەر ئەو پرژێنەرە ڕووناکییانە کردووە کە لەسەر بنەمای مێتا-ڕووەکان دروووست دەکرێن.

ئەم تێزە شێوازێکی هەنگاو-بە-هەنگاو دەگرێتە بەر و مەبەستیەتی ببێتە سەرچاوەیەکی بەهێز و گشتگیر بۆ توێژینەوەکانی داهاتوو لەم بوارەدا.

Contents

Publications

Selected peer-reviewed articles

Publications presented within this thesis are highlighted in bold letters.

[1] **Rahimzadegan, A.*, Karamanos, T.D.*, Alaee, R., Lamprianidis, A.G., Beutel, D., Boyd, R.W. and Rockstuhl, C., 2022. A comprehensive multipolar theory for periodic metasurfaces. Advanced Optical Materials, 10 (10), 2102059.**

[2] Yang, L., Rahimzadegan, A., Hahn, V., Blasco, E., Rockstuhl, C., and Wegener, M., 2022. In situ diagnostics and role of light-induced forces in metal laser nanoprinting. Laser & Photonics Reviews, 16 (3), 2100411.

[3] **Arslan, D.*, Rahimzadegan, A.*, Fasold, S., Falkner, M., Kroychuk, M., Rockstuhl, C., Pertsch, T., Staude, I., 2022. Towards perfect optical diffusers: Dielectric Huygens' metasurfaces with critical positional disorder. Advanced Materials, 34 (5), 2105868**.

[4] **Rahimzadegan, A., Alaee, R., Karamanos, T.D., Boyd, R.W. and Rockstuhl, C., 2021. Colossal enhancement of the magnetic dipole moment by exploiting lattice coupling in metasurfaces. Journal of the Optical Society of America B, 38(9), pp.C217-C224.**

[5] Gieseler, N., Rahimzadegan, A. and Rockstuhl, C., 2021. Self-stabilizing curved metasurfaces as a sail for light-propelled spacecrafts. Optics Express, 29(14), pp.21562-21575.

[6] **Rahimzadegan, A., Alaee, R., Rockstuhl, C. and Boyd, R.W., 2020. Minimalist Mie coefficient model. Optics Express, 28(11), pp.16511-16525.**

[7] **Rahimzadegan, A., Arslan, D., Dams, D., Groner, A., Garcia-Santiago, X., Alaee, R., Fernandez-Corbaton, I., Pertsch, T., Staude, I. and Rockstuhl, C., 2020. Beyond dipolar Huygens' metasurfaces for full-phase coverage and unity transmittance. Nanophotonics, 9(1), pp.75-82.**

[8] **Rahimzadegan, A.*, Arslan, D.*, Suryadharma, R.N.S., Fasold, S., Falkner, M., Pertsch, T., Staude, I. and Rockstuhl, C., 2019. Disorder-induced phase transitions in the transmission of dielectric metasurfaces. Physical Review Letters, 122(1), p.015702.**

[9] Mobini, E., Rahimzadegan, A., Rockstuhl, C. and Alaee, R., 2018. Theory of optical forces on small particles by multiple plane waves. Journal of Applied Physics, 124(17), p.173102.

[10] **Rahimzadegan, A., Rockstuhl, C. and Fernandez-Corbaton, I., 2018. Core-shell particles as building blocks for systems with high duality symmetry. Physical Review Applied, 9(5), p.054051.**

[11] Mobini, E., Rahimzadegan, A., Alaee, R. and Rockstuhl, C., 2017. Optical alignment of oval graphene flakes. Optics Letters, 42(6), pp.1039-1042.

[12] **Rahimzadegan, A., Alaee, R., Fernandez-Corbaton, I. and Rockstuhl, C., 2017. Fundamental limits of optical force and torque. Physical Review B, 95(3), p.035106.**

[13] **Rahimzadegan, A., Fruhnert, M., Alaee, R., Fernandez-Corbaton, I. and Rockstuhl, C., 2016. Optical force and torque on dipolar dual chiral particles. Physical Review B, 94(12), p.125123.**

[14] Alaee, R., Albooyeh, M., Rahimzadegan, A., Mirmoosa, M.S., Kivshar, Y.S. and Rockstuhl, C., 2015. All-dielectric reciprocal bianisotropic nanoparticles. Physical Review B, 92(24), p.245130.

* denotes an equal contribution by the authors.

Selected conference contributions

[1] Rahimzadegan, A., Karamanos, T.D., Alaee, R., Lamprianidis, A.G., Beutel, D., Boyd, R.W. and Rockstuhl, C., 2021, September. Perfect diffractive metagratings designed with a multipolar lattice method (Conference Presentation). In the 15th International Congress on Artificial Materials for Novel Wave Phenomena (Metamaterials'2021), New York, USA.

[2] Rahimzadegan, A., Rockstuhl, C. and Alaee, R., 2020, April. Expressing Mie coefficients for absorbing isotropic particles in a generic fashion (Conference Presentation). In Metamaterials XII (Vol. 11344, p. 113441Q). International Society for Optics and Photonics.

[3] Rahimzadegan, A., Arslan, D., Suryadharma, R.N.S., Fasold, S., Falkner, M., Pertsch, T., Staude, I. and Rockstuhl, C., 2019, June. Disorder-induced phase transitions in an optical metasurface (Conference Presentation). In PhotonIcs & Electromagnetics Research Symposium (PIERS 2019), Rome, Italy.

[4] Rahimzadegan, A., Arslan, D., Dams, D., Groner, A., Garcia-Santiago, X., Alaee, R., Suryadarma, R.N.S., Fernandez-Corbaton, I., Pertsch, T., Staude, I. and Rockstuhl, C., 2019, May. Quadrupolar Huygens' metasurfaces for full-phase coverage holograms (Conference Presentation). In Photonics North 2019, Quebec City, Canada.

[5] Staude, I., Fasold, S., Arslan, D., Rahimzadegan, A., Kawde, T., Linss, S., Abbasirad, N., Falkner, M., Decker, M., Rockstuhl, C. and Pertsch, T., 2018, September. Disordered photonic metasurfaces for complex light field control

(Conference Presentation). In Plasmonics: Design, Materials, Fabrication, Characterization, and Applications XVI (Vol. 10722, p. 107221E). International Society for Optics and Photonics.

[6] Rahimzadegan, A., Arslan, D., Suryadharma, R.N.S., Fasold, S., Falkner, M., Pertsch, T., Staude, I. and Rockstuhl, C., 2018, August. Disorder-induced phase transitions in dielectric metasurfaces (Conference Presentation). In the 12th International Congress on Artificial Materials for Novel Wave Phenomena (Metamaterials'2018), Espoo, Finland.

[7] Arslan, D., Fasold, S., Rahimzadegan, A., Kawde, T., Linss, S., Abbasirad, N., Falkner, M., Decker, M., Rockstuhl, C., Pertsch, T. and Staude, I., 2018, July. Tailored structural disorder in optical metasurfaces. In 2018 Conference on Lasers and Electro-Optics Pacific Rim (CLEO-PR) (pp. 1-2). IEEE.

[8] Rahimzadegan, A., Alaee, R., Fernandez-Corbaton, I., Rahmanpanah, H., Jalali, A. and Rockstuhl, C., 2016, September. Maximum optical force and torque on multipolar meta-atoms (Conference Presentation). In the 10th International Congress on Advanced Electromagnetic Materials in Microwaves and Optics (Metamaterials'2016), Crete, Greece.

1. Introduction

Computers, smartphones, color televisions, smartwatches, and many other electronic devices widely accessible in our daily lives directly result from the miniaturization of various technologies [1, 2]. The rapid growth of nanofabrication in the past two decades has been a prominent driver for such a device miniaturization. Optical components are a crucial part of numerous high-tech applications. However, high-precision conventional optical components such as lenses, mirrors, polarizers, diffusers, splitters, etc., are bulky and often expensive [3]. These bulky components are a huge technological barrier against exploiting the immense potential of light in a future shaped by miniaturized technology. This challenge has motivated nanophotonics researchers for years to search for alternative approaches to mold the flow of light at the nanoscale.

Metasurfaces, i.e., 2D arrangement of nanoparticles, are promising candidates to replace bulky optical components [4–15]. The nanoparticles are referred to as *meta-atoms* throughout the thesis, as they are like the atoms, i.e., the building blocks, of metasurfaces and metamaterials. Metamaterials are bulk materials with properties not observed in nature [16–19]. Meta-atoms, made from high refractive index materials, and with a size comparable to the wavelength, can strongly interact with light. The strong interaction of a carefully arranged array of these meta-atoms enables the control of the light wave within an ultra-thin surface. Another prominent advantage of metasurfaces is their flat interface that makes them very suited to be fabricated within the mature field of nanofabrication [20–23]. Optical metasurfaces can efficiently control the amplitude, phase, and polarization of an incidence light wave-front. As a result, they are already integrated in a wide range of applications. Examples are absorbers [24, 25], reciprocal and nonreciprocal polarization rotators [26, 27], holograms [13, 14, 28–31], lenses [22, 32–35], splitters [36], diffusers [37, 38], light sails for space explorations [39, 40], sensing and biomedical applications [41–43], as well as computational and quantum applications [44, 45].

The growth of nanofabrication and the possibility of manufacturing many types of metasurfaces, whether ordered or disordered, has made the design and analysis of metasurfaces an ever-growing necessity. While full-wave numerical solutions are always an option, analytical tools can be much more appealing as they facilitate the

design and provide valuable insights into the underlying physics of metasurfaces. While periodic metasurfaces are more straightforward and computationally cheap to evaluate, the solution to the optical scattering of a disordered arrangement is very challenging and computationally expensive.

The most general and versatile approach to derive the optical scattering of metasurfaces is a bottom-up approach that reconstructs the scattered field by summing the radiation from all the meta-atoms. To solve such a scattering problem, we break it down into four phases from the bottom up:

I   Developing a suitable basis to describe electromagnetic wave propagation in a homogenous medium.

II Describing the optical response of a single meta-atom to an electromagnetic excitation inside the homogenous medium.

III Describing the optical response of a periodic arrangement of the meta-atoms.

IV Describing the optical response of disordered arrangements of the meta-atoms.

In *Phase I*, the electromagnetic waves, using *vector spherical harmonics*, are expanded into an orthonormal multipolar basis set. This expansion serves as a versatile platform to study scattering scenarios, i.e., the interaction of an incident field with an object that is localized in space [6, 46–49]. Throughout the thesis, we only consider plane waves as the illumination for these objects. However, any electromagnetic wave can be decomposed into a series of plane waves, which renders our approach quite versatile. The multipole expansion is discussed in detail in Chapter 2.

After developing an appropriate basis to expand an electromagnetic field, in *Phase II*, the optical scattering of a meta-atom upon a plane wave illumination is expressed in a series of multipole moments. Depending on the operating wavelength, size, shape, and material of the meta-atom, an ever-increasing number of multipole moments is required to accurately capture the meta-atom's response. In such a scenario, the relation between the expansion coefficient of the incident and the scattered field is expressed by a matrix. Two different but interchangeable formulations for this matrix exist. They are called the polarizability matrix and the T matrix. The equivalence of the two matrices has been explicitly documented up to octupolar order [50, 51]. The polarizability matrix expresses the scattering response in the Cartesian coordinates, while the T matrix expresses the scattering response in the spherical coordinates. Several methodologies have been developed to acquire the polarizability, and the T matrix for different geometries [52–57].

For an isotropic meta-atom, i.e., a sphere, the T matrix is diagonal, and the entries of the T matrix are derived from the well-known Mie coefficients [58]. Mie coefficients depend on many parameters, including the dimensions and optical properties of the spherical object and the medium. However, for fundamental research, as is the main aim of this thesis, it is essential to have expressions with the least number of degrees of freedom that cover all possible values of Mie coefficients within the existing physical constraints. While such expressions are known for spheres made from non-absorbing materials, in Chapter 3, based on our work in Ref. [59], we provide general expressions for isotropic meta-atoms, absorbing or non-absorbing.

Using this minimalist model, we can scan the entire accessible parameter space of spheres for specific functionalities in systems made from spherical scatterers, as we will show multiple times throughout the thesis. Additionally, based on our works in Ref. [31, 60, 61], we explore the optical response of anisotropic and bianisotropic meta-atoms.

In *Phase III*, the effort builds up from describing a single meta-atom to an infinitely periodic array of identical meta-atoms. In the infinitely periodic arrangement, deriving the optical response involves a challenging infinite sum over the lattice sites. Moreover, a description of the interaction among all the meta-atoms forming the periodic metasurfaces is crucial. Earlier works involved approximate expression for this purpose. They failed to accurately capture the spatial dispersion occurring in many applications where the metasurfaces are not operated in a deep sub-wavelength regime [62]. Later, efforts shifted into expressing the lattice interaction via fast converging Green's function summations [63]. Following this approach, modeling periodic arrangement of dipole moments at oblique incidence has been made possible [64–67]. Moreover, periodic arrangement of dipole and quadrupole [68], and even up to octupole moments at normal incidence [69], has been accommodated. However, these efforts were generally limited in scope, e.g., focusing on specific meta-atoms with specific combinations of multipole moments, or were limited to normal incidence. Furthermore, diffracting metasurfaces were not studied.

Recently, in the spherical coordinates, a numerical method was developed to calculate the complete response of a metasurface for arbitrary but identical meta-atom sand up to a desired multipolar order [70]. This approach that was based on previous efforts on isotropic meta-atoms [71, 72], employs the Ewald summation [73, 74] for the fast-converging determination of the lattice coupling. Although efficient, the method lacks closed-form analytical expressions and the interchangeability between spherical and Cartesian representations.

In Chapter 4, based on our work in Ref. [75], we provide a unifying and comprehensive framework to derive the optical response from periodic metasurfaces in the spherical and Cartesian bases. The derived expressions are based on a multipole expansion and accurately express the amplitudes of propagating diffraction orders of periodic metasurfaces upon illumination at normal or oblique incidence up to an octupolar order. In addition, assuming isotropic meta-atoms and the minimalist Mie model, we derive handy closed-form analytical formulas for specific cases. Such reduction eases physical explorations and simplifies the design process of a metasurface for specific applications. For instance, based on our work in Ref. [31], we have identified the upper limits for the induced multipole moments inside an infinitely periodic lattice.

When analyzing metasurfaces in this thesis, we frequently assume equal electric and magnetic induced moments. Such assumption for periodic metasurfaces results in the suppression of the reflection [19]. Such metasurface is called a *Huygens' metasurface*. The term "Huygens" refers to the Huygens' principle, which states that a set of secondary spherical wavelets can reconstruct a wavefront. This is similar to a Huygens' metasurface, where the induced moments of the meta-atoms, caused by the incident plane wave, act like a secondary source that reconstructs the plane wavefront in the forward direction. When the metasurface is made from non-absorbing meta-atoms, a unity optical transmittance is observed. At the same

time, the phase-angle of the transmission can be controlled by tuning the operating wavelength, or the periodicity of the lattice [76–81]. This high transmittance and phase shift control make Huygens' metasurfaces very efficient holograms [29, 82–84]. Huygens' metasurfaces are mostly considered within their dipolar response, i.e., only made from dipolar meta-atoms [77, 84–86]. In dipolar Huygens' metasurfaces made from identical meta-atoms, the achievable phase coverage by tuning the periodicity at a fixed wavelength is smaller than 2π. This disability to provide full phase-shift coverage is a clear limitation for applications in holograms. To lift such limitation, in Chapter 5, based on our work in Ref. [31], we consider dipolar-quadrupolar Huygens' metasurfaces and show that such metasurfaces offer access to the desired 2π phase-shift coverage.

After analyzing periodic metasurfaces, in *Phase IV*, we shift our focus to one of the most challenging scattering scenarios, i.e., describing the optical response of disordered metasurfaces. Disorder is ubiquitous, and hence, its analysis is essential for the understanding of nature. Complex systems are challenging to analyze, but the results are rewarding. This year's Nobel Prize in Physics (2021) was dedicated to the endeavors to handle complexity, from climate to the disorder in glass [87]. Light interaction with disordered materials is likewise intractable and, at the same time, fascinating. The theoretical study of light interactions in disordered media is a notoriously tricky problem. Especially for the considered resonant meta-atoms that strongly couple to each other, the analysis is even more challenging. Why disorder? The response to this question has many aspects. The disorder is ubiquitous in nature and is instead the norm. For understanding many phenomena in nature, the understanding of the disorder is crucial. Moreover, the disorder is not a nuisance but rather a design opportunity for novel optical devices. There are distinct features of disordered arrangements that are not always accessible with periodic arrays. The disorder itself unlocks a plethora of physical effects worth exploring, not only out of intellectual curiosity but also from an application perspective [66, 88–92].

The disorder that we study in this thesis involves *positional disorder* of identical meta-atoms on a surface. The disorder is not mere chaos [93] but rather a disturbance in otherwise ordered structures. What is a disorder? If this question was asked 40 years ago, the response seemed trivial; any *point configuration* that is not periodic is disordered. However, discovering quasicrystal as aperiodic but ordered structures initiated a paradigm shift. Quasicrystals do not have translational symmetry (i.e., no periodicity). However, they have strong Bragg peaks in their diffraction patterns [94]. These Bragg peaks were only found in periodic crystals. As a result of these discussions, the question might shift from "What is disorder?" to "What is the *degree of disorder*?".

The study of order (or disorder) metrics is an active area of research [95]. Several order metrics have been introduced [93, 96–98]. However, they can only capture a specific aspect, for example, translational or orientational pair correlations, and these metrics are often biased towards a reference. Since there is no perfect order metric [99, 100], it is inherently difficult to find a metric that correlates well with the optical effects seen in the conceptually vastly different disorder *point processes*. Therefore, the question that we address for several disorder models in this thesis is "What is the degree of disorder for a specific disorder point process?". The disorder point processes that we study in Chapter 6 are perturbed array, defected array,

Poisson's disorder, Matérn type-III soft-core and hard-core disorder, and selected hyperuniform point configurations. Although there is no universal disorder metric, we will study several disorder models with statistical measures such as the *pair correlation function*, the *structure factor*, and the *configurational entropy*. Using these measures, we can have a qualitative discussion over the long-range or short-range order with identifying *range of local order*.

After statistically analyzing the disordered point processes, we study the impact of the positional disorder on the optical response of dipolar Huygens' metasurfaces, namely the zeroth-order transmission and reflection, the effective dipole moments, and the directional scatterance. Based on our work in Ref. [101], we reveal an intriguing and unexplored feature: A disorder-induced phase transition in the phase angle of the transmission coefficient that changes from normal to anomalous dispersion above a critical threshold in the positional disorder. Based on this intriguing phenomenon, and grounded on our work in Ref. [38], we study the possibility of perfect metasurface-based optical diffusers.

Optical diffusers are key elements in various applications as diverse as illumination [102–104], imaging [90, 105–107], screens [108], microscopy [109–113], colorants [114–116], spectroscopy [117–119], photovoltaics [120–122] or wavefront shaping [123–125]. The main advantage of metasurface based diffusers would be the ultra-thin footprint of the device. Conventional diffusers are bulky and lack the potential to be integrated into miniaturized devises [126–137]. Moreover, the non-absorbing meta-atoms considered here, are preferred in terms of the optical response strength as compared to plasmonic counterparts [138–144].

In summary, the thesis aims to address the optical scattering of light from a metasurface in four steps: first, developing a basis for electromagnetic propagation in a homogenous medium (Chapter 2). Next, we analyze the interaction of a single meta-atom with a given illumination (Chapter 3). Then, we provide the analytical formalism for the optical response of arbitrary meta-atoms when arranged periodically (Chapter 4). Next, we study Huygens' metasurfaces and some other simplified specific cases (Chapter 5). Last but not least, we introduce statistical measures and disorder point processes and investigate the optical response of disordered metasurfaces using the insights and tools at hand (Chapter 6).

We have provided extensive formulations and systematic analysis of different ordered and disordered arrangements throughout the thesis. The systematic approach that we have followed aims at making a solid reference for future research.

Thesis structure

The thesis is structured as follows:

In Chapter 2, we discuss the propagation of an electromagnetic wave in a homogenous medium. In particular, we develop the multipole expansion of the electromagnetic waves that works as the basis for the rest of the thesis. Moreover, electromagnetic duality symmetry and helicity are introduced.

In Chapter 3, we discuss the optical scattering of light at a single meta-atom in a homogenous medium. We build the framework to analyze the electromagnetic response of an isolated meta-atom and introduce the normalized polarizability matrix

and T matrix. In particular, isotropic meta-atoms, as the backbone of our analysis, are investigated in depth. A minimalist model to parametrize any possible Mie coefficient of a spherical meta-atom is provided. Moreover, symmetries of the normalized polarizability and T matrices for meta-atoms with different geometrical symmetries are explored.

In Chapter 3, we discuss the optical scattering of light from a periodic metasurface. We build a comprehensive and unifying framework to analytically derive the optical scattering from a periodic arrangement of arbitrary meta-atoms under arbitrary plane wave excitation up to an octupolar order in the Cartesian and the spherical coordinates. Assuming isotropic meta-atoms, we derive analytical expressions for effective induced parameters of a meta-atom inside a lattice. Finally, transmission and reflection from single-resonance metasurfaces are studied.

In Chapter 5, we mostly explore Huygens' metasurfaces, dipolar, quadrupolar, and dipolar-quadrupolar. These three categories of Huygens' metasurfaces are classified based on the multipolar composition of their meta-atoms. We explore the phase-shift coverage of these unity-transmittance metasurfaces. Later, we analyze metagratings, as metasurfaces that diffract light due to periodicities that are longer than the wavelength. The focus is on the analytical equations that can describe the propagating diffracting modes from a periodic arrangement of isotropic meta-atoms illuminated under normal incidence up to a quadrupole order. The last section of the chapter explores dipolar metasurfaces under oblique incidence angles. In particular, we realize the Brewster angle for a single-resonance metasurface.

In Chapter 6, we discuss the optical scattering of disordered metasurfaces. We start by introducing statistical parameters that can be used to characterize disordered arrangements. Then, we introduce multiple types of disordered point processes and analyze them with statistical measures. Later, we calculate the optical transmission and reflection through the disordered metasurfaces and compare their optical response to their statistical measures. For the analysis, we assume dipolar Huygens' metasurfaces as the reference measure. Finally, the directional scatterance of the disordered metasurfaces are measured and analyzed, and metasurfaces with strong optical diffusion are identified.

2. Electromagnetic Waves

This chapter introduces bases to describe the electromagnetic waves inside a homogenous medium. In the first section, we introduce Maxwell's equations as the backbone of electromagnetics, and the response of homogenous materials with different symmetries to a given optical excitation is formulated. The following section explores the solutions to Maxwell's equations using the plane wave or multipolar waves in dedicated subsections. Finally, we introduce the electromagnetic duality symmetry and helicity.

The content of this chapter is partly based on our works in Ref. [38, 60, 145].

2.1 The Maxwell equations

Electromagnetism is one of the four fundamental forces in nature. Empirical Maxwell's equations govern the world of electromagnetism. The macroscopic Maxwell equations, in their differential form, read as [146, 147]:

$$
\begin{aligned}
\varepsilon_0 \nabla \cdot \underline{\mathbf{E}}\,(\mathbf{r},t) &= \underline{\rho}\,(\mathbf{r},t), & (2.1) \\
\nabla \cdot \underline{\mathbf{B}}\,(\mathbf{r},t) &= 0, & (2.2) \\
\nabla \times \underline{\mathbf{E}}\,(\mathbf{r},t) &= -\partial_t \underline{\mathbf{B}}\,(\mathbf{r},t), & (2.3) \\
\mu_0^{-1} \nabla \times \underline{\mathbf{B}}\,(\mathbf{r},t) &= \underline{\mathbf{j}}\,(\mathbf{r},t) + \varepsilon_0 \partial_t \underline{\mathbf{E}}\,(\mathbf{r},t), & (2.4)
\end{aligned}
$$

where $\mathbf{r}$ denotes the position vector, t denotes time, $\underline{\mathbf{E}}\,(\mathbf{r},t)$ is the *electric field* vector, $\underline{\mathbf{B}}\,(\mathbf{r},t)$ is the *magnetic induction* (or magnetic flux density) field vector, and $\underline{\mathbf{j}}\,(\mathbf{r},t)$ and $\underline{\rho}\,(\mathbf{r},t)$ are the *total current* and *charge densities*, respectively. $\varepsilon_0 \approx 8.85 \times 10^{-12}\,\mathrm{F/m}$ is the *free-space permittivity* and $\mu_0 = 4\pi \times 10^{-7}\,\mathrm{H/m}$ is the *free-space permeability*. The underline denotes quantities in the time domain, and it is used to distinguish them from quantities in the frequency domain.

The total current and charge densities comprise free and bound quantities and can be written as:

$$
\underline{\mathbf{j}}\,(\mathbf{r},t) = \underline{\mathbf{j}}_{\mathrm{free}}\,(\mathbf{r},t) + \underline{\mathbf{j}}_{\mathrm{bound}}\,(\mathbf{r},t) = \underline{\mathbf{j}}_{\mathrm{free}}\,(\mathbf{r},t) + \nabla \times \underline{\mathbf{M}}\,(\mathbf{r},t) - \partial_t \underline{\mathbf{P}}\,(\mathbf{r},t), \quad (2.5)
$$

$$
\underline{\rho}\,(\mathbf{r},t) = \underline{\rho}_{\mathrm{free}}\,(\mathbf{r},t) + \underline{\rho}_{\mathrm{bound}}\,(\mathbf{r},t) = \underline{\rho}_{\mathrm{free}}\,(\mathbf{r},t) - \nabla \cdot \underline{\mathbf{P}}\,(\mathbf{r},t), \quad (2.6)
$$

where $\underline{\mathbf{P}}\left(\mathbf{r},t\right)$ and $\underline{\mathbf{M}}\left(\mathbf{r},t\right)$ are the *electric* and *magnetic polarization* vectors inside the medium, respectively. The bound current and charge densities are caused by electromagnetic forces and depend on the excitation fields. Therefore, they can be integrated into new quantities to facilitate the solution of Maxwell's equations. Consequently, Maxwell's equations in a medium can be written as:

$$\nabla \cdot \underline{\mathbf{D}}\left(\mathbf{r},t\right) \;=\; \underline{\rho}_{\text{free}}\left(\mathbf{r},t\right), \tag{2.7}$$

$$\nabla \cdot \underline{\mathbf{B}}\left(\mathbf{r},t\right) \;=\; 0, \tag{2.8}$$

$$\nabla \times \underline{\mathbf{E}}\left(\mathbf{r},t\right) \;=\; -\partial_t \underline{\mathbf{B}}\left(\mathbf{r},t\right), \tag{2.9}$$

$$\nabla \times \underline{\mathbf{H}}\left(\mathbf{r},t\right) \;=\; \underline{\mathbf{j}}_{\text{free}}\left(\mathbf{r},t\right) + \partial_t \underline{\mathbf{D}}\left(\mathbf{r},t\right), \tag{2.10}$$

where $\underline{\mathbf{H}}$ is the *magnetic field* vector and $\underline{\mathbf{D}}$ is the *electric displacement field* vector [146], respectively. The newly defined fields are formulated as [146, 147]:

$$\underline{\mathbf{D}}\left(\mathbf{r},t\right) \;=\; \varepsilon_0 \underline{\mathbf{E}}\left(\mathbf{r},t\right) + \underline{\mathbf{P}}\left(\mathbf{r},t\right), \tag{2.11}$$

$$\underline{\mathbf{H}}\left(\mathbf{r},t\right) \;=\; \mu_0^{-1} \underline{\mathbf{B}}\left(\mathbf{r},t\right) - \underline{\mathbf{M}}\left(\mathbf{r},t\right). \tag{2.12}$$

For a general dispersive medium, the polarization vectors not only depend on the spatial distribution of the fields in the vicinity of the desired point in space $\mathbf{r}_0$ (spatial dispersion) but also on the temporal distribution of the fields before the desired point in time (temporal dispersion or simply dispersion). Suppose that the response of a medium to an electromagnetic excitation is linear and has a *weak spatial dispersion*. In that case, the fields inside the medium can be expressed using the most general linear and local *constitutive relations* [148]:

$$\underline{\mathbf{D}}\left(\mathbf{r},t\right) = \int_{t'} \left[\bar{\bar{\varepsilon}}\left(\mathbf{r},t'\right) \cdot \underline{\mathbf{E}}\left(\mathbf{r},t-t'\right) + \bar{\bar{\xi}}\left(\mathbf{r},t'\right) \cdot \underline{\mathbf{H}}\left(\mathbf{r},t-t'\right) \right] \mathrm{d}t', \tag{2.13}$$

$$\underline{\mathbf{B}}\left(\mathbf{r},t\right) = \int_{t'} \left[\bar{\bar{\zeta}}\left(\mathbf{r},t'\right) \cdot \underline{\mathbf{E}}\left(\mathbf{r},t-t'\right) + \bar{\bar{\mu}}\left(\mathbf{r},t'\right) \cdot \underline{\mathbf{H}}\left(\mathbf{r},t-t'\right) \right] \mathrm{d}t', \tag{2.14}$$

where $\bar{\bar{\varepsilon}}\left(\mathbf{r},t'\right)$, $\bar{\bar{\xi}}\left(\mathbf{r},t'\right)$, $\bar{\bar{\zeta}}\left(\mathbf{r},t'\right)$ and $\bar{\bar{\mu}}\left(\mathbf{r},t'\right)$ are the *constitutive dyadics*. A dyad is a second order tensor or a 3 by 3 square matrix. Equations 2.13-2.14 describe the general linear constitutive relations for a bianisotropic medium and can be used to supplement the Maxwell's equations. Moreover, the polarization vectors $\underline{\mathbf{P}}\left(\mathbf{r},t\right)$ and $\underline{\mathbf{M}}\left(\mathbf{r},t\right)$ can be derived from the constitutive relations. The nomenclature prefix "bi" reflects the magneto-electric effect these constitutive relations do capture, in which a magnetic field induces an electric polarization and an electric field induces a magnetic polarization [148, 149], respectively.

It is worth noting that for the linear, local and dispersive medium described above, the standard interface conditions hold; the tangential components of $\underline{\mathbf{E}}\left(\mathbf{r},t\right)$ and the normal components of $\underline{\mathbf{B}}\left(\mathbf{r},t\right)$ are continuous. Moreover, there is a jump equal to the free surface current density in the tangential components of $\underline{\mathbf{H}}\left(\mathbf{r},t\right)$ and a jump equal to the free charge density in the normal components of $\mathbf{D}\left(\mathbf{r},t\right)$ [149].

The following section explores some selected solutions to Maxwell's equations for a homogenous medium. For a homogenous medium, the constitutive dyadics do not depend on the position vector.

2.2   Solving Maxwell's equations

After considering additional assumptions based on our problem, this section provides some known analytical solutions to Maxwell's equation.

We often encounter time-harmonic electromagnetic oscillations, and we restrict our considerations to the realm of linear electromagnetism, which renders the Fourier basis a versatile platform to solve Maxwell's equations. In the Fourier series, a mathematical function is projected into an infinite sum of sinusoidal harmonic oscillations having different weights.

The Fourier transform pair may be defined as [146]:

$$\mathbf{A}\left(\mathbf{r},\omega\right)=\int_{-\infty}^{-\infty}\underline{\mathbf{A}}\left(\mathbf{r},t\right)e^{i\omega t}\mathrm{d}t,\quad\underline{\mathbf{A}}\left(\mathbf{r},t\right)=\frac{1}{2\pi}\int_{-\infty}^{-\infty}\mathbf{A}\left(\mathbf{r},\omega\right)e^{-i\omega t}\mathrm{d}\omega. \tag{2.15}$$

where, here, we transform the quantities between the time domain and the frequency domain. Note that the real-valued fields are derived by taking the real part of the complex Fourier counterpart. We continue using complex quantities as they are easier to handle.

We start by transforming the constitutive relations in Equations 2.13-2.14 into the frequency domain:

$$\mathbf{D}\left(\mathbf{r},\omega\right)=\bar{\bar{\varepsilon}}\left(\mathbf{r},\omega\right)\cdot\mathbf{E}\left(\mathbf{r},\omega\right)+\bar{\bar{\xi}}\left(\mathbf{r},\omega\right)\cdot\mathbf{H}\left(\mathbf{r},\omega\right), \tag{2.16}$$
$$\mathbf{B}\left(\mathbf{r},\omega\right)=\bar{\bar{\zeta}}\left(\mathbf{r},\omega\right)\cdot\mathbf{E}\left(\mathbf{r},\omega\right)+\bar{\bar{\mu}}\left(\mathbf{r},\omega\right)\cdot\mathbf{H}\left(\mathbf{r},\omega\right). \tag{2.17}$$

Throughout the thesis, we assume linear, isotropic, and homogenous media with no bianisotropic coupling. These assumptions greatly simplify the relations, and the constitutive dyadics become scalar quantities. Consequently, the constitutive relations simplify to:

$$\mathbf{D}\left(\mathbf{r},\omega\right)=\varepsilon_0\varepsilon_\mathrm{e}\left(\omega\right)\mathbf{E}\left(\mathbf{r},\omega\right),\quad\mathbf{B}\left(\mathbf{r},\omega\right)=\mu_0\mu_\mathrm{e}\left(\omega\right)\mathbf{H}\left(\mathbf{r},\omega\right), \tag{2.18}$$

where $\varepsilon\left(\omega\right)=\varepsilon_0\varepsilon_\mathrm{e}\left(\omega\right)$ and $\mu\left(\omega\right)=\mu_0\mu_\mathrm{e}\left(\omega\right)$ are the permittivity and permeability of the medium, and $\varepsilon_\mathrm{e}\left(\omega\right)$ and $\mu_\mathrm{e}\left(\omega\right)$ are the relative permittivity and permeability of the medium, respectively.

Another simplification concerns the free sources that in optics are frequently considered as absent (i.e., $\underline{\mathbf{j}}_\mathrm{free}\left(\mathbf{r},t\right)=\underline{\rho}_\mathrm{free}\left(\mathbf{r},t\right)=0$). Therefore, altogether, the differential Maxwell equations in the frequency domain in a source-free medium are simplified to:

$$\nabla\cdot\mathbf{E}\left(\mathbf{r},\omega\right)\ =\ 0, \tag{2.19}$$
$$\nabla\cdot\mathbf{H}\left(\mathbf{r},\omega\right)\ =\ 0, \tag{2.20}$$
$$\nabla\times\mathbf{E}\left(\mathbf{r},\omega\right)\ =\ i\omega\mu\left(\omega\right)\mathbf{H}\left(\mathbf{r},\omega\right), \tag{2.21}$$
$$\nabla\times\mathbf{H}\left(\mathbf{r},\omega\right)\ =\ -i\omega\varepsilon\left(\omega\right)\mathbf{E}\left(\mathbf{r},\omega\right). \tag{2.22}$$

By combining the latter two equations, the vector wave equation, known as the *vector Helmholtz equation*, can be derived for the electric and magnetic fields:

$$\left[\triangle+k^2\left(\omega\right)\right]\mathbf{E}\left(\mathbf{r},\omega\right)=0, \tag{2.23}$$
$$\left[\triangle+k^2\left(\omega\right)\right]\mathbf{H}\left(\mathbf{r},\omega\right)=0, \tag{2.24}$$

where $k(\omega) = \omega n(\omega)/c$ is the *wavenumber*, $c_0 = 1/\sqrt{\varepsilon_0 \mu_0} \approx 2.998 \times 10^8 \, \text{m/s}$, is the speed of light in free space, and $n(\omega) = \sqrt{\mu_\text{e}(\omega) \varepsilon_\text{e}(\omega)}$ is the refractive index of the medium, respectively.

The wave equation relates the time evolution of an electric or a magnetic field to its space evolution, i.e., it describes wave propagation. Of course, the wave equation needs to be solved to determine if a propagating wave is permissible. Any field vector pair ($\mathbf{E}(\mathbf{r}, \omega)$ and $\mathbf{H}(\mathbf{r}, \omega)$) satisfying Eq. 2.23-2.24 that is in addition free of divergence (i.e., *solenoidal*), is a solution to Maxwell's equations. Equations 2.23-2.24 can be solved in many coordinate systems [150].

Vector differential equations are complicated to solve. Therefore, to ease the solution, we transform the vector wave equations into scalar equations. For that aim, we define an orthogonal basis (known as *vector harmonics*) as:

$$\mathbf{L}(\mathbf{r}, \omega) = \frac{\nabla \psi(\mathbf{r}, \omega)}{k(\omega)}, \tag{2.25}$$

$$\mathbf{M}(\mathbf{r}, \omega) = \nabla \times [\mathbf{v}(\mathbf{r}, \omega) \psi(\mathbf{r}, \omega)], \tag{2.26}$$

$$\mathbf{N}(\mathbf{r}, \omega) = \frac{\nabla \times \nabla \times [\mathbf{v}(\mathbf{r}, \omega) \psi(\mathbf{r}, \omega)]}{k(\omega)}, \tag{2.27}$$

where $\psi(\mathbf{r}, \omega)$ is the *scalar generating function* and $\mathbf{v}(\mathbf{r}, \omega)$ is the *pilot vector*. The pilot vector is chosen based on the coordinate system in which we want to solve the equation. Note that $\mathbf{M}(\mathbf{r}, \omega)$ and $\mathbf{N}(\mathbf{r}, \omega)$ are solenoidal vectors.

While assuming that the pilot vector is a linear function of the position vector $\mathbf{r}$ (i.e., $\mathbf{v}(\mathbf{r}, \omega) = c_1(\omega) \mathbf{r} + c_2(\omega)$), and inserting $\mathbf{M}(\mathbf{r}, \omega)$, as a potential field solution, into the vector Helmholtz equation, it is rewritten as:

$$\left[\nabla^2 + k^2(\omega) \right] \mathbf{M}(\mathbf{r}, \omega) = \nabla \times \left\{ \mathbf{v}(\mathbf{r}, \omega) \left[\nabla^2 \psi(\mathbf{r}, \omega) + k^2(\omega) \psi(\mathbf{r}, \omega) \right] \right\} = 0. \tag{2.28}$$

It can be seen that if the scalar function $\psi(\mathbf{r}, \omega)$ solves the *scalar Helmholtz equation* (the equation inside the square brackets), then the vector harmonics $\mathbf{M}(\mathbf{r}, \omega)$ is a solution of the vector Helmholtz equation. The same can also be shown for the vector harmonics $\mathbf{N}(\mathbf{r}, \omega)$. Therefore, in case, a solution $\psi(\mathbf{r}, \omega)$ is found, $\mathbf{M}(\mathbf{r}, \omega)$ and $\mathbf{N}(\mathbf{r}, \omega)$, that are also divergence-free, can be used to generate electric or magnetic fields. Hence, these fields are the solutions to the Maxwell equations.

If $\psi(\mathbf{r}, \omega)$ is a solution of the scalar Helmholtz equation, $\mathbf{L}(\mathbf{r}, \omega)$ satisfies the vector Helmholtz equation. However, $\mathbf{L}(\mathbf{r}, \omega)$ is not divergence-free. Therefore, here, it cannot be used to expand the electric or the magnetic field, and we do not consider it in the future calculations. Nevertheless, in a medium with free sources, $\mathbf{L}(\mathbf{r}, \omega)$ can be exploited [151–154].

As a result of the above discussions, the vector Helmholtz equation transforms into a scalar equation:

$$\nabla^2 \psi(\mathbf{r}, \omega) + k^2(\omega) \psi(\mathbf{r}, \omega) = 0, \tag{2.29}$$

and when a solution is found, the electric and magnetic fields can be built using equations 2.26-2.27 that will be the solutions to the vector Helmholtz equation. The vector harmonics $\mathbf{M}(\mathbf{r}, \omega)$ and $\mathbf{N}(\mathbf{r}, \omega)$ also satisfy the following equations:

$$\nabla \cdot \mathbf{M}(\mathbf{r}, \omega) = \nabla \cdot \mathbf{N}(\mathbf{r}, \omega) = 0, \tag{2.30}$$

$$\nabla \times \mathbf{M}(\mathbf{r}, \omega) = k(\omega)\mathbf{N}(\mathbf{r}, \omega), \tag{2.31}$$

$$\nabla \times \mathbf{N}(\mathbf{r}, \omega) = k(\omega)\mathbf{M}(\mathbf{r}, \omega). \tag{2.32}$$

In the following subsections, we will solve the scalar Helmholtz equation in the plane wave and spherical bases.

2.2.1 Plane-wave expansion

Using the vector harmonics mentioned above, this subsection solves the wave equation in the Cartesian coordinates.

The scalar Helmholtz equation (Eq. 2.29) in the Cartesian basis reads as:

$$\nabla^2 \psi(x, y, z, \omega) + k^2(\omega)\psi(x, y, z, \omega) = 0. \tag{2.33}$$

By applying the operator, the equation is written as:

$$\left[\partial_{xx}^2 + \partial_{yy}^2 + \partial_{zz}^2 + k(\omega)^2\right]\psi(x, y, z, \omega) = 0. \tag{2.34}$$

For solving the above linear partial differential equation, we use the method of separation of variables. This method was initially suggested by J. d'Alembert (1749) to solve the wave equation [155]. We can simplify the partial differential equations to ordinary differential equations and facilitate its solution using this method. The scalar function $\psi(x, y, z, \omega)$ is separated into three functions, each depending on only a single position argument:

$$\psi(x, y, z, \omega) = X(x, \omega)Y(y, \omega)Z(z, \omega). \tag{2.35}$$

Replacing the scalar function $\psi(x, y, z, \omega)$ into Eq. 2.34, the wave equation is written as:

$$\frac{\partial_x^2 X(x, \omega)}{k(\omega)^2 X(x, \omega)} + \frac{\partial_y^2 Y(y, \omega)}{k(\omega)^2 Y(y, \omega)} + \frac{\partial_z^2 Z(z, \omega)}{k(\omega)^2 Z(z, \omega)} + 1 = 0. \tag{2.36}$$

Each term of the above equation, at a given frequency, only depends on a single but different function. Therefore, the only viable solution to the differential equation is when each term is constant. In other words, any solution to Eq. 2.36 satisfies the following equations:

$$\frac{\partial_x^2 X(x, \omega)}{X(x, \omega)} = -[c_x(\omega)k(\omega)]^2, \tag{2.37}$$

$$\frac{\partial_y^2 Y(y, \omega)}{Y(y, \omega)} = -[c_y(\omega)k(\omega)]^2, \tag{2.38}$$

$$\frac{\partial_z^2 Z(z, \omega)}{Z(z, \omega)} = -[c_z(\omega)k(\omega)]^2, \tag{2.39}$$

where $c_x(\omega)^2 + c_y(\omega)^2 + c_z(\omega)^2 = 1$. Without loss of generality, we can define:

$$k_x(\omega) = c_x(\omega) k(\omega), \quad k_y(\omega) = c_y(\omega) k(\omega), \quad k_z(\omega) = c_z(\omega) k(\omega), \quad (2.40)$$

where $k_x(\omega)^2 + k_y(\omega)^2 + k_z(\omega)^2 = k(\omega)^2$. As it will be more clear later, $k(\omega)$ is the *wavenumber*. Then, the equations to be solved simplify to:

$$\frac{\partial_x^2 X(x,\omega)}{X(x,\omega)} + k_x(\omega)^2 = 0, \quad \frac{\partial_y^2 Y(y,\omega)}{Y(y,\omega)} + k_y(\omega)^2 = 0, \quad \frac{\partial_z^2 Z(z,\omega)}{Z(z,\omega)} + k_z(\omega)^2 = 0.$$
$$(2.41)$$

The solution to the above ordinary differential equations are known and can be written as:

$$X(x,\omega) = g_{x1}(\omega) e^{ik_x(\omega)x} + g_{x2}(\omega) e^{-ik_x(\omega)x}, \qquad (2.42)$$
$$Y(y,\omega) = g_{y1}(\omega) e^{ik_y(\omega)y} + g_{y2}(\omega) e^{-ik_y(\omega)y}, \qquad (2.43)$$
$$Z(z,\omega) = g_{z1}(\omega) e^{ik_z(\omega)z} + g_{z2}(\omega) e^{-ik_z(\omega)z}. \qquad (2.44)$$

Therefore, from the solution, we can construct the following basis:

$$\psi_{\mathbf{k}}(\mathbf{r},\omega) = e^{i\mathbf{k}(\omega)\cdot\mathbf{r}}, \qquad (2.45)$$

where $\mathbf{k}(\omega) = [k_x(\omega), k_y(\omega), k_z(\omega)]$ is the *wavevector*. Equation 2.45 is the eigenfunction of the scalar Helmholtz equation 2.33 and can be used to expand electromagnetic fields. The $e^{-i\mathbf{k}(\omega)\cdot\mathbf{r}}$ solutions are ignored to respect the physical constraints.

To define the electromagnetic fields, using equations 2.26-2.27, we need to define a pilot vector. Since, in this thesis, we mostly deal with metasurfaces, we define a constant normal surface $\mathbf{n}$ and use it to define the pilot vector in the Cartesian basis. We define the pilot vector as $\mathbf{v}(\mathbf{r},\omega) = \hat{\mathbf{n}}/(k(\omega)\sin\theta)$, where $\hat{\mathbf{n}}$ is the unit normal vector to the metasurface and θ is the angle that the wavevector makes with the metasurface normal $\mathbf{n}$, i.e, $\cos\theta = \mathbf{k}(\omega)\cdot\hat{\mathbf{n}}/k(\omega)$. Then, the vector harmonics become [38]:

$$\mathbf{M}_{\mathbf{k}}(\mathbf{r},\omega) = \nabla \times \left[\frac{\hat{\mathbf{n}}}{k(\omega)\sin\theta}\psi_{\mathbf{k}}(\mathbf{r},\omega)\right] = \frac{i}{\sin\theta}\hat{\mathbf{k}} \times \hat{\mathbf{n}}e^{i\mathbf{k}(\omega)\cdot\mathbf{r}}, \qquad (2.46)$$

$$\mathbf{N}_{\mathbf{k}}(\mathbf{r},\omega) = \frac{\nabla \times \nabla \times}{k(\omega)}\left[\frac{\hat{\mathbf{n}}\psi_{\mathbf{k}}(\mathbf{r},\omega)}{k\sin\theta}\right] = \frac{-e^{i\mathbf{k}(\omega)\cdot\mathbf{r}}}{\sin\theta}\hat{\mathbf{k}} \times \mathbf{M}(\mathbf{r},\omega) = \frac{e^{i\mathbf{k}(\omega)\cdot\mathbf{r}}}{\sin\theta}\left(\cos\theta\hat{\mathbf{n}} - \hat{\mathbf{k}}\right),$$

where $\hat{\mathbf{k}}$ is the unit wavevector. Assuming a metasurface in the x-y plane (i.e., $\hat{\mathbf{n}} = \hat{\mathbf{z}}$), and transforming the wavevector into the spherical coordinates (i.e., $\mathbf{k}(\omega) = k_0(\omega)\hat{\mathbf{k}} = k_0(\omega)[\sin\theta\cos\phi\hat{\mathbf{x}} + \sin\theta\sin\phi\hat{\mathbf{y}} + \cos\theta]$), we can write:

$$\mathbf{M}_{\mathbf{k}}(\mathbf{r},\omega) = \begin{bmatrix} \sin\phi \\ -\cos\phi \\ 0 \end{bmatrix} ie^{i\mathbf{k}(\omega)\cdot\mathbf{r}}, \quad \mathbf{N}_{\mathbf{k}}(\mathbf{r},\omega) = -\begin{bmatrix} \cos\theta\cos\phi \\ \cos\theta\sin\phi \\ -\sin\theta \end{bmatrix} e^{i\mathbf{k}(\omega)\cdot\mathbf{r}}, \quad (2.47)$$

where $\mathbf{M}_{\mathbf{k}}(\mathbf{r},\omega)$ ($\mathbf{N}_{\mathbf{k}}(\mathbf{r},\omega)$) is oriented along TE (TM) polarization. Then, we can write any electric field distribution in terms of these vector harmonics as:

$$\mathbf{E}(\mathbf{r},\omega) = \frac{1}{4\pi^2}\int_{\mathbf{k}(\omega)}\left[b_{\mathbf{k}}^{\mathrm{TM}}(\omega)\mathbf{N}_{\mathbf{k}}(\mathbf{r},\omega) + b_{\mathbf{k}}^{\mathrm{TE}}(\omega)\mathbf{M}_{\mathbf{k}}(\mathbf{r},\omega)\right]d\mathbf{k}(\omega), \qquad (2.48)$$

where, $b_{\mathbf{k}}^{\mathrm{TM}}(\omega)$ and $b_{\mathbf{k}}^{\mathrm{TE}}(\omega)$ are the amplitude coefficients with TE and TM polarizations, respectively. The spatial Fourier transform of the above equation, at a constant plane $z = z_0$, is [38, 156]:

$$\mathbf{E}(\mathbf{k}) = \int_{-\infty}^{\infty} \int_{-\infty}^{\infty} \mathbf{E}(x, y, z_0, \omega) e^{-i\mathbf{k}\cdot\mathbf{r}} dxdy = i b_{\mathbf{k}}^{\mathrm{TE}}(\mathbf{k}) \hat{\mathbf{M}}_{\mathbf{k}} - b_{\mathbf{k}}^{\mathrm{TM}}(\mathbf{k}) \hat{\mathbf{N}}_{\mathbf{k}}, \quad (2.49)$$

where:

$$\hat{\mathbf{M}}_{\mathbf{k}} = \begin{bmatrix} \sin\phi \\ -\cos\phi \\ 0 \end{bmatrix}, \quad \hat{\mathbf{N}}_{\mathbf{k}} = -\begin{bmatrix} \cos\theta\cos\phi \\ \cos\theta\sin\phi \\ -\sin\theta \end{bmatrix}, \quad (2.50)$$

where $\hat{\mathbf{M}}_{\mathbf{k}}$ and $\hat{\mathbf{N}}_{\mathbf{k}}$ are the expanding unit vectors. The expansion coefficients can be found from scalar projections:

$$b_{\mathbf{k}}^{\mathrm{TE}}(\mathbf{k}) = -i\,\hat{\mathbf{M}}_{\mathbf{k}} \cdot \mathbf{E}(\mathbf{k}), \quad b_{\mathbf{k}}^{\mathrm{TM}}(\mathbf{k}) = -\hat{\mathbf{N}}_{\mathbf{k}} \cdot \mathbf{E}(\mathbf{k}). \quad (2.51)$$

Alternatively, using the orthogonality relations [38], the amplitude coefficients can also be derived through the following equations:

$$b_{\mathbf{k}}^{\mathrm{TE}}(\omega) = \int_{-\infty}^{\infty} \int_{-\infty}^{\infty} \mathbf{M}_{\mathbf{k}}^{*}(x, y, z_0, \omega) \cdot \mathbf{E}(x, y, z_0, \omega)\, dxdy, \quad (2.52)$$

$$b_{\mathbf{k}}^{\mathrm{TM}}(\omega) = \int_{-\infty}^{\infty} \int_{-\infty}^{\infty} \mathbf{N}_{\mathbf{k}}^{*}(x, y, z_0, \omega) \cdot \mathbf{E}(x, y, z_0, \omega)\, dxdy. \quad (2.53)$$

For a monochromatic plane-wave excitation that is propagating in the z-direction (i.e., $\theta = 0$, and $\mathbf{k}(\omega) = k_0(\omega) n\hat{\mathbf{z}}$), the electric field can be written as:

$$\mathbf{E}^{\mathrm{TE}}(\mathbf{r}, \omega) = \frac{i}{4\pi^2} b^{\mathrm{TE}}(\omega) \begin{bmatrix} \sin\phi \\ -\cos\phi \\ 0 \end{bmatrix} e^{i\mathbf{k}(\omega)\cdot\mathbf{r}}, \quad (2.54)$$

$$\mathbf{E}^{\mathrm{TM}}(\mathbf{r}, \omega) = \frac{-1}{4\pi^2} b^{\mathrm{TM}}(\omega) \begin{bmatrix} \cos\phi \\ \sin\phi \\ 0 \end{bmatrix} e^{i\mathbf{k}(\omega)\cdot\mathbf{r}}. \quad (2.55)$$

The plane-wave basis, developed here, is used in Chapter 6, to define the diffusion of light from disordered metasurfaces.

The following subsection solves Maxwell's equations in the spherical coordinates.

2.2.2 Multipole expansion

In the spherical coordinates, the scalar Helmholtz equation (2.29) is written as:

$$\nabla^2 \psi(r, \theta, \phi, \omega) + k^2(\omega) \psi(r, \theta, \phi, \omega) = \quad (2.56)$$

$$\left[\frac{1}{r^2} \partial_r (r^2 \partial_r) + \frac{1}{r^2 \sin\theta} \partial_\theta (\sin\theta \partial_\theta) + \frac{1}{r^2 \sin^2\theta} \partial_\phi^2 + k(\omega)^2 \right] \psi(r, \theta, \phi, \omega) = 0.$$

Similar to the previous subsection, we utilize the method of separation of variables to solve the wave equation in the spherical coordinates. The scalar function $\psi(r, \theta, \phi, \omega)$ is separated into three functions:

$$\psi(r, \theta, \phi, \omega) = R(r, \omega)\,\Theta(\theta, \omega)\,\Phi(\phi, \omega). \tag{2.57}$$

Plugging the above ansatz into Eq. 2.56 and solving it for each separate function, the final result can be written as the following infinite sum [48, 146, 157]:

$$\psi^{(J)}(kr, \theta, \phi) = \sum_{j,m} \gamma_{jm} z_j^{(J)}(kr)\,Y_j^m(\theta, \phi), \tag{2.58}$$

where $j = \{1, 2, 3, ...\}$ denotes the multipolar order corresponding to dipole ($j = 1$), quadrupole ($j = 2$), octupole ($j = 3$), and so on. Alternatively, j can be labeled as the total angular momentum quantum number. $m = \{-j, -j+1, ..., j-1, j\}$ denotes the angular momentum quantum number along a certain quantization axis. $J = 1, 2, 3, 4$ specifies the radial function used to expand the function: $z_j^{(1)}(kr) = j_j(kr)$, $z_j^{(2)}(kr) = y_j(kr)$, $z_j^{(3)}(kr) = h_j^{(1)}(kr)$, and $z_j^{(4)}(kr) = h_j^{(2)}(kr)$. $j_j(kr)$ and $y_j(kr)$ denote the spherical Bessel functions of first and second kind, respectively. Moreover, $h_j^{(1)}(kr)$ and $h_j^{(2)}(kr)$ denote the spherical Hankel functions of first and second kind, respectively. Subsequently, $Y_j^m(\theta, \phi) = P_j^m(\cos\theta)\exp(im\phi)$ are the well-known spherical harmonics. $P_j^m(x)$ are the associated Legendre polynomials defined as [48]:

$$P_j^m(x) = (-1)^m \left(1 - x^2\right)^{m/2} \frac{\mathrm{d}^m}{\mathrm{d}x^m} P_j(x), \tag{2.59}$$

where $P_j(x)$ are the Legendre polynomials:

$$P_j(x) = \frac{1}{2^j j!} \frac{\mathrm{d}^j}{\mathrm{d}x^j} \left(x^2 - 1\right)^j, \tag{2.60}$$

and γ_{jm} are the normalization constants:

$$\gamma_{jm} = \frac{1}{\sqrt{4\pi}} \sqrt{\frac{(2j+1)}{j(j+1)}} \sqrt{\frac{(j-m)!}{(j+m)!}}. \tag{2.61}$$

Finally, to write down the vector solution, we use the pilot vector $\mathbf{v}(\mathbf{r}, \omega) = \mathbf{r}$ [48]. Then, the *vector spherical harmonics* (VSH) are derived as:

$$\mathbf{L}_{jm}^{(J)}(\mathbf{r}, \omega) = \frac{1}{k} \nabla \left[\gamma_{jm} z_j^{(J)}(kr) P_j^m(\cos\theta)\exp(im\phi)\right], \tag{2.62}$$

$$\mathbf{M}_{jm}^{(J)}(\mathbf{r}, \omega) = \gamma_{jm} z_j^{(J)}(kr)\exp(im\phi)\left[i\pi_{jm}(\cos\theta)\,\mathbf{e}_\theta - \tau_{jm}(\cos\theta)\,\mathbf{e}_\phi\right], \tag{2.63}$$

$$\mathbf{N}_{jm}^{(J)}(\mathbf{r}, \omega) = \gamma_{jm} j(j+1) P_j^m(\cos\theta) \frac{z_j^{(J)}(kr)}{kr}\exp(im\phi)\,\mathbf{e}_r \tag{2.64}$$

$$+ \frac{\gamma_{jm}}{kr} \frac{d}{dr}\left[r\, z_j^{(J)}(kr)\right]\exp(im\phi)\left[\tau_{jm}(\cos\theta)\,\mathbf{e}_\theta + i\pi_{jm}(\cos\theta)\,\mathbf{e}_\phi\right],$$

where:

$$\pi_{jm}(\cos\theta) = \frac{m}{\sin\theta} P_j^m(\cos\theta), \quad \tau_{jm}(\cos\theta) = \frac{d}{d\theta} P_j^m(\cos\theta). \tag{2.65}$$

In addition to the properties in Eq. 2.30-2.32, the following orthogonality relations hold for all possible j, m, j', and m': $\int \mathbf{M}_{nm}^{(J)}(\mathbf{r},\omega) \cdot \mathbf{N}_{n'm'}^{(J)}(\mathbf{r},\omega) \, d\Omega = \int \mathbf{M}_{nm}^{(J)}(\mathbf{r},\omega) \cdot \mathbf{L}_{n'm'}^{(J)}(\mathbf{r},\omega) \, d\Omega = \int \mathbf{N}_{nm}^{(J)}(\mathbf{r},\omega) \cdot \mathbf{L}_{n'm'}^{(J)}(\mathbf{r},\omega) \, d\Omega = 0$, where Ω is a closed solid angle.

Vector spherical harmonics form a complete base in the three-dimensional vector space and, therefore, any electromagnetic wave field can be expanded as a superposition of the vector bases weighted with suitable amplitude coefficients $b_{jm}^{\mathrm{e}}(\omega)$ and $b_{jm}^{\mathrm{m}}(\omega)$ as:

$$\mathbf{E}(\mathbf{r},\omega) = \sum_{j=1}^{\infty} \sum_{m=-n}^{n} \left[b_{jm}^{\mathrm{e}}(\omega) \, \mathbf{N}_{jm}^{(J)}(\mathbf{r},\omega) + b_{jm}^{\mathrm{m}}(\omega) \, \mathbf{M}_{jm}^{(J)}(\mathbf{r},\omega) \right]. \tag{2.66}$$

The choice of J should respect the physical constraints on the fields at the origin ($kr \to 0$) and infinity ($kr \to \infty$). $\mathbf{N}_{jm}^{(1)}(\mathbf{r},\omega)$ and $\mathbf{N}_{jm}^{(1)}(\mathbf{r},\omega)$ are the *regular VSH* that are finite at the origin and, hence, are used to expand the incident field. $\mathbf{N}_{jm}^{(3)}(\mathbf{r},\omega)$ and $\mathbf{N}_{jm}^{(3)}(\mathbf{r},\omega)$ are the *outgoing VSH* that are finite at infinity and, hence, are used to expand the scattered field.

At the far-field, where ($kr \to \infty$), the scattered field, expanded by the outgoing fields, can be written as [48]:

$$\lim_{kr \to \infty} \mathbf{E}(\mathbf{r},\omega) = \frac{e^{i\mathbf{k}(\omega)\cdot\mathbf{r}}}{k(\omega)r} \boldsymbol{f}(\theta,\phi,\omega), \tag{2.67}$$

where $\boldsymbol{f}(\theta,\phi,\omega)$ contains the sum over j and m. This function, does not have the position dependency, and denotes the form of the angular optical scattering of the meta-atom and, hence, is known as the *form factor*.

If the fields are known, using the orthogonality relations [48], the amplitude coefficients of the VSH $b_{jm}^{\mathrm{e}}(\omega)$ and $b_{jm}^{\mathrm{m}}(\omega)$ can be derived by integrating the fields across a closed spherical surface of arbitrary radius r_0 as:

$$b_{jm}^{\mathrm{e}}(\omega) = \frac{\int_0^{2\pi} d\phi \int_0^{\pi} \mathbf{E}(r_0,\theta,\phi,\omega) \cdot \left[\mathbf{N}_{jm}^{(J)}(r_0,\theta,\phi,\omega) \right]^* \sin\theta \, d\theta}{\int_0^{2\pi} d\phi \int_0^{\pi} \left| \mathbf{N}_{jm}^{(J)}(r_0,\theta,\phi,\omega) \right|^2 \sin\theta \, d\theta}, \tag{2.68}$$

$$b_{jm}^{\mathrm{m}}(\omega) = \frac{\int_0^{2\pi} d\phi \int_0^{\pi} \mathbf{E}(r_0,\theta,\phi,\omega) \cdot \left[\mathbf{M}_{jm}^{(J)}(r_0,\theta,\phi,\omega) \right]^* \sin\theta \, d\theta}{\int_0^{2\pi} d\phi \int_0^{\pi} \left| \mathbf{M}_{jm}^{(J)}(r_0,\theta,\phi,\omega) \right|^2 \sin\theta \, d\theta}. \tag{2.69}$$

To expand the scattered field from a meta-atom, choosing a radius r_0 that is larger than the radius of the smallest sphere circumscribing the meta-atom is crucial.

Considering the symmetry properties of the VSH $\mathbf{M}^{(J)}(\mathbf{r},\omega)$ and $\mathbf{N}^{(J)}(\mathbf{r},\omega)$, it can be concluded that the coefficients of $\mathbf{M}^{(J)}(\mathbf{r},\omega)$ contain the information of the magnetic moments and the coefficients of $\mathbf{N}^{(J)}(\mathbf{r},\omega)$ contain the information of the electric moments [154].

2.3   Duality symmetry and helicity

An interesting feature of the source-free Maxwell equations (2.19-2.22) is the invariance of the equations under the non-geometric duality transformation of [146]:

$$\mathbf{E}(\mathbf{r}, \omega) \quad \rightarrow \quad \mathbf{E}(\mathbf{r}, \omega) \cos\theta - Z(\omega)\mathbf{H}(\mathbf{r}, \omega)\sin\theta, \qquad (2.70)$$

$$Z(\omega)\mathbf{H}(\mathbf{r}, \omega) \quad \rightarrow \quad \mathbf{E}(\mathbf{r}, \omega)\sin\theta + Z(\omega)\mathbf{H}(\mathbf{r}, \omega)\cos\theta, \qquad (2.71)$$

where θ is an arbitrary real angle, and $Z(\omega) = \sqrt{\mu(\omega)/\varepsilon(\omega)}$ is the impedance of the medium. This duality symmetry implies that for any solution $([\mathbf{E}(\mathbf{r}, \omega), \mathbf{H}(\mathbf{r}, \omega)])$ there are infinite different solutions to the Maxwell's equation (2.19-2.22). The generator of the electromagnetic duality transformation is known as the helicity operator [158, 159]. In other words, the electromagnetic duality symmetry ensures that the helicity of an electromagnetic wave is preserved upon propagation.

Helicity $\breve{\Lambda}(\omega)$ is the light's total angular momentum $\mathbf{J}(\omega)$ in the direction of the light's linear momentum $\mathbf{P}(\omega)$, i.e., $\breve{\Lambda}(\omega) = \mathbf{P}(\omega) \cdot \mathbf{J}(\omega)/|\mathbf{P}(\omega)|$ [160]. We have used the superscript $\breve{\ }$ to distinguish the symbol from the lattice periodicity Λ that will be used later in the thesis. For a massless particle like a photon, it can only get certain values ± 1.

In the Fourier space in the frequency domain (cf. Eq. 2.15), where the electromagnetic waves are decomposed into plane waves, the helicity operator measures the polarization handedness of the plane waves and is defined as $\breve{\Lambda}(\omega) = \frac{\nabla \times}{k(\omega)}$. Suppose all the plane waves have the same handedness, i.e., the same circular polarization in the direction of propagation. In that case the helicity, like a photon, will get ± 1, and we call this a well-defined helicity.

It can be shown that in an interface where the impedance of the two media are equal, i.e., $Z_1(\omega) = Z_2(\omega)$, the helicity of the electromagnetic field is preserved upon an optical interaction [159]. A system, e.g., a meta-atom that preserves the helicity of an electromagnetic excitation upon scattering is called an electromagnetically dual-symmetric or, in short, *dual* system. Likewise, a meta-atom that flips the helicity is called *anti-dual* [161]. In the remainder of the thesis, we will explore the significance of dual meta-atoms in light-matter interactions.

To summarize this section, we have built the framework for electromagnetic field propagation in a linear, homogenous, and isotropic medium. We have shown how to expand the EM wave fields in vector harmonics in free space, both in the Cartesian and spherical bases. In the following chapters, these equations are heavily used to develop different concepts and applications.

3. Meta-atoms: Symmetries and Models

This chapter explores the electromagnetic response of a single scatterer, i.e., a meta-atom, as represented by its normalized polarizability or transition matrix, in the assigned coordinate systems. Moreover, the symmetries of these matrices for meta-atoms with different geometries are explored. We propose a minimalist model to describe the contribution of each entry of these matrices to the scattering response for isotropic meta-atoms, e.g., homogenous spheres. These isotropic meta-atoms are the backbone of our analysis and development of later concepts. The model is minimal since it parametrizes any possible entry of these matrices with just a single number for conservative and with two numbers for dissipative systems. These numbers, moreover, take values within a finite range. The considered single scatterers will serve as the building blocks and, hence, the (meta)atoms of the metasurfaces that we will explore in the following chapters.

In the first section, we build the framework to analyze the scattering of an isolated meta-atom in the spherical or Cartesian basis. In the following section, which comprises the bulk of this chapter, we focus on the response and features of isotropic meta-atoms. Finally, in the last section, we briefly explore anisotropic and bianisotropic meta-atoms through their polarizability and transition matrices.

The content of this chapter is mainly based on our works in Ref. [59, 75, 162, 163].

3.1 Scattering of light from a meta-atom

We consider, here, the following situation. Inside a homogenous, isotropic and non-absorbing medium, an *incident field* illuminates a meta-atom and induces oscillating local current and charge densities (Fig. 3.1). Consequently, these induced oscillations generate a *scattered field* in the medium and an *internal field* inside the meta-atom. The incident field and the scattered field together form the *total field* in the medium.

To solve the scattering problem for a given meta-atom, we need to derive the scattered and internal fields from the given incident field. A proper basis is essential to expand the fields and formulate the scattering problem in a suitable algebraic
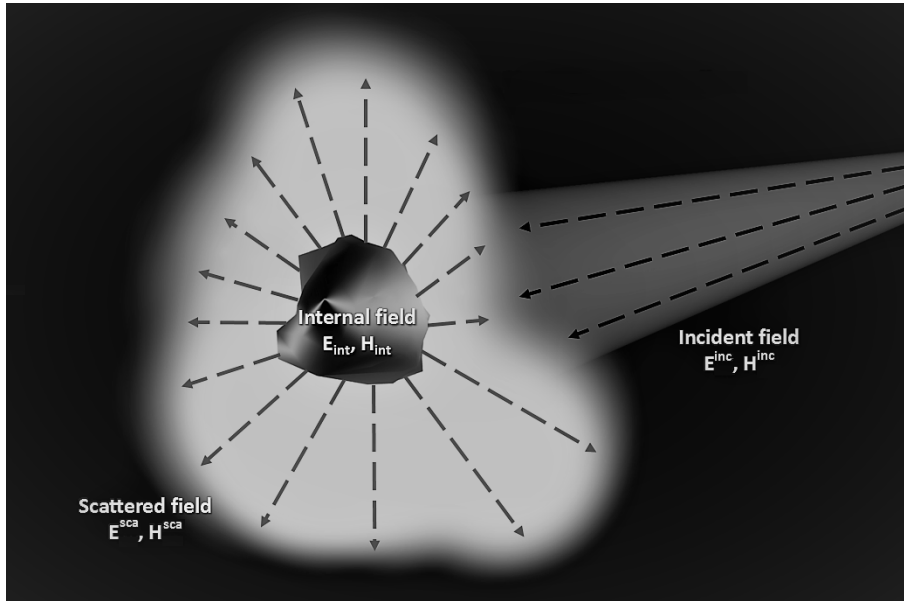
Figure 3.1: **A scattering scenario [163]:** An elastic scattering scenario in which an incident field polarizes a meta-atom and induces scattering and internal fields.

language. Here, we utilize the vector spherical harmonics (VSH) basis for solving the problem. Subsequently, we develop an alternative solution in the Cartesian basis. The *transition matrix (T matrix)* and the polarizability matrix link the incident to the scattered field in the VSH and Cartesian bases, respectively. Therefore, the solution to the scattering problem requires finding the matrices that link the two field expansions.

Note that throughout the thesis, we assume a medium that is linear, isotropic, homogenous, and non-absorbing. These properties are essential for deriving the subsequent equations.

The first subsection introduces the T-matrix method. The following subsection presents the primitive and the normalized dynamic polarizability. Finally, we explore the optical cross-sections in the two bases.

3.1.1   T-matrix method

The *transition matrix*, or shortly the *T matrix*, was initially developed by Waterman in 1965 [164] as a method to describe the scattering of light from an arbitrarily shaped scatterer within the multipole expansion method [48]. If an isotropic meta-atom, e.g., a homogenous sphere, is considered, the T-matrix method simplifies to the well-known Lorenz-Mie theory, or, in short, the *Mie theory* [58, 146, 147, 151, 157, 165–167]. The T-matrix method is a robust and widely used algorithm for efficiently computing the optical scattering from an aggregate of wavelength-sized meta-atoms [48].

In the multipole expansion method, as discussed in Chapter 2, any field can be projected onto the vector spherical harmonics. Therefore, exploiting Eq. 2.66, we can write the incident and scattered fields as [75, 168]:

$$\mathbf{E}^{\mathrm{inc}}(\mathbf{r},\omega) = \sum_{j=1}^{\infty} \sum_{m=-j}^{j} q_{jm}^{\mathrm{e}}(\omega)\, \mathbf{N}_{jm}^{(1)}(\mathbf{r},\omega) + q_{jm}^{\mathrm{m}}(\omega)\, \mathbf{M}_{jm}^{(1)}(\mathbf{r},\omega), \qquad (3.1)$$

$$\mathbf{E}^{\mathrm{sca}}(\mathbf{r},\omega) = \sum_{j=1}^{\infty} \sum_{m=-j}^{j} b_{jm}^{\mathrm{e}}(\omega)\, \mathbf{N}_{jm}^{(3)}(\mathbf{r},\omega) + b_{jm}^{\mathrm{m}}(\omega)\, \mathbf{M}_{jm}^{(3)}(\mathbf{r},\omega), \qquad (3.2)$$

where $q_{jm}^{\mathrm{e/m}}(\omega)$ and $b_{jm}^{\mathrm{e/m}}(\omega)$ are the *electric/magnetic incident and scattered field coefficients*, respectively. $b_{jm}^{\mathrm{e/m}}(\omega)$ are the induced multipole moments in the spherical coordinates.

Consider an arbitrary meta-atom placed into an embedding medium (Fig. 3.1). Then, from Eq. 3.1-3.2, we define the transition matrix $\bar{\bar{T}}(\omega)$ that connects the incident to the scattered coefficients, up to the octupolar order, i.e., $j = 3$, as:

$$\begin{bmatrix} \mathbf{b}_1^{\mathrm{e}}(\omega) \\ \mathbf{b}_2^{\mathrm{e}}(\omega) \\ \mathbf{b}_3^{\mathrm{e}}(\omega) \\ \mathbf{b}_1^{\mathrm{m}}(\omega) \\ \mathbf{b}_2^{\mathrm{m}}(\omega) \\ \mathbf{b}_3^{\mathrm{m}}(\omega) \end{bmatrix} = \begin{bmatrix} \bar{\bar{T}}_{11}^{\mathrm{ee}}(\omega) & \bar{\bar{T}}_{12}^{\mathrm{ee}}(\omega) & \bar{\bar{T}}_{13}^{\mathrm{ee}}(\omega) & \bar{\bar{T}}_{11}^{\mathrm{em}}(\omega) & \bar{\bar{T}}_{12}^{\mathrm{em}}(\omega) & \bar{\bar{T}}_{13}^{\mathrm{em}}(\omega) \\ \bar{\bar{T}}_{21}^{\mathrm{ee}}(\omega) & \bar{\bar{T}}_{22}^{\mathrm{ee}}(\omega) & \bar{\bar{T}}_{23}^{\mathrm{ee}}(\omega) & \bar{\bar{T}}_{21}^{\mathrm{em}}(\omega) & \bar{\bar{T}}_{22}^{\mathrm{em}}(\omega) & \bar{\bar{T}}_{23}^{\mathrm{em}}(\omega) \\ \bar{\bar{T}}_{31}^{\mathrm{ee}}(\omega) & \bar{\bar{T}}_{32}^{\mathrm{ee}}(\omega) & \bar{\bar{T}}_{33}^{\mathrm{ee}}(\omega) & \bar{\bar{T}}_{31}^{\mathrm{em}}(\omega) & \bar{\bar{T}}_{32}^{\mathrm{em}}(\omega) & \bar{\bar{T}}_{33}^{\mathrm{em}}(\omega) \\ \bar{\bar{T}}_{11}^{\mathrm{me}}(\omega) & \bar{\bar{T}}_{12}^{\mathrm{me}}(\omega) & \bar{\bar{T}}_{13}^{\mathrm{me}}(\omega) & \bar{\bar{T}}_{11}^{\mathrm{mm}}(\omega) & \bar{\bar{T}}_{12}^{\mathrm{mm}}(\omega) & \bar{\bar{T}}_{13}^{\mathrm{mm}}(\omega) \\ \bar{\bar{T}}_{21}^{\mathrm{me}}(\omega) & \bar{\bar{T}}_{22}^{\mathrm{me}}(\omega) & \bar{\bar{T}}_{23}^{\mathrm{me}}(\omega) & \bar{\bar{T}}_{21}^{\mathrm{mm}}(\omega) & \bar{\bar{T}}_{22}^{\mathrm{mm}}(\omega) & \bar{\bar{T}}_{23}^{\mathrm{mm}}(\omega) \\ \bar{\bar{T}}_{31}^{\mathrm{me}}(\omega) & \bar{\bar{T}}_{32}^{\mathrm{me}}(\omega) & \bar{\bar{T}}_{33}^{\mathrm{me}}(\omega) & \bar{\bar{T}}_{31}^{\mathrm{mm}}(\omega) & \bar{\bar{T}}_{32}^{\mathrm{mm}}(\omega) & \bar{\bar{T}}_{33}^{\mathrm{mm}}(\omega) \end{bmatrix} \begin{bmatrix} \mathbf{q}_1^{\mathrm{e}}(\omega) \\ \mathbf{q}_2^{\mathrm{e}}(\omega) \\ \mathbf{q}_3^{\mathrm{e}}(\omega) \\ \mathbf{q}_1^{\mathrm{m}}(\omega) \\ \mathbf{q}_2^{\mathrm{m}}(\omega) \\ \mathbf{q}_3^{\mathrm{m}}(\omega) \end{bmatrix},$$

$$(3.3)$$

where the multipolar scattering coefficient vectors are defined as:

$$\mathbf{b}_1^v(\omega) = [b_{1-1}^v(\omega)\, b_{10}^v(\omega)\, b_{11}^v(\omega)]^T, \qquad (3.4)$$

$$\mathbf{b}_2^v(\omega) = [b_{2-2}^v(\omega)\, b_{2-1}^v(\omega)\, b_{20}^v(\omega)\, b_{21}^v(\omega)\, b_{22}^v(\omega)]^T, \qquad (3.5)$$

$$\mathbf{b}_3^v(\omega) = [b_{3-3}^v(\omega),\, b_{3-2}^v(\omega)\, b_{3-1}^v(\omega)\, b_{30}^v(\omega)\, b_{31}^v(\omega)\, b_{32}^v(\omega)\, b_{33}^v(\omega)]^T, \qquad (3.6)$$

with $v = \{\mathrm{e}, \mathrm{m}\}$ and superscript "T" denoting the transpose operation. The multipolar incident field coefficient vectors $\mathbf{q}_j^v(\omega)$ are defined similarly. The T matrix consists of smaller sub T matrices $\bar{\bar{T}}_{jm}^{v,v'}(\omega)$ that describe different channels of transferring the incident field to the scattered field. The sorting of the T matrix, up to the octupolar order, is shown in Fig. 3.2a. Equation 3.3 can be concisely written as:

$$\mathbf{b}(\omega) = \bar{\bar{T}}(\omega)\, \mathbf{q}(\omega), \qquad (3.7)$$

where $\mathbf{b}(\omega)$ ($\mathbf{q}(\omega)$) is the *scattered (incident) field coefficient vector*. The T matrix describes the electromagnetic properties of a scatterer in the VSH basis. Depending on the geometry of the meta-atom, the T matrix can take different symmetries. We will explore these symmetries throughout this chapter.

The calculation of the T matrix for a general meta-atom is mostly based on Eq. 2.68-2.69 in which the scattered and incident field coefficients are calculated for multiple excitations. Using the derived coefficients, the entries of the T matrix can be calculated. The excitation fields can be plane waves [55], or sources characterized by an individual multipole moment [56, 57]. To simulate the scattering of a meta-atom by such excitations, full-wave Maxwell solvers such as COMSOL™ Multiphysics or JCM suite can be used. For meta-atoms with specific symmetries, analytic expressions exit. For instance, for homogenous spheres, Mie theory provides analytical

a) T matrix Template					
$\bar{\bar{T}}^{\mathrm{ee}}_{11}$	$\bar{\bar{T}}^{\mathrm{ee}}_{21}$	$\bar{\bar{T}}^{\mathrm{ee}}_{31}$	$\bar{\bar{T}}^{\mathrm{me}}_{11}$	$\bar{\bar{T}}^{\mathrm{me}}_{21}$	$\bar{\bar{T}}^{\mathrm{me}}_{31}$
$\bar{\bar{T}}^{\mathrm{ee}}_{12}$	$\bar{\bar{T}}^{\mathrm{ee}}_{22}$	$\bar{\bar{T}}^{\mathrm{ee}}_{32}$	$\bar{\bar{T}}^{\mathrm{me}}_{12}$	$\bar{\bar{T}}^{\mathrm{me}}_{22}$	$\bar{\bar{T}}^{\mathrm{me}}_{32}$
$\bar{\bar{T}}^{\mathrm{ee}}_{13}$	$\bar{\bar{T}}^{\mathrm{ee}}_{23}$	$\bar{\bar{T}}^{\mathrm{ee}}_{33}$	$\bar{\bar{T}}^{\mathrm{me}}_{13}$	$\bar{\bar{T}}^{\mathrm{me}}_{23}$	$\bar{\bar{T}}^{\mathrm{me}}_{33}$
$\bar{\bar{T}}^{\mathrm{em}}_{11}$	$\bar{\bar{T}}^{\mathrm{em}}_{21}$	$\bar{\bar{T}}^{\mathrm{em}}_{31}$	$\bar{\bar{T}}^{\mathrm{mm}}_{11}$	$\bar{\bar{T}}^{\mathrm{mm}}_{21}$	$\bar{\bar{T}}^{\mathrm{mm}}_{31}$
$\bar{\bar{T}}^{\mathrm{em}}_{12}$	$\bar{\bar{T}}^{\mathrm{em}}_{22}$	$\bar{\bar{T}}^{\mathrm{em}}_{32}$	$\bar{\bar{T}}^{\mathrm{mm}}_{12}$	$\bar{\bar{T}}^{\mathrm{mm}}_{22}$	$\bar{\bar{T}}^{\mathrm{mm}}_{32}$
$\bar{\bar{T}}^{\mathrm{em}}_{13}$	$\bar{\bar{T}}^{\mathrm{em}}_{23}$	$\bar{\bar{T}}^{\mathrm{em}}_{33}$	$\bar{\bar{T}}^{\mathrm{mm}}_{13}$	$\bar{\bar{T}}^{\mathrm{mm}}_{23}$	$\bar{\bar{T}}^{\mathrm{mm}}_{33}$

b) Normalized Polarizability Template					
$\bar{\bar{\alpha}}^{\mathrm{ee}}_{11}$	$\bar{\bar{\alpha}}^{\mathrm{ee}}_{21}$	$\bar{\bar{\alpha}}^{\mathrm{ee}}_{31}$	$\bar{\bar{\alpha}}^{\mathrm{me}}_{11}$	$\bar{\bar{\alpha}}^{\mathrm{me}}_{21}$	$\bar{\bar{\alpha}}^{\mathrm{me}}_{31}$
$\bar{\bar{\alpha}}^{\mathrm{ee}}_{12}$	$\bar{\bar{\alpha}}^{\mathrm{ee}}_{22}$	$\bar{\bar{\alpha}}^{\mathrm{ee}}_{32}$	$\bar{\bar{\alpha}}^{\mathrm{me}}_{12}$	$\bar{\bar{\alpha}}^{\mathrm{me}}_{22}$	$\bar{\bar{\alpha}}^{\mathrm{me}}_{32}$
$\bar{\bar{\alpha}}^{\mathrm{ee}}_{13}$	$\bar{\bar{\alpha}}^{\mathrm{ee}}_{23}$	$\bar{\bar{\alpha}}^{\mathrm{ee}}_{33}$	$\bar{\bar{\alpha}}^{\mathrm{me}}_{13}$	$\bar{\bar{\alpha}}^{\mathrm{me}}_{23}$	$\bar{\bar{\alpha}}^{\mathrm{me}}_{33}$
$\bar{\bar{\alpha}}^{\mathrm{em}}_{11}$	$\bar{\bar{\alpha}}^{\mathrm{em}}_{21}$	$\bar{\bar{\alpha}}^{\mathrm{em}}_{31}$	$\bar{\bar{\alpha}}^{\mathrm{mm}}_{11}$	$\bar{\bar{\alpha}}^{\mathrm{mm}}_{21}$	$\bar{\bar{\alpha}}^{\mathrm{mm}}_{31}$
$\bar{\bar{\alpha}}^{\mathrm{em}}_{12}$	$\bar{\bar{\alpha}}^{\mathrm{em}}_{22}$	$\bar{\bar{\alpha}}^{\mathrm{em}}_{32}$	$\bar{\bar{\alpha}}^{\mathrm{mm}}_{12}$	$\bar{\bar{\alpha}}^{\mathrm{mm}}_{22}$	$\bar{\bar{\alpha}}^{\mathrm{mm}}_{32}$
$\bar{\bar{\alpha}}^{\mathrm{em}}_{13}$	$\bar{\bar{\alpha}}^{\mathrm{em}}_{23}$	$\bar{\bar{\alpha}}^{\mathrm{em}}_{33}$	$\bar{\bar{\alpha}}^{\mathrm{mm}}_{13}$	$\bar{\bar{\alpha}}^{\mathrm{mm}}_{23}$	$\bar{\bar{\alpha}}^{\mathrm{mm}}_{33}$

Figure 3.2: The sorting and template for a) a T matrix and b) a normalized polarizability matrix, up to the octupolar order.

solutions. Moreover, for core-multishell spheres, generalized Mie coefficients can be used [169].

The T-matrix method provides an efficient numerical and also analytical tool to solve a scattering scenario. However, the quantities in the spherical basis are not always easy to grasp. The following subsection explores the electromagnetic scattering of a meta-atom in the Cartesian basis.

3.1.2 Dynamic polarizability

We continue to consider the same scattering scenario, and the new concepts and terms are gradually introduced. An incident field illuminates a meta-atom and induces local current densities $\mathbf{J}(\mathbf{r}, \omega)$. The exact *primitive Cartesian moments*, up to quadrupolar order, can be derived by integrating the induced current densities over the meta-atom volume V as [170]:

$$p_\alpha(\omega) = \frac{-1}{\mathrm{i}\,\omega}\left[\int_V \left(\{3[\mathbf{r}\cdot\mathbf{J}(\mathbf{r},\omega)]\alpha - r^2 J_\alpha(\mathbf{r},\omega)\}\frac{j_2(\tilde{r})}{2r^2} + J_\alpha(\mathbf{r},\omega)\,j_0(\tilde{r})\right)\mathrm{d}V\right],$$

$$m_\alpha(\omega) = \frac{3}{2}\int_V [\mathbf{r}\times\mathbf{J}(\mathbf{r},\omega)]_\alpha\frac{j_1(\tilde{r})}{\tilde{r}}\,\mathrm{d}V,$$

$$Q^{\mathrm{e}}_{\alpha\beta}(\omega) = \frac{-3}{\mathrm{i}\,\omega}\left(\int_V \mathrm{d}V\,\{3\,[\beta J_\alpha(\mathbf{r},\omega) + \alpha J_\beta(\mathbf{r},\omega)] - 2\,[\mathbf{r}\cdot\mathbf{J}(\mathbf{r},\omega)]\,\delta_{\alpha\beta}\}\frac{j_1(\tilde{r})}{\tilde{r}}\right.$$

$$\left.+ \int_V \mathrm{d}V\ \frac{2j_3(\tilde{r})}{\tilde{r}}\left\{\frac{5\alpha\beta\,[\mathbf{r}\cdot\mathbf{J}(\mathbf{r},\omega)]}{r^2} - \alpha J_\beta(\mathbf{r},\omega) - \beta J_\alpha(\mathbf{r},\omega) - \mathbf{r}\cdot\mathbf{J}(\mathbf{r},\omega)\delta_{\alpha\beta}\right\}\right),$$

$$Q^{\mathrm{m}}_{\alpha\beta}(\omega) = 15\int_V \left\{\alpha\,[\mathbf{r}\times\mathbf{J}(\mathbf{r},\omega)]_\beta + \beta\,[\mathbf{r}\times\mathbf{J}(\mathbf{r},\omega)]_\alpha\right\}\frac{j_2(\tilde{r})}{\tilde{r}^2}\mathrm{d}V, \tag{3.8}$$

where $\{\alpha,\beta\} = \{x,y,z\}$ denote the Cartesian coordinates, $\tilde{r} = k(\omega)\,r$ is the normalized position, $j_i(\tilde{r})$ (where $i = 1,2,...$) is the Bessel function of the i's kind;

and $p_\alpha(\omega)$ $(m_\alpha(\omega))$, $Q^e_{\alpha\beta}(\omega)$ $(Q^m_{\alpha\beta}(\omega))$ are the primitive electric (magnetic) dipole and quadrupole moments, respectively. Higher-order terms, such as the primitive Cartesian electric and magnetic octupole moments $O^e_{\alpha\beta\gamma}(\omega)$ and $O^m_{\alpha\beta\gamma}(\omega)$ can also be written as a function of the current densities [171]. However, since we do not use these formulations to derive the Cartesian moments, we have not included them here. The derivation of these moments, as we will show later, are based on the induced moments in the VHS basis. The nomenclature is justified shortly. Note that the meta-atom is assumed to be centered at a fixed position, here $\mathbf{r}_0 = 0$, and, hence, the derived moments are only a function of the excitation frequency.

The *primitive Cartesian dipole and quadrupole moment matrices* for an arbitrary meta-atom can be formulated as [146]:

$$
\check{\mathbf{p}}(\omega) = \begin{bmatrix} p_x(\omega) \\ p_y(\omega) \\ p_z(\omega) \end{bmatrix}, \check{\mathbf{m}}(\omega) = \begin{bmatrix} m_x(\omega) \\ m_y(\omega) \\ m_z(\omega) \end{bmatrix}, \check{\bar{\bar{Q}}}^v(\omega) = \begin{bmatrix} Q^v_{xx}(\omega) & Q^v_{xy}(\omega) & Q^v_{xz}(\omega) \\ Q^v_{yx}(\omega) & Q^v_{yy}(\omega) & Q^v_{yz}(\omega) \\ Q^v_{zx}(\omega) & Q^v_{zy}(\omega) & Q^v_{zz}(\omega) \end{bmatrix},
$$

$$(3.9)$$

where $v = \{e, m\}$. The accent "$\check{\ }$" is used to denote the primitive moments as compared to the irreducible vectors that are defined later.

Radiating fields

When considering the primitive Cartesian moments defined in Eq. 3.8, the *far-field radiation* of a meta-atom, up to an octupolar order, is described as [51]:

$$
\begin{aligned}
\mathbf{E}^{\text{sca}}(\mathbf{r}, \omega) = \frac{k(\omega)^2 e^{\mathrm{i}k(\omega)r}}{4\pi r} \Bigg\{ & \hat{\mathbf{r}} \times \left[\frac{1}{\varepsilon}\check{\mathbf{p}}(\omega) \times \hat{\mathbf{r}} \right] + \left[Z\,\check{\mathbf{m}}(\omega) \times \hat{\mathbf{r}} \right] \\
& - \frac{\mathrm{i}k(\omega)}{6}\hat{\mathbf{r}} \times \left[\frac{1}{\varepsilon}\check{\boldsymbol{\mathcal{Q}}}^e(\omega) \times \hat{\mathbf{r}} \right] - \frac{\mathrm{i}k(\omega)}{6}\left[Z\,\check{\boldsymbol{\mathcal{Q}}}^m(\omega) \times \hat{\mathbf{r}} \right] \\
& - \frac{k(\omega)^2}{16}\hat{\mathbf{r}} \times \left[\frac{1}{\varepsilon}\check{\boldsymbol{\mathcal{O}}}^e(\omega) \times \hat{\mathbf{r}} \right] - \frac{k(\omega)^2}{16}\left[Z\,\check{\boldsymbol{\mathcal{O}}}^m(\omega) \times \hat{\mathbf{r}} \right] \Bigg\},
\end{aligned}
$$

$$(3.10)$$

$$
\begin{aligned}
\mathbf{H}^{\text{sca}}(\mathbf{r}, \omega) = -\frac{k(\omega)\,\omega e^{\mathrm{i}k(\omega)r}}{4\pi r} \Bigg\{ & \left[\frac{1}{\varepsilon}\check{\mathbf{p}}(\omega) \times \hat{\mathbf{r}} \right] + \hat{\mathbf{r}} \times \left[Z\,\check{\mathbf{m}}(\omega) \times \hat{\mathbf{r}} \right] \\
& - \frac{\mathrm{i}k(\omega)}{6}\left[\frac{1}{\varepsilon}\check{\boldsymbol{\mathcal{Q}}}^e(\omega) \times \hat{\mathbf{r}} \right] - \hat{\mathbf{r}} \times \frac{\mathrm{i}k(\omega)}{6}\left[Z\,\check{\boldsymbol{\mathcal{Q}}}^m(\omega) \times \hat{\mathbf{r}} \right] \\
& - \frac{k(\omega)^2}{16}\left[\frac{1}{\varepsilon}\check{\boldsymbol{\mathcal{O}}}^e(\omega) \times \hat{\mathbf{r}} \right] - \hat{\mathbf{r}} \times \frac{k(\omega)^2}{16}\left[Z\,\check{\boldsymbol{\mathcal{O}}}^m(\omega) \times \hat{\mathbf{r}} \right] \Bigg\},
\end{aligned}
$$

$$(3.11)$$

where $\mathbf{r} = \sin\theta\cos\phi\,\mathbf{x} + \sin\theta\sin\phi\,\mathbf{y} + \cos\theta\,\mathbf{z}$ is the position vector and $\hat{\mathbf{r}}$ is the unit position vector. The *primitive Cartesian moment vectors* $\check{\boldsymbol{\mathcal{Q}}}(\omega)$ and $\check{\boldsymbol{\mathcal{O}}}(\omega)$ are defined as:

$$
\check{\mathcal{Q}}^v_\alpha(\omega) = \sum_\beta Q^v_{\alpha\beta}(\omega)\,\hat{\beta}, \tag{3.12a}
$$

$$
\check{\mathcal{O}}^v_\alpha(\omega) = \sum_{\beta\gamma} O^v_{\alpha\beta\gamma}(\omega)\,\hat{\beta}\,\hat{\gamma}, \tag{3.12b}
$$

with $\{\alpha, \beta, \gamma\} = \{x, y, z\}$ and $v = \{e, m\}$.

Primitive polarizability

For an isotropic meta-atom, it is common to define the primitive dipole and quadrupole moments as a function of the incident field as [50, 146, 172, 173]:

$$\breve{\mathbf{p}}\left(\omega\right) = \breve{\alpha}_1^{\mathrm{e}}\left(\omega\right)\mathbf{E}^{\mathrm{inc}}\left(\mathbf{r},\omega\right)_{|\mathbf{r}=0}\,\varepsilon\left(\omega\right), \tag{3.13}$$

$$\breve{\mathbf{m}}\left(\omega\right) = \breve{\alpha}_1^{\mathrm{m}}\left(\omega\right)\mathbf{H}^{\mathrm{inc}}\left(\mathbf{r},\omega\right)_{|\mathbf{r}=0}, \tag{3.14}$$

$$\breve{\overline{\overline{Q}}}^{\mathrm{e}}\left(\omega\right) = \breve{\alpha}_2^{\mathrm{e}}\left(\omega\right)\frac{\nabla\mathbf{E}^{\mathrm{inc}}\left(\mathbf{r},\omega\right)+\mathbf{E}^{\mathrm{inc}}\left(\mathbf{r},\omega\right)\nabla}{2}\Bigg|_{\mathbf{r}=0}\varepsilon\left(\omega\right), \tag{3.15}$$

$$\breve{\overline{\overline{Q}}}^{\mathrm{m}}\left(\omega\right) = \breve{\alpha}_2^{\mathrm{m}}\left(\omega\right)\frac{\nabla\mathbf{H}^{\mathrm{inc}}\left(\mathbf{r},\omega\right)+\mathbf{H}^{\mathrm{inc}}\left(\mathbf{r},\omega\right)\nabla}{2}\Bigg|_{\mathbf{r}=0}, \tag{3.16}$$

where $\breve{\alpha}_j^v$ is the *primitive (dynamic) polarizability* of j's order. It is dynamic as, in contrast to static polarizability, it describes the response of a meta-atom to dynamic electromagnetic excitation. The polarizability links the incident field to the multipolar moments in the Cartesian basis.

For subwavelength non-isotropic meta-atoms with no magneto-electric or multipolar coupling, the primitive dipolar polarizabilities become a matrix of size 3×3, and the primitive quadrupolar polarizabilities become a tensor of the fourth rank with a size of $3\times3\times3\times3$.

From Eq. 3.8, it can be easily generalized and calculated that the number of possible combinations of the primitive moments is 3^j, where j is the multipole order. Consequently, for a general dipolar-quadrupolar meta-atom with electromagnetic coupling, it can be derived that the primitive polarizability matrix has $(2\times3^1+2\times3^2)^2=576$ entries, while for a general dipolar-quadrupolar-octupolar meta-atom, this goes to $(2\times3^1+2\times3^2+2\times3^3)^2=6084$ entries. These bulky primitive moments and polarizabilities are cumbersome to use with many redundancies. Therefore, we seek an irreducible representation by using the symmetries and relations implied in Eq. 3.8 [50, 51, 75, 171].

From Eq. 3.8, it is noticed that $Q_{ij}^v\left(\omega\right)=Q_{ji}^v\left(\omega\right)$. Moreover, after some basic algebraic calculations, it can be shown that the primitive Cartesian quadrupole moment matrix is traceless, i.e., $Q_{xx}^v\left(\omega\right)+Q_{yy}^v\left(\omega\right)+Q_{zz}^v\left(\omega\right)=0$. Therefore, out of the 9 entries of $\breve{\overline{\overline{Q}}}^v\left(\omega\right)$, only 5 are independent. This number is consistent with the number of quadrupole moments in the VSH basis (Eq. 3.5). Similarly, for the primitive Cartesian octupolar moments [171], it can be shown that $O_{ijk}^v\left(\omega\right)=O_{jik}^v\left(\omega\right)=O_{kji}^v\left(\omega\right)=O_{kij}^v\left(\omega\right)=O_{ikj}^v\left(\omega\right)$ and $O_{ixx}^v\left(\omega\right)+O_{iyy}^v\left(\omega\right)+O_{izz}^v\left(\omega\right)=0$, with $\{i,j,k\}=\{x,y,z\}$. Therefore, there are, in total, only three, five, and seven independent entries for the primitive dipole, quadrupole and octupole moment matrices, respectively. As a result, we can develop an irreducible representation for the primitive Cartesian moments. However, there are several distinct ways to achieve this representation and, consequently, there are multiple different irreducible representations in the literature [51].

Here, we base our derivations on the already-discussed quantities in the spherical basis. Furthermore, we have used the relations for real spherical harmonics corresponding to atomic orbitals p, d, and f [174] as the basis for forming the irreducible representation. This correspondence conserves certain symmetries between

Cartesian and spherical bases, such as the diagonality of T matrices for isotropic meta-atoms. The derivations of these equations and further discussions can be found in Ref. [75]. Following this procedure, we will develop an irreducible representation for the primitive Cartesian moment and polarizability and define the *Cartesian moment* and *normalized dynamic polarizability matrix* (or, in short, the *polarizability matrix*). We use normalized polarizabilities, as, like their spherical counterpart, they are dimensionless and, hence, extensively facilitates the solutions and the relations for derived optical quantities. To convert the equations from the VSH basis to the Cartesian basis, we have used modified and enhanced versions of the relations used in Ref. [51].

Normalized polarizability

Assuming a single meta-atom placed at the origin of an embedding medium that is illuminated by a plane wave:

$$\mathbf{E}^{\text{inc}}(\mathbf{r},\omega) = [E_x(\mathbf{r},\omega), E_y(\mathbf{r},\omega), E_z(\mathbf{r},\omega)]^T = \mathbf{E}_0 \, e^{i\mathbf{k}^{\text{inc}}(\omega)\cdot\mathbf{r}}, \quad (3.17)$$

$$\mathbf{H}^{\text{inc}}(\mathbf{r},\omega) = [H_x(\mathbf{r},\omega), H_y(\mathbf{r},\omega), H_z(\mathbf{r},\omega)]^T = \mathbf{H}_0 \, e^{i\mathbf{k}^{\text{inc}}(\omega)\cdot\mathbf{r}}, \quad (3.18)$$

the expression linking the incident field to the induced Cartesian moments through the *normalized (dynamic) polarizability matrix* $\bar{\bar{\alpha}}(\omega)$, or shortly the *polarizability matrix*, defined up to octupolar order, can be written as [75]:

$$
\begin{bmatrix}
(\varepsilon\zeta_1)^{-1}\mathbf{p} \\
k(\varepsilon\zeta_2)^{-1}\mathbf{Q}^{\text{e}} \\
k^2(\varepsilon\zeta_3)^{-1}\mathbf{O}^{\text{e}} \\
iZ(\zeta_1)^{-1}\mathbf{m} \\
iZk(\zeta_2)^{-1}\mathbf{Q}^{\text{m}} \\
iZk^2(\zeta_3)^{-1}\mathbf{O}^{\text{m}}
\end{bmatrix}
= \frac{1}{k^3}
\begin{bmatrix}
\bar{\bar{\alpha}}^{\text{ee}}_{11} & \bar{\bar{\alpha}}^{\text{ee}}_{12} & \bar{\bar{\alpha}}^{\text{ee}}_{13} & \bar{\bar{\alpha}}^{\text{em}}_{11} & \bar{\bar{\alpha}}^{\text{em}}_{12} & \bar{\bar{\alpha}}^{\text{em}}_{13} \\
\bar{\bar{\alpha}}^{\text{ee}}_{21} & \bar{\bar{\alpha}}^{\text{ee}}_{22} & \bar{\bar{\alpha}}^{\text{ee}}_{23} & \bar{\bar{\alpha}}^{\text{em}}_{21} & \bar{\bar{\alpha}}^{\text{em}}_{22} & \bar{\bar{\alpha}}^{\text{em}}_{23} \\
\bar{\bar{\alpha}}^{\text{ee}}_{31} & \bar{\bar{\alpha}}^{\text{ee}}_{32} & \bar{\bar{\alpha}}^{\text{ee}}_{33} & \bar{\bar{\alpha}}^{\text{em}}_{31} & \bar{\bar{\alpha}}^{\text{em}}_{32} & \bar{\bar{\alpha}}^{\text{em}}_{33} \\
\bar{\bar{\alpha}}^{\text{me}}_{11} & \bar{\bar{\alpha}}^{\text{me}}_{12} & \bar{\bar{\alpha}}^{\text{me}}_{13} & \bar{\bar{\alpha}}^{\text{mm}}_{11} & \bar{\bar{\alpha}}^{\text{mm}}_{12} & \bar{\bar{\alpha}}^{\text{mm}}_{13} \\
\bar{\bar{\alpha}}^{\text{me}}_{21} & \bar{\bar{\alpha}}^{\text{me}}_{22} & \bar{\bar{\alpha}}^{\text{me}}_{23} & \bar{\bar{\alpha}}^{\text{mm}}_{21} & \bar{\bar{\alpha}}^{\text{mm}}_{22} & \bar{\bar{\alpha}}^{\text{mm}}_{23} \\
\bar{\bar{\alpha}}^{\text{me}}_{31} & \bar{\bar{\alpha}}^{\text{me}}_{32} & \bar{\bar{\alpha}}^{\text{me}}_{33} & \bar{\bar{\alpha}}^{\text{mm}}_{31} & \bar{\bar{\alpha}}^{\text{mm}}_{32} & \bar{\bar{\alpha}}^{\text{mm}}_{33}
\end{bmatrix}
\begin{bmatrix}
\zeta_1\mathbf{E}_1 \\
k^{-1}\zeta_2\mathbf{E}_2 \\
k^{-2}\zeta_3\mathbf{E}_3 \\
iZ\zeta_1\mathbf{H}_1 \\
iZk^{-1}\zeta_2\mathbf{H}_2 \\
iZk^{-2}\zeta_3\mathbf{H}_3
\end{bmatrix},
$$
$$(3.19\text{a})$$

where, $\zeta_j = \sqrt{(2j+1)!\,\pi}$ is the multipolar factor. Due to space restriction, we have ignored the ω argument, but the argument is implicitly assumed all the time. The vectors $\mathbf{E}_j(\omega)$ and $\mathbf{H}_j(\omega)$ are the electric and magnetic *multipolar amplitudes* of the incident field. They contain spatial derivatives of the Cartesian incident field, considered at the center of the meta-atom [75]:

$$
\mathbf{E}_1(\omega) = \begin{bmatrix} E_x(\mathbf{r},\omega) \\ E_y(\mathbf{r},\omega) \\ E_z(\mathbf{r},\omega) \end{bmatrix}_{|\mathbf{r}=0}, \quad
\mathbf{E}_2(\omega) = \frac{1}{2\sqrt{3}}
\begin{bmatrix}
\partial_y E_x(\mathbf{r},\omega) + \partial_x E_y(\mathbf{r},\omega) \\
\partial_y E_z(\mathbf{r},\omega) + \partial_z E_y(\mathbf{r},\omega) \\
\sqrt{3}\,\partial_z E_z(\mathbf{r},\omega) \\
\partial_x E_z(\mathbf{r},\omega) + \partial_z E_x(\mathbf{r},\omega) \\
\partial_x E_x(\mathbf{r},\omega) - \partial_y E_y(\mathbf{r},\omega)
\end{bmatrix}_{|\mathbf{r}=0},
$$

$$
\mathbf{E}_3(\omega) = \frac{\sqrt{6}}{24}
\begin{bmatrix}
\frac{1}{2}\left[2\partial_{xy}E_x(\mathbf{r},\omega) + (\partial_x^2-\partial_y^2)E_y(\mathbf{r},\omega)\right] \\
\frac{2}{\sqrt{6}}\left[\partial_{yz}E_x(\mathbf{r},\omega) + \partial_{xz}E_y(\mathbf{r},\omega) + \partial_{xy}E_z(\mathbf{r},\omega)\right] \\
\frac{2}{\sqrt{15}}\left[\frac{1}{4}(2\partial_{xy}-\partial_y^2)E_x(\mathbf{r},\omega) + (\partial_z^2-\frac{3}{4}\partial_y^2)E_y(\mathbf{r},\omega) + 2\,\partial_{yz}E_z(\mathbf{r},\omega)\right] \\
\frac{1}{\sqrt{10}}\left[-2\,\partial_{xz}E_x(\omega) - 2\,\partial_{yz}E_y(\mathbf{r},\omega) + (2\partial_z^2-\partial_x^2-\partial_y^2)E_z(\mathbf{r},\omega)\right] \\
\frac{2}{\sqrt{15}}\left[(\partial_z^2-\frac{1}{4}\partial_y^2-\frac{3}{4}\partial_x^2)E_x(\mathbf{r},\omega) - \frac{1}{2}\,\partial_{xy}E_y(\mathbf{r},\omega) + 2\,\partial_{xz}E_z(\mathbf{r},\omega)\right] \\
\frac{1}{\sqrt{6}}\left[2\,\partial_{xz}E_x(\mathbf{r},\omega) - 2\,\partial_{yz}E_y(\mathbf{r},\omega) + (\partial_x^2-\partial_y^2)E_z(\mathbf{r},\omega)(\mathbf{r},\omega)\right] \\
\frac{1}{2}\left[(\partial_x^2-\partial_y^2)E_x(\mathbf{r},\omega) - 2\,\partial_{xy}E_y(\mathbf{r},\omega)\right]
\end{bmatrix}_{|\mathbf{r}=0}.
$$
$$(3.20)$$

The $\mathbf{H}_j(\omega)$ components are defined identically by replacing E with H. The multipolar amplitudes can be alternatively calculated using their spherical counterparts:

$$k(\omega)^{-j+1}\,\mathbf{E}_j(\omega) = \frac{1}{\zeta_j}\,\bar{\bar{F}}_j\,\mathbf{q}_j^{\mathrm{e}}(\omega),\qquad(3.21)$$

$$k(\omega)^{-j+1}\,\mathrm{i}Z(\omega)\,\mathbf{H}_j(\omega) = \frac{1}{\zeta_j}\,\bar{\bar{F}}_j\,\mathbf{q}_j^{\mathrm{m}}(\omega),\qquad(3.22)$$

with the *transformation matrices* defined as:

$$\bar{\bar{F}}_1 = \frac{1}{\sqrt{2}}\begin{bmatrix} 1 & 0 & -1 \\ -\mathrm{i} & 0 & -\mathrm{i} \\ 0 & \sqrt{2} & 0 \end{bmatrix},\qquad(3.23)$$

$$\bar{\bar{F}}_2 = \frac{1}{\sqrt{2}}\begin{bmatrix} -\mathrm{i} & 0 & 0 & 0 & \mathrm{i} \\ 0 & -\mathrm{i} & 0 & -\mathrm{i} & 0 \\ 0 & 0 & \sqrt{2} & 0 & 0 \\ 0 & 1 & 0 & -1 & 0 \\ 1 & 0 & 0 & 0 & 1 \end{bmatrix},\qquad(3.24)$$

$$\bar{\bar{F}}_3 = \frac{1}{\sqrt{2}}\begin{bmatrix} -\mathrm{i} & 0 & 0 & 0 & 0 & 0 & -\mathrm{i} \\ 0 & -\mathrm{i} & 0 & 0 & 0 & \mathrm{i} & 0 \\ 0 & 0 & -\mathrm{i} & 0 & -\mathrm{i} & 0 & 0 \\ 0 & 0 & 0 & \sqrt{2} & 0 & 0 & 0 \\ 0 & 0 & 1 & 0 & -1 & 0 & 0 \\ 0 & 1 & 0 & 0 & 0 & 1 & 0 \\ 1 & 0 & 0 & 0 & 0 & 0 & -1 \end{bmatrix}.\qquad(3.25)$$

Note that, unlike Ref. [51], $\bar{\bar{F}}_j = (\bar{\bar{F}}_j^{-1})^{\dagger}$. This property facilitates simplifications of some prospective meta-atom properties.

The vectors $\mathbf{p}(\omega)$ ($\mathbf{m}(\omega)$), $\mathbf{Q}^{\mathrm{e}}(\omega)$ ($\mathbf{Q}^{\mathrm{m}}(\omega)$), and $\mathbf{O}^{\mathrm{e}}(\omega)$ ($\mathbf{O}^{\mathrm{m}}(\omega)$), are the irreducible induced Cartesian electric (magnetic) dipole, quadrupole, and octupole moment vectors, respectively. We refer to them, in short, by the *Cartesian moments*. They are derived from their spherical counterparts, through the following equations:

$$\varepsilon(\omega)^{-1}\,\mathbf{p}(\omega) = \frac{\zeta_1}{\mathrm{i}k(\omega)^3}\,\bar{\bar{F}}_1\,\mathbf{b}_1^{\mathrm{e}}(\omega),\qquad(3.26)$$

$$k(\omega)\,\varepsilon(\omega)^{-1}\,\mathbf{Q}^{\mathrm{e}}(\omega) = \frac{\zeta_2}{\mathrm{i}k(\omega)^3}\,\bar{\bar{F}}_2\,\mathbf{b}_2^{\mathrm{e}}(\omega),\qquad(3.27)$$

$$k(\omega)^2\,\varepsilon(\omega)^{-1}\,\mathbf{O}^{\mathrm{e}}(\omega) = \frac{\zeta_3}{\mathrm{i}k(\omega)^3}\,\bar{\bar{F}}_3\,\mathbf{b}_3^{\mathrm{e}}(\omega),\qquad(3.28)$$

$$\mathrm{i}Z(\omega)\,\mathbf{m}(\omega) = \frac{\zeta_1}{\mathrm{i}k(\omega)^3}\,\bar{\bar{F}}_1\,\mathbf{b}_1^{\mathrm{m}}(\omega),\qquad(3.29)$$

$$k(\omega)\,\mathrm{i}Z(\omega)\,\mathbf{Q}^{\mathrm{m}}(\omega) = \frac{\zeta_2}{\mathrm{i}k(\omega)^3}\,\bar{\bar{F}}_2\,\mathbf{b}_2^{\mathrm{m}}(\omega),\qquad(3.30)$$

$$k(\omega)^2\,\mathrm{i}Z(\omega)\,\mathbf{O}^{\mathrm{m}}(\omega) = \frac{\zeta_3}{\mathrm{i}k(\omega)^3}\,\bar{\bar{F}}_3\,\mathbf{b}_3^{\mathrm{m}}(\omega).\qquad(3.31)$$

Finally, these Cartesian moment vectors are connected to the primitive Cartesian moments through:

$$\mathbf{p}(\omega) = \begin{bmatrix} p_x(\omega) \\ p_y(\omega) \\ p_z(\omega) \end{bmatrix}, \qquad\qquad \mathbf{m}(\omega) = \begin{bmatrix} m_x(\omega) \\ m_y(\omega) \\ m_z(\omega) \end{bmatrix}, \qquad (3.32)$$

$$\mathbf{Q}^v(\omega) = \frac{1}{\sqrt{3}} \begin{bmatrix} Q_{xy}^v(\omega) \\ Q_{yz}^v(\omega) \\ \frac{\sqrt{3}}{2} Q_{zz}^v(\omega) \\ Q_{xz}^v(\omega) \\ \frac{1}{2}\left[Q_{xx}^v(\omega) - Q_{yy}^v(\omega)\right] \end{bmatrix}, \mathbf{O}^v(\omega) = \frac{\sqrt{6}}{8} \begin{bmatrix} 3O_{xxy}^v(\omega) - O_{yyy}^v(\omega) \\ \frac{\sqrt{6}}{2} O_{xyz}^v(\omega) \\ \sqrt{15}O_{yzz}^v(\omega) \\ \sqrt{10}O_{zzz}^v(\omega) \\ \sqrt{15}O_{xzz}^v(\omega) \\ \sqrt{6}\left[O_{zxx}^v(\omega) - O_{zyy}^v(\omega)\right] \\ O_{xxx}^v(\omega)(\omega) - 3O_{xyy}^v(\omega) \end{bmatrix},$$

where $v = \{\mathrm{e}, \mathrm{m}\}$.

The normalized polarizability can also be derived directly from the T matrix. These two matrices are interchangeable. By employing transformation formulas in Eq. 3.23-3.25, the elements of the T matrix are linked to the polarizability matrix through:

$$\bar{\bar{T}}_{jj'}^{vv'}(\omega) = \mathrm{i}\,\bar{\bar{F}}_j^{-1}\,\bar{\bar{\alpha}}_{jj'}^{vv'}(\omega)\,\bar{\bar{F}}_{j'}, \qquad (3.33)$$

$$\bar{\bar{\alpha}}_{jj'}^{vv'}(\omega) = -\mathrm{i}\,\bar{\bar{F}}_j\,\bar{\bar{T}}_{jj'}^{vv'}(\omega)\,\bar{\bar{F}}_{j'}^{-1}, \qquad (3.34)$$

where $\{j, j'\} = \{1, 2, 3\}$ and $\{v, v'\} = \{\mathrm{e}, \mathrm{m}\}$.

The normalized polarizability submatrices are dimensionless and, hence, can be directly compared to each other. Figure 3.2b shows the sorting of the polarizability matrix, as used throughout the thesis.

If the polarizabilities in SI units ($[\mathrm{m}^{j+j'+1}]$) are required, they can be obtained from:

$$\bar{\bar{\alpha}}_{jj'}^{vv'}(\omega) = \frac{\zeta_j \zeta_{j'}}{k(\omega)^{j+j'+1}}\,\bar{\bar{\alpha}}_{jj'}^{vv'}(\omega). \qquad (3.35a)$$

These *denormalized polarizabilities* are helpful when dealing with dipolar isotropic meta-atoms. That is because, for dipolar isotropic meta-atom, the denormalized polarizability and the primitive polarizability are identical, i.e.:

$$\bar{\bar{\alpha}}_{11}^{vv}(\omega) = \alpha_1^v(\omega)\,\bar{\bar{I}}_3 = \breve{\alpha}_1^v(\omega)\,\bar{\bar{I}}_3, \qquad (3.36a)$$

where $\bar{\bar{I}}_3$ is the identity matrix of size 3.

3.1.3 Optical cross-sections

The scattering cross-section, expressed in the spherical coordinates, is defined as [48]:

$$\sigma_{\mathrm{sca}}^{\mathrm{s}}(\omega) = \frac{1}{|\mathbf{E}_0|^2 k(\omega)^2} \sum_{j=1}^{3} \left(|\mathbf{b}_j^{\mathrm{e}}(\omega)|^2 + |\mathbf{b}_j^{\mathrm{m}}(\omega)|^2 \right), \qquad (3.37)$$

where $|.|^2$ is the 2-norm of a vector or a matrix. In the Cartesian coordinates, the scattering cross-section as a function of the Cartesian moment vectors can be derived as [75]:

$$
\sigma_{\mathrm{sca}}^{\mathrm{c}}(\omega) = \frac{k(\omega)^4}{|\mathbf{E}_0|^2}\left[\frac{1}{3!\pi\varepsilon(\omega)^2}|\mathbf{p}(\omega)|^2 + \frac{Z(\omega)^2}{3!\pi}|\mathbf{m}(\omega)|^2 + \frac{k(\omega)^2}{5!\pi\varepsilon(\omega)^2}|\mathbf{Q}^{\mathrm{e}}(\omega)|^2\right.
$$
$$
\left.+ \frac{k(\omega)^2 Z(\omega)^2}{5!\pi}|\mathbf{Q}^{\mathrm{m}}(\omega)|^2 + \frac{k(\omega)^4}{7!\pi\varepsilon(\omega)^2}|\mathbf{O}^{\mathrm{e}}(\omega)|^2 + \frac{k(\omega)^4 Z(\omega)^2}{7!\pi}|\mathbf{O}^{\mathrm{m}}(\omega)|^2\right].
$$
$$
\tag{3.38}
$$

Similarly, the extinction cross-section in the VSH basis and the spherical coordinates can be calculated as [48, 75]:

$$
\sigma_{\mathrm{ext}}^{\mathrm{s}}(\omega) = \frac{-1}{|\mathbf{E}_0|^2 k(\omega)^2}\Re\left\{\sum_{j=1}^{3}\left[\mathbf{q}_j^{\mathrm{e}}(\omega)\cdot\mathbf{b}_j^{\mathrm{e}}(\omega)^* + \mathbf{q}_j^{\mathrm{m}}(\omega)\cdot\mathbf{b}_j^{\mathrm{m}}(\omega)^*\right].\right\}, \tag{3.39}
$$

$$
\sigma_{\mathrm{ext}}^{\mathrm{c}}(\omega) = \frac{-k(\omega)}{|\mathbf{E}_0|^2}\Im\left[\frac{\mathbf{E}_1(\omega)\cdot\mathbf{p}(\omega)^*}{\varepsilon(\omega)} + Z(\omega)^2\mathbf{H}_1(\omega)\cdot\mathbf{m}(\omega)^* + \frac{\mathbf{E}_2(\omega)\cdot\mathbf{Q}^{\mathrm{e}}(\omega)^*}{\varepsilon(\omega)}+\right.
$$
$$
\left. Z(\omega)^2\mathbf{H}_2(\omega)\cdot\mathbf{Q}^{\mathrm{m}}(\omega)^* + \frac{\mathbf{E}_3(\omega)\cdot\mathbf{O}^{\mathrm{e}}(\omega)^*}{\varepsilon(\omega)} + Z(\omega)^2\mathbf{H}_3(\omega)\cdot\mathbf{O}^{\mathrm{m}}(\omega)^*\right]. \tag{3.40}
$$

The *optical theorem* dictates:

$$
\sigma_{\mathrm{ext}}(\omega) = \sigma_{\mathrm{abs}}(\omega) + \sigma_{\mathrm{sca}}(\omega). \tag{3.41}
$$

Therefore, the absorption cross-section can be calculated from (3.38) and (3.40), as $\sigma_{\mathrm{abs}}(\omega) = \sigma_{\mathrm{ext}}(\omega) - \sigma_{\mathrm{sca}}(\omega)$.

In summary, we have provided the tools required to analyze a single meta-atom with arbitrary symmetry in the Cartesian basis. Moreover, formulas to move from the spherical to the Cartesian basis were presented. In the following sections, we discuss meta-atoms with certain symmetries.

3.2   Isotropic meta-atoms

The optical response of an isotropic medium, whose properties are quantified by a permittivity, is direction-independent. The permittivity at a given frequency is then simply a scalar. Isotropic meta-atoms are the most symmetric objects in the spherical basis and also the Cartesian basis in use in this thesis. Isotropic meta-atoms include homogeneous, core-multishell, and colloidal [169, 175] spheres. Please note that we assume, throughout the thesis, that the meta-atoms are made from linear materials. In this section, we study isotropic meta-atoms through their polarizability and T matrices. Furthermore, we present models, such as the Lorentzian or the minimalist Mie model, to describe the possible values the entries in the polarizability or the T matrix can attain in the case of such isotropic meta-atoms.

Mie coefficients

For a homogeneous sphere, the problem of light scattering can be analytically solved by the well-known Mie theory [58]. In this theory, the scattered field coefficients are linked to the incident field coefficients in Eq. 3.1-3.2 as:

$$b_{jm}^{\mathrm{e}}(\omega) = -a_j(\omega)\, q_{jm}^{\mathrm{e}}(\omega), \tag{3.42}$$
$$b_{jm}^{\mathrm{m}}(\omega) = -b_j(\omega)\, q_{jm}^{\mathrm{m}}(\omega), \tag{3.43}$$

where $a_j(\omega)$ and $b_j(\omega)$ are the electric and magnetic *Mie coefficients*, respectively. The Mie coefficients of a homogeneous sphere are expressed as [146, 151, 157]:

$$a_j(\omega) = \frac{\mu_{\mathrm{e}}(\omega)Z(\omega)^2 j_j\left(\tilde{R}_{\mathrm{s}}(\omega)\right)[x(\omega)j_j(x(\omega))]' - \mu_{\mathrm{s}}(\omega)j_j(x(\omega))\left[\tilde{R}_{\mathrm{s}}(\omega)j_j\left(\tilde{R}_{\mathrm{s}}(\omega)\right)\right]'}{\mu_{\mathrm{e}}(\omega)Z(\omega)^2 j_j\left(\tilde{R}_{\mathrm{s}}(\omega)\right)\left[x(\omega)h_j^{(1)}(x(\omega))\right]' - \mu_{\mathrm{s}}(\omega)h_j^{(1)}(x(\omega))\left[\tilde{R}_{\mathrm{s}}(\omega)j_j\left(\tilde{R}_{\mathrm{s}}(\omega)\right)\right]'}, \tag{3.44}$$

$$b_j(\omega) = \frac{\mu_{\mathrm{s}}(\omega)j_j\left(\tilde{R}_{\mathrm{s}}(\omega)\right)[x(\omega)j_j(x(\omega))]' - \mu_{\mathrm{e}}(\omega)j_j(x(\omega))\left[\tilde{R}_{\mathrm{s}}(\omega)j_j\left(\tilde{R}_{\mathrm{s}}(\omega)\right)\right]'}{\mu_{\mathrm{s}}(\omega)j_j\left(\tilde{R}_{\mathrm{s}}(\omega)\right)\left[x(\omega)h_j^{(1)}(x(\omega))\right]' - \mu_{\mathrm{e}}(\omega)h_j^{(1)}(x(\omega))\left[\tilde{R}_{\mathrm{s}}(\omega)j_j\left(\tilde{R}_{\mathrm{s}}(\omega)\right)\right]'}, \tag{3.45}$$

where subscript "e" and "s" denote the optical properties of the embedding medium and the sphere, respectively. Moreover, $j_j(x)$ and $h_j(x)$ denote the spherical Bessel and Hankel functions of j's order, respectively. The primes are derivatives with respect to the argument. The parameters $x(\omega)$, $\eta(\omega)$, and $\tilde{R}_{\mathrm{s}}(\omega)$ are defined as:

$$x(\omega) = \frac{\omega}{c}\sqrt{\varepsilon_{\mathrm{e}}(\omega)\,\mu_{\mathrm{e}}(\omega)}\,R_s, \quad \eta(\omega) = \sqrt{\frac{\varepsilon_s(\omega)\,\mu_s(\omega)}{\varepsilon_{\mathrm{e}}(\omega)\,\mu_{\mathrm{e}}(\omega)}}, \quad \tilde{R}_{\mathrm{s}}(\omega) = x(\omega)\,\eta(\omega), \quad (3.46)$$

where $R_s(\omega)$ is the radius of the sphere. Bohren and Huffman suggest a multipolar order of $N = x + 4x^{1/3} + 2$ to be sufficient for capturing the full response of a homogenous sphere [46, 157].

Dual spheres

For a dual meta-atom, where the impedance of the medium $Z_{\mathrm{e}}(\omega)$ is equal to the impedance of the sphere's material $Z_{\mathrm{s}}(\omega)$:

$$Z_{\mathrm{s}}(\omega) = Z_{\mathrm{e}}(\omega), \tag{3.47}$$
$$\sqrt{\frac{\mu_s(\omega)}{\varepsilon_s(\omega)}} = \sqrt{\frac{\mu_{\mathrm{e}}(\omega)}{\varepsilon_{\mathrm{e}}(\omega)}}, \tag{3.48}$$

it is straightforward to show, from Eq. 3.44-3.45, that $a_j(\omega) = b_j(\omega)$. Alternatively, we can show that if $a_{j>0}(\omega) = b_{j>0}(\omega)$, then, the meta-atom preserves the helicity of the impinging light upon interaction, and, hence, is dual [159].

In optics, materials do not show magnetic response, i.e., $\mu_s(\omega) = \mu_e(\omega) = 1$. Therefore, realizing perfectly dual meta-atoms is not plausible. Nevertheless, meta-atoms like helices [176], core-multishell [145], and homogeneous spheres [177, 178] can be engineered to approximate the dual behavior, e.g., for spheres, $a_j(\omega) \approx b_j(\omega)$. A meta-atom which have equal electric and magnetic dipolar but vanishing higher-order Mie coefficients (i.e., $a_1(\omega) = b_1(\omega)$, $a_{j>1}(\omega) = b_{j>1}(\omega) \approx 0$) is called an isotropic *dual dipolar* meta-atom.
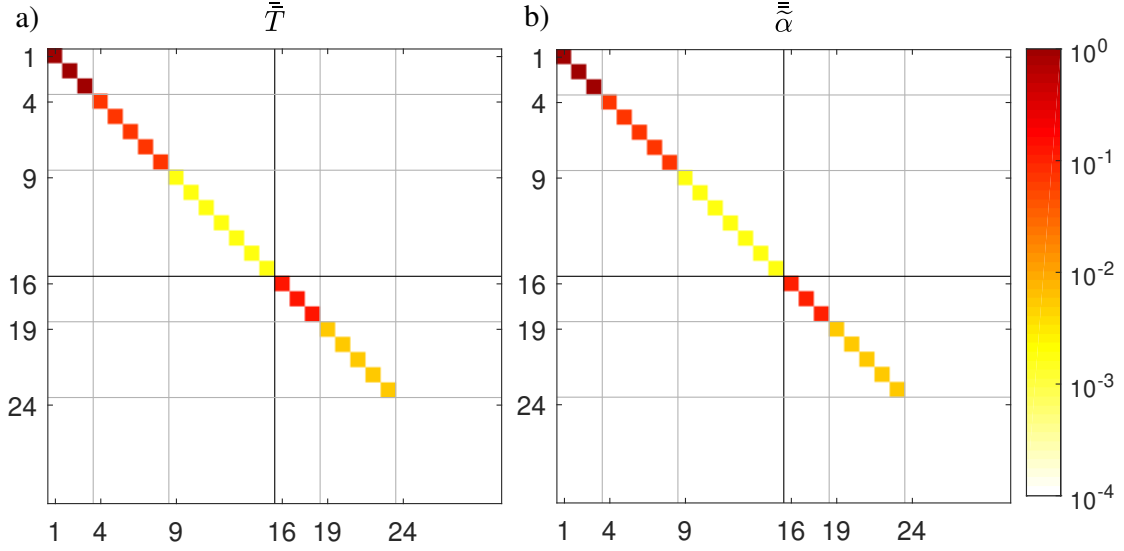
Figure 3.3: **Isotropic meta-atoms:** a) The T-matrix amplitude and b) the normalized polarizability matrix amplitude of an isotropic silver-silica core-shell sphere embedded in free space with $r_1 = 120\,\mathrm{nm}$, $r_2 = 120 + 30\,\mathrm{nm}$ as the radii of the core and the shell, at a wavelength of $\lambda = 780\,\mathrm{nm}$. The permittivity for silver and silica are taken from Ref. [179] and Ref. [180], respectively.

3.2.1   Polarizability and T-matrix symmetry

Due to the symmetry of spherical meta-atoms, the T matrix of spherical objects is diagonal. From Eq. 3.42, we can find out that the diagonal elements of the T-matrix are the Mie coefficients with a negative sign, i.e.:

$$\bar{\bar{T}}_{jj'}^{vv'}(\omega) = -a_j(\omega)\,\delta_{jj'}\delta_{vv'}\bar{\bar{I}}_j, \qquad (3.49)$$

where $\bar{\bar{I}}_j$ is the identity matrix of size j. For up to the quadrupolar order, the T matrix of an isotropic particle can be modeled as:

$$\bar{\bar{T}} = -\begin{pmatrix}
a_1 & 0 & 0 & 0 & 0 & 0 & 0 & 0 & 0 & 0 & 0 & 0 & 0 & 0 & 0 & 0 \\
0 & a_1 & 0 & 0 & 0 & 0 & 0 & 0 & 0 & 0 & 0 & 0 & 0 & 0 & 0 & 0 \\
0 & 0 & a_1 & 0 & 0 & 0 & 0 & 0 & 0 & 0 & 0 & 0 & 0 & 0 & 0 & 0 \\
0 & 0 & 0 & a_2 & 0 & 0 & 0 & 0 & 0 & 0 & 0 & 0 & 0 & 0 & 0 & 0 \\
0 & 0 & 0 & 0 & a_2 & 0 & 0 & 0 & 0 & 0 & 0 & 0 & 0 & 0 & 0 & 0 \\
0 & 0 & 0 & 0 & 0 & a_2 & 0 & 0 & 0 & 0 & 0 & 0 & 0 & 0 & 0 & 0 \\
0 & 0 & 0 & 0 & 0 & 0 & a_2 & 0 & 0 & 0 & 0 & 0 & 0 & 0 & 0 & 0 \\
0 & 0 & 0 & 0 & 0 & 0 & 0 & a_2 & 0 & 0 & 0 & 0 & 0 & 0 & 0 & 0 \\
0 & 0 & 0 & 0 & 0 & 0 & 0 & 0 & b_1 & 0 & 0 & 0 & 0 & 0 & 0 & 0 \\
0 & 0 & 0 & 0 & 0 & 0 & 0 & 0 & 0 & b_1 & 0 & 0 & 0 & 0 & 0 & 0 \\
0 & 0 & 0 & 0 & 0 & 0 & 0 & 0 & 0 & 0 & b_1 & 0 & 0 & 0 & 0 & 0 \\
0 & 0 & 0 & 0 & 0 & 0 & 0 & 0 & 0 & 0 & 0 & b_2 & 0 & 0 & 0 & 0 \\
0 & 0 & 0 & 0 & 0 & 0 & 0 & 0 & 0 & 0 & 0 & 0 & b_2 & 0 & 0 & 0 \\
0 & 0 & 0 & 0 & 0 & 0 & 0 & 0 & 0 & 0 & 0 & 0 & 0 & b_2 & 0 & 0 \\
0 & 0 & 0 & 0 & 0 & 0 & 0 & 0 & 0 & 0 & 0 & 0 & 0 & 0 & b_2 & 0 \\
0 & 0 & 0 & 0 & 0 & 0 & 0 & 0 & 0 & 0 & 0 & 0 & 0 & 0 & 0 & b_2
\end{pmatrix}. \qquad (3.50)$$

Note that different definitions of the VSH functions in Eq. 3.1-3.2 can lead to a different conclusion concerning the prefactors. The T matrix, up to an octupolar order, for a given core-shell sphere at a specific wavelength is shown in Fig. 3.3a. The white elements in the matrix are either *symmetry-protected* strictly zero or express a vanishing response of the small meta-atom for higher multipolar orders.

The normalized polarizability for an isotropic meta-atom is also diagonal and can be derived from the respective T matrix via Eq. 3.34:

$$\bar{\bar{\widetilde{\alpha}}}_{jj'}^{vv'}(\omega) = \mathrm{i}a_j(\omega)\,\delta_{jj'}\delta_{vv'}\bar{\bar{I}}_j = \widetilde{\alpha}_j^v(\omega)\,\delta_{jj'}\delta_{vv'}\bar{\bar{I}}_j, \tag{3.51}$$

where $\widetilde{\alpha}_j^v(\omega)$ is the scalar electric ($v = \mathrm{e}$) or magnetic ($v = \mathrm{m}$) normalized polarizability of j's order. As evident from the equation, the diagonal elements of the normalized polarizability matrix are the Mie coefficients with an i multiplicand. Exemplarily, Fig. 3.3b, shows the normalized polarizability matrix for the same core-shell sphere as considered in Fig. 3.3a. For simplicity, we may use $\widetilde{\alpha}_\mathrm{p}(\omega)$ ($\widetilde{\alpha}_\mathrm{m}(\omega)$) and $\widetilde{\alpha}_\mathrm{Q}(\omega)$ ($\widetilde{\alpha}_\mathrm{M}(\omega)$) for the normalized electric (magnetic) dipolar and quadrupolar polarizabilities. Up to quadrupolar order, the normalized polarizability of an isotropic meta-atom can be modeled as:

$$\bar{\bar{\widetilde{\alpha}}} = - \begin{pmatrix}
\widetilde{\alpha}_\mathrm{p} & 0 & 0 & 0 & 0 & 0 & 0 & 0 & 0 & 0 & 0 & 0 & 0 & 0 & 0 & 0 \\
0 & \widetilde{\alpha}_\mathrm{p} & 0 & 0 & 0 & 0 & 0 & 0 & 0 & 0 & 0 & 0 & 0 & 0 & 0 & 0 \\
0 & 0 & \widetilde{\alpha}_\mathrm{p} & 0 & 0 & 0 & 0 & 0 & 0 & 0 & 0 & 0 & 0 & 0 & 0 & 0 \\
0 & 0 & 0 & \widetilde{\alpha}_\mathrm{Q} & 0 & 0 & 0 & 0 & 0 & 0 & 0 & 0 & 0 & 0 & 0 & 0 \\
0 & 0 & 0 & 0 & \widetilde{\alpha}_\mathrm{Q} & 0 & 0 & 0 & 0 & 0 & 0 & 0 & 0 & 0 & 0 & 0 \\
0 & 0 & 0 & 0 & 0 & \widetilde{\alpha}_\mathrm{Q} & 0 & 0 & 0 & 0 & 0 & 0 & 0 & 0 & 0 & 0 \\
0 & 0 & 0 & 0 & 0 & 0 & \widetilde{\alpha}_\mathrm{Q} & 0 & 0 & 0 & 0 & 0 & 0 & 0 & 0 & 0 \\
0 & 0 & 0 & 0 & 0 & 0 & 0 & \widetilde{\alpha}_\mathrm{Q} & 0 & 0 & 0 & 0 & 0 & 0 & 0 & 0 \\
0 & 0 & 0 & 0 & 0 & 0 & 0 & 0 & \widetilde{\alpha}_\mathrm{m} & 0 & 0 & 0 & 0 & 0 & 0 & 0 \\
0 & 0 & 0 & 0 & 0 & 0 & 0 & 0 & 0 & \widetilde{\alpha}_\mathrm{m} & 0 & 0 & 0 & 0 & 0 & 0 \\
0 & 0 & 0 & 0 & 0 & 0 & 0 & 0 & 0 & 0 & \widetilde{\alpha}_\mathrm{m} & 0 & 0 & 0 & 0 & 0 \\
0 & 0 & 0 & 0 & 0 & 0 & 0 & 0 & 0 & 0 & 0 & \widetilde{\alpha}_\mathrm{M} & 0 & 0 & 0 & 0 \\
0 & 0 & 0 & 0 & 0 & 0 & 0 & 0 & 0 & 0 & 0 & 0 & \widetilde{\alpha}_\mathrm{M} & 0 & 0 & 0 \\
0 & 0 & 0 & 0 & 0 & 0 & 0 & 0 & 0 & 0 & 0 & 0 & 0 & \widetilde{\alpha}_\mathrm{M} & 0 & 0 \\
0 & 0 & 0 & 0 & 0 & 0 & 0 & 0 & 0 & 0 & 0 & 0 & 0 & 0 & \widetilde{\alpha}_\mathrm{M} & 0 \\
0 & 0 & 0 & 0 & 0 & 0 & 0 & 0 & 0 & 0 & 0 & 0 & 0 & 0 & 0 & \widetilde{\alpha}_\mathrm{M}
\end{pmatrix}. \tag{3.52}$$

The denormalized scalar polarizabilities can also be calculated as:

$$\alpha_j^\mathrm{e}(\omega) = \frac{(2j+1)!\pi\mathrm{i}}{k^{2j+1}}a_j(\omega), \tag{3.53}$$

$$\alpha_j^\mathrm{m}(\omega) = \frac{(2j+1)!\pi\mathrm{i}}{k^{2j+1}}b_j(\omega), \tag{3.54}$$

where j is the multipolar order. For simplicity, we use the $\alpha_\mathrm{p}(\omega)$ ($\alpha_\mathrm{m}(\omega)$) and $\alpha_\mathrm{Q}(\omega)$ ($\alpha_\mathrm{M}(\omega)$) for the denormalized electric (magnetic) dipolar and quadrupolar polarizabilities.

3.2.2 The Lorentzian polarizability model

A fundamental question concerns the possible dispersion of the polarizability. Of course, as outlined before, the polarizability can be retrieved numerically for a given meta-atom. Still, it would be of paramount importance for fundamental design problems to express the essential functional dependency. That would imply the ability to have a phenomenological model that expresses the possible typical frequency dependency. A well-known phenomenological model for the entries of the polarizability matrix of isotropic meta-atoms is the Lorentzian dispersion profile. The Lorentzian profile models the temporal dispersion of the polarizability of an isotropic scatterer in the spectral proximity of a resonance. The model is based on the Lorentz oscillator model, in which an atom is assumed to comprise a negatively charged electron bound to a positively charged nucleus. The force between the electron and the nucleus is assumed to follow Hook's law, i.e., a spring-like force with

a spring constant [181]. The oscillation of the electron can be driven into resonance when the time-harmonic excitation corresponds to its resonance frequency.

Based on the Lorentz oscillator model, the denormalized polarizability for an isotropic dipolar meta-atom characterized by an individual resonance can be written as:

$$\frac{1}{\alpha_{\mathrm{p}}(\omega)} = \frac{\omega_{0\mathrm{p}}^2 - \omega^2}{\alpha_{0\mathrm{p}}} - \mathrm{i}\frac{\omega}{\alpha_{0\mathrm{p}}}\gamma_{\Omega\mathrm{p}} - \mathrm{i}\frac{k(\omega)^3}{3!\pi}, \tag{3.55}$$

$$\frac{1}{\alpha_{\mathrm{m}}(\omega)} = \frac{\omega_{0\mathrm{m}}^2 - \omega^2}{\alpha_{0\mathrm{m}}} - \mathrm{i}\frac{\omega}{\alpha_{0\mathrm{m}}}\gamma_{\Omega\mathrm{m}} - \mathrm{i}\frac{k(\omega)^3}{3!\pi}, \tag{3.56}$$

where $\alpha_{\mathrm{p}}(\omega)$ $(\alpha_{\mathrm{m}}(\omega))$ is the denormalized electric (magnetic) dipolar polarizability, $\omega_{0\mathrm{p}}$ $(\omega_{0\mathrm{m}})$ is the *resonance frequency* of the electric (magnetic) resonance, $\alpha_{0\mathrm{p}}$ $(\alpha_{0\mathrm{m}})$ is the *oscillator strength*, and $\gamma_{\Omega\mathrm{p}}$ $(\gamma_{\Omega\mathrm{m}})$ is the *ohmic loss* of the resonance for the electric (magnetic) dipole. The last expression on the right is the corrected term for the radiation losses to satisfy the optical theorem [101, 162, 181–183]. In literature, sometimes, the dispersion of the magnetic dipole is modeled differently than that of the electric dipole [62]. However, the dispersion of the dipoles depends on the geometry of the design and, here, we only focus on the implications that a certain model provides while the actual meta-atom pertaining to the desired Mie coefficient is a secondary concern. Through multiple examples, we will show that this systematic approach has been consistently successful.

Similarly, we can use the Lorentzian profile to model the denormalized quadrupolar polarizabilities [31]:

$$\frac{1}{\alpha_{\mathrm{Q}}(\omega)} = k(\omega)^2\frac{\omega_{0\mathrm{Q}}^2 - \omega^2}{\alpha_{0\mathrm{Q}}} - \mathrm{i}k(\omega)^2\frac{\omega}{\alpha_{0\mathrm{Q}}}\gamma_{\Omega\mathrm{Q}} - \mathrm{i}\frac{k(\omega)^5}{5!\pi}, \tag{3.57}$$

$$\frac{1}{\alpha_{\mathrm{M}}(\omega)} = k(\omega)^2\frac{\omega_{0\mathrm{M}}^2 - \omega^2}{\alpha_{0\mathrm{M}}} - \mathrm{i}k(\omega)^2\frac{\omega}{\alpha_{0\mathrm{M}}}\gamma_{\Omega\mathrm{M}} - \mathrm{i}\frac{k(\omega)^5}{5!\pi}, \tag{3.58}$$

where $\alpha_{\mathrm{Q}}(\omega)$ $(\alpha_{\mathrm{M}}(\omega))$ is the denormalized electric (magnetic) quadrupolar polarizability, $\omega_{0\mathrm{Q}}$ $(\omega_{0\mathrm{M}})$ is the *resonance frequency* of the electric (magnetic) resonance, $\alpha_{0\mathrm{Q}}$ $(\alpha_{0\mathrm{M}})$ is the *oscillator strength*, and $\gamma_{\Omega\mathrm{Q}}$ $(\gamma_{\Omega\mathrm{M}})$ is the *ohmic loss* of the resonance for the electric (magnetic) quadrupole. The expressions with $k(\omega)^5$ are related to the radiation losses and guarantees that the profile satisfies the optical theorem.

From Eq. 3.53-3.54, the electric dipolar and quadrupolar Mie coefficients can also be rewritten with the Lorentzian profile:

$$\frac{1}{a_1(\omega)} = \frac{\omega_{0\mathrm{p}}^2 - \omega^2}{\alpha_{0\mathrm{p}}}\frac{3!\pi i}{k(\omega)^3} + \frac{3!\pi}{k(\omega)^3}\frac{\omega}{\alpha_{0\mathrm{p}}}\gamma_{\Omega\mathrm{p}} + 1, \tag{3.59}$$

$$\frac{1}{a_2(\omega)} = \frac{\omega_{0\mathrm{Q}}^2 - \omega^2}{\alpha_{0\mathrm{Q}}}\frac{5!\pi}{k(\omega)^3}\mathrm{i} + \frac{5!\pi}{k(\omega)^3}\frac{\omega}{\alpha_{0\mathrm{Q}}}\gamma_{\Omega\mathrm{Q}} + 1. \tag{3.60}$$

The magnetic Mie coefficients can also be similarly modeled.

The denormalized polarizability of a sharp dipolar resonance (e.g., for atoms), at the proximity of the resonance, can be simplified as [184]:

$$\alpha(\omega) = -\frac{6\pi}{k_0^3}\frac{\gamma_r(\omega)/2}{\delta(\omega) + [\gamma_{\mathrm{nr}}(\omega) + \gamma_\mathrm{r}(\omega)]\,\mathrm{i}/2}, \tag{3.61}$$
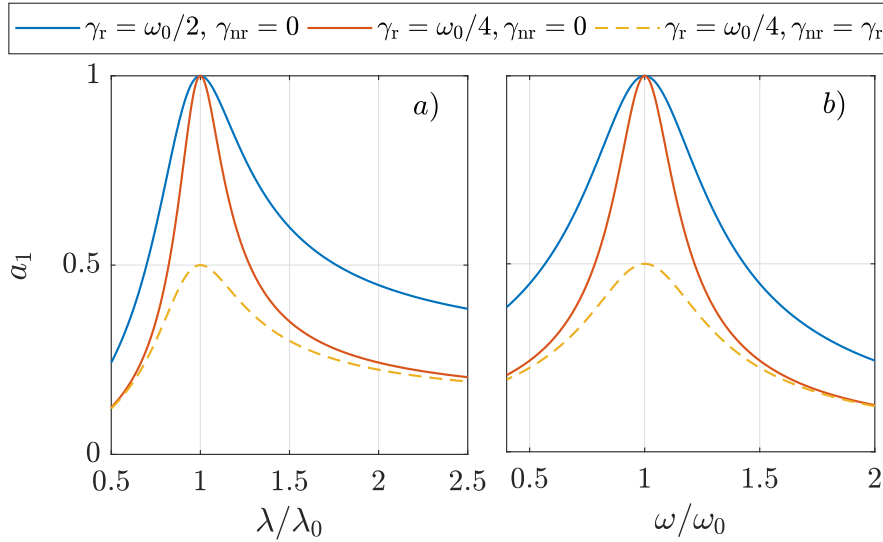
Figure 3.4: **A Lorentzian resonance**: The electric dipolar Mie coefficient modeled by a Lorentzian resonance (Eq. 3.61) with three different loss parameter combinations as a function of the a) wavelength and b) angular frequency. The resonance wavelength is $\lambda_0 = 1000\,\mathrm{nm}$.

where, $\delta(\omega) = \omega - \omega_0$, with $|\delta(\omega)| << \omega_0$ is the frequency detuning between excitation and resonance frequency ω_0, k_0 is the wavenumber at the resonance, and $\gamma_\mathrm{r}(\omega)$ and $\gamma_\mathrm{nr}(\omega)$ are the *radiative* and *non-radiative losses* of the resonance. Although this model is developed for sharp atomic transitions, we use it more liberally to explore physical concepts. Therefore, we may use the model for any resonance, sharp or not. In our studies, the actual bandwidth of a resonance is mostly not a critical factor. Figure 3.4 shows the electric dipolar Mie coefficient modeled by sharp Lorentzian polarizability (Eq. 3.61) for three different loss parameters in wavelength and frequency domain. A smaller radiative loss leads to a wider and, hence, stronger resonance. Without non-radiative loss, the peak of the Mie coefficient, which is unity, is always reached.

3.2.3 Minimalist Mie coefficient model

The analytical expressions for Mie coefficients of homogeneous spheres in Eq. 3.44-3.45 are exact but too complicated for fundamental investigations. The same is true for the Mie coefficients of core-multishell spheres. In these equations, the Mie coefficients depend on many variables from core and shells' radii and the dynamic material properties of the core, the shells, and the medium. Of course, all the electric and magnetic Mie coefficients are determined for a given set of parameters. However, the interdependency of the electric and magnetic Mie coefficients of different multipolar orders is complex and challenging to assess. The interdependence and multi-variable dependency is a significant obstacle in theoretical electromagnetic analysis. For example, the scattering properties of an array of electric octupoles cannot be investigated right away if only physical objects are to be considered. For such an investigation, a homogenous or core-multishell sphere that can be described by a single electric octupole moment while all the other multipolar orders are zero at the operating wavelength needs to be designed. Then these spheres need to be
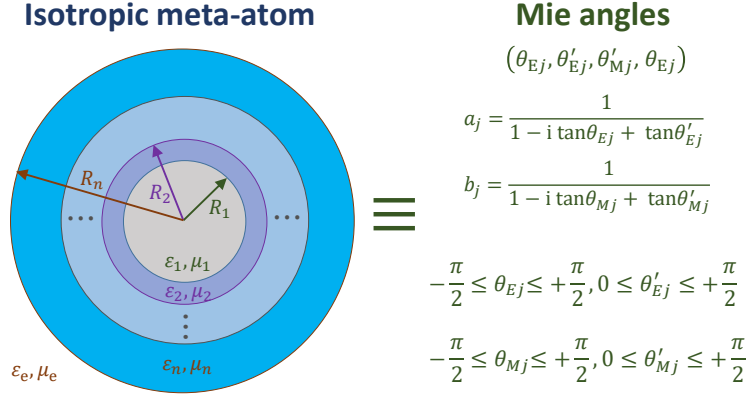
Figure 3.5: **The Mie angles [59]:** A minimal model for the Mie coefficients of isotropic meta-atoms. Adapted with permission from Ref. [59] © The Optical Society.

put on an array to study the properties. This approach is time-consuming and cumbersome.

There are many approximations for calculating the Mie coefficients [185–188]. However, interdependence and multi-variable dependence persist, hindering a systematic analysis of an individual's physically accessible optical properties or an aggregate of spherical meta-atoms. We seek an easy expression with a minimal number of degrees of freedom that can capture all physically possible values of Mie coefficients independently. Then, we can systematically search for the desired combination of Mie coefficients that provides a desired optical function at a design wavelength. The geometrical and material properties of an isotropic meta-atom with these coefficients can be realized in a secondary step. The importance of the method is that in this second step, the search for the desired meta-atom is performed outside the lattice or the aggregate and, hence, extensively reduces the computations.

Minimalist and straightforward expressions have been previously suggested for non-absorbing spheres [162, 189–194]. In the next subsubsection, primarily based on the work presented in Ref. [59], a general minimalist model for absorbing or non-absorbing materials are provided. The derivations rely on the optical theorem, and we derive generic expressions for any possible Mie coefficient a sphere made from any isotropic and linear materials may offer. These expressions depend on only two parameters (for each multipolar order and each parity) that we call the *Mie angles*. Figure 3.5 shows the general idea of the minimalist model.

In the following subsubsections, we provide insights into the physical meaning of these Mie angles. At the example of the dipolar coefficients, we show that the analytical space provided by the model is densely filled with electric and magnetic dipolar Mie coefficients of actual non-magnetic spheres.

3.2.3.1   Developing the minimalist model

Based on the optical theorem, the extinction cross-section is equal to the sum of the scattering and the absorption cross-section. From Eq. 3.37, 3.39, and 3.41, the scattering, extinction, and absorption cross-sections of an isotropic meta-atom, as

a function of the Mie coefficients, that is illuminated with a plane wave, can be calculated as [165]:

$$\sigma_{\text{sca}}(\omega) = \frac{\lambda(\omega)^2}{2\pi} \sum_{j=1}^{\infty} (2j+1) \left[|a_j(\omega)|^2 + |b_j(\omega)|^2 \right], \tag{3.62}$$

$$\sigma_{\text{ext}}(\omega) = \frac{\lambda(\omega)^2}{2\pi} \sum_{j=1}^{\infty} (2j+1) \Re\left[a_j(\omega) + b_j(\omega) \right], \tag{3.63}$$

$$\sigma_{\text{abs}}(\omega) = \frac{\lambda(\omega)^2}{2\pi} \sum_{j=1}^{\infty} (2j+1) \left\{ \Re\left[a_j(\omega) + b_j(\omega) \right] - |a_j(\omega)|^2 - |b_j(\omega)|^2 \right\}, \tag{3.64}$$

where $\lambda(\omega) = \lambda_0/n(\omega)$ is the illumination wavelength in an embedding medium with a refractive index $n(\omega)$.

For an isotropic meta-atom, the different scattering channels do not mix; therefore, we can independently investigate each channel. Without loss of generality, we only consider the magnetic contribution here. The electric contribution will follow the same procedure, and the conclusions will be the same due to the electromagnetic duality symmetry. The contribution of a single magnetic Mie channel $b_j(\omega)$ to the total cross-sections is:

$$\sigma_{\text{sca},\text{M}j}(\omega) = (2j+1) \frac{\lambda(\omega)^2}{2\pi} |b_j(\omega)|^2, \tag{3.65}$$

$$\sigma_{\text{ext},\text{M}j}(\omega) = (2j+1) \frac{\lambda(\omega)^2}{2\pi} \Re\left[b_j(\omega) \right], \tag{3.66}$$

$$\sigma_{\text{abs},\text{M}j}(\omega) = (2j+1) \frac{\lambda(\omega)^2}{2\pi} \left\{ \Re\left[b_j(\omega) \right] - |b_j(\omega)|^2 \right\}, \tag{3.67}$$

where Mj refers to the j's magnetic channel.

Mie angles for non-absorbing meta-atoms: For an isotropic meta-atom made from a non-absorbing material, i.e., $\sigma_{\text{abs},\text{M}j}(\omega) = 0$, the optical theorem requires:

$$\sigma_{\text{ext},\text{M}j}(\omega) = \sigma_{\text{abs},\text{M}j}(\omega) + \sigma_{\text{sca},\text{M}j}(\omega), \tag{3.68}$$

$$\Re\left[b_j(\omega) \right] = |b_j(\omega)|^2. \tag{3.69}$$

The magnetic coefficient $b_j(\omega)$ is a complex number and, hence, we can write it in an exponential form as $b_j(\omega) = |b_j(\omega)| \exp(i\theta_{\text{M}j}(\omega))$, with $\theta_{\text{M}j}(\omega) = \arg(b_j(\omega))$ as what we call the *Mie angle*. Replacing the exponential form in Eq. 3.69, we can derive that $\cos(\theta_{\text{M}j}(\omega)) = |b_j(\omega)|$. Therefore, we can write the Mie coefficient model as [162]:

$$b_j(\omega) = \cos(\theta_{\text{M}j}(\omega)) \exp(i\theta_{\text{M}j}(\omega)), \tag{3.70}$$

where $-\pi/2 \leqslant \theta_{\text{M}j}(\omega) \leqslant +\pi/2$ directly follows. The expression in Eq. 3.70 captures all possible values for the magnetic Mie coefficient that agrees with the optical theorem, i.e., is physical. Note that we will assume a single frequency. If we sweep through the full angular range $-\pi/2 \leqslant \theta_{\text{M}j}(\omega) \leqslant +\pi/2$, the magnetic Mie coefficients trace out a circle in the complex plane with a radius of 0.5 that is centered at $(0i, 0.5)$. An illustration of that functional dependence of the Mie coefficient is

shown in Fig. 3.6a as the dark violet line. At a magnetic Mie angle of $\theta_{\mathrm{M}j}(\omega) = 0$, the magnetic Mie coefficient attains its maximum value, which is 1. According to Eq. 3.65-3.66, at this point of operation, the scattering/extinction cross-section maximizes to $(2j+1)\lambda(\omega)^2/(2\pi)$ [162, 195].

Although the minimalist model is developed for magnetic Mie coefficients, exactly the same equations can be derived for electric Mie coefficients by replacing $b_j(\omega)$ with $a_j(\omega)$ and Mj with Ej.

Mie angles for absorbing meta-atoms: Here, we assume an absorbing passive isotopic meta-atom. Passivity implies that the absorption cross-section is positive. Therefore, based on the optical theorem, we obtain:

$$\sigma_{\mathrm{ext},\mathrm{M}j}(\omega) \geq \sigma_{\mathrm{sca},\mathrm{M}j}(\omega) \implies \Re(b_j(\omega)) \geq |b_j(\omega)|^2 \implies \cos\theta_{\mathrm{M}j}(\omega) \geq |b_j(\omega)|. \quad (3.71)$$

The derived inequality equals the space enclosed by a circle of radius 0.5 that is centered at $(0\mathrm{i}, 0.5)$. This is the violet space in Fig. 3.6a. The same is true for the electric Mie coefficients.

Therefore, as a general conclusion, the Mie coefficient of a passive isotropic meta-atom, be it absorbing or non-absorbing, must be on or inside a circle of radius 0.5 that is centered at $(0\mathrm{i}, 0.5)$ as shown in Fig. 3.6a. Having reached this conclusion, we aspire to find a model that first and foremost respects physical limitations. Furthermore, the model should cover the entire accessible area with the smallest number of degrees of freedom. Moreover, the model parameters should allow a physical interpretation. After several attempts, we suggest the following general model for the Mie coefficients of an isotropic meta-atom:

$$a_j(\omega) = \frac{1}{\frac{1}{\cos\theta_{\mathrm{E}j}(\omega)\exp\mathrm{i}\theta_{\mathrm{E}j}(\omega)} + \tan\theta'_{\mathrm{E}j}(\omega)} = \frac{1}{1 - \mathrm{i}\tan\theta_{\mathrm{E}j}(\omega) + \tan\theta'_{\mathrm{E}j}(\omega)}, \quad (3.72)$$

$$b_j(\omega) = \frac{1}{1 - \mathrm{i}\tan\theta_{\mathrm{E}j}(\omega) + \tan\theta'_{\mathrm{E}j}(\omega)}, \quad (3.73)$$

where $-\frac{\pi}{2} \leqslant \theta_{\mathrm{E}j}(\omega), \theta_{\mathrm{M}j}(\omega) \leqslant +\frac{\pi}{2}$ and $0 \leqslant \theta'_{\mathrm{E}j}(\omega), \theta'_{\mathrm{M}j}(\omega) \leqslant +\frac{\pi}{2}$ are the *detuning and absorption Mie angles*, respectively. We will justify this nomenclature, shortly.

Mie angles of actual homogenous spheres

So far, we have identified the physically possible values of the Mie coefficients in the complex plane. Here, we want to see if all sections of the physically feasible space, i.e., the interior of a circle, are filled by the Mie coefficients of an actual homogenous sphere or some sections are systematically unreachable. To that aim, we exemplarily, sweep through the radius R_s and complex permittivity of a non-magnetic sphere and calculate the dipolar Mie coefficients (using Eq. 3.44-3.45). The calculated electric and magnetic dipolar Mie coefficients are shown in Fig. 3.6b-c. Even with a homogeneous sphere and without resorting to more complicated core-multishell spheres, all sections of the physically accessible complex plane are reached with realistic parameters. This small test shows that our model can be reliably exploited in analytic investigations. Note that the white spaces seen in the figures are only due to inhomogeneous coverage by the linear spacing of the input parameters. With discrete points, we may never fill an entire space. However, the

fact that we do not see a vast inaccessible region is reassuring. Similar results are obtained for higher Mie coefficient orders. As a result, our model is valid for dipoles, quadrupoles, and so forth.

Using the Mie angles, unlike using actual spheres, allows us to change all Mie coefficients independently. Moreover, we can be sure that the Mie angles are physical, and with sufficient effort, an object can, in principle, be identified that offers these coefficients. This *Mie angle method* is especially beneficial for smaller isotropic meta-atoms that require a fewer number of multipoles to capture their complete response, i.e., up to quadrupolar order.

It is worth mentioning that for homogeneous spheres, recurrence equations exist such that octupolar Mie coefficients can be derived from dipolar and quadrupolar Mie coefficients [196].
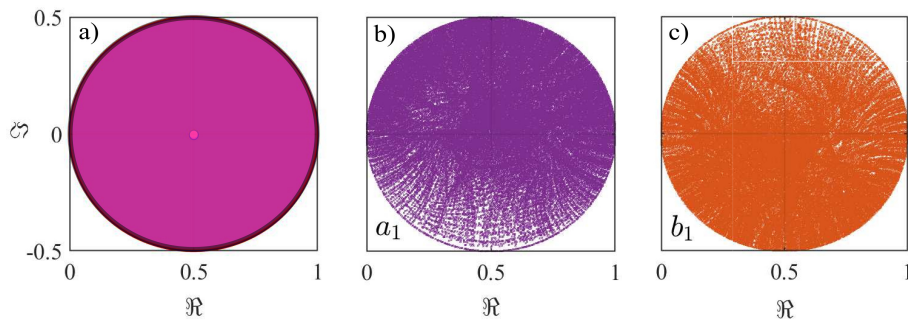
Figure 3.6: **Physically feasible and actual Mie coefficient values [59]:** a) The physically allowed space for Mie coefficients in the complex plane based on the optical theorem (using Eq. 3.73). For a non-absorbing sphere, the physically accessible values are on the dark-violet circle. For an absorbing sphere, the physically accessible values are within the violet disk. The pink dot in the center of the circle shows the point in which absorption cross-section maximizes. b) Electric and c) magnetic dipolar Mie coefficient of homogeneous spheres embedded in the free space with discrete radius $R_s \in [0.45 : 0.005 : 0.75]\lambda$, discrete permittivity $\Re(\varepsilon_r) \in [0 : 0.5 : 20]$, $\Im(\varepsilon_r) \in [0 : 0.025 : 1]$, and permeability $\mu_r = 1$ using Eq. 3.44-3.45. Each marker point shows an individual realization. Adapted with permission from Ref. [59] © The Optical Society.

Optical cross-sections

Assuming a single magnetic channel, the optical cross-sections as a function of the Mie angles are [59]:

$$\sigma_{\mathrm{sca},\mathrm{M}j}(\omega) = (2j+1)\frac{\lambda(\omega)^2}{2\pi}\frac{1}{\left[1+\tan\theta'_{\mathrm{M}j}(\omega)\right]^2 + \tan^2\theta_{\mathrm{M}j}(\omega)}, \qquad (3.74)$$

$$\sigma_{\mathrm{ext},\mathrm{M}j}(\omega) = (2j+1)\frac{\lambda(\omega)^2}{2\pi}\frac{1+\tan\theta'_{\mathrm{M}j}(\omega)}{\left[1+\tan\theta'_{\mathrm{M}j}(\omega)\right]^2 + \tan^2\theta_{\mathrm{M}j}(\omega)}, \qquad (3.75)$$

$$\sigma_{\mathrm{abs},\mathrm{M}j}(\omega) = (2j+1)\frac{\lambda(\omega)^2}{2\pi}\frac{\tan\theta'_{\mathrm{M}j}(\omega)}{\left[1+\tan\theta'_{\mathrm{M}j}(\omega)\right]^2 + \tan^2\theta_{\mathrm{M}j}(\omega)}. \qquad (3.76)$$

The optical cross-sections for the electric contributions are exactly the same by replacing $\theta_{\mathrm{M}j}(\omega)$, and $\theta'_{\mathrm{M}j}(\omega)$ with $\theta_{\mathrm{E}j}(\omega)$, and $\theta'_{\mathrm{E}j}(\omega)$, respectively. The normalized
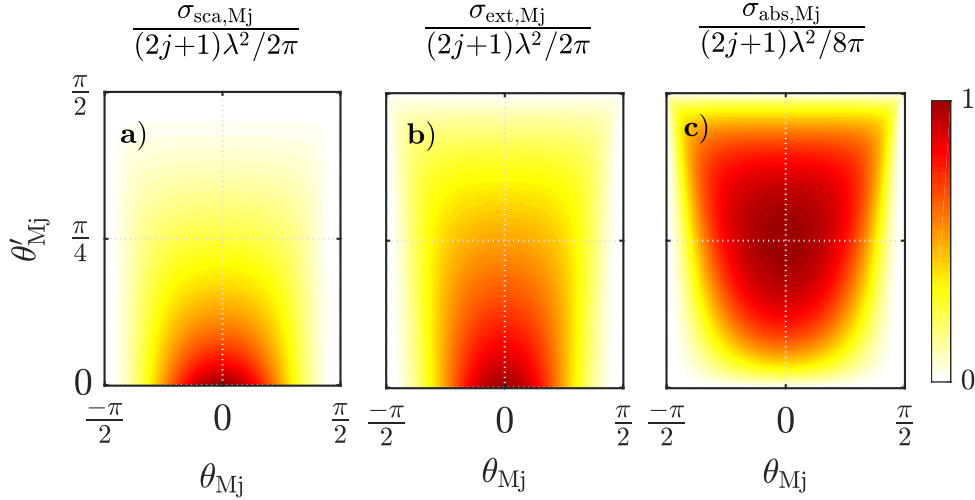
Figure 3.7: **Optical cross-sections with Mie angles [59]:** The normalized a) scattering, b) extinction, and c) absorption cross-sections as a function of the magnetic detuning θ_{Mj} and absorption θ'_{Mj} Mie angles using Eq. 3.74-3.76. Adapted with permission from Ref. [59] © The Optical Society.

optical cross-sections as a function of the Mie angles for an individual magnetic multipolar contribution are shown in Fig. 3.7. The normalization factors $(2j + 1)\lambda(\omega)^2/2\pi$, $(2j+1)\lambda(\omega)^2/2\pi$, and $(2j+1)\lambda(\omega)^2/8\pi$ are the maximum scattering, extinction, and absorption cross-section of a single resonance with multipolar order of j, respectively [162, 195]. The scattering cross-section in Fig. 3.7a is maximum when there is no absorption (i.e., $\theta'_{Ej}(\omega) = 0$) and the detuning from the resonance is zero (i.e., $\theta_{Ej}(\omega) = 0$). The same holds for the extinction cross-section. The maximum of the absorption cross-section occurs when the detuning is zero ($\theta_{Ej}(\omega) = 0$) and the absorption angle is $\pi/4$ ($\theta'_{Ej}(\omega) = \pi/4$).

3.2.3.2 Physical interpretation of Mie angles

To provide a physical interpretation of the Mie angles, we use the sharp Lorentzian dispersion profile for the polarizability of an isotropic meta-atom that we have introduced in Eq. 3.61. We look at how the parameters in the Mie-angle-based model fit the physical properties of a resonance within the Lorentzian model. Using the relation between the Mie coefficients and the denormalized polarizability (Eq. 3.54) for the magnetic dipolar Mie coefficient, we can rewrite the sharp Lorentzian profile as:

$$\frac{1}{b_1(\omega)} = \frac{-2\delta(\omega)}{\gamma_r(\omega)}i + \frac{\gamma_{nr}(\omega)}{\gamma_r(\omega)} + 1. \tag{3.77}$$

A direct comparison of the above equation with Eq. 3.73 leads to the following conclusion:

$$\tan\theta_{M1}(\omega) = \frac{2\delta(\omega)}{\gamma_r(\omega)}, \qquad \tan\theta'_{M1}(\omega) = \frac{\gamma_{nr}(\omega)}{\gamma_r(\omega)}. \tag{3.78}$$

Exploiting the electromagnetic duality symmetry, the same expressions can be derived for the electric Mie coefficient. Therefore, for any Mie resonance, we can say that $\theta_{Mj}(\omega)$ represents detuning and $\theta'_{Mj}(\omega)$ represents Ohmic losses, i.e., absorption. This conclusion assumes that the polarizability corresponding to the Mie resonance is a sharp Lorentzian profile. High refractive index spheres can have sharp Lorentzian polarizability [197, 198].

3.2.4 Trimer with maximum absorption

In this subsection, we use the Mie angle method in a specific design challenge to demonstrate the applicability of the minimalist model. The challenge concerns finding the maximum absorption cross-section of a trimer made from three isotropic meta-atoms for a predefined illumination.

Intuitively, two methods to address the problem come to mind. The full-search approach to solve the problem is to simulate all possible spherical (homogeneous, or core-multishell) meta-atoms with different radii and materials and determine the maximum absorption cross-section. Such an approach is computationally costly, if possible at all. Another approach is to simulate the problem and incorporate a heuristic optimization method. For each iteration of this optimization approach, three meta-atoms are simulated. The meta-atoms can be homogenous or core-multishell spheres. Apart from the many degrees of freedom that increase the computational time, the optimization method can never guarantee that the global maximum is reached, especially since the optical functions are non-convex and multi-modal.

Using the minimalist model and the Mie angle method, one can efficiently address such fundamental questions quasi-analytically without dealing with the problems associated with the two methods discussed above. Here, we want to show the Mie angle method within an elementary problem. Therefore, we limit the trimer to be made from three identical electric dipoles, ignoring the magnetic dipoles and higher-order Mie coefficients. The analysis can be extended to include many more multipoles to address the problem in a general fashion. However, this only adds to the technical discussion that might sacrifice the discussion of the concept. The interested reader can see more complicated scenarios in our published article in Ref. [59].

We consider a trimer with a fixed side length d, where, at the corners, identical isotropic electric dipolar spheres are placed (inset figure of Fig. 3.8b). Their properties are expressed with the Mie model in Eq. 3.72. Note that for an illuminating wavevector perpendicular to the surface of the triangle made by connecting the coordinates of the trimer meta-atoms, due to symmetry reasons, the optical cross-sections are independent of the direction of the linear polarization [199].

The simulations of the trimer are based on the multipole expansion method [46, 145, 200–202]. For the calculation of the absorption cross-section, we have used a local-coordinate T-matrix method with multipolar order of 2. However, we have verified the results with a global-coordinate T-matrix method of multipolar order of 20. In the local-coordinate system, we define all the VSH coefficients in the local coordinate system of each meta-atom. In contrast, in the global T-matrix method, all the VSH coefficients are computed for a global reference point, i.e., here in the center of the trimer. A large multipolar order of 20 is required for converging results for considerable distances.

For the trimer, if the meta-atoms are very far away from each other, the coupling is negligible and the maximum cross-section is $3 \times \sigma_{\mathrm{abs,E1}}^{\max}(\omega)$. In other words, three times larger than the maximum absorption cross-section of an isolated electric dipolar meta-atom, i.e., $\sigma_{\mathrm{abs,E1}}^{\max}(\omega) = 3\lambda^2/(8\pi)$ (Fig. 3.7c). However, if the meta-atoms
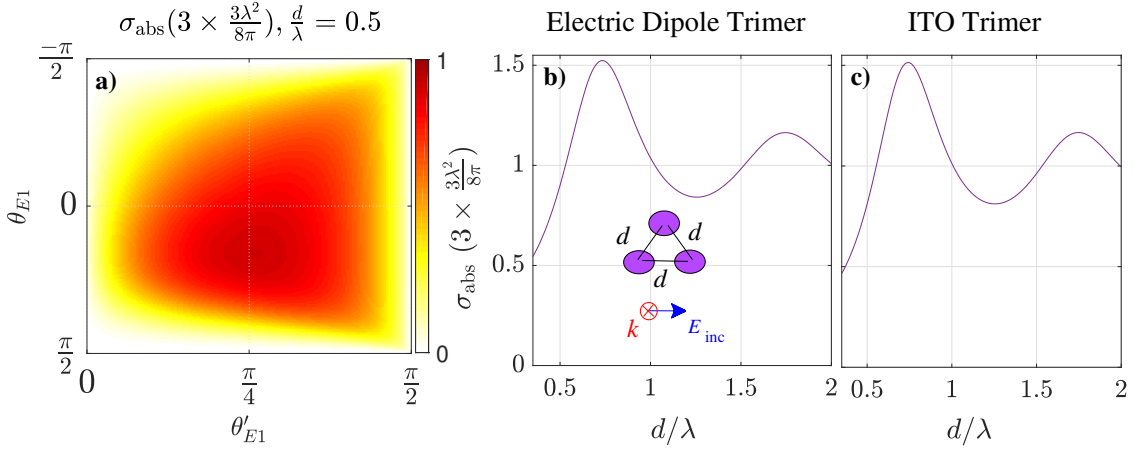
Figure 3.8: **Maximum absorption cross-section of a trimer [59]:** a) The full map of the absorption cross-section of an equilateral trimer made from isotropic electric dipoles with a side length of $d = 0.5\lambda$ as a function of the Mie angles of the individual meta-atom normalized to the maximum absorption cross-section of the trimer at $d \to \infty$. The polarization and direction of the plane wave excitation are shown in the inset of (b). b) The maximum absorption cross-section of the trimer for any given distance. The global maximal absorption cross-section occurs at a distance of $d = 0.725\lambda$ and the required Mie angles are: $\theta_{E1} = 4^o$, $\theta'_{E1} = 34.5^o$ ($a_1 = 0.59 + 0.02i$). The inset shows the trimer with the assumed plane wave excitation polarization. c) The maximal absorption cross-section for an optimized ITO trimer at a wavelength of $\lambda = 1740\,\text{nm}$ designed based on the theoretical results derived from Fig. 3.8b. The radius of the ITO spheres in the trimer is $179\,\text{nm}$. Adapted with permission from Ref. [59] © The Optical Society.

are brought closer, the coupling between the meta-atoms comes into play and complicates the problem. As the first step of the Mie angle method, we identify the Mie angles that provide maximum absorption cross-section. To that aim, using the multipole expansion method, we sweep through the full Mie angle space (i.e., $-\frac{\pi}{2} \leqslant \theta_{Ej}(\omega) \leqslant +\frac{\pi}{2}$ and $0 \leqslant \theta'_{Ej}(\omega) \leqslant +\frac{\pi}{2}$) for a given side length of the equilateral trimer. Representative results for a normalized distance of $d/\lambda = 0.5$ are shown in Fig. 3.8a. The results are normalized to $3 \times 3\lambda^2/(8\pi)$ as a reference. For each distance d, there is a maximum absorption cross-section. Then, a global maximum is identified by sweeping through the side length d. Figure 3.8b shows the maximum absorption cross-section for any given distance d. The maximum possible absorption cross-section of the trimer occurs at a distance of 0.725λ and it amounts to $1.52 \times 3 \times 3\lambda^2/(8\pi)$. This maximum theoretical limit occurs for the Mie angles of $\theta_{E1} = 4^o$, $\theta'_{Ej} = 34.5^o$ that translate to the Mie coefficient of $a_1 = 0.59 + 0.02i$.

Once we know the necessary Mie coefficients, we can identify actual spheres from natural materials that offer these coefficients. Note that we have assumed other Mie coefficients to be zero. And we should consider this as part of the necessary conditions. Here, we want to study spheres made from ITO. The permittivity of ITO is expressed as [203]:

$$\varepsilon(\omega) = \varepsilon_\infty - \frac{\omega_p^2}{\omega(\omega + i\gamma)}, \tag{3.79}$$

where $\omega_{\mathrm{p}} = 2\pi \times 4.24 \times 10^{14}\,\mathrm{rad/s}$, $\varepsilon_{\infty} = 2.97$, $\gamma = 1.27 \times 10^{14}\,\mathrm{Hz}$. We start our search algorithm by the simplest geometry, i.e., a homogenous sphere. For that, we use a full search through the radius and wavelength of operation, and at a wavelength of 1740 nm an ITO sphere with a radius of 179 nm offers the required Mie coefficients. The absorption cross-section of an equilateral triangle of such spheres as a function of the trimer side length is shown in Fig. 3.8c. At a distance of $0.75\lambda = 1305$ nm, a maximum absorption cross-section of $1.51 \times 3 \times 3\lambda^2/(8\pi)$ is reproduced as predicted by the theory.

Note that our primitive search is successful, and, hence, we do not resort to more complicated geometries such as core-multishell spheres, and more advanced search methods are not required. If a homogenous sphere cannot provide the required Mie coefficients for a given problem, we must search core-multishell spheres. As core-multishell spheres have many degrees of freedom, full-search algorithms are not suitable, and, hence, we may need to resort to a heuristic approach. In the following subsection, we will briefly discuss these approaches.

3.2.5 Core-multishell optimization methods

In the Mie angle method, for any given optical function that depends on wavelength-scale spherical constituents' properties, we sweep through all possible Mie angles and calculate the optical function with the computational tool we have. Then, at the secondary step, which concerns the topic of this subsection, we search for the meta-atom or meta-atoms that satisfy the required Mie coefficients. This subsection explores the optimization methods that can be used to find a meta-atom that satisfies the conditions on the Mie coefficients or the T matrix in general. Although non-isotropic meta-atoms can also be investigated, our focus is mostly on isotropic meta-atoms.

After a set of Mie coefficients were found to give a desired output, we search for an actual meta-atom realization, mostly a core-multishell sphere, to provide those Mie coefficients. For that aim, we could, in principle, use a full-search approach and sweep through all degrees of freedom that are accessible within the problem. This search algorithm is computationally expensive; however, it can be used for homogenous spheres with few degrees of freedom. For more complicated core-multishell spheres, heuristic optimizations can be implemented. In the Mie angle method, we have extensively used the *particle swarm optimization* (PSO). However, other approaches like genetic algorithms or neural networks can be exploited.

Particle swarm optimization [162]

Particle swarm optimization (PSO) is a search-based optimization method in a multidimensional space, based on the motion and intelligence of swarms, i.e., input parameter vectors, in which individuals orient their motion and velocity towards the personal (P_{best}) and overall (G_{best}) best locations imposed by an associated objective function of particles. The iterative velocity and position of the swarm particles are determined as [204]:

$$\nu_i^{it+1} = w^{it}\nu_i^{it} + c_1 \times \mathrm{rand} \times \left(P_{\mathrm{best}\,i} - s_i^{it}\right) + c_2 \times \mathrm{rand} \times \left(G_{\mathrm{best}\,i} - s_i^{it}\right), \quad (3.80)$$

$$s_i^{it+1} = s_i^{it} + \nu_i^{it+1}, \quad (3.81)$$

$$w^{it} = w_{\mathrm{max}} - \left(\frac{w_{\mathrm{max}} - w_{\mathrm{min}}}{iter_{\mathrm{max}}}\right) \times it, \quad (3.82)$$

where ν_i^{it} and s_i^{it} are the velocity and position of the particle i at the iteration it. rand is a random number between 0 and 1, $iter_{max}$ is the maximum iteration number, and w is the weighting factor. The values $c_1 = c_2 = 2$, $w_{max} = 0.9$, and $w_{min} = 0.4$ are used in our optimizations which are suggested as proper input values, independent of the problem [204].
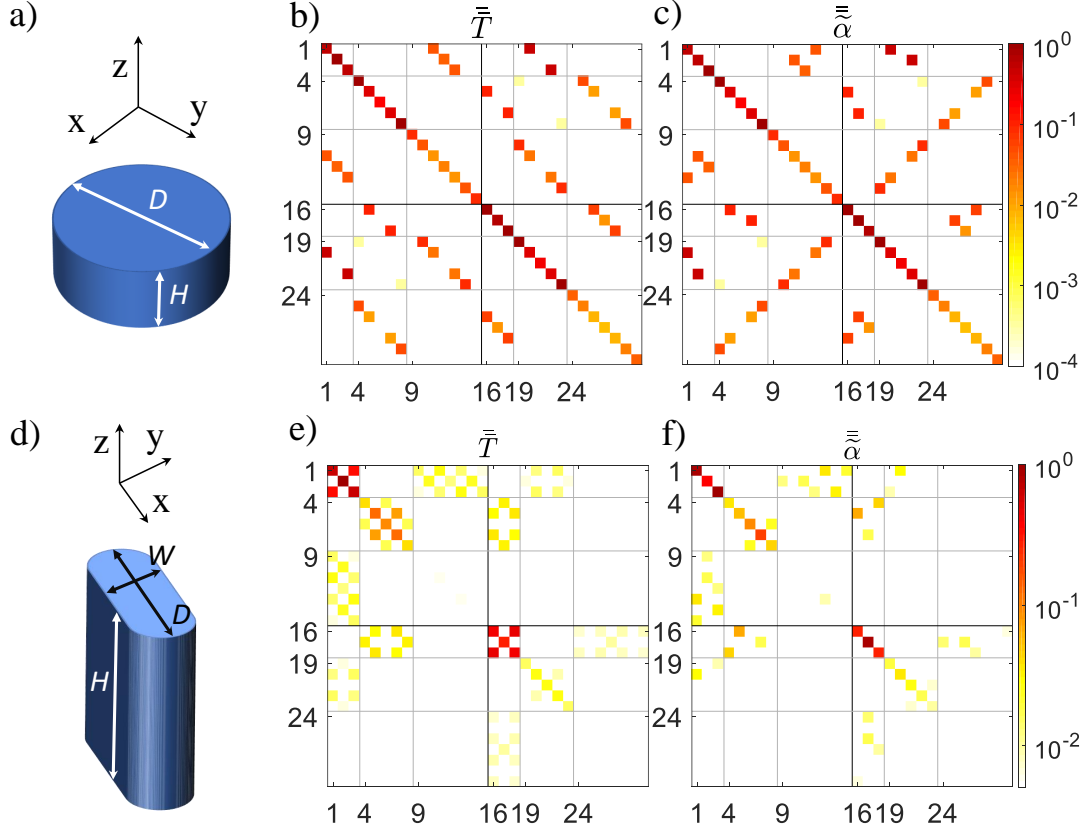
Figure 3.9: **Anisotropic meta-atoms:** a) An isolated nanocylinder ($D = 2 \times 291\,\text{nm}, H = 211\,\text{nm}$) made from amorphous silicon ($n = 3.959 + 0.009i$) embedded in silica ($n = 1.44$) and its b) T matrix and c) normalized polarizability amplitudes at a free space wavelength of $\lambda_0 = 1300$ nm. d) An isolated curved box ($D = 229\,\text{nm} + 142\,\text{nm}, W = 142\,\text{nm}, H = 403\,\text{nm}$) made from amorphous silicon ($n = 3.950 + 0.016i$), embedded in silica ($n = 1.44$) and its e) T matrix and f) normalized polarizability amplitudes at a free space wavelength of $\lambda_0 = 1333$ nm.

For the simulation of the core-multishell spheres, we use the multipole expansion method. A large vector containing random input parameters is generated to realize the best core-multishell sphere parameters that provide the desired Mie coefficients. These parameters are the radii and material indices and are restricted to the boundaries enforced by the problem. The objective function is the distance from the realized Mie coefficients for each set and the desired Mie coefficients. Through several iterations, each set of parameters search for the minimum point. In the end, the optimized core-multishell sphere can be found.

We have used PSO in several examples. In Ref. [162], we have used the method to maximize the optical force exerted on a core-shell sphere in dipolar approximation. In Ref. [145], we have identified a core-shell sphere that has exponentially improved

electromagnetic duality symmetry. In Ref. [31], we have identified a core-multishell sphere that can provide full phase-shift coverage when arranged periodically. Furthermore, in the same reference, we have gone beyond spherical meta-atoms and have optimized a ring-disc meta-atom for full phase-shift coverage. In Ref. [205], we have identified a core-shell sphere that shows a colossal magnetic dipole enhancement inside a periodic lattice. In Ref. [75], we have designed a core-shell sphere that, when periodically arranged, can fully diffract an impinging plane wave excitation.

3.3 Non-isotropic meta-atoms

This section briefly explores the symmetries of the polarizability and T matrices for non-isotropic meta-atoms. Non-isotropic meta-atoms include anisotropic and bianisotropic meta-atoms. This section provides a better insight into the relationship between certain geometrical symmetries to the symmetries in the polarizability and T matrices. The T matrices in this section are calculated using COMSOL™ Multiphysics or JCM suite. The normalized polarizabilities are calculated using Eq. 3.34.

Anisotropic Meta-atoms

Figure 3.9 shows the polarizability and T matrices of two anisotropic meta-atoms: a nanocylinder and a curved box. For a nanocylinder (Fig. 3.9a-c), the optical response up to a dipolar approximation is diagonal, but unlike an isotropic meta-atom, there is not a single Mie coefficient value in the diagonal of the matrix. When the quadrupolar response is considered, the electric (magnetic) dipole to magnetic (electric) quadrupole coupling in the polarizability and T matrices is an exciting feature. Although this is a coupling of the magnetic and electric fields, the fields do not change parity, and, hence, a nanocylinder is not categorized as a bianisotropic meta-atom. When modeling nanocylinders up to the quadrupolar order, this coupling term plays a significant role. The T matrix of a nanocylinder can be modeled as:

$$\bar{\bar{T}}_{\text{disc}} = -1 \times \tag{3.83}$$

$$
\begin{pmatrix}
a_1 & 0 & 0 & 0 & 0 & 0 & 0 & 0 & 0 & 0 & 0 & 0 & c_{\text{p}} & 0 & 0 & 0 \\
0 & a_z & 0 & 0 & 0 & 0 & 0 & 0 & 0 & 0 & 0 & 0 & 0 & 0 & 0 & 0 \\
0 & 0 & a_1 & 0 & 0 & 0 & 0 & 0 & 0 & 0 & 0 & 0 & 0 & 0 & -c_{\text{p}} & 0 \\
0 & 0 & 0 & a_t & 0 & 0 & 0 & 0 & 0 & 0 & 0 & 0 & 0 & 0 & 0 & 0 \\
0 & 0 & 0 & 0 & a_2 & 0 & 0 & 0 & -c_{\text{Q}} & 0 & 0 & 0 & 0 & 0 & 0 & 0 \\
0 & 0 & 0 & 0 & 0 & a_h & 0 & 0 & 0 & 0 & 0 & 0 & 0 & 0 & 0 & 0 \\
0 & 0 & 0 & 0 & 0 & 0 & a_2 & 0 & 0 & 0 & c_{\text{Q}} & 0 & 0 & 0 & 0 & 0 \\
0 & 0 & 0 & 0 & 0 & 0 & 0 & a_t & 0 & 0 & 0 & 0 & 0 & 0 & 0 & 0 \\
0 & 0 & 0 & 0 & c_{\text{Q}} & 0 & 0 & 0 & b_1 & 0 & 0 & 0 & 0 & 0 & 0 & 0 \\
0 & 0 & 0 & 0 & 0 & 0 & 0 & 0 & 0 & b_z & 0 & 0 & 0 & 0 & 0 & 0 \\
0 & 0 & 0 & 0 & 0 & 0 & -c_{\text{Q}} & 0 & 0 & 0 & b_1 & 0 & 0 & 0 & 0 & 0 \\
0 & 0 & 0 & 0 & 0 & 0 & 0 & 0 & 0 & 0 & 0 & b_t & 0 & 0 & 0 & 0 \\
-c_{\text{p}} & 0 & 0 & 0 & 0 & 0 & 0 & 0 & 0 & 0 & 0 & 0 & b_2 & 0 & 0 & 0 \\
0 & 0 & 0 & 0 & 0 & 0 & 0 & 0 & 0 & 0 & 0 & 0 & 0 & b_h & 0 & 0 \\
0 & 0 & c_{\text{p}} & 0 & 0 & 0 & 0 & 0 & 0 & 0 & 0 & 0 & 0 & 0 & b_2 & 0 \\
0 & 0 & 0 & 0 & 0 & 0 & 0 & 0 & 0 & 0 & 0 & 0 & 0 & 0 & 0 & b_t
\end{pmatrix},
$$

where the variables show different symmetries. Here, a_1 and b_1 are especially important, as within dipolar approximation, they are the only terms that are excited,
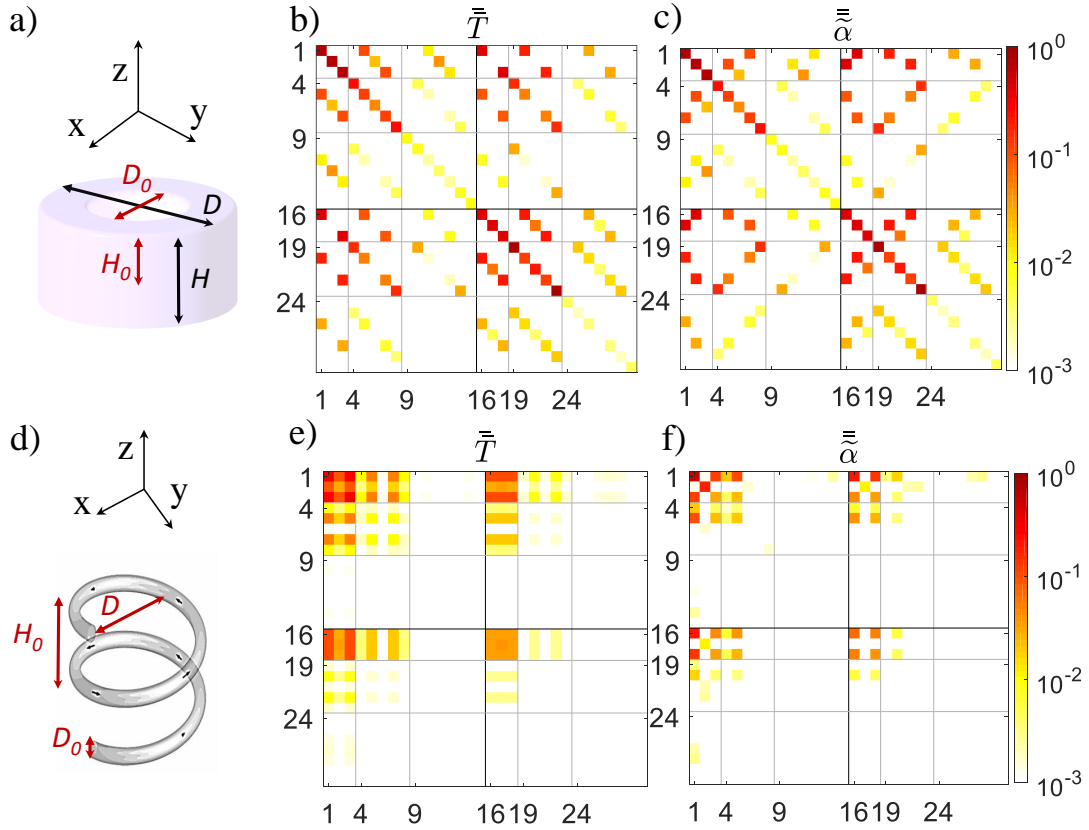
Figure 3.10: **Bianisotropic meta-atoms:** a) An isolated nanocylinder with a dent ($D = 2 \times 150$ nm, $H = 150$ nm, $D_0 = 2 \times 75$ nm, $H_0 = 75$ nm) made from a material with a refractive index $n = 3.5$ embedded in the free space and its b) T matrix and c) normalized polarizability amplitudes at a wavelength of $\lambda_0 = 740$ nm. d) An isolated helix ($D = 160$ nm, $D_0 = 40$ nm, $H_0 = 105$ nm, and $N_{\mathrm{turn}} = 2$) made from silver ($n = 0.095 + 8.675i$ [206]), embedded in the free space and its e) T matrix and f) normalized polarizability amplitudes at a wavelength of $\lambda_0 = 1180$ nm.

if a metasurface made from a periodic arrangement of nanocylinders is illuminated by a normally incident plane wave.

Figures 3.9d-f shows the polarizability and T matrices of a curved box. Interestingly, the dipolar response of the meta-atom as seen by the polarizability matrix (Fig. 3.9f) is diagonal, while the T matrix loses its diagonality (Fig. 3.9e). These differences in the symmetry of the polarizability and T matrices can help decide which coordinate system is more appropriate to study a specific geometry analytically.

Bianisotropic Meta-atoms

Bianisotropic materials were theoretically described by Landau and Lifshitz [207]. A bianisotropic meta-atoms is both magneto-electric and anisotropic [61, 148, 149]. The prefix "bi" is due to the magneto-electric effect, in which an external magnetic field induces an electric polarization, and an electric field induces a magnetic polarization with a change of parity. Bianisotropic meta-atoms are classified into reciprocal and nonreciprocal meta-atoms. Natural materials and meta-atom are all reciprocal without external field bias or specific cases (i.e., moving particles). Reciprocal meta-atoms are either chiral or achiral (also called omega-type meta-atoms).

A meta-atom is chiral if the mirrored polarizability or the T matrix cannot be superimposed on itself under any rotations in the real space. While dual meta-atoms necessitate the preservation of the incident light's helicity after scattering, chirality allows for a different strength in the response of the meta-atom to light possessing an opposite helicity [16, 148, 149, 208–216]. Chirality, as an intrinsic asymmetry in nature, is a vital footprint of biological systems [217, 218].

If a bianisotropic meta-atom can be superimposed on its mirror, then it is an omega-type meta-atom. The terminology is because of the resemblance of these meta-atoms to the letter Ω. Figures 3.10a-c, show an example of an omega-type meta-atom with its polarizability and T matrices. This dented nanocylinder is taken from Ref. [219]. Figures 3.10d-f, shows a helix as an example of a chiral meta-atom along with its polarizability and T matrices. Comparing the T matrix of the two meta-atoms reveals a feature of the chiral meta-atoms, in which, here, for the dipolar response (i.e., $j = 1$), none of the diagonal entries of the $\bar{\bar{T}}_{jj}^{\mathrm{em/me}}$ is zero.

To summarize this chapter, we have built a platform to efficiently study the scattering of meta-atoms in the spherical and Cartesian bases. The defined expressions provide a consistent, versatile, and robust analytical tool for further investigations of more complicated systems. In particular, We have presented the concept of primitive and normalized polarizability. Extensive investigations are performed for isotropic meta-atoms, and a minimalist model concerning the observable optical response is proposed. It is a minimalist model in the sense that it requires the least number of parameters to express all possible values Mie coefficients might attain. Furthermore, optimization methods are discussed that realize an actual core-multishell sphere from a set of desired Mie coefficients. Last but not least, the symmetries of multiple meta-atoms with different geometric symmetries are explored through their polarizability and T matrices. The next chapter explores how these single meta-atoms contribute to the overall optical response of their periodic arrangements.

4. Infinitely Periodic Metasurfaces

The previous chapter focused on the optical response of isolated meta-atoms. This chapter builds upon that and develops the analytic basis to study the scattering of light from a periodic arrangement of meta-atoms embedded in a homogenous, isotropic, linear, and non-absorbing medium. The content of this chapter sets the basis to study the Huygens' and disordered metasurfaces in the subsequent chapters.

We start this chapter with a general description of scattering by an aggregate of arbitrary meta-atoms arranged arbitrarily in space. The following sections impose additional assumptions and, eventually, consider a periodic 2D lattice made from identical meta-atoms excited with a plane wave. We develop general equations for the scattering of light from periodic metasurfaces in the spherical and Cartesian coordinate systems.

In particular, we will explore a numerical approach to achieve convergence to summate the response from the infinite number of particles forming the lattice. This is an essential prerequisite to optically describe metasurfaces. We identify a matrix, called the *lattice coupling matrix*, or, in short, the *C matrix*, to accurately determine the lattice summation of a particular array. Later, we study the C-matrix symmetry for different 2D lattice arrays. Having identified the C matrix for different arrays, we explore the effective optical parameters characterizing the particles inside the lattice such as the polarizabilities, T matrices, Mie coefficients, and induced multipole moments, and compare them to their counterparts when considering the particles isolated and outside the lattice. In the last chapter, we introduce closed-form equations for the transmission and reflection of single-resonance metasurfaces.

The content of this chapter is based on our works in Ref. [75, 205].

4.1   Optical scattering from an aggregate of meta-atoms

We consider a metasurface made from an aggregate of N meta-atoms arranged arbitrarily in a homogenous, isotropic, linear and non-absorbing embedding medium characterized by a wavenumber k. The meta-atoms, represented by their T matrix $\bar{\bar{T}}_n$, are located at $\mathbf{R}_n = (x_n, y_n, z_n)$, where $n = 1, 2, ..., N$. Alternatively, we might

use $\widetilde{\mathbf{R}}_n = k\mathbf{R}_n$ and $\widetilde{\mathbf{r}} = k\mathbf{r}$ as the normalized position vectors. Let us assume that the metasurface is illuminated with some external optical field. The scattering from the metasurface is then the sum of scattered light from all the meta-atoms. Using Eq. 3.1, the total scattering from the metasurface can be written as:

$$\mathbf{E}^{\text{sca}}\left(\mathbf{r},\omega,\widetilde{\mathbf{R}}_n\right) = \sum_{n=1}^{N}\sum_{j=1}^{\infty}\sum_{m=-j}^{j} b_{jm}^{\text{e},n}\left(\omega,\widetilde{\mathbf{R}}_n\right)\mathbf{N}_{jm}^{(3)}\left(\widetilde{\mathbf{r}}-\widetilde{\mathbf{R}}_n\right) + b_{jm}^{\text{m},n}\left(\omega,\widetilde{\mathbf{R}}_n\right)\mathbf{M}_{jm}^{(3)}\left(\widetilde{\mathbf{r}}-\widetilde{\mathbf{R}}_n\right),$$
(4.1)

where $b_{jm}^{\text{e},n}(\omega,\widetilde{\mathbf{R}}_n)$ $(b_{jm}^{\text{m},n}(\omega,\widetilde{\mathbf{R}}_n))$ are the electric (magnetic) scattering coefficients of the n's meta-atom that depend on the arrangement of the neighboring scatterers. Knowing the meta-atoms' T matrices, we need to know the entire incident field impinging on each meta-atom to calculate the scattered field coefficients. The whole incident field comprises the incident field from the external illumination and the scattering from all the other meta-atoms of the metasurface. In other words, the total incident field at the reference position of the meta-atom n' is:

$$\mathbf{E}_{n'}^{\text{inc}}\left(\mathbf{r}=\mathbf{R}_{n'},\omega,\widetilde{\mathbf{R}}_n\right) = \mathbf{E}_{\text{ext},n'}^{\text{inc}}\left(\mathbf{r}=\mathbf{R}_{n'},\omega\right) + \sum_{n\neq n'}\mathbf{E}_{n}^{\text{sca}}\left(\mathbf{r}=\mathbf{R}_{n'}-\mathbf{R}_n,\omega,\widetilde{\mathbf{R}}_n\right),$$
(4.2)

where $\mathbf{E}_{\text{ext},n'}^{\text{inc}}\left(\mathbf{r}=\mathbf{R}_{n'},\omega\right)$ is the external incident field at a position $\mathbf{r}=\mathbf{R}_{n'}$ that can be written in the VSH basis as:

$$\mathbf{E}_{\text{ext},n'}^{\text{inc}}\left(\mathbf{r}=\mathbf{R}_{n'},\omega\right) = \sum_{j=1}^{\infty}\sum_{m=-j}^{j} q_{\text{ext},jm}^{\text{e},n'}\left(\omega\right)\mathbf{N}_{jm}^{(1)}(\widetilde{\mathbf{R}}_{n'}) + q_{\text{ext},jm}^{\text{m},n'}\left(\omega\right)\mathbf{M}_{jm}^{(1)}(\widetilde{\mathbf{R}}_{n'}),$$
(4.3)

where $q_{\text{ext},jm}^{\text{e},n'}\left(\omega\right)$ $(q_{\text{ext},jm}^{\text{m},n'}\left(\omega\right))$ is the electric (magnetic) external incident coefficient of the n's meta-atom. $\mathbf{E}_{n}^{\text{sca}}\left(\mathbf{R}_{n'}-\mathbf{R}_n,\omega,\widetilde{\mathbf{R}}_n\right)$ is the scattered field of the n's particle that can also be written in the VSH basis as:

$$\mathbf{E}_{n}^{\text{sca}}\left(\mathbf{r}=\mathbf{R}_{n'}-\mathbf{R}_n,\omega,\widetilde{\mathbf{R}}_n\right) = \sum_{j=1}^{\infty}\sum_{m=-j}^{j} b_{jm}^{\text{e},n}\left(\omega,\widetilde{\mathbf{R}}_n\right)\mathbf{N}_{jm}^{(3)}\left(\widetilde{\mathbf{R}}_{n'}-\widetilde{\mathbf{R}}_n\right)$$
$$+ \sum_{j=1}^{\infty}\sum_{m=-j}^{j} b_{jm}^{\text{m},n}\left(\omega,\widetilde{\mathbf{R}}_n\right)\mathbf{M}_{jm}^{(3)}\left(\widetilde{\mathbf{R}}_{n'}-\widetilde{\mathbf{R}}_n\right). \quad (4.4)$$

Equation 4.3 is expanded in terms of the regular VSH, while Eq. 4.4 is expanded using the outgoing VSH. To describe the total incident field in the same basis, we need to project the outgoing vectors on the regular vectors. To that aim, we use the addition theorem [220]. Based on the addition theorem, we can change the basis via the following expressions [46, 48, 221]:

$$\mathbf{M}_{jm}^{(3)}(\widetilde{\mathbf{R}}_{n'}-\widetilde{\mathbf{R}}_n) = \sum_{\iota=1}^{\infty}\sum_{\mu=-\iota}^{\iota} A_{\iota\mu jm}(-\widetilde{\mathbf{R}}_n)\mathbf{M}_{\iota\mu}^{(1)}(\widetilde{\mathbf{R}}_{n'}) + B_{\iota\mu jm}(-\widetilde{\mathbf{R}}_n)\mathbf{N}_{\iota\mu}^{(1)}(\widetilde{\mathbf{R}}_{n'}), \quad (4.5)$$

$$\mathbf{N}_{jm}^{(3)}(\widetilde{\mathbf{R}}_{n'}-\widetilde{\mathbf{R}}_n) = \sum_{\iota=1}^{\infty}\sum_{\mu=-\iota}^{\iota} B_{\iota\mu jm}(-\widetilde{\mathbf{R}}_n)\mathbf{M}_{\iota\mu}^{(1)}(\widetilde{\mathbf{R}}_{n'}) + A_{\iota\mu jm}(-\widetilde{\mathbf{R}}_n)\mathbf{N}_{\iota\mu}^{(1)}(\widetilde{\mathbf{R}}_{n'}), \quad (4.6)$$

where the *translation coefficients* $A_{\iota\mu jm}(-\widetilde{\mathbf{R}}_n)$ and $B_{\iota\mu jm}(-\widetilde{\mathbf{R}}_n)$ are defined as:

$$A_{\iota\mu jm}(kr,\theta,\phi) = \frac{\gamma_{jm}}{\gamma_{\iota\mu}}(-1)^m \frac{2\iota+1}{\iota(\iota+1)} \mathrm{i}^{\iota-j}\sqrt{\pi\frac{(j+m)!(\iota-\mu)!}{(j-m)!(\iota+\mu)!}} \sum_p \mathrm{i}^p\sqrt{2p+1}h_p^{(1)}(kr)\times$$

$$Y_{p,m-\mu}(\theta,\phi)\begin{pmatrix} j & \iota & p \\ m & -\mu & -m+\mu \end{pmatrix}\begin{pmatrix} j & \iota & p \\ 0 & 0 & 0 \end{pmatrix}[j(j+1)+\iota(\iota+1)-p(p+1)],$$

$$(4.7\text{a})$$

$$B_{\iota\mu jm}(kr,\theta,\phi) = \frac{\gamma_{jm}}{\gamma_{\iota\mu}}(-1)^m \frac{2\iota+1}{\iota(\iota+1)} \mathrm{i}^{\iota-j}\sqrt{\pi\frac{(j+m)!(\iota-\mu)!}{(j-m)!(\iota+\mu)!}} \sum_p \mathrm{i}^p\sqrt{2p+1}h_p^{(1)}(kr)\times$$

$$Y_{p,m-\mu}(\theta,\phi)\begin{pmatrix} j & \iota & p \\ m & -\mu & -m+\mu \end{pmatrix}\begin{pmatrix} j & \iota & p-1 \\ 0 & 0 & 0 \end{pmatrix}\sqrt{[(j+\iota+1)^2-p^2][p^2-(j-\iota)^2]},$$

$$(4.7\text{b})$$

where $h_p^{(1)}(kr)$ is the spherical Hankel function of the first kind, $Y_{jm}(\theta,\phi)$ are the well-known spherical harmonics, γ_{jm} is the normalization factor (Eq. 2.61), and the six-element brackets $\begin{pmatrix} j_1 & j_2 & j_3 \\ m_1 & m_2 & m_3 \end{pmatrix}$ are the Wigner 3j-symbols [222, 223]. The summation on p runs through all combinations of the Wigner 3j-symbol. The non-zero Wigner 3j-symbols are determined by the selection rules.

Therefore, using the addition theorem, we can expand the scattered field of each meta-atom n in the local reference coordinates of the meta-atom n'. This equal basis enables writing the total incident field onto the regular VSH in the reference of the meta-atom n'. Hence, the total incident field coefficient on meta-atom n' can be expressed as:

$$q_{jm}^{\mathrm{e},n'} = q_{\mathrm{ext},jm}^{\mathrm{e},n'} + \sum_{n\neq n'}\sum_{\iota=1}^{\infty}\sum_{\mu=-\iota}^{\iota} A_{\iota\mu jm}(-\widetilde{\mathbf{R}}_n)b_{jm}^{\mathrm{e},n} + \sum_{n\neq n'}\sum_{\iota=1}^{\infty}\sum_{\mu=-\iota}^{\iota} B_{\iota\mu jm}(-\widetilde{\mathbf{R}}_n)b_{jm}^{\mathrm{m},n}, \quad (4.8)$$

$$q_{jm}^{\mathrm{m},n'} = q_{\mathrm{ext},jm}^{\mathrm{m},n'} + \sum_{n\neq n'}\sum_{\iota=1}^{\infty}\sum_{\mu=-\iota}^{\iota} B_{\iota\mu jm}(-\widetilde{\mathbf{R}}_n)b_{jm}^{\mathrm{e},n} + \sum_{n\neq n'}\sum_{\iota=1}^{\infty}\sum_{\mu=-\iota}^{\iota} A_{\iota\mu jm}(-\widetilde{\mathbf{R}}_n)b_{jm}^{\mathrm{m},n}. \quad (4.9)$$

Due to space restrictions, we have ignored the arguments for the incident and scattered field coefficients. We will continue to do so unless the arguments that are already explicitly mentioned in Eq. 4.1 and 4.3 are changed. Note that these dependencies are implicitly assumed and should be considered. The equation above can be written in a matrix form as:

$$\mathbf{q}^{n'} = \mathbf{q}_{\mathrm{ext}}^{n'} + \sum_{n\neq n'}\begin{bmatrix} \mathbf{A}(-\widetilde{\mathbf{R}}_n) & \mathbf{B}(-\widetilde{\mathbf{R}}_n) \\ \mathbf{B}(-\widetilde{\mathbf{R}}_n) & \mathbf{A}(-\widetilde{\mathbf{R}}_n) \end{bmatrix}\mathbf{b}^n = \mathbf{q}_{\mathrm{ext}}^{n'} + \sum_{n\neq n'}\mathcal{C}(-\widetilde{\mathbf{R}}_n)\mathbf{b}^n, \quad (4.10)$$

where $\mathbf{q}^{n'}$ is the total incident field coefficient vector (defined in Eq. 3.7) for the meta-atom n'. $\mathcal{C}(-\widetilde{\mathbf{R}}_n)$ is the *translation coefficient matrix* for the meta-atom n to any meta-atom n'. For an arrangement of N meta-atoms, we can write the general equation for the incident field coefficients as:

$$\begin{bmatrix} \mathbf{q}^1 \\ \mathbf{q}^2 \\ \vdots \\ \mathbf{q}^N \end{bmatrix} = \begin{bmatrix} \mathbf{q}_{\mathrm{ext}}^1 \\ \mathbf{q}_{\mathrm{ext}}^2 \\ \vdots \\ \mathbf{q}_{\mathrm{ext}}^N \end{bmatrix} + \begin{bmatrix} \mathbf{0} & \mathcal{C}(-\widetilde{\mathbf{R}}_2) & \dots & \mathcal{C}(-\widetilde{\mathbf{R}}_N) \\ \mathcal{C}(-\widetilde{\mathbf{R}}_1) & \mathbf{0} & \dots & \mathcal{C}(-\widetilde{\mathbf{R}}_N) \\ \vdots & \vdots & \vdots & \vdots \\ \mathcal{C}(-\widetilde{\mathbf{R}}_1) & \mathcal{C}(-\widetilde{\mathbf{R}}_2) & \dots & \mathbf{0} \end{bmatrix}\begin{bmatrix} \mathbf{b}^1 \\ \mathbf{b}^2 \\ \vdots \\ \mathbf{b}^N \end{bmatrix}. \quad (4.11)$$
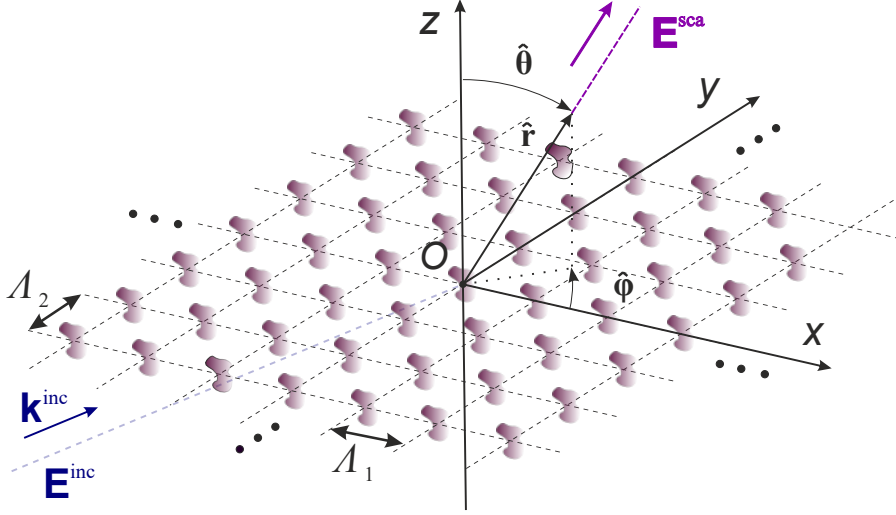
Figure 4.1: **Optical scattering from an infinitely periodic metasurface:** Identical meta-atoms that are arranged in a rectangular lattice with periodicities Λ_1 and Λ_2. The infinitely periodic arrangement is illuminated by a plane wave $\mathbf{E}^{\text{inc}}$ characterized by a wavevector $\mathbf{k}_{\text{inc}}$ and radiates the scattered field $\mathbf{E}^{\text{sca}}$. The figure is adapted with permission from a drawing by Dr. Theodosios Karamanos [75].

Knowing the T matrix of all the meta-atoms, the scattered field coefficients can be expressed as:

$$
\begin{bmatrix} \mathbf{b}^1 \\ \mathbf{b}^2 \\ \vdots \\ \mathbf{b}^N \end{bmatrix} = \begin{bmatrix} \bar{\bar{T}}_1 & \mathbf{0} & \dots & \mathbf{0} \\ \mathbf{0} & \bar{\bar{T}}_2 & \dots & \mathbf{0} \\ \vdots & \vdots & \vdots & \vdots \\ \mathbf{0} & \mathbf{0} & \dots & \bar{\bar{T}}_N \end{bmatrix}
$$

$$
\times \left\{ \begin{bmatrix} \mathbf{q}^1_{\text{ext}} \\ \mathbf{q}^2_{\text{ext}} \\ \vdots \\ \mathbf{q}^N_{\text{ext}} \end{bmatrix} + \begin{bmatrix} \mathbf{0} & \mathcal{C}(-\widetilde{\mathbf{R}}_2) & \dots & \mathcal{C}(-\widetilde{\mathbf{R}}_N) \\ \mathcal{C}(-\widetilde{\mathbf{R}}_1) & \mathbf{0} & \dots & \mathcal{C}(-\widetilde{\mathbf{R}}_N) \\ \vdots & \vdots & \vdots & \vdots \\ \mathcal{C}(-\widetilde{\mathbf{R}}_1) & \mathcal{C}(-\widetilde{\mathbf{R}}_2) & \dots & \mathbf{0} \end{bmatrix} \begin{bmatrix} \mathbf{b}^1 \\ \mathbf{b}^2 \\ \vdots \\ \mathbf{b}^N \end{bmatrix} \right\} .
$$

(4.12)

Equation 4.12 is a system of linear equations that can be solved, and, hence, the scattered field coefficients of all the meta-atoms can be computed for a given external illumination. Having these coefficients, the total scattering from the metasurface can be calculated using Eq. 4.1. A home-built code based on the algorithm explained in this section has been developed in the institute of theoretical solid-state physics (TFP). In developing the code, several doctoral researchers have contributed. I acknowledge contributions from Dr. Stefan Mülig, Dr. Martin Fruhnert, and Dr. Radius Suryadharma.

In summary, we have assumed a general finite metasurface made from N arbitrary meta-atoms illuminated with an arbitrary optical excitation and expressed its effective scattering coefficients inside the ensemble. In the next section, we will consider further assumptions that help us derive simplified equations for infinitely extended metasurface made from identical meta-atoms.

4.2   Periodic arrangement of identical meta-atoms

In this section, we consider a metasurface made from identical and periodically arranged meta-atoms that is illuminated by a plane wave characterized by a wavevector $\mathbf{k}_{\text{inc}}$ (Figure 4.1 shows the setup for a rectangular lattice with periodicities Λ_1 and Λ_2). We use the subscript "inc" to distinguish parameters characterizing the incident field from those characterizing the scattered field. The meta-atoms are characterized by an identical T matrix $\bar{\bar{T}}_0$. The meta-atom arrangement forming the lattice can be described by two base vectors $\mathbf{u}_1$ and $\mathbf{u}_2$ that are assumed to be parallel to the x-y plane. Hence, the position of every meta-atom in the lattice can be express by:

$$\mathbf{R}_n = \nu_1 \mathbf{u}_1 + \nu_2 \mathbf{u}_2 = \nu_1 \frac{\widetilde{\mathbf{u}}_1}{k} + \nu_2 \frac{\widetilde{\mathbf{u}}_2}{k} = \frac{1}{k} \begin{bmatrix} \nu_1 & 0 \\ 0 & \nu_2 \end{bmatrix} \begin{bmatrix} \widetilde{\mathbf{u}}_1 \\ \widetilde{\mathbf{u}}_2 \end{bmatrix} = \frac{1}{k} \boldsymbol{\nu} \widetilde{\mathbf{u}}, \qquad (4.13)$$

with $\nu_1, \nu_2 \in \mathbb{Z}$. The normalized parameters $\widetilde{\mathbf{R}}_n = k\mathbf{R}_n$, $\widetilde{R}_n = |\widetilde{\mathbf{R}}_n|$, $\widetilde{\mathbf{u}}_1 = k\mathbf{u}_1$, $\widetilde{\mathbf{u}}_2 = k\mathbf{u}_2$ and $\widetilde{\mathbf{u}} = [\widetilde{\mathbf{u}}_1; \widetilde{\mathbf{u}}_2]$ will be beneficial in the following expressions. While considering such an arrangement, we can define some useful quantities that will be used later. The area of the unit cell is $A = (\mathbf{u}_1 \times \mathbf{u}_2) \cdot \hat{\mathbf{z}}$ and the reciprocal lattice vector can be defined as $\mathbf{G} = n_1 \mathbf{u}_1' + n_2 \mathbf{u}_2'$, with $\mathbf{u}_1' = \frac{2\pi}{A}(\mathbf{u}_2 \times \hat{\mathbf{z}})$, $\mathbf{u}_2' = \frac{2\pi}{A}(\hat{\mathbf{z}} \times \mathbf{u}_1)$ and with $n_1, n_2 \in \mathbb{Z}$. As we will show later, n_1 and n_2 lead to the discrete number of diffraction orders from the lattice.

In the following, we derive a general expression for the effective T matrix of a meta-atom inside the periodic lattice. As we will shortly demonstrate, the derivation of the effective T matrix involves an infinite sum over the meta-atom positions. To solve the infinite sum, a method known as the *Ewald summation* is introduced. Finally, we provide closed-form equations describing light scattering from a periodic metasurface in the spherical and Cartesian bases.

4.2.1   The effective T matrix

Assuming a plane wave excitation, the involved coefficients characterizing the incident field on and the scattered field from the periodically arranged identical meta-atoms can be assumed to be related by a phase difference. The coefficients of the meta-atom n are related to reference coefficients through the following equation:

$$\mathbf{q}_{\text{ext}}^n (\mathbf{k}_{\text{inc}}) = \mathbf{q}_0 (\mathbf{k}_{\text{inc}}) e^{i\mathbf{k}_\parallel \cdot \mathbf{R}_n}, \qquad (4.14)$$

$$\mathbf{b}^n (\mathbf{k}_{\text{inc}}, \widetilde{\mathbf{u}}) = \mathbf{b}_0 (\mathbf{k}_{\text{inc}}, \widetilde{\mathbf{u}}) e^{i\mathbf{k}_\parallel \cdot \mathbf{R}_n}, \qquad (4.15)$$

where $\mathbf{q}_0 (\mathbf{k}_{\text{inc}})$ ($\mathbf{b}_0 (\mathbf{k}_{\text{inc}}, \widetilde{\mathbf{u}})$) are the *universal incident (scattering) field coefficient* or, as considered here, the coefficients of the meta-atom that is at the center of the coordinate system and $\widetilde{\mathbf{u}}$ is the *normalized lattice base vector*. $\mathbf{k}_\parallel = \mathbf{k}_{\text{inc}} - \mathbf{k}_{\text{inc}} \cdot \hat{z}$ is the plane wave wavevector component parallel to the plane of the lattice. Using the above two equations and also Eq. 4.12, we can write:

$$\mathbf{b}_0 (\mathbf{k}_{\text{inc}}, \widetilde{\mathbf{u}}) = \bar{\bar{T}}_0 (k) \left[\mathbf{q}_0 (\mathbf{k}_{\text{inc}}) + \sum_{\mathbf{R}_n}' \mathcal{C}(-\widetilde{\mathbf{R}}_n) e^{i\mathbf{k}_\parallel \cdot \mathbf{R}_n} \mathbf{b}_0 (\mathbf{k}_{\text{inc}}, \widetilde{\mathbf{u}}) \right], \qquad (4.16)$$

where the summation runs across all lattice sites except the origin. We have primed the sum symbol to show the omission of the origin, i.e., $\mathbf{R}_{\boldsymbol{\nu}=\mathbf{0}} = (0,0,0)$. Solving the above equation yields:

$$
\begin{aligned}
\mathbf{b}_0\left(\mathbf{k}_{\mathrm{inc}}, \widetilde{\mathbf{u}}\right) &= \left[\bar{\bar{I}} - \bar{\bar{T}}_0\left(k\right) \sideset{}{'}\sum_{\mathbf{R}_n} \mathcal{C}(-\widetilde{\mathbf{R}}_n)e^{\mathrm{i}\mathbf{k}_\parallel \cdot \mathbf{R}_n}\right]^{-1} \bar{\bar{T}}_0\left(k\right) \mathbf{q}_0\left(\mathbf{k}_{\mathrm{inc}}\right) \\
&= \left[\bar{\bar{I}} - \bar{\bar{T}}_0\left(k\right) \bar{\bar{C}}_{\mathrm{s}}\left(\hat{\mathbf{k}}_{\mathrm{inc}}, \widetilde{\mathbf{u}}\right)\right]^{-1} \bar{\bar{T}}_0\left(k\right) \mathbf{q}_0\left(\mathbf{k}_{\mathrm{inc}}\right),
\end{aligned}
\tag{4.17}
$$

where $\bar{\bar{C}}_{\mathrm{s}}\left(\hat{\mathbf{k}}_{\mathrm{inc}}, \widetilde{\mathbf{u}}\right)$ is the *spherical lattice coupling matrix*. It is called spherical, here, because it is derived in the spherical basis. The nomenclature helps to distinguish a similar matrix that can be derived when discussing the problem in the Cartesian basis. This matrix is dimensionless and only depends on the lattice arrangement and the plane wave excitation orientation. Using Eq. 4.17, it is helpful to define an *effective T matrix* $\bar{\bar{T}}_{\mathrm{eff}}\left(\mathbf{k}_{\mathrm{inc}}, \widetilde{\mathbf{u}}\right)$, that relates the external incident field to the effective scattered field coefficients of the meta-atoms inside the lattice:

$$
\bar{\bar{T}}_{\mathrm{eff}}\left(\mathbf{k}_{\mathrm{inc}}, \widetilde{\mathbf{u}}\right) = \left[\bar{\bar{I}} - \bar{\bar{T}}_0\left(k\right) \bar{\bar{C}}_{\mathrm{s}}\left(\hat{\mathbf{k}}_{\mathrm{inc}}, \widetilde{\mathbf{u}}\right)\right]^{-1} \bar{\bar{T}}_0\left(k\right).
\tag{4.18}
$$

Next subsection deals with the solution of the infinite lattice summation.

4.2.2 The lattice summation

The spherical lattice coupling matrix $\bar{\bar{C}}_s$ can be expressed using Eq. 4.8-4.10 and 4.17 as:

$$
\bar{\bar{C}}_s\left(\hat{\mathbf{k}}_{\mathrm{inc}}, \widetilde{\mathbf{u}}\right) = \sideset{}{'}\sum_{\mathbf{R}_n} \begin{pmatrix} \mathbf{A}(-\widetilde{\mathbf{R}}_n) & \mathbf{B}(-\widetilde{\mathbf{R}}_n) \\ \mathbf{B}(-\widetilde{\mathbf{R}}_n) & \mathbf{A}(-\widetilde{\mathbf{R}}_n) \end{pmatrix} e^{\mathrm{i}\mathbf{k}_\parallel \cdot \mathbf{R}_n},
\tag{4.19}
$$

where the summation runs over all the meta-atom positions except for the meta-atom at the origin (indicated by the prime). Solving this infinite summation is not trivial. The summation contains the translation coefficients defined in Eq. 4.7. To derive the lattice matrix, two summations needs to be calculated: an infinite summation over $\mathbf{R}_n$ and a finite summation over p. Since the infinite summation is the numerically challenging part, we put our focus only on the solution for that part. Therefore, for simplicity, here, we do not show the summation over p any further. The infinite summation to be calculated to derive the lattice coupling matrix is:

$$
D_{jm}\left(\hat{\mathbf{k}}_{\mathrm{inc}}, \widetilde{\mathbf{u}}\right) = \sideset{}{'}\sum_{\mathbf{R}_n} h_j^{(1)}(\widetilde{R}_n) Y_{jm}\left(-\hat{\widetilde{\mathbf{R}}}_n\right) e^{\mathrm{i}\mathbf{k}_\parallel \cdot \mathbf{R}_n}.
\tag{4.20}
$$

This infinite series converges very slowly when summed directly over the meta-atom positions. However, using a method known as the Ewald summation [73], we separate long and short-range contributions to this series and break it into two main summations. The short-range contribution is evaluated in real space using a direct summation, while the long-range contribution is summed in the Fourier space. These transformed series converge quickly.

We separate the summation in Eq. 4.20 into three parts $D_{jm} = D_{jm}^{(1)} + D_{jm}^{(2)} + D_{jm}^{(3)}$, where the first and the second term are the Fourier and real space summations. The third term is a correction that accounts for the missing lattice point at the origin

when applying the transformation from the real to Fourier space. Eventually, after some algebra, these parts can be calculated via the following equations [70, 224–226]:

$$D_{jm}^{(1)}\left(\hat{\mathbf{k}}_{\text{inc}}, \widetilde{\mathbf{u}}\right) = \frac{\sqrt{(2j+1)(j-m)!(j+m)!}}{A k \, \mathrm{i}^{-m}} \tag{4.21}$$

$$\times \sum_{\mathbf{G}} \left(\frac{|\mathbf{k}_{\parallel} + \mathbf{G}|}{2k}\right)^j \frac{e^{im\varphi_{\mathbf{k}_{\parallel}+\mathbf{G}}}}{k_{\mathbf{G},z}^+} \sum_{\lambda=0}^{\frac{j-|m|}{2}} \frac{\left(\frac{k_{\mathbf{G},z}^+}{|\mathbf{k}_{\parallel}+\mathbf{G}|}\right)^{2\lambda} \Gamma\left(\frac{1}{2}-\lambda, -\frac{(k_{\mathbf{G},z}^+)^2}{4T^2}\right)}{\lambda! \left(\frac{j+m}{2}-\lambda\right)! \left(\frac{j-m}{2}-\lambda\right)!},$$

$$D_{jm}^{(2)}\left(\hat{\mathbf{k}}_{\text{inc}}, \widetilde{\mathbf{u}}\right) = \frac{-\mathrm{i}(-1)^{\frac{j+m}{2}} \sqrt{(2j+1)(j-m)!(j+m)!}}{2^{j+1}\pi \frac{j-m}{2}! \frac{j+m}{2}!}$$

$$\times \sum_{\mathbf{R}_n}' e^{\mathrm{i}\mathbf{k}_{\parallel}\cdot\mathbf{R}_n + im\varphi_{-\mathbf{R}_n}} \frac{1}{k}\left(\frac{2|\mathbf{R}_n|}{k}\right)^j \int_{T^2}^{\infty} u^{j-\frac{1}{2}} e^{-|\mathbf{R}_n|^2 u + \frac{k^2}{4u}} \mathrm{d}u,$$

$$D_{jm}^{(3)}\left(\hat{\mathbf{k}}_{\text{inc}}, \widetilde{\mathbf{u}}\right) = \frac{\delta_{j0}}{4\pi} \Gamma\left(-\frac{1}{2}, -\frac{k^2}{4T^2}\right),$$

where in $D_{jm}^{(1)}\left(\hat{\mathbf{k}}_{\text{inc}}, \widetilde{\mathbf{u}}\right)$ the summation runs over the reciprocal lattice points $\mathbf{G}$. The series contains the upper incomplete Gamma function Γ where $k_{\mathbf{G},z}^+ = \sqrt{k^2 - (\mathbf{k}_{\parallel} + \mathbf{G})^2}$. In $D_{jm}^{(2)}\left(\hat{\mathbf{k}}_{\text{inc}}, \widetilde{\mathbf{u}}\right)$ we have used the integral representation of the spherical Hankel function. The parameter T defines the splitting between the real and Fourier space summation. $T = \sqrt{\pi/A}$ is considered as a proper splitting factor [70]. The integral in $D_{jm}^{(2)}\left(\hat{\mathbf{k}}_{\text{inc}}, \widetilde{\mathbf{u}}\right)$ can be computed by a recursion relation.

Using the above equations, the lattice summation can be calculated. A home-built algorithm has been developed by Achim Groner [226] and Dominik Beutel [225] that can numerically calculate the summation. We use this code throughout the thesis. Having the lattice summation, it is possible to insert the result in Eq. 4.19 and, hence, obtain the lattice coupling matrix finally. Consequently, knowing the T matrix of the isolated particle and the external incident field coefficient, the scattering coefficient can be derived from Eq. 4.17. In the next subsection, the overall scattered field from the metasurface is explored.

4.2.3 Diffraction modes in the spherical coordinate system

The scattered field from a periodic metasurface made from identical meta-atoms illuminated with a plane wave is the sum of the scattering from all the meta-atoms. The optical scattering from the meta-atom n can be written as:

$$\mathbf{E}_n^{\text{sca}}\left(\mathbf{r}, \mathbf{k}_{\text{inc}}, \widetilde{\mathbf{u}}\right) = \sum_{j=1}^{\infty} \sum_{m=-j}^{j} b_{0,jm}^{\text{e}}\left(\mathbf{k}_{\text{inc}}, \widetilde{\mathbf{u}}\right) \sum_{\mathbf{R}_n} \mathbf{N}_{jm}^{(3)}\left(\widetilde{\mathbf{r}} - \widetilde{\mathbf{R}}_n\right) e^{\mathrm{i}\mathbf{k}_{\parallel}\cdot\mathbf{R}_n}$$

$$+ \sum_{j=1}^{\infty} \sum_{m=-j}^{j} b_{0,jm}^{\text{m}}\left(\mathbf{k}_{\text{inc}}, \widetilde{\mathbf{u}}\right) \sum_{\mathbf{R}_n} \mathbf{M}_{jm}^{(3)}\left(\widetilde{\mathbf{r}} - \widetilde{\mathbf{R}}_n\right) e^{\mathrm{i}\mathbf{k}_{\parallel}\cdot\mathbf{R}_n}, \tag{4.22}$$

where $b_{0,jm}^{\text{e}}\left(\mathbf{k}_{\text{inc}}, \widetilde{\mathbf{u}}\right)$ $(b_{0,jm}^{\text{m}}\left(\mathbf{k}_{\text{inc}}, \widetilde{\mathbf{u}}\right))$ is the electric (magnetic) scattering field coefficient of the meta-atom at the origin of the coordinates. For simplicity, we remove

the "0" subscript from now on. Knowing the scattering field coefficients, the calculation of the scattering is reduced to the summations of the VSH over the meta-atom positions, which are in turn calculated by applying the Poisson summation formula as [227]:

$$\sum_{\mathbf{R}_n} \mathbf{M}_{jm}^{(3)} \left(\widetilde{\mathbf{r}} - \widetilde{\mathbf{R}}_n \right) e^{\mathrm{i}\mathbf{k}_\parallel \cdot \mathbf{R}_n} = \frac{2\pi \mathrm{i}^{-j}}{Ak} \sum_{\mathbf{G}} \frac{\mathbf{X}_{jm}(\mathbf{k}_{\mathbf{G}}^{\pm})}{|k_{\mathbf{G},z}^{\pm}|} e^{\mathrm{i}\mathbf{k}_{\mathbf{G}}^{\pm} \cdot \mathbf{r}}, \qquad (4.23)$$

$$\sum_{\mathbf{R}_n} \mathbf{N}_{jm}^{(3)} \left(\widetilde{\mathbf{r}} - \widetilde{\mathbf{R}}_n \right) e^{\mathrm{i}\mathbf{k}_\parallel \cdot \mathbf{R}_n} = \frac{2\pi \mathrm{i}^{1-j}}{Ak} \sum_{\mathbf{G}} \frac{\hat{\mathbf{r}} \times \mathbf{X}_{jm}(\mathbf{k}_{\mathbf{G}}^{\pm})}{|k_{\mathbf{G},z}^{\pm}|} e^{\mathrm{i}\mathbf{k}_{\mathbf{G}}^{\pm} \cdot \mathbf{r}}, \qquad (4.24)$$

with

$$\hat{\mathbf{r}} \times \mathbf{X}_{jm}(kr,\theta,\phi) = \gamma_{jm}[\tau_{jm}(\cos\theta)\hat{\theta} + \mathrm{i}\pi_{jm}(\cos\theta)\hat{\phi}]e^{\mathrm{i}m\phi} = \mathbf{Z}_{jm}(kr,\theta,\phi), \qquad (4.25)$$

and

$$\mathbf{k}_{\mathbf{G}}^{\pm} = \mathbf{k}_\parallel + \mathbf{G} \pm \hat{\mathbf{z}}\sqrt{k^2 - (\mathbf{k}_\parallel + \mathbf{G})^2} = \mathbf{k}_\parallel + \mathbf{G} \pm k_{\mathbf{G},z}^{\pm}\hat{\mathbf{z}}. \qquad (4.26)$$

After substituting of Eq. 4.23-4.24 in Eq. 4.22, we arrive to:

$$\mathbf{E}^{\mathrm{sca}}\left(\mathbf{r}, \mathbf{k}_{\mathrm{inc}}, \widetilde{\mathbf{u}} \right) = \qquad\qquad\qquad\qquad\qquad\qquad\qquad\qquad\qquad (4.27)$$

$$\frac{2\pi}{Ak} \sum_{j=1}^{\infty} \sum_{m=-j}^{j} \frac{1}{\mathrm{i}^j} \sum_{\mathbf{G}} \left[\mathrm{i}b_{jm}^{\mathrm{e}}\left(\mathbf{k}_{\mathrm{inc}}, \widetilde{\mathbf{u}} \right) \mathbf{Z}_{jm}(\mathbf{k}_{\mathbf{G}}^{\pm}) + b_{jm}^{\mathrm{m}}\left(\mathbf{k}_{\mathrm{inc}}, \widetilde{\mathbf{u}} \right) \mathbf{X}_{jm}(\mathbf{k}_{\mathbf{G}}^{\pm}) \right] \frac{e^{\mathrm{i}\mathbf{k}_{\mathbf{G}}^{\pm} \cdot \mathbf{r}}}{|k_{\mathbf{G},z}^{\pm}|},$$

where $\mathbf{k}_{\mathbf{G}}^{\pm}$ is the wavevector of the scattered field. We have used $\pm$ to distinguish the forward (+) and backward (-) propagation. The formula (4.27) provides the total scattered field, in terms of propagating or evanescent diffraction orders, from a 2D lattice. The diffraction orders are propagating if the z component of the associated wavevector is real-valued, i.e., $k_{\mathbf{G},z}^{\pm} \in \mathbb{R}$. In the following, however, to simplify the equations, we only use the real-valued angles, and hence our relations will be limited to the propagating diffraction orders. The extension to describe the evanescent diffraction orders is straightforward but requires further considerations for the simplification that we have ignored for the thesis. Note that this restriction only concerns the final optical scattering of the metasurface. In contrast, the description of the meta-atoms up to a given multipolar order considered is exact, and near-field coupling is accurately and precisely taken into account.

For the low multipolar orders, it is possible to rewrite the $\pi_{jm}(\cos\theta)$ and $\tau_{jm}(\cos\theta)$ equations with short trigonometric functions and, after simplification, we can derive closed-form relations for the scattered field. We have done so up to octupolar order, i.e., $j_{\max} = 3$ [75]. After some algebra, we can derive the following general equation for the amplitude of a diffraction order $\mathbf{G}$ from an infinitely periodic metasurface made from identical particles that is illuminated by a plane wave:

$$\mathbf{E}_{\mathbf{G}}^{\mathrm{sca}}\left(\mathbf{r}, \mathbf{k}_{\mathrm{inc}}, \widetilde{\mathbf{u}} \right) = \begin{bmatrix} E_\theta^{\mathrm{sca}}\left(\mathbf{r}, \mathbf{k}_{\mathrm{inc}}, \widetilde{\mathbf{u}} \right) \\ E_\phi^{\mathrm{sca}}\left(\mathbf{r}, \mathbf{k}_{\mathrm{inc}}, \widetilde{\mathbf{u}} \right) \end{bmatrix} = \frac{\mathrm{i}\sqrt{\pi}}{2Ak^2} \frac{e^{\mathrm{i}\mathbf{k}_{\mathbf{G}}^{\pm} \cdot \mathbf{r}}}{|\cos\theta|} \sum_{j=1}^{3} \frac{\sqrt{2j+1}}{\mathrm{i}^j} \bar{\bar{W}}_j\left(\theta, \phi \right) \begin{bmatrix} \mathbf{b}_j^{\mathrm{e}}\left(\mathbf{k}_{\mathrm{inc}}, \widetilde{\mathbf{u}} \right) \\ \mathbf{b}_j^{\mathrm{m}}\left(\mathbf{k}_{\mathrm{inc}}, \widetilde{\mathbf{u}} \right) \end{bmatrix},$$
$$(4.28)$$

where θ and ϕ are the polar and azimuth angles of the wavevector $\mathbf{k}_{\mathbf{G}}^{\pm}$ characterizing the diffraction order, respectively:

$$\cos\theta = \frac{k_{\mathbf{G},z}^{\pm}}{|\mathbf{k}_{\mathbf{G}}^{\pm}|} \quad \text{and} \quad \phi = \arctan\left(\frac{k_{\mathbf{G},y}}{k_{\mathbf{G},x}} \right). \qquad (4.29)$$

Needless to say that these angles could have a different value from the incident field polar θ_{inc} and azimuth ϕ_{inc} angles, and should not be confused with them. $\bar{\bar{W}}(\theta, \phi)$ is the spherical multipole-field translation matrix defined as:

$$\bar{\bar{W}}_j(\theta, \phi) = \begin{bmatrix} \mathbf{W}_j & \mathbf{W}'_j \\ \mathrm{i}\,\mathbf{W}'_j & \mathrm{i}\,\mathbf{W}_j \end{bmatrix}, \tag{4.30}$$

where:

$$\mathbf{W}_1 = \begin{bmatrix} e^{-\mathrm{i}\phi}\cos\theta \\ -\sqrt{2}\sin\theta \\ -e^{\mathrm{i}\phi}\cos\theta \end{bmatrix}^T , \quad \mathbf{W}'_1 = \begin{bmatrix} -e^{-\mathrm{i}\phi} \\ 0 \\ -e^{\mathrm{i}\phi} \end{bmatrix}^T , \tag{4.31}$$

$$\mathbf{W}_2 = \begin{bmatrix} \frac{1}{2}e^{-\mathrm{i}2\phi}\sin2\theta \\ e^{-\mathrm{i}\phi}\cos2\theta \\ -\sqrt{\frac{3}{2}}\sin2\theta \\ -e^{\mathrm{i}\phi}\cos2\theta \\ \frac{1}{2}e^{\mathrm{i}2\phi}\sin2\theta \end{bmatrix}^T , \quad \mathbf{W}'_2 = \begin{bmatrix} -e^{-\mathrm{i}2\phi}\sin\theta \\ -e^{-\mathrm{i}\phi}\cos\theta \\ 0 \\ -e^{\mathrm{i}\phi}\cos\theta \\ e^{\mathrm{i}2\phi}\sin\theta \end{bmatrix}^T ,$$

$$\mathbf{W}_3 = \begin{bmatrix} \frac{\sqrt{15}}{4}e^{-\mathrm{i}3\phi}\sin^2\theta\,\cos\theta \\ \frac{1}{4}\sqrt{\frac{5}{2}}e^{-\mathrm{i}2\phi}\sin\theta\,(3\cos2\theta+1) \\ \frac{1}{16}e^{-\mathrm{i}\phi}\,(\cos\theta+15\cos3\theta) \\ -\frac{\sqrt{3}}{8}\,(\sin\theta+5\sin3\theta) \\ -\frac{1}{16}e^{-\mathrm{i}\phi}\,(\cos\theta+15\cos3\theta) \\ \frac{1}{4}\sqrt{\frac{5}{2}}e^{-\mathrm{i}2\phi}\sin\theta\,(3\cos2\theta+1) \\ -\frac{\sqrt{15}}{4}e^{-\mathrm{i}3\phi}\sin^2\theta\,\cos\theta \end{bmatrix}^T , \quad \mathbf{W}'_3 = \begin{bmatrix} -\frac{\sqrt{15}}{4}e^{-\mathrm{i}3\phi}\sin^2\theta \\ -\frac{1}{2}\sqrt{\frac{5}{2}}e^{-\mathrm{i}2\phi}\sin2\theta \\ -\frac{1}{4}e^{-\mathrm{i}\phi}\,(5\cos^2\theta-1) \\ 0 \\ -\frac{1}{4}e^{\mathrm{i}\phi}\,(5\cos^2\theta-1) \\ \frac{1}{2}\sqrt{\frac{5}{2}}e^{\mathrm{i}2\phi}\sin2\theta \\ -\frac{\sqrt{15}}{4}e^{\mathrm{i}3\phi}\sin^2\theta \end{bmatrix}^T .$$

For rectangular lattices, $\mathbf{k}_{\mathbf{G}}^{\pm}$ and the subsequent wavevector components are calculated as [75]:

$$\mathbf{k}_{\mathbf{G}}^{\pm} = k_{\mathbf{G},x}\hat{\mathbf{x}} + k_{\mathbf{G},y}\hat{\mathbf{y}} + k_{\mathbf{G},z}^{\pm}\,\hat{\mathbf{z}}, \tag{4.32}$$

$$k_{\mathbf{G},x} = k_x^{\text{inc}} + \frac{2\pi n_1}{\Lambda_1}, \tag{4.33}$$

$$k_{\mathbf{G},y} = k_y^{\text{inc}} + \frac{2\pi n_2}{\Lambda_2}, \tag{4.34}$$

$$k_{\mathbf{G},z}^{\pm} = \pm\sqrt{k^2 - \left(k_x^{\text{inc}} + \frac{2\pi n_1}{\Lambda_1}\right)^2 - \left(k_y^{\text{inc}} + \frac{2\pi n_2}{\Lambda_2}\right)^2} = k\cos\theta, \tag{4.35}$$

where Λ_1 and Λ_2 are the two periodicities of the lattice. For a square array $\Lambda = \Lambda_1 = \Lambda_2$, which we extensively use, we can write the wave-vector components as:

$$k_{\mathbf{G},x} = \frac{2\pi}{\lambda}\left(\sin\theta_{\text{inc}}\cos\phi_{\text{inc}} + \frac{1}{\widetilde{\Lambda}}n_1\right), \quad k_{\mathbf{G},y} = \frac{2\pi}{\lambda}\left(\sin\theta_{\text{inc}}\sin\phi_{\text{inc}} + \frac{1}{\widetilde{\Lambda}}n_2\right), \tag{4.36}$$

$$k_{\mathbf{G},z}^{\pm} = \pm\frac{2\pi}{\lambda}\sqrt{1 - \left(\sin\theta_{\text{inc}}\cos\phi_{\text{inc}} + \frac{1}{\widetilde{\Lambda}}n_1\right)^2 - \left(\sin\theta_{\text{inc}}\sin\phi_{\text{inc}} + \frac{1}{\widetilde{\Lambda}}n_2\right)^2}, \tag{4.37}$$

where θ_{inc} and ϕ_{inc} are the polar and azimuth angle of the incident field, respectively. $\widetilde{\Lambda} = \Lambda/\lambda$ is the *normalized lattice constant*. For a normally incident illumination, i.e., $\theta_{\text{inc}} = 0$, irrespective of ϕ_{inc}, the corresponding scattering angles simplify to:

$$\cos\theta = \pm\sqrt{1 - \frac{1}{\widetilde{\Lambda}^2}(n_1^2 + n_2^2)}, \quad \tan\phi = \frac{n_2}{n_1}. \tag{4.38}$$

4.2.4   Diffraction modes in the Cartesian coordinate system

In this subsection, we use the transformation matrices defined in Chapter 3 and derive the scattering of a metasurface in the Cartesian coordinates. After employing Eq. 3.26-3.27 and applying the transformation in Eq. 4.28 to the Cartesian coordinates, we arrive to [75]:

$$
\mathbf{E}_{\mathbf{G}}^{\mathrm{sca}}\left(\mathbf{r},\mathbf{k}_{\mathrm{inc}},\widetilde{\mathbf{u}}\right) = \begin{bmatrix} E_{\mathbf{G},x}^{\mathrm{sca}}\left(\mathbf{r},\mathbf{k}_{\mathrm{inc}},\widetilde{\mathbf{u}}\right) \\ E_{\mathbf{G},y}^{\mathrm{sca}}\left(\mathbf{r},\mathbf{k}_{\mathrm{inc}},\widetilde{\mathbf{u}}\right) \\ E_{\mathbf{G},z}^{\mathrm{sca}}\left(\mathbf{r},\mathbf{k}_{\mathrm{inc}},\widetilde{\mathbf{u}}\right) \end{bmatrix} \tag{4.39}
$$

$$
= \frac{\mathrm{i}k\sqrt{\pi}}{2A}\frac{e^{\mathrm{i}\mathbf{k}_{\mathbf{G}}^{\pm}\cdot\mathbf{r}}}{\left|\cos\theta\right|}\bar{\bar{S}}\left(\theta,\phi\right) \begin{bmatrix} \left(\varepsilon\zeta_1\right)^{-1}\mathbf{p}\ \left(\mathbf{k}_{\mathrm{inc}},\widetilde{\mathbf{u}}\right) \\ k\left(\varepsilon\zeta_2\right)^{-1}\mathbf{Q}^{\mathrm{e}}\left(\mathbf{k}_{\mathrm{inc}},\widetilde{\mathbf{u}}\right) \\ k^2\left(\varepsilon\zeta_3\right)^{-1}\mathbf{O}^{\mathrm{e}}\left(\mathbf{k}_{\mathrm{inc}},\widetilde{\mathbf{u}}\right) \\ \mathrm{i}\eta\left(\zeta_1\right)^{-1}\mathbf{m}\ \left(\mathbf{k}_{\mathrm{inc}},\widetilde{\mathbf{u}}\right) \\ \mathrm{i}\eta k\left(\zeta_2\right)^{-1}\mathbf{Q}^{\mathrm{m}}\left(\mathbf{k}_{\mathrm{inc}},\widetilde{\mathbf{u}}\right) \\ \mathrm{i}\eta k^2\left(\zeta_3\right)^{-1}\mathbf{O}^{\mathrm{m}}\left(\mathbf{k}_{\mathrm{inc}},\widetilde{\mathbf{u}}\right) \end{bmatrix},
$$

where:

$$
\begin{bmatrix} \left(\varepsilon\zeta_1\right)^{-1}\mathbf{p}\ \left(\mathbf{k}_{\mathrm{inc}},\widetilde{\mathbf{u}}\right) \\ k\left(\varepsilon\zeta_2\right)^{-1}\mathbf{Q}^{\mathrm{e}}\left(\mathbf{k}_{\mathrm{inc}},\widetilde{\mathbf{u}}\right) \\ k^2\left(\varepsilon\zeta_3\right)^{-1}\mathbf{O}^{\mathrm{e}}\left(\mathbf{k}_{\mathrm{inc}},\widetilde{\mathbf{u}}\right) \\ \mathrm{i}\eta\left(\zeta_1\right)^{-1}\mathbf{m}\ \left(\mathbf{k}_{\mathrm{inc}},\widetilde{\mathbf{u}}\right) \\ \mathrm{i}\eta k\left(\zeta_2\right)^{-1}\mathbf{Q}^{\mathrm{m}}\left(\mathbf{k}_{\mathrm{inc}},\widetilde{\mathbf{u}}\right) \\ \mathrm{i}\eta k^2\left(\zeta_3\right)^{-1}\mathbf{O}^{\mathrm{m}}\left(\mathbf{k}_{\mathrm{inc}},\widetilde{\mathbf{u}}\right) \end{bmatrix} = \frac{1}{k^3}\bar{\bar{\alpha}}_{\mathrm{eff}}\left(\mathbf{k}_{\mathrm{inc}},\widetilde{\mathbf{u}}\right) \begin{bmatrix} \zeta_1\mathbf{E}_1\left(\mathbf{k}_{\mathrm{inc}}\right) \\ k^{-1}\zeta_2\mathbf{E}_2\left(\mathbf{k}_{\mathrm{inc}}\right) \\ k^{-2}\zeta_3\mathbf{E}_3\left(\mathbf{k}_{\mathrm{inc}}\right) \\ \mathrm{i}\eta\zeta_1\mathbf{H}_1\left(\mathbf{k}_{\mathrm{inc}}\right) \\ \mathrm{i}\eta k^{-1}\zeta_2\mathbf{H}_2\left(\mathbf{k}_{\mathrm{inc}}\right) \\ \mathrm{i}\eta k^{-2}\zeta_3\mathbf{H}_3\left(\mathbf{k}_{\mathrm{inc}}\right) \end{bmatrix}, \tag{4.40}
$$

where $\bar{\bar{S}}\left(\theta,\phi\right)$ is the Cartesian multipole-field translation matrix, defined as:

$$
\bar{\bar{S}}\left(\theta,\phi\right) = \begin{bmatrix} \mathbf{S}_1^{\mathrm{xe}}\left(\theta,\phi\right) & \mathbf{S}_2^{\mathrm{xe}}\left(\theta,\phi\right) & \mathbf{S}_3^{\mathrm{xe}}\left(\theta,\phi\right) & \mathbf{S}_1^{\mathrm{xm}}\left(\theta,\phi\right) & \mathbf{S}_2^{\mathrm{xm}}\left(\theta,\phi\right) & \mathbf{S}_3^{\mathrm{xm}}\left(\theta,\phi\right) \\ \mathbf{S}_1^{\mathrm{ye}}\left(\theta,\phi\right) & \mathbf{S}_2^{\mathrm{ye}}\left(\theta,\phi\right) & \mathbf{S}_3^{\mathrm{xe}}\left(\theta,\phi\right) & \mathbf{S}_1^{\mathrm{ym}}\left(\theta,\phi\right) & \mathbf{S}_2^{\mathrm{ym}}\left(\theta,\phi\right) & \mathbf{S}_3^{\mathrm{ym}}\left(\theta,\phi\right) \\ \mathbf{S}_1^{\mathrm{ze}}\left(\theta,\phi\right) & \mathbf{S}_2^{\mathrm{ze}}\left(\theta,\phi\right) & \mathbf{S}_3^{\mathrm{ze}}\left(\theta,\phi\right) & \mathbf{S}_1^{\mathrm{zm}}\left(\theta,\phi\right) & \mathbf{S}_2^{\mathrm{zm}}\left(\theta,\phi\right) & \mathbf{S}_3^{\mathrm{zm}}\left(\theta,\phi\right) \end{bmatrix}. \tag{4.41}
$$

and with the vector elements of the matrix:

$$
\mathbf{S}_j\left(\theta,\phi\right) = \begin{bmatrix} \mathbf{S}_j^{\mathrm{xe}}\left(\theta,\phi\right) & \mathbf{S}_j^{\mathrm{xm}}\left(\theta,\phi\right) \\ \mathbf{S}_j^{\mathrm{ye}}\left(\theta,\phi\right) & \mathbf{S}_j^{\mathrm{ym}}\left(\theta,\phi\right) \\ \mathbf{S}_j^{\mathrm{ze}}\left(\theta,\phi\right) & \mathbf{S}_j^{\mathrm{zm}}\left(\theta,\phi\right) \end{bmatrix} = \frac{\sqrt{2j+1}}{\mathrm{i}^{1-j}}\left[\bar{\bar{R}}\left(\theta,\phi\right)^T\bar{\bar{W}}\left(\theta,\phi\right)\right]\bar{\bar{F}}_j^{-1}. \tag{4.42}
$$

The $\bar{\bar{R}}\left(\theta,\phi\right)$ matrix is the transformation operator from the spherical to the Cartesian coordinates. The vectors $\hat{\theta}$ and $\hat{\phi}$ can be expressed as a function of the vectors $\hat{\mathbf{x}}$, $\hat{\mathbf{y}}$, and $\hat{\mathbf{z}}$ using the matrix $\bar{\bar{R}}\left(\theta,\phi\right)$ as:

$$
\begin{bmatrix} \hat{\theta} \\ \hat{\phi} \end{bmatrix} = \bar{\bar{R}}\left(\theta,\phi\right)\begin{bmatrix} \hat{\mathbf{x}} \\ \hat{\mathbf{y}} \\ \hat{\mathbf{z}} \end{bmatrix} = \begin{bmatrix} \cos\theta\cos\phi & \cos\theta\sin\phi & \sin\theta \\ \sin\phi & -\cos\phi & 0 \end{bmatrix}\begin{bmatrix} \hat{\mathbf{x}} \\ \hat{\mathbf{y}} \\ \hat{\mathbf{z}} \end{bmatrix}. \tag{4.43}
$$

In Eq. 4.40, $\bar{\bar{\alpha}}_{\mathrm{eff}}$ is the *effective polarizability matrix*. The effective polarizability can be either calculated from the $\bar{\bar{T}}_{\mathrm{eff}}$ via applying the transformations of Eq. 3.33, or directly via:

$$
\bar{\bar{\alpha}}_{\mathrm{eff}}\left(\mathbf{k}_{\mathrm{inc}},\widetilde{\mathbf{u}}\right) = \left[\bar{\bar{I}} - \bar{\bar{\alpha}}_0\left(k\right)\bar{\bar{C}}\left(\hat{\mathbf{k}}_{\mathrm{inc}},\widetilde{\mathbf{u}}\right)\right]^{-1}\bar{\bar{\alpha}}_0\left(k\right), \tag{4.44}
$$

where $\bar{\bar{\bar{\alpha}}}_0$ is the polarizability matrix of the isolated particle and $\bar{\bar{C}}$ is the Cartesian lattice coupling defined as [75]:

$$\bar{\bar{C}}\left(\hat{\mathbf{k}}_{\text{inc}}, \widetilde{\mathbf{u}}\right) = \mathrm{i}F\bar{\bar{C}}_{\text{s}}\left(\hat{\mathbf{k}}_{\text{inc}}, \widetilde{\mathbf{u}}\right) F^{-1}. \tag{4.45}$$

In summary, we have provided analytical expressions for the optical response of periodic metasurfaces made from arbitrary but identical meta-atoms illuminated with a plane wave of arbitrary orientation. Our analysis is limited to an octupolar order approximation. For the development of the analytical equations in this section, as stated in Ref. [75], I acknowledge an equal contribution of Dr. Theodosios Karamanos.

In the next section, we explore the symmetry of the lattice coupling matrix for different periodic arrays.

4.3 Lattice coupling symmetries

The lattice coupling matrix is dimensionless and has the same sorting as the polarizability or the T matrix. Depending on the symmetry of the 2D lattice and the illumination orientation, the lattice coupling matrix has multiple symmetry-protected zero entries. Exploiting these symmetry-protected zeros is essential in deriving simplified equations for the optical response of periodic metasurfaces. This section explores the symmetries of lattice coupling matrices for different lattices and the models to express them.

The general lattice coupling matrix in the Cartesian coordinate system $\bar{\bar{C}}$ up to octupolar order can be expressed as:

$$\bar{\bar{C}} = \begin{bmatrix} \bar{\bar{C}}_{11}^{\text{ee}} & \bar{\bar{C}}_{12}^{\text{ee}} & \bar{\bar{C}}_{13}^{\text{ee}} & \bar{\bar{C}}_{11}^{\text{em}} & \bar{\bar{C}}_{12}^{\text{em}} & \bar{\bar{C}}_{13}^{\text{em}} \\ \bar{\bar{C}}_{21}^{\text{ee}} & \bar{\bar{C}}_{22}^{\text{ee}} & \bar{\bar{C}}_{23}^{\text{ee}} & \bar{\bar{C}}_{21}^{\text{em}} & \bar{\bar{C}}_{22}^{\text{em}} & \bar{\bar{C}}_{23}^{\text{em}} \\ \bar{\bar{C}}_{31}^{\text{ee}} & \bar{\bar{C}}_{32}^{\text{ee}} & \bar{\bar{C}}_{33}^{\text{ee}} & \bar{\bar{C}}_{31}^{\text{em}} & \bar{\bar{C}}_{32}^{\text{em}} & \bar{\bar{C}}_{33}^{\text{em}} \\ \bar{\bar{C}}_{11}^{\text{me}} & \bar{\bar{C}}_{12}^{\text{me}} & \bar{\bar{C}}_{13}^{\text{me}} & \bar{\bar{C}}_{11}^{\text{mm}} & \bar{\bar{C}}_{12}^{\text{mm}} & \bar{\bar{C}}_{13}^{\text{mm}} \\ \bar{\bar{C}}_{21}^{\text{me}} & \bar{\bar{C}}_{22}^{\text{me}} & \bar{\bar{C}}_{23}^{\text{me}} & \bar{\bar{C}}_{21}^{\text{mm}} & \bar{\bar{C}}_{22}^{\text{mm}} & \bar{\bar{C}}_{23}^{\text{mm}} \\ \bar{\bar{C}}_{31}^{\text{me}} & \bar{\bar{C}}_{32}^{\text{me}} & \bar{\bar{C}}_{33}^{\text{me}} & \bar{\bar{C}}_{31}^{\text{mm}} & \bar{\bar{C}}_{32}^{\text{mm}} & \bar{\bar{C}}_{33}^{\text{mm}} \end{bmatrix}, \tag{4.46}$$

where the superscript "e" and "m" refer to electric or magnetic coupling and the number subscripts are the multipolar order coupling. For brevity, in this section, we have ignored the arguments $\hat{\mathbf{k}}_{\text{inc}}$ and $\widetilde{\mathbf{u}}$ for the lattice coupling matrix. However, they are always assumed. Figure 4.2 visualizes the template used to show the lattice coupling matrix. Note that the lattice coupling matrix in the spherical coordinate system $\bar{\bar{C}}_{\text{s}}$ has also the same matrix format as $\bar{\bar{C}}$.

For different lattice arrangements and orientations of the incident field, the coupling matrix takes different symmetries. Figure 4.3 shows the spherical and Cartesian coupling matrices' amplitude for five different lattice symmetries under normal incidence for a specific normalized periodicity. The considered lattices are square, hexagonal, rectangular, oblique, and rhombic lattices. As can be seen from the figure, there are several zero entries in the coupling matrix of each array. These symmetry-protected zeros, like the symmetry-protected zeros of the polarizability and T matrices, can

$\bar{\bar{C}}^{ee}_{11}$	$\bar{\bar{C}}^{ee}_{21}$	$\bar{\bar{C}}^{ee}_{31}$	$\bar{\bar{C}}^{me}_{11}$	$\bar{\bar{C}}^{me}_{21}$	$\bar{\bar{C}}^{me}_{31}$
$\bar{\bar{C}}^{ee}_{12}$	$\bar{\bar{C}}^{ee}_{22}$	$\bar{\bar{C}}^{ee}_{32}$	$\bar{\bar{C}}^{me}_{12}$	$\bar{\bar{C}}^{me}_{22}$	$\bar{\bar{C}}^{me}_{32}$
$\bar{\bar{C}}^{ee}_{13}$	$\bar{\bar{C}}^{ee}_{23}$	$\bar{\bar{C}}^{ee}_{33}$	$\bar{\bar{C}}^{me}_{13}$	$\bar{\bar{C}}^{me}_{23}$	$\bar{\bar{C}}^{me}_{33}$
$\bar{\bar{C}}^{em}_{11}$	$\bar{\bar{C}}^{em}_{21}$	$\bar{\bar{C}}^{em}_{31}$	$\bar{\bar{C}}^{mm}_{11}$	$\bar{\bar{C}}^{mm}_{21}$	$\bar{\bar{C}}^{mm}_{31}$
$\bar{\bar{C}}^{em}_{12}$	$\bar{\bar{C}}^{em}_{22}$	$\bar{\bar{C}}^{em}_{32}$	$\bar{\bar{C}}^{mm}_{12}$	$\bar{\bar{C}}^{mm}_{22}$	$\bar{\bar{C}}^{mm}_{32}$
$\bar{\bar{C}}^{em}_{13}$	$\bar{\bar{C}}^{em}_{23}$	$\bar{\bar{C}}^{em}_{33}$	$\bar{\bar{C}}^{mm}_{13}$	$\bar{\bar{C}}^{mm}_{23}$	$\bar{\bar{C}}^{mm}_{33}$

Figure 4.2: **Lattice coupling matrix template:** The sorting of the lattice coupling matrix up to octupolar order.

help develop models for the lattices. These models, in turn, help to derive simpler equations for effective parameters and scattering equations. That is because the lengthy sums at the end collapse to a few terms for which the coupling matrices take non-zero values

Square and hexagonal lattices are the two most commonly used lattices in meta-surface research. Compared to other lattices in Fig 4.3, they also have a higher symmetry, i.e., more symmetry-protected zeros. Hence, we will focus more on these two lattices. A square and a hexagonal lattice under normal incidence have the exact symmetry up to the quadrupolar order (Fig. 4.3a,b and Fig. 4.4a,d) and can be expressed as:

$$\bar{\bar{C}} = \begin{bmatrix}
C_{dd} & 0 & 0 & 0 & 0 & 0 & 0 & 0 & 0 & 0 & 0 & 0 & -C_{dQ} & 0 & 0 & 0 \\
0 & C_{dd} & 0 & 0 & 0 & 0 & 0 & 0 & 0 & 0 & 0 & 0 & 0 & 0 & C_{dQ} & 0 \\
0 & 0 & C^{zz}_{dd} & 0 & 0 & 0 & 0 & 0 & 0 & 0 & 0 & 0 & 0 & 0 & 0 & 0 \\
0 & 0 & 0 & C^{xy}_{QQ} & 0 & 0 & 0 & 0 & 0 & 0 & 0 & 0 & 0 & 0 & 0 & 0 \\
0 & 0 & 0 & 0 & C_{QQ} & 0 & 0 & 0 & -C_{dQ} & 0 & 0 & 0 & 0 & 0 & 0 & 0 \\
0 & 0 & 0 & 0 & 0 & C^{zz}_{QQ} & 0 & 0 & 0 & 0 & 0 & 0 & 0 & 0 & 0 & 0 \\
0 & 0 & 0 & 0 & 0 & 0 & C_{QQ} & 0 & 0 & C_{dQ} & 0 & 0 & 0 & 0 & 0 & 0 \\
0 & 0 & 0 & 0 & 0 & 0 & 0 & C^{xy}_{QQ} & 0 & 0 & 0 & 0 & 0 & 0 & 0 & 0 \\
0 & 0 & 0 & 0 & -C_{dQ} & 0 & 0 & 0 & C_{dd} & 0 & 0 & 0 & 0 & 0 & 0 & 0 \\
0 & 0 & 0 & 0 & 0 & 0 & C_{dQ} & 0 & 0 & C_{dd} & 0 & 0 & 0 & 0 & 0 & 0 \\
0 & 0 & 0 & 0 & 0 & 0 & 0 & 0 & 0 & 0 & C^{zz}_{dd} & 0 & 0 & 0 & 0 & 0 \\
0 & 0 & 0 & 0 & 0 & 0 & 0 & 0 & 0 & 0 & 0 & C^{xy}_{QQ} & 0 & 0 & 0 & 0 \\
-C_{dQ} & 0 & 0 & 0 & 0 & 0 & 0 & 0 & 0 & 0 & 0 & 0 & C_{QQ} & 0 & 0 & 0 \\
0 & 0 & 0 & 0 & 0 & 0 & 0 & 0 & 0 & 0 & 0 & 0 & 0 & C^{zz}_{QQ} & 0 & 0 \\
0 & C_{dQ} & 0 & 0 & 0 & 0 & 0 & 0 & 0 & 0 & 0 & 0 & 0 & 0 & C_{QQ} & 0 \\
0 & 0 & 0 & 0 & 0 & 0 & 0 & 0 & 0 & 0 & 0 & 0 & 0 & 0 & 0 & C^{xy}_{QQ}
\end{bmatrix}. \tag{4.47}$$

Not all the coupling elements are excited with each illumination for a certain meta-atom symmetry. The relevant entries of the above matrix for isotropic meta-atoms under normal incidence are the dipole-dipole C_{dd}, quadrupole-quadrupole C_{QQ}, and dipole-quadrupole C_{dQ} coupling elements. Figures 4.4b,c,e,f show the imaginary and real parts of the coupling terms for square and hexagonal arrays under normal
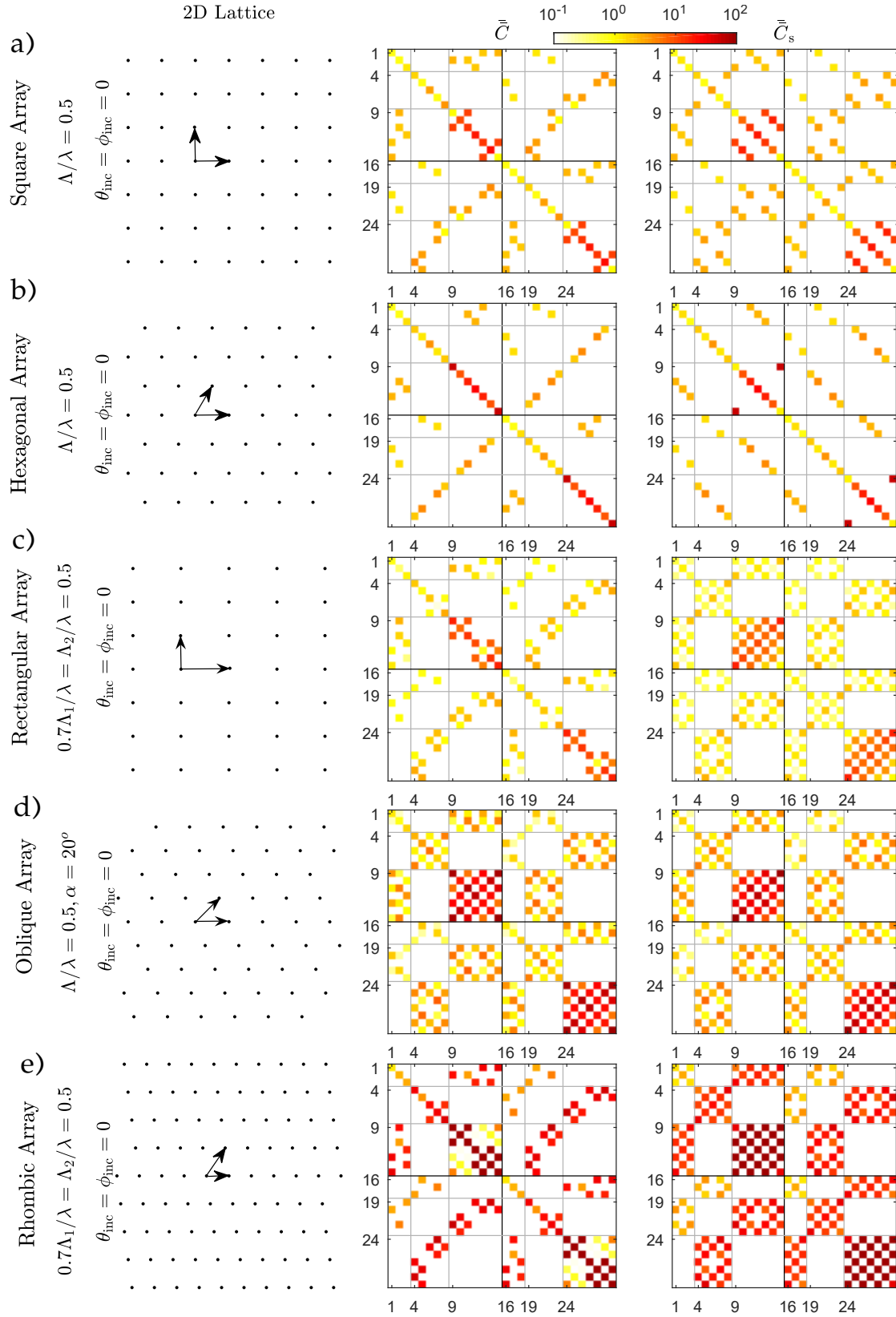
Figure 4.3: **Lattice coupling symmetries:** The spherical (right) and Cartesian (middle) lattice coupling matrix amplitude for a) square, b) hexagonal, c) rectangular, d) oblique, and e) rhombic arrays under normal incidence up to an octupolar order for a given normalized periodicity.
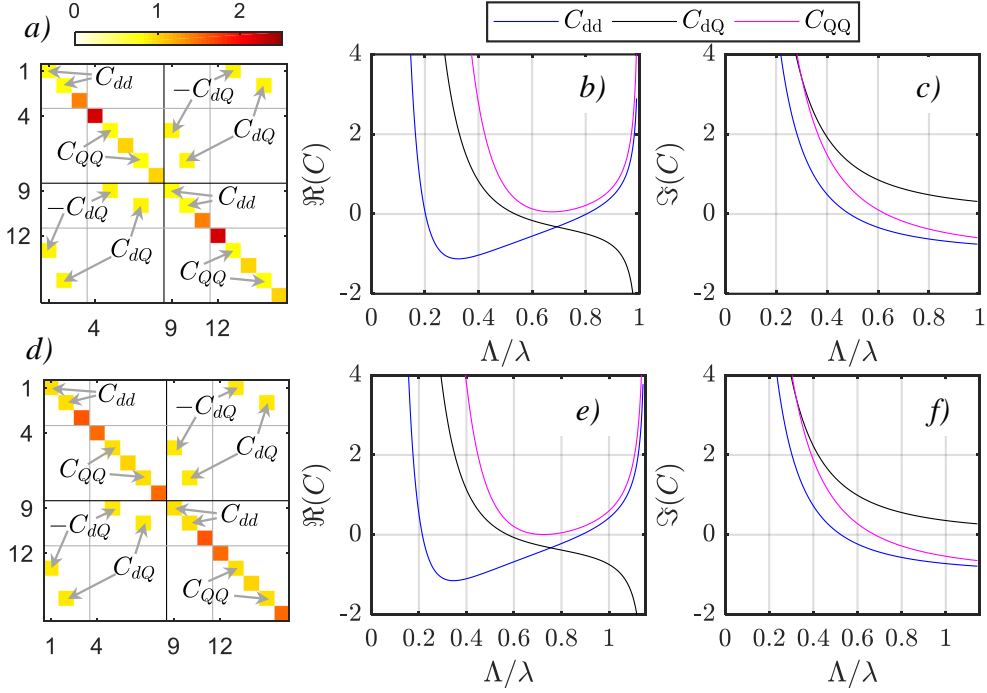
Figure 4.4: **The Cartesian lattice coupling matrix:** The Cartesian lattice coupling matrix amplitude for a) a square and d) a hexagonal array with a normalized periodicity of $\Lambda/\lambda = 0.9$ under normal incidence ($\theta_{\text{inc}} = \phi_{\text{inc}} = 0$), up to quadrupolar order. The relevant matrix elements for a metasurface made from isotropic particles are dipole-dipole C_{dd}, quadrupole-quadrupole C_{QQ}, and dipole-quadrupole C_{dQ} couplings. They are marked with an arrow. b,e) The real and c,f) imaginary parts of the relevant lattice couplings as a function of the normalized periodicity Λ/λ.

incidence for subwavelength periods, i.e., $\widetilde{\Lambda} < 1$. As we will show in the last section, the imaginary parts of these coefficients can also be analytically calculated using energy conservation considerations. The imaginary parts of these coefficients for sub-wavelength metasurfaces are [75]:

$$\Im(C_{\text{dd}}) = \frac{3}{4\pi\widetilde{\Lambda}^2} - 1, \tag{4.48}$$

$$\Im(C_{\text{QQ}}) = \frac{5}{4\pi\widetilde{\Lambda}^2} - 1, \tag{4.49}$$

$$\Im(C_{\text{dQ}}) = \frac{\sqrt{15}}{4\pi\widetilde{\Lambda}^2}. \tag{4.50}$$

Unlike the imaginary parts, we do not have analytical expressions for the real parts of the lattice couplings. They are numerically calculated using the equations provided in Section 4.2.2. The real part of the dipole-dipole coupling $\Re(C_{\text{dd}})$ crosses zero for two normalized periodicities $\widetilde{\Lambda} \approx 0.2, 0.8$ ($\widetilde{\Lambda} \approx 0.21, 0.88$ for a Hexagonal lattice). As we will show later, this "magic lattice spacing" [228] is where the "cooperative resonance" [229] of the meta-atoms reflects all the incident light. At this point of operation, the resonance of the isolated meta-atom experiences no detuning, and hence the effective resonance also occurs at the same lattice constant. For the quadrupole-quadrupole coupling, $\Re(C_{\text{QQ}})$ does not cross the zero point. The absence of a root does not mean that no resonance occurs. However, it means that a detuning of the resonance wavelength is inevitable for a quadrupolar metasurface.

For a normalized periodicity of $\widetilde{\Lambda} = 1$ ($\widetilde{\Lambda} = 1/\sqrt{\cos(\pi/6)}$ for the hexagonal lattice), i.e., at the onset of a new diffraction order, the real part of the coupling constants diverges to infinity. This point of operation is essential to consider when performing numerical calculations. The same is true for very small lattice constants. However, these dense points of operations are usually avoided in metamaterials. Note that an infinitely large coupling term does not mean an infinite coupling strength. Indeed, as we will shortly discuss, the coupling strength has an inverse relation to the coupling terms.

For a dipolar metasurface, illuminated at oblique incidence with a plane wave ($\phi_{\text{inc}} = 0$), the Cartesian C matrix for both the square and hexagonal arrangement looks like the following:

$$
\bar{\bar{C}} = \begin{bmatrix}
C_{\text{dd}}^{\text{xx}} & 0 & 0 & 0 & 0 & 0 \\
0 & C_{\text{dd}}^{\text{yy}} & 0 & 0 & 0 & C_{\text{dd}}^{\text{yz}} \\
0 & 0 & C_{\text{dd}}^{\text{zz}} & 0 & C_{\text{dd}}^{\text{zy}} & 0 \\
0 & 0 & 0 & C_{\text{dd}}^{\text{xx}} & 0 & 0 \\
0 & 0 & C_{\text{dd}}^{\text{yz}} & 0 & C_{\text{dd}}^{\text{yy}} & 0 \\
0 & C_{\text{dd}}^{\text{zy}} & 0 & 0 & 0 & C_{\text{dd}}^{\text{zz}}
\end{bmatrix} = \begin{bmatrix}
C_{\text{xx}} & 0 & 0 & 0 & 0 & 0 \\
0 & C_{\text{yy}} & 0 & 0 & 0 & C_{\text{yz}} \\
0 & 0 & C_{\text{zz}} & 0 & -C_{\text{yz}} & 0 \\
0 & 0 & 0 & C_{\text{xx}} & 0 & 0 \\
0 & 0 & C_{\text{yz}} & 0 & C_{\text{yy}} & 0 \\
0 & -C_{\text{yz}} & 0 & 0 & 0 & C_{\text{zz}}
\end{bmatrix},
$$

(4.51)

where, for simplicity, we use $C_{\text{dd}}^{\text{xx}} = C_{\text{xx}}$, $C_{\text{dd}}^{\text{yy}} = C_{\text{yy}}$, $C_{\text{dd}}^{\text{zz}} = C_{\text{zz}}$, and $C_{\text{dd}}^{\text{yz}} = -C_{\text{dd}}^{\text{zy}} = C_{\text{yz}}$. Note that it is antisymmetric.

4.4 Effective parameters

This section explores the closed-form expressions for parameters such as the polarizability/T matrix and the induced multipole moments inside a lattice. These *effective* parameters depend on the meta-atoms' isolated response, the lattice base vectors along which the meta-atoms are arranged, and the plane wave illumination orientation. In the following subsection, effective polarizability and T matrices of isotropic and anisotropic meta-atoms inside square and hexagonal lattices are studied. The last subsection calculates the effective induced multipole moments inside the lattice and their fundamental limits.

The main focus of this and the following sections is the optical response of an infinitely periodic arrangement of isotropic meta-atoms that are illuminated by a normal incident plane wave (Fig. 4.5).

4.4.1 Effective polarizability and T matrices

In Chapter 3, we explored the polarizability and T matrices of meta-atoms with different symmetries. These meta-atoms, when arranged in an infinitely periodic lattice, are modified with the lattice coupling matrix and this leads to effective polarizability $\bar{\bar{\alpha}}_{\text{eff}}$ and T matrix $\bar{\bar{T}}_{\text{eff}}$. These effective parameters might have very different symmetries in comparison to their isolated counterpart. The added complexity might complicate the calculations. However, the additional degrees of freedom provided are design opportunities for enhanced functionalities in optics.

In Eq. 4.18 and Eq. 4.44, we identified the expression relating the isolated polarizability and T matrices of a meta-atom to its effective counterpart via the lattice coupling matrix. In the previous section, we identified the lattice coupling matrix for
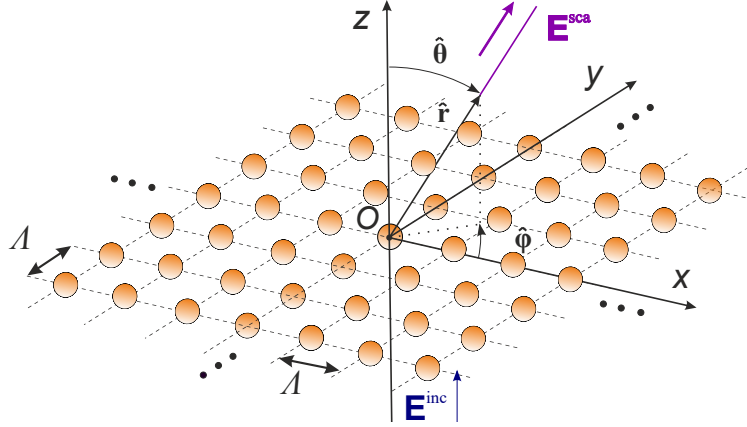
Figure 4.5: **Optical scattering from an infinitely periodic arrangement of isotropic meta-atoms:** Identical spherical meta-atoms arranged on a square array lattice with a periodicity Λ. The infinitely periodic arrangement is illuminated by a normally incident plane wave $\mathbf{E}^{\mathrm{inc}}$ and radiates the scattered field $\mathbf{E}^{\mathrm{sca}}$. The figure is adapted with permission from a drawing by Dr. Theodosios D Karamanos [75]
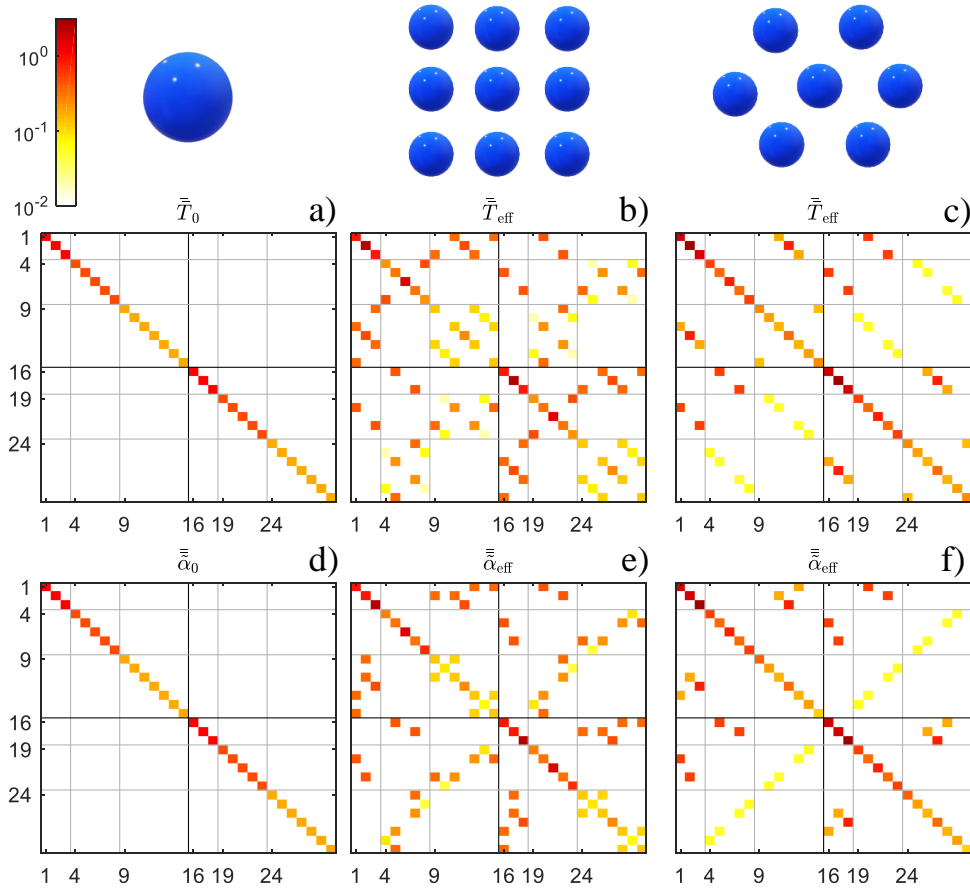
Figure 4.6: **Effective isotropic meta-atoms:** The isolated a) T matrix and d) polarizability matrix amplitude for a dual Mie sphere with Mie angles $\theta_{\mathrm{E}1} = \theta_{\mathrm{M}1} = 0$, $\theta_{\mathrm{E}2} = \theta_{\mathrm{M}2} = \pi/3$, and $\theta_{\mathrm{E}3} = \theta_{\mathrm{M}3} = 4\pi/9$. The effective b-c) T matrix and e-f) polarizability matrix of the dual sphere inside a b,e) square and c,f) hexagonal lattice array, with a normalized lattice constant of $\widetilde{\Lambda} = 0.5$ for the square, and $\widetilde{\Lambda} = 0.5/\sqrt{\cos \pi/6}$ for the hexagonal lattice, under normal plane wave incidence.

different lattices. This section calculates the effective polarizability and T matrices of isotropic and anisotropic meta-atoms inside a few periodic lattices under normal incidence.
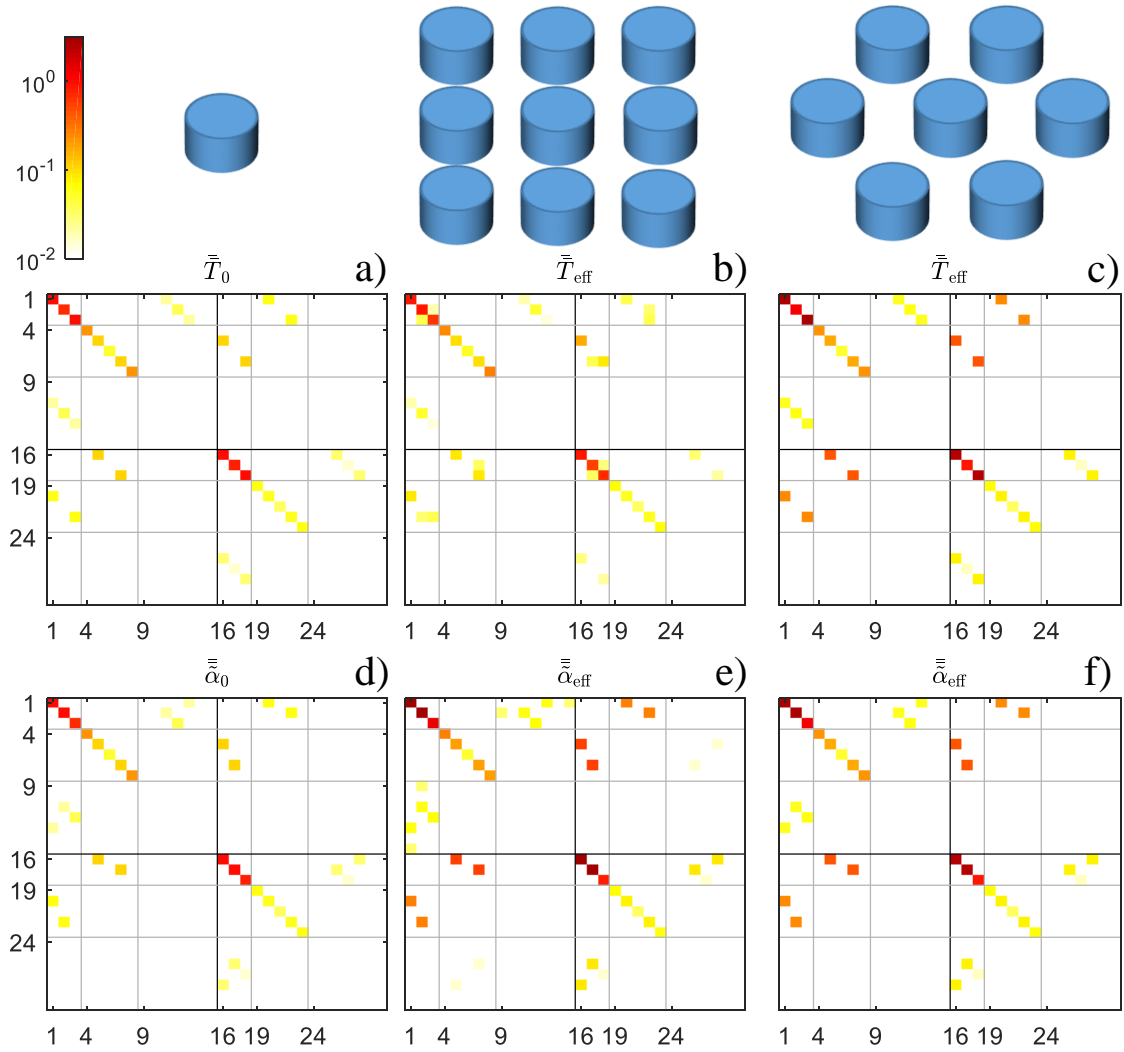
Figure 4.7: **Effective anisotropic meta-atoms:** The isolated a) T matrix and d) polarizability matrix amplitude of a nanocylinder (diameter $D = 2 \times 234$ nm, height $H = 213$ nm) made from amorphous silicon ($n = 3.714$) embedded in silica ($n = 1.44$) at an operating wavelength of $\lambda_0 = 1420$ nm. The effective b-c) T matrix and e-f) polarizability matrix of the nanocylinder inside a b,e) square and c,f) hexagonal lattice array, with a lattice constant of $\Lambda = 800$ nm for the square, and $\Lambda = 800/\sqrt{\cos \pi/6}$ nm for the hexagonal lattice, under normal plane wave incidence.

Figure 4.6 shows the calculated isolated/effective polarizability/T matrix for an isotropic meta-atom modeled with the Mie angles outside/inside a square/hexagonal array that is illuminated with a normal-incident plane wave. Although the isolated polarizability and T matrices are diagonal, as evident from the figure, the effective matrices take the symmetry of the lattice (cf. 4.3).

Next, we have calculated the effective matrices for a nanocylinder as an example for an anisotropic meta-atom. Figure 4.7 shows the isolated and effective matrices of

a nanocylinder outside and inside a square/hexagonal array that is illuminated with a normal-incident plane wave. Interestingly, up to quadrupolar order, the symmetry of the effective polarizability does not change compared to its isolated counterpart. This finding can help in deriving simplified expressions for the optical scattering of metasurfaces made from nanocylinders.

In Ref. [75], we have also calculated the effective polarizability and T matrices of a helix inside a square and a hexagonal lattice.

4.4.2 Effective induced multipole moments

In this subsection, we explore the effect of the lattice on the induced multipole moments of the individual meta-atoms inside a square lattice with a normalized periodicity $\widetilde{\Lambda}$ in comparison to the induced multipole moments of the isolated meta-atoms.

We assume a metasurface made from isotropic meta-atoms that is illuminated with a linearly polarized plane wave propagating in the z-direction (Eq. 2.54):

$$
\mathbf{E}^{\mathrm{TE}}\left(\mathbf{r}, \mathbf{k}_{\mathrm{inc}}\right) = E_0 \begin{bmatrix} 0 \\ 1 \\ 0 \end{bmatrix} e^{\mathrm{i}\mathbf{k}_{\mathrm{inc}}\cdot\mathbf{r}}, \quad \mathbf{E}^{\mathrm{TM}}\left(\mathbf{r}, \mathbf{k}_{\mathrm{inc}}\right) = E_0 \begin{bmatrix} 1 \\ 0 \\ 0 \end{bmatrix} e^{\mathrm{i}\mathbf{k}_{\mathrm{inc}}\cdot\mathbf{r}}. \tag{4.52}
$$

We discuss, in the following, the modifications in the effective Cartesian multipole moments in a closed-form formula. Starting from Eq. 4.40, up to the quadrupolar order, we can write the effective Cartesian induced multipole moments as [68, 146]:

$$
\begin{bmatrix} \frac{1}{\varepsilon}\mathbf{p}\left(\mathbf{k}_{\mathrm{inc}}, \widetilde{\Lambda}\right) \\ \frac{1}{\varepsilon}\frac{k}{\sqrt{20}}\mathbf{Q}^{\mathrm{e}}\left(\mathbf{k}_{\mathrm{inc}}, \widetilde{\Lambda}\right) \\ \mathrm{i}Z\mathbf{m}\left(\mathbf{k}_{\mathrm{inc}}, \widetilde{\Lambda}\right) \\ \mathrm{i}Z\frac{k}{\sqrt{20}}\mathbf{Q}^{\mathrm{m}}\left(\mathbf{k}_{\mathrm{inc}}, \widetilde{\Lambda}\right) \end{bmatrix} = \frac{6\pi}{k^3}\bar{\bar{\alpha}}_{\mathrm{eff}}\left(\mathbf{k}_{\mathrm{inc}}, \widetilde{\Lambda}\right) \begin{bmatrix} \mathbf{E}_1\left(\mathbf{k}_{\mathrm{inc}}\right) \\ \frac{\sqrt{20}}{k}\mathbf{E}_2\left(\mathbf{k}_{\mathrm{inc}}\right) \\ \mathrm{i}Z\mathbf{H}_1\left(\mathbf{k}_{\mathrm{inc}}\right) \\ \mathrm{i}Z\frac{\sqrt{20}}{k}\mathbf{H}_2\left(\mathbf{k}_{\mathrm{inc}}\right) \end{bmatrix}. \tag{4.53}
$$

We assume that the isotropic meta-atom is represented with the Mie coefficients a_1, a_2, b_1, b_2. Then, for TM incidence, the induced Cartesian multipole moments can be derived as:

$$
\begin{bmatrix} p_x/\varepsilon \\ Q^{\mathrm{e}}_{\mathrm{xz}}/\varepsilon \\ \eta m_y \\ \eta Q^{\mathrm{m}}_{\mathrm{yz}} \end{bmatrix} = \begin{bmatrix} \frac{6\pi\mathrm{i}}{k^3}a_{1,\mathrm{mod}}^{\overset{b_2}{\curvearrowleft}} \\ \frac{-60\pi}{k^4}a_{2,\mathrm{mod}}^{\overset{b_1}{\curvearrowleft}} \\ \frac{6\pi\mathrm{i}}{k^3}b_{1,\mathrm{mod}}^{\overset{a_2}{\curvearrowleft}} \\ \frac{-60\pi}{k^4}b_{2,\mathrm{mod}}^{\overset{a_1}{\curvearrowleft}} \end{bmatrix} E_0, \tag{4.54}
$$

and, for a TE polarized incidence:

$$
\begin{bmatrix} p_y/\varepsilon \\ Q^{\mathrm{e}}_{\mathrm{yz}}/\varepsilon \\ \eta m_x \\ \eta Q^{\mathrm{m}}_{\mathrm{xz}} \end{bmatrix} = \begin{bmatrix} \frac{6\pi\mathrm{i}}{k^3}a_{1,\mathrm{mod}}^{\overset{b_2}{\curvearrowleft}} \\ \frac{-60\pi}{k^4}a_{2,\mathrm{mod}}^{\overset{b_1}{\curvearrowleft}} \\ \frac{-6\pi\mathrm{i}}{k^3}b_{1,\mathrm{mod}}^{\overset{a_2}{\curvearrowleft}} \\ \frac{60\pi}{k^4}b_{2,\mathrm{mod}}^{\overset{a_1}{\curvearrowleft}} \end{bmatrix} E_0, \tag{4.55}
$$

where $a_{j,\text{mod}}^{\overset{b_g}{\frown}}$ $(b_{j,\text{mod}}^{\overset{a_g}{\frown}})$ $j = 1, 2, g = |2 - j| + 1$ is the effective electric (magnetic) Mie coefficient that is modulated with the lattice and also coupled to the magnetic (electric) Mie coefficient of a different multipolar order. The effective Mie coefficients/polarizabilities of the particles in these expressions above depend on (a) the modulation of the elements of the same multipolar order through C_{dd} and C_{QQ} couplings and (b) the coupling with other multipole moments in the lattice through C_{dQ}. The $\overset{b_2}{\frown}$ superscript shows the coupled parameters, and the coupling term is written in the circle. Electric (magnetic) dipole moments are coupled to magnetic (electric) quadrupole moments and vice versa. The modulated and coupled Mie coefficients, that we call here, in short, the *effective Mie coefficients*, can be written as:

$$\frac{1}{a_{1,\text{eff}}} = \frac{1}{a_{1,\text{mod}}^{\overset{b_2}{\frown}}} = \frac{1 + C_{\text{dQ}}^2 b_{2,\text{mod}} a_{1,\text{mod}}}{a_{1,\text{mod}}\left(1 + i\sqrt{5/3}C_{\text{dQ}}b_{2,\text{mod}}\right)}, \tag{4.56}$$

$$\frac{1}{b_{1,\text{eff}}} = \frac{1}{b_{1,\text{mod}}^{\overset{a_2}{\frown}}} = \frac{1 + C_{\text{dQ}}^2 a_{2,\text{mod}} b_{1,\text{mod}}}{b_{1,\text{mod}}\left(1 + i\sqrt{5/3}C_{\text{dQ}}a_{2,\text{mod}}\right)}, \tag{4.57}$$

$$\frac{1}{a_{2,\text{eff}}} = \frac{1}{a_{2,\text{mod}}^{\overset{b_1}{\frown}}} = \frac{1 + C_{\text{dQ}}^2 b_{1,\text{mod}} a_{2,\text{mod}}}{a_{2,\text{mod}}\left(1 + i\sqrt{3/5}C_{\text{dQ}}b_{1,\text{mod}}\right)}, \tag{4.58}$$

$$\frac{1}{b_{2,\text{eff}}} = \frac{1}{b_{2,\text{mod}}^{\overset{a_1}{\frown}}} = \frac{1 + C_{\text{dQ}}^2 a_{1,\text{mod}} b_{2,\text{mod}}}{b_{2,\text{mod}}\left(1 + i\sqrt{3/5}C_{\text{dQ}}a_{1,\text{mod}}\right)}. \tag{4.59}$$

The Mie coefficients that appear in these expressions on the right-hand side are modulated thanks to their coupling in the lattice. They are explicitly written as:

$$\frac{1}{a_{1,\text{mod}}} = \frac{1}{a_1} - iC_{\text{dd}}, \tag{4.60}$$

$$\frac{1}{b_{1,\text{mod}}} = \frac{1}{b_1} - iC_{\text{dd}}, \tag{4.61}$$

$$\frac{1}{a_{2,\text{mod}}} = \frac{1}{a_2} - iC_{\text{QQ}}, \tag{4.62}$$

$$\frac{1}{b_{2,\text{mod}}} = \frac{1}{b_2} - iC_{\text{QQ}}. \tag{4.63}$$

Writing the above equations in such a manner has many advantages. Primarily, we can immediately distinguish the impact of the lattice on the multipole moments of the same or different order. Note that in the above equations, we have ignored the arguments due to space restrictions.
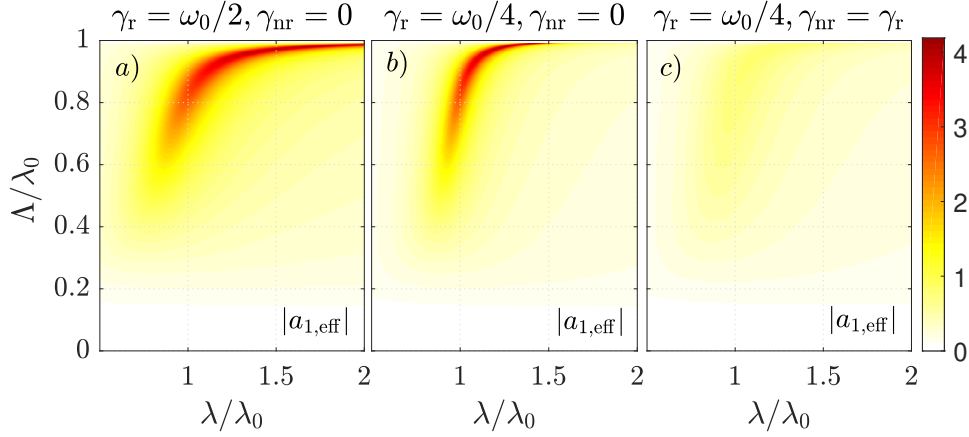
Figure 4.8: **Effective dipolar Mie coefficient:** The effective electric dipolar Mie coefficient of a single-resonance isotropic meta-atom inside a square array of periodicity Λ/λ made from electric dipoles modeled with a Lorentzian profile as a function of the periodicity and wavelength (cf. Eq. 3.61, $\lambda_0 = 1000\,\text{nm}$). Different radiative γ_r and nonradiative γ_nr losses are assumed in the Lorentzian models in a-c. The effective parameters are calculated using Eq. 4.64.
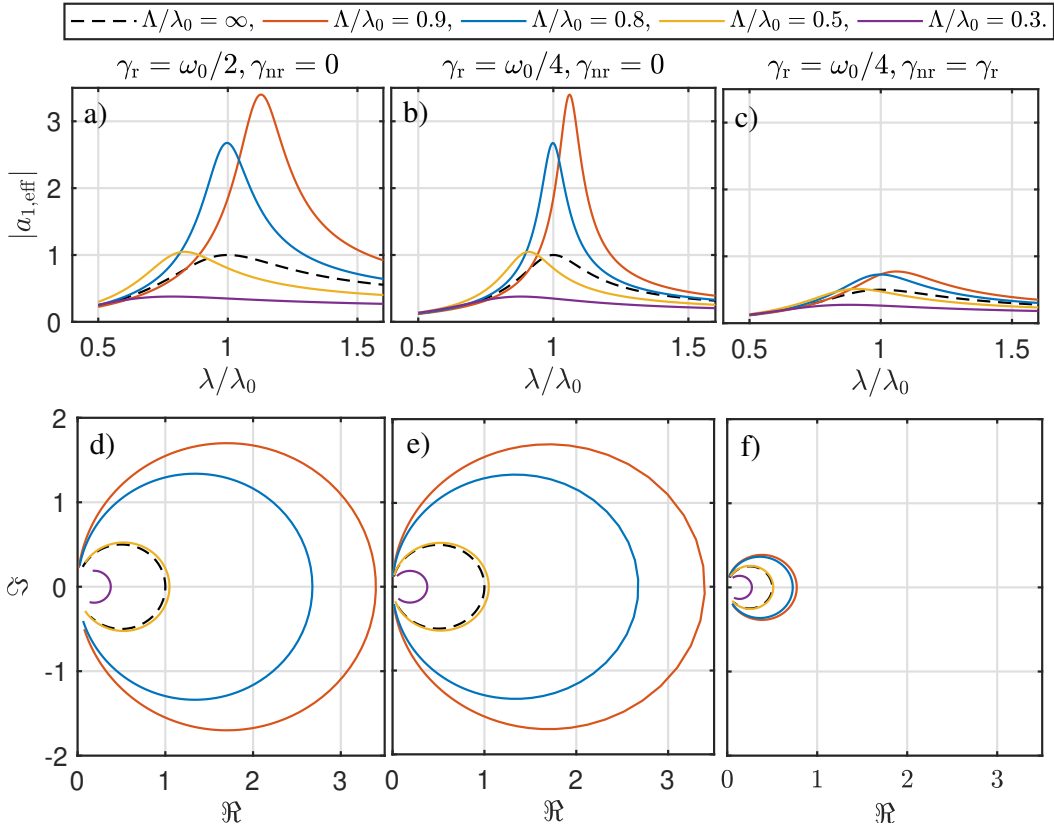
Figure 4.9: **Effective Lorentzian resonance:** a-c) The wavelength dependency of the amplitude of the effective electric dipolar Mie coefficient when an electric dipolar particle decorates inside a square array of periodicity Λ/λ. The electric dipoles are modeled with a Lorentzian profile (cf. Eq. 3.61). A few selected periodicities are considered, and different radiative γ_r and nonradiative γ_nr losses are assumed for the Lorentzian model. d-f) The real and imaginary parts of the effective Mie coefficient resonance for the selected loss parameters and periodicities. $\Lambda/\lambda = \infty$ represents the response of an isolated meta-atom. The effective parameters are calculated using Eq. 4.64.

4.4.3 Upper limits for effective moments

In case only a single resonance captures the complete response of an isotopic meta-atom, or in cases where the coupling of the (a_1, b_2) and (a_2, b_1) are zero, the effective Mie coefficients can directly be calculated via:

$$\frac{1}{a_{1,\text{eff}}} = \frac{1}{a_{1,\text{mod}}} = \frac{1}{a_1} - \mathrm{i}C_{\text{dd}}, \tag{4.64}$$

$$\frac{1}{b_{1,\text{eff}}} = \frac{1}{b_{1,\text{mod}}} = \frac{1}{b_1} - \mathrm{i}C_{\text{dd}}, \tag{4.65}$$

$$\frac{1}{a_{2,\text{eff}}} = \frac{1}{a_{2,\text{mod}}} = \frac{1}{a_2} - \mathrm{i}C_{\text{QQ}}, \tag{4.66}$$

$$\frac{1}{b_{2,\text{eff}}} = \frac{1}{b_{2,\text{mod}}} = \frac{1}{b_2} - \mathrm{i}C_{\text{QQ}}. \tag{4.67}$$

Therefore, studying these effective Mie coefficients is essential in determining the overall response of single-resonance metasurfaces.

Here, we consider the Lorentzian profile defined in Chapter 3 Eq. 3.61. We assume a metasurface made from isotropic meta-atoms, where the meta-atoms sustain a single electric dipole resonance. We seek to explore the effect of the lattice on the effective resonance of the metasurface. The Mie coefficients of the meta-atoms are modeled with a Lorentzian profile with different parameters. Figure 4.8 shows the effective electric dipolar Mie coefficient inside a square array. The resonance wavelength of the Lorentzian profile is at $\lambda_0 = 1000\,\text{nm}$.

To have a better insight, in Fig.4.9 we have plotted the resonances for a few selected periodicities. There are a few points to notice in the two figures:

- At a normalized periodicity of $\widetilde{\Lambda} \approx 0.8$, where the real part of the dipole-dipole lattice coupling vanishes, the spectral position of the resonance is unaltered. The real part of the coupling coefficients can be linked to the detuning of the response of the isolated meta-atoms [228, 229].

- At a normalized periodicity of $\widetilde{\Lambda} \approx 0.5$, where the imaginary part of the dipole-dipole lattice constant vanishes, the amplitude of the resonance equals the amplitude of the isolated Mie coefficient. We can show that the imaginary part of the dipole-dipole lattice coefficient is related to the resonance amplitude. It will be shown, shortly, that the maximum of the amplitude occurs where the imaginary part is smallest, i.e., at near $\widetilde{\Lambda} \approx 1$. Note that the lattice should remain subwavelength, i.e. $\widetilde{\Lambda} \leq 1$.

Upper limits for the induced electric dipole moment

Next, we directly study the induced multipole moments and explore the fundamental upper limits of an electric dipole moment inside a lattice. If there is a single electric dipole resonance, represented by a_1, from Eq. 4.54-4.55, irrespective of the polarization, we can write the induced multipole moment as:

$$p = \frac{\varepsilon 6\pi \mathrm{i}E_0}{k^3}\, a_{1,\text{mod}} = \frac{\varepsilon 6\pi \mathrm{i}E_0}{k^3}\, \frac{a_1}{1 - \mathrm{i}\,a_1 C_{\text{dd}}}. \tag{4.68}$$
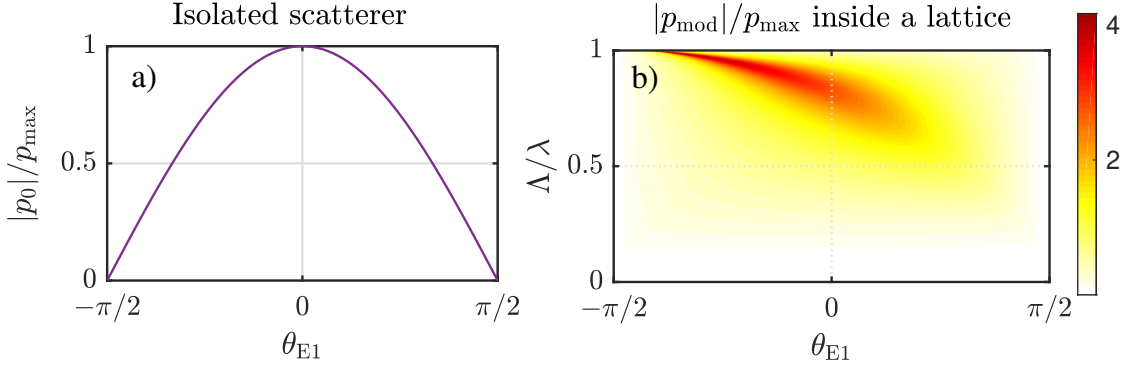
Figure 4.10: **Electric dipole moment enhancement inside a lattice:** Magnitude of the induced electric dipole moment normalized to the maximum induced electric dipole moment of an isolated scatterer in vacuum as a function of the electric dipolar Mie angle for **a**) an isolated electric dipole and **b**) an electric dipole inside a lattice with a normalized periodicity of Λ/λ.

In the following, we wish to study the problem systematically. Any possible value the electric dipolar Mie coefficient can take is, herein, parameterized using the Mie angle θ_{E1}. If the meta-atom is isolated outside a lattice, i.e., $C_{dd} = 0$, the maximal magnitude of the electric dipole moment is at resonance (i.e., $\theta_{E1} = 0$) and is equal to:

$$p_{max} = \left| \frac{\varepsilon 6\pi \mathrm{i} E_0}{k^3} \right| = \frac{6\pi \varepsilon E_0}{k^3}. \tag{4.69}$$

This maximal value is used to normalize the effective induced multipole moment and serves as the reference value for the electric dipole enhancement inside a lattice. The normalized electric dipole moment as a function of the Mie angle is illustrated in Fig. 4.10a. Notice that the normalized electric dipole moment takes the value of one at resonance (i.e., $\theta_{E1} = 0$).

The question is, how much this electric dipole moment can be enhanced when placing the electric dipolar scatterer inside a lattice. The question can be answered by specifying the previously considered equations applicable to purely electric dipolar particles. Therefore, the induced electric dipole moment inside a square lattice array upon normal plane wave illuminations reads as:

$$p_{mod} = \frac{6\pi \mathrm{i} E_0}{\eta k^3} a_{1,mod} = \frac{6\pi \mathrm{i} E_0}{\eta k^3} \frac{a_1}{1 - \mathrm{i}\, a_1 C_{dd}}, \tag{4.70}$$

where the normalized modulated electric dipole moment is:

$$\frac{p_{mod}}{p_{max}} = \frac{\mathrm{i}\, a_1}{1 - \mathrm{i}\, a_1 C_{dd}}. \tag{4.71}$$

Any possible value of the electric dipole moment at a given operating wavelength depends on only two parameters: the Mie angle, which parameterizes the response of the individual particle, and the periodicity of the lattice. Therefore, a sweep search through periodicity and Mie angle can give us the upper limit. The magnitude of the modulated normalized electric dipole moment is plotted in Fig. 4.10b.

The maximal enhancement thanks to the lattice interaction is $4\pi/3$ and occurs in a parameter region where the lattice is still sub-wavelength but very close to the diffraction zone. The meta-atom has to be primarily operated below its resonance frequency. The lattice interaction drives the meta-atom into a resonance, where it gets enhanced far beyond the value it can attain when placed outside the lattice.

The same approach can be followed to find the upper limit for the other multipolar moments. Furthermore, we can also incorporate the coupling of multipoles together and hence study a more rich interaction in the lattice. In Ref. [205], we have explored a scenario in which the electric quadrupole moment is coupled to the magnetic dipole moments of the meta-atoms in a lattice and, hence, the induced magnetic dipole moment is two orders of magnitude enhanced in comparison to the maximum induced dipole moment of an isolated meta-atom.

To summarize, in this section, we explored the effective parameters in the lattice. In the following section, we look at the scattering of metasurfaces with a single resonance.

4.5   Transmission and reflection of single-resonance meta-surfaces

We have studied the effective parameters inside a lattice. Here, we want to see how these effective parameters contribute to light's overall transmission and reflection from the metasurface. We define the TE and TM transmission and reflection coefficients through the following equations:

$$t_{\mathrm{TE}} = \frac{\mathbf{E}^{\mathrm{sca}}_{\hat{\phi}}(\mathbf{r}) + \mathbf{E}^{\mathrm{inc}}_{\hat{\phi}}(\mathbf{r})}{\mathbf{E}^{\mathrm{inc}}_{\hat{\phi}}(\mathbf{r})}, \; t_{\mathrm{TM}} = \frac{\mathbf{E}^{\mathrm{sca}}_{\hat{\theta}}(\mathbf{r}) + \mathbf{E}^{\mathrm{inc}}_{\hat{\theta}}(\mathbf{r})}{\mathbf{E}^{\mathrm{inc}}_{\hat{\theta}}(\mathbf{r})}, \; r_{\mathrm{TE}} = \frac{\mathbf{E}^{\mathrm{sca}}_{\hat{\phi}}(\mathbf{r})}{\mathbf{E}^{\mathrm{inc}}_{\hat{\phi}}(\mathbf{r})}, \; r_{\mathrm{TM}} = \frac{\mathbf{E}^{\mathrm{sca}}_{\hat{\theta}}(\mathbf{r})}{\mathbf{E}^{\mathrm{inc}}_{\hat{\theta}}(\mathbf{r})},$$

$$(4.72)$$

where the subscripts $\hat{\phi}$ and $\hat{\theta}$ refers to the direction of the fields to be considered in the definitions. Following Eq. 4.39 and incorporating the effective derived parameters, we can derive the transmission and reflections coefficients for a metasurface made from single-resonance isotropic meta-atoms that are arranged in a square array and are illuminated with a plane wave as:

$$t_{\mathrm{p}} = 1 - \frac{3}{4\pi\widetilde{\Lambda}^2}a_{1,\mathrm{mod}} \quad , \quad r_{\mathrm{p}} = \frac{-3}{4\pi\widetilde{\Lambda}^2}a_{1,\mathrm{mod}}, \tag{4.73}$$

$$t_{\mathrm{m}} = 1 - \frac{3}{4\pi\widetilde{\Lambda}^2}b_{1,\mathrm{mod}} \quad , \quad r_{\mathrm{m}} = \frac{3}{4\pi\widetilde{\Lambda}^2}b_{1,\mathrm{mod}}, \tag{4.74}$$

$$t_{\mathrm{Q^e}} = 1 - \frac{5}{4\pi\widetilde{\Lambda}^2}a_{2,\mathrm{mod}} \quad , \quad r_{\mathrm{Q^e}} = \frac{5}{4\pi\widetilde{\Lambda}^2}a_{2,\mathrm{mod}}, \tag{4.75}$$

$$t_{\mathrm{Q^m}} = 1 - \frac{5}{4\pi\widetilde{\Lambda}^2}b_{2,\mathrm{mod}} \quad , \quad r_{\mathrm{Q^m}} = \frac{-5}{4\pi\widetilde{\Lambda}^2}b_{2,\mathrm{mod}}, \tag{4.76}$$

where subscript p (m) and $\mathrm{Q^e}$ ($\mathrm{Q^m}$) refers to the electric (magnetic) dipolar and quadrupolar resonance, respectively. The above calculations are done for a TE excitation. Although the response of the metasurface is the same for TE and TM polarization, there will be an extra minus sign in the reflection equations due to the specific definition of the reflection coefficient.

Figure 4.11 shows the amplitude and phase of the transmission and reflection coefficients of different metasurfaces made from identical and non-absorbing meta-atoms with different single resonances that are arranged on a square lattice. We have covered the full possible values by sweeping through the full detuning Mie angles and the entire subwavelength periodicity range. The duality symmetry of electric and magnetic response amplitude is an interesting but expected observation. For dipole metasurfaces, when the isolated particle is at resonance, i.e., when $\theta_{E1} = \theta_{M1} = 0$, the reflectance is maximum at the normalized periodicities of $\widetilde{\Lambda} \approx 0.2, 0.8$ (4.11a-b). The phase of the reflected wave is π for an electric dipole array and 0 for a magnetic dipole array. At these points of operation, the cooperative response of the meta-atoms can cancel the incident field in the forward direction and push the transmittance to zero. For the quadrupolar metasurfaces, the transmittance crosses zero for slightly detuned meta-atoms, i.e., $\theta_{E2}, \theta_{M2} < 0$.
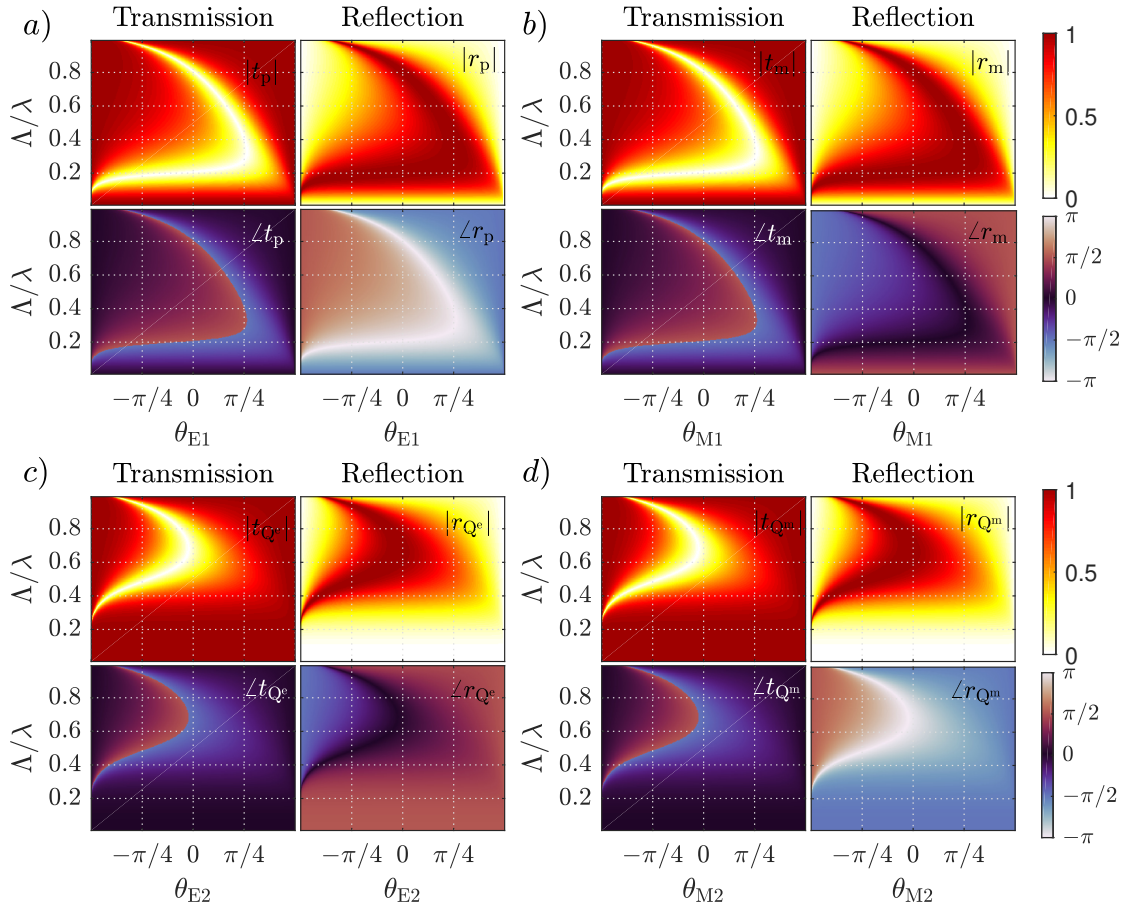
Figure 4.11: **Transmission and reflection of single-resonance metasurfaces:** The full map of transmission and reflection through a subwavelength square array metasurface made from isotropic non-absorbing meta-atoms as a function of the Mie angles and normalized periodicity under a normal TE-polarized plane wave. We assume that the identical meta-atoms have only a single resonance. The amplitude (up) and phase (down) of the transmission (left) and reflection coefficients (right) for a single a) electric and b) magnetic dipole and c) electric, and d) magnetic quadrupole. The reflection and transmission for TE and TM excitations are the same; however, there will be an extra minus sign for the TM excitation due to the specific definition, here.

Energy conservation and lattice couplings

For a single-resonance metasurface that is periodic, subwavelength, and is made from identical, non-absorbing and isotropic meta-atoms, the energy conservation dictates:

$$|t|^2 + |r|^2 = R + T = 1, \tag{4.77}$$

where R (T) is the reflectance (transmittance) from the metasurface. Using Eq. 4.73 for the electric dipole resonance, we can write $t = 1 + r = 1 - A$ and hence:

$$|A|^2 + |1 - A|^2 = 2AA^* + 1 - A^* - A = 1 \Rightarrow AA^* = \Re(A^*) \Rightarrow 1 = \Re\left(\frac{1}{A}\right). \tag{4.78}$$

Then, we can use the Mie angle model and write:

$$\Re\left(\frac{1}{\frac{3}{4\pi\widetilde{\Lambda}^2} a_{1,\text{eff}}}\right) = \frac{4\pi\widetilde{\Lambda}^2}{3}\left[\Re\left(\frac{e^{-i\theta_{\text{E1}}}}{\cos\theta_{\text{E1}}}\right) + \Im(C_{\text{dd}})\right] = \frac{4\pi\widetilde{\Lambda}^2}{3}\left[1 + \Im(C_{\text{dd}})\right] = 1. \tag{4.79}$$

Then, it directly follows [62, 75]:

$$\Im(C_{\text{dd}}) = \frac{3}{4\pi\widetilde{\Lambda}^2} - 1. \tag{4.80}$$

Although we have assumed non-absorbing or isotropic particles, the physical restriction on the lattice couplings still holds as they are independent of meta-atoms. Using a similar approach, we can derive the imaginary part of the other lattice couplings.

In summary, this section has provided the analytical tools required to describe a periodic arrangement of identical meta-atoms. Notably, we have modeled the lattice coupling matrix of different arrays and described their influence on the effective response of meta-atoms compared to their isolated counterpart. With the tools at hand, we can study Huygens' metasurfaces, as an essential class of metasurfaces, in the next chapter.

5. Huygens' and Higher-Order Metasurfaces

In the previous chapter, we derived the general equations governing light scattering from periodic metasurfaces, made from arbitrary but identical meta-atoms, under plane-wave illumination, up to an octupolar order approximation.

This chapter considers a few further assumptions and analyzes specific types of metasurfaces made, mostly, from isotropic meta-atoms. We derive closed-form analytical equations linking the isolated meta-atoms' optical response to the emerging optical scattering of the metasurface via the lattice coupling matrix.

In particular, Huygens' metasurfaces are extensively studied. A *Huygens' metasurface* is a 2D arrangement of identical meta-atoms in which, upon illumination, as a result of the destructive interference of the radiation from the induced multipole moments, the zeroth-order reflection is suppressed. We use this general definition throughout the thesis. In case, non-absorbing meta-atoms are assumed, the zeroth-order transmittance of these non-absorbing Huygens' metasurface tends to unity. Using either a variation of the geometrical details of the unit cell for a fixed operational wavelength or by changing the operational wavelength for a fixed geometry, the phase angle of the transmission coefficient can be tuned over an extended range. Our study does not only deal with conventional dipolar Huygens' metasurfaces (first section) but also quadrupolar (second section) and dipolar-quadrupolar (third section) scenarios. Furthermore, in the fourth section, we explore the phase-shift coverage of the different categories of non-absorbing Huygens' metasurfaces as an actual application of these metasurfaces.

In the fifth section, diffraction modes from metasurfaces, beyond the zeroth-order transmission and reflection, are addressed. We provide analytical equations for the propagating modes of diffracting metasurfaces, i.e., *metagratings*. Finally, in the last section, metasurfaces under an oblique incidence angle are investigated.

The content of this chapter is based on our works in Ref. [31, 59, 75, 101].

5.1   Dipolar metasurfaces

In this section, we explore the zeroth-order diffraction modes from dipolar metasurfaces under normal plane wave incidence. We start from more general rotationally symmetric meta-atoms (i.e., nanocylinders) and, later, assume dual and isotropic meta-atoms as the main building blocks of dipolar Huygens' metasurfaces. Note that, here, for a subwavelength periodicity, the zeroth-order diffraction modes are the only propagating modes of the metasurface. In the following, for brevity, we may use transmission and reflection instead of zeroth-order transmission and reflection.

Although Huygens' metasurfaces, particularly in the electrical engineering community, might be loosely referred to as metasurfaces made from identical meta-atoms with any ratio of the electric and magnetic response [80], here, we strictly require that the meta-atoms have an equal electric and magnetic response.

Transmission and reflection

Assuming a square (or hexagonal) periodic arrangement of isotropic dipolar meta-atoms, using Eq. 4.39 and 4.40, the zeroth-order transmission and reflection for normally incident TE and TM excitation are derived as:

$$t_{\mathrm{TE}} = t_{\mathrm{TM}} = 1 - \frac{3}{4\pi\widetilde{\Lambda}^2}\left(a_{1,\mathrm{mod}} + b_{1,\mathrm{mod}}\right) = 1 - \frac{3}{4\pi\widetilde{\Lambda}^2}\left(\frac{a_1}{1 - \mathrm{i}a_1 C_{\mathrm{dd}}} + \frac{b_1}{1 - \mathrm{i}b_1 C_{\mathrm{dd}}}\right),$$

$$r_{\mathrm{TE}} = -r_{\mathrm{TM}} = \frac{-3}{4\pi\widetilde{\Lambda}^2}\left(a_{1,\mathrm{mod}} - b_{1,\mathrm{mod}}\right) = \frac{-3}{4\pi\widetilde{\Lambda}^2}\left(\frac{a_1}{1 - \mathrm{i}a_1 C_{\mathrm{dd}}} - \frac{b_1}{1 - \mathrm{i}b_1 C_{\mathrm{dd}}}\right), \quad (5.1)$$

where a_1 (b_1) is the electric (magnetic) dipolar Mie coefficient of the isolated sphere, $a_{1,\mathrm{mod}}$ ($b_{1,\mathrm{mod}}$) is the modulated electric (magnetic) dipolar Mie coefficients of the sphere inside the lattice (cf. Eq. 4.64-4.67), C_{dd} is the dipole-dipole lattice coupling, and $\widetilde{\Lambda}$ is the normalized periodicity of the square/hexagonal lattice.

The equation above also applies to rotationally symmetric meta-atoms such as nanocylinders (cf. Eq. 3.83). In the following, without losing generality, we only consider the TE response and, for simplicity, we denote them as t and r. Furthermore, we exploit the developed concepts and restrictions and derive an easier-to-grasp expression for the transmission and reflection.

Effective Mie angles

For non-absorbing and isotropic meta-atoms, we can exploit the Mie angles (cf. Eq. 3.72-3.73) and write the modulated Mie coefficients as:

$$a_{1,\mathrm{mod}} = \left(\frac{\mathrm{i}}{\mathrm{i} + \tan\theta_{\mathrm{E1}} + C_{\mathrm{dd}}}\right), \quad (5.2)$$

$$b_{1,\mathrm{mod}} = \left(\frac{\mathrm{i}}{\mathrm{i} + \tan\theta_{\mathrm{M1}} + C_{\mathrm{dd}}}\right), \quad (5.3)$$

where θ_{E1} (θ_{M1}) is the electric (magnetic) dipolar Mie angle. The imaginary part of the lattice coupling is dictated by the energy conservation restrictions (cf. Eq. 4.48), and, hence, the modulated parameters can be rewritten as:

$$a_{1,\mathrm{mod}} = \left(\frac{\frac{1}{1+\Im C_{\mathrm{dd}}}}{1 - \mathrm{i}\frac{\tan\theta_{\mathrm{E1}} + \Re C_{\mathrm{dd}}}{1+\Im C_{\mathrm{dd}}}}\right) = \left[\frac{\frac{4\pi\widetilde{\Lambda}^2}{3}}{1 - \mathrm{i}\frac{4\pi}{3}\widetilde{\Lambda}^2(\tan\theta_{\mathrm{E1}} + \Re C_{\mathrm{dd}})}\right] = \frac{\frac{4\pi\widetilde{\Lambda}^2}{3}}{1 - \mathrm{i}\tan\theta_{\mathrm{E1,eff}}},$$

$$b_{1,\mathrm{mod}} = \frac{4\pi\widetilde{\Lambda}^2}{3}\left[\frac{1}{1 - \mathrm{i}\frac{4\pi}{3}\widetilde{\Lambda}^2(\tan\theta_{\mathrm{M1}} + \Re C_{\mathrm{dd}})}\right] = \frac{\frac{4\pi\widetilde{\Lambda}^2}{3}}{1 - \mathrm{i}\tan\theta_{\mathrm{M1,eff}}}, \quad (5.4)$$
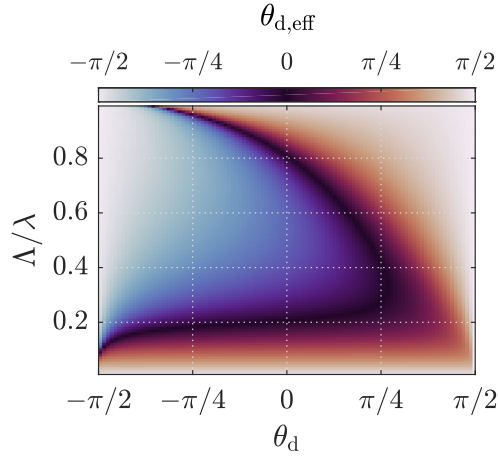
Figure 5.1: **Effective dipolar Mie angle:** The effective dipolar Mie angle as a function of the normalized periodicity of a square array Λ/λ and the dipolar Mie angle θ_d of the isolated sphere. E1 or M1 can replace the subscript d.

where $\theta_{E1,eff}$ ($\theta_{M1,eff}$) is the *effective electric (magnetic) dipolar Mie angle*, defined as:

$$\theta_{E1,eff} = \arctan\left[\frac{4\pi}{3}\widetilde{\Lambda}^2(\tan\theta_{E1} + \Re C_{dd})\right], \tag{5.5}$$

$$\theta_{M1,eff} = \arctan\left[\frac{4\pi}{3}\widetilde{\Lambda}^2(\tan\theta_{M1} + \Re C_{dd})\right]. \tag{5.6}$$

Figure 5.1 shows the relation between the dipolar (electric or magnetic) Mie angle θ_d of an isolated sphere, the periodicity of the lattice, and the effective (electric or magnetic) dipolar Mie angle $\theta_{d,eff}$. It shows the modifications of the Mie angle at different lattice periodicities. The modulations are getting stronger as the lattice gets denser or when the periodicity tends to the wavelength, i.e., $\Lambda \approx \lambda$. From Eq. 5.5-5.6, it is evident that similar to the Mie angles, the effective Mie angles are real-valued and also span an interval of $[-\pi/2, \pi/2]$.

Therefore, the transmission and reflection coefficients in Eq. 5.1 can be written as:

$$t = 1 - \cos\theta_{E1,eff}\exp(i\theta_{E1,eff}) - \cos\theta_{M1,eff}\exp(i\theta_{M1,eff}), \tag{5.7}$$
$$r = \cos\theta_{M1,eff}\exp(i\theta_{M1,eff}) - \cos\theta_{E1,eff}\exp(i\theta_{E1,eff}). \tag{5.8}$$

The above equation guarantees that the transmission and reflection do not cross unity. It constitutes the most general equation for the zeroth-order transmission and reflection of metasurfaces made from non-absorbing, isotropic, and dipolar meta-atoms. The effective dipolar Mie angle has the same interpretation as the Mie angle of the isolated sphere. For instance, at resonance, the angle is zero, and when entirely off-resonant, the angle is $\pm\pi/2$.

Dipolar and dual Huygens' metasurfaces

Here, we assume that the meta-atoms are characterized by an equal and non-absorbing dipolar electric and magnetic Mie coefficient. Using equal dipolar Mie

angles for the non-absorbing meta-atoms, i.e., $\theta_{\mathrm{d}} = \theta_{\mathrm{E1}} = \theta_{\mathrm{M1}}$, and Eq. 5.7-5.8, we can write the zeroth-order transmission and reflection as:

$$
\begin{aligned}
t &= 1 - \frac{3}{4\pi\widetilde{\Lambda}^2}\left(\frac{2\mathrm{i}}{\mathrm{i} + \tan\theta_{\mathrm{d}} + C_{\mathrm{dd}}}\right) = 1 - 2\cos\theta_{\mathrm{d,eff}}\exp\left(\mathrm{i}\theta_{\mathrm{d,eff}}\right), \quad (5.9) \\
r &= 0. \quad\quad\quad\quad\quad\quad\quad\quad\quad\quad\quad\quad\quad\quad\quad\quad\quad\quad\quad\quad\quad\quad\quad\quad\quad\quad\quad\quad (5.10)
\end{aligned}
$$

As expected, the zeroth-order reflection from periodic and dual meta-atoms illuminated by a normally incident plane wave, is, by definition, zero. The zero reflection of dipolar Huygens' metasurfaces is due to the destructive interference of the radiation from the electric and magnetic dipole moments in the backward direction. This suppression of the reflection for a dipolar Huygens' metasurface is sometimes referred to as the first Kerker condition or the *Huygens' condition.* Kerker conditions are originally defined for single meta-atoms. However, they were later extended to metasurfaces and aggregates [230–233]. The vanishing reflection can also be justified with the electromagnetic duality symmetry of the meta-atoms and the discrete rotational symmetry $C_{n>2}$ of the lattice [234, 235]. Note that electromagnetic duality symmetry, and, hence, the helicity preservation, does not guarantee a zero backscattering. An additional requirement is the discrete rotational symmetry $C_{n>2}$ of the lattice [234]. This point becomes more clear when we explore the reflection from a perfectly dual metasurface under oblique incidence. A dual metasurface preserves helicity but does not necessarily suppress reflection.

A confusing point that requires clarification is that not all Huygens' metasurfaces are dual. Electromagnetic duality symmetry should be independent of illumination angle. Huygens' metasurfaces made from nanocylinders are designed such that their electric and magnetic radiation are equal upon normal incidence (i.e., in Eq. 3.83, $a_1 = b_1$ in dipolar response). They preserve helicity upon normal incidence; however, the nanocylinders might not necessarily be dual, and, hence, the helicity is not preserved for oblique incidence.

Unlike in the reflection, in Huygens' metasurfaces, the radiation of the electric and magnetic dipole moments is constructive in the forward direction. If we sweep through the whole $\theta_{\mathrm{d,eff}}$ (i.e., $-\pi/2 \leq \theta_{\mathrm{d,eff}} \leq \pi/2$), the transmission traces out a circle with a radius of 1 in the complex plane (cf. Fig. 5.2a). The transmission amplitude for Huygens' metasurfaces is always unity. However, the real part of the dipole-dipole lattice coupling and the isolated dipolar Mie angle determine the transmission phase angle. To span the full accessible phase angle, in Fig. 5.2b, we have plotted the phase-shift that is introduced in the forward direction as a function of the periodicity and the isolated dipolar Mie angle. Fixing the Mie angle or the periodicity while detuning the other parameter controls the phase shift of the transmitted field. In Section 5.4, we explore this capability of Huygens' metasurfaces.

In the next section, we explore the effect of induced quadrupole moments in the transmission and reflection of metasurfaces.

5.2 Quadrupolar metasurfaces

In this section, we explore metasurfaces that are only made from isotropic and non-absorbing quadrupolar meta-atoms, i.e., dipolar, octupolar, and other higher-order terms do not exist.
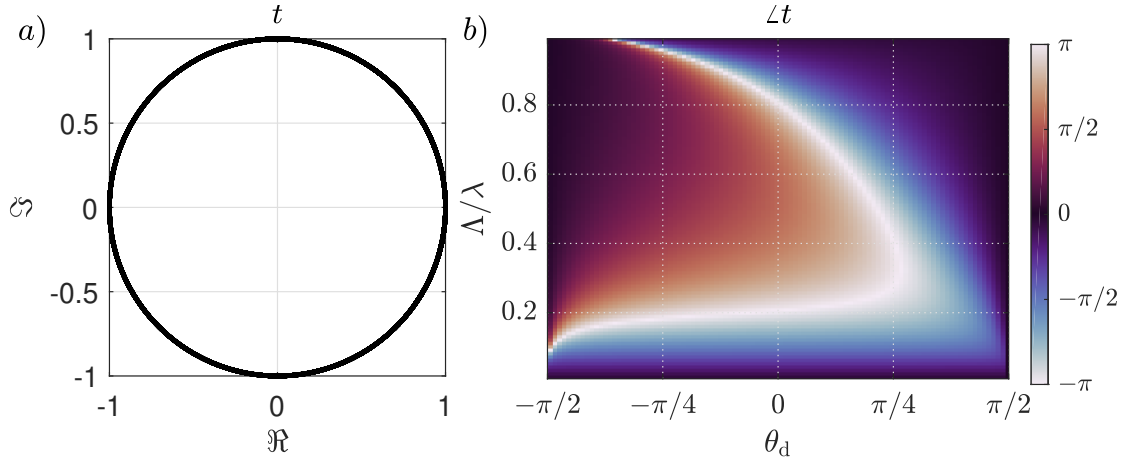
Figure 5.2: **Dipolar Huygens' metasurface:** a) The complex zeroth-order transmission of a dipolar Huygens' metasurface when sweeping through the full effective Mie angle region, i.e., $-\pi/2 \leq \theta_{\mathrm{d,eff}} \leq \pi/2$. The transmittance is always unity. b) The phase angle of the complex transmission coefficient of Huygens' dipolar metasurface as a function of the isolated dual dipolar Mie angle of the meta-atoms and the periodicity of the square array. The calculations are based on Eq. 5.9. Note that $a_1 = b_1$.

Transmission and reflection

Assuming a square-periodic arrangement of isotropic quadrupolar meta-atoms, using Eq. 4.39 and 4.40, the zeroth-order transmission and reflection for normally incident TE and TM excitation are derived as:

$$t_{\mathrm{TE}} = t_{\mathrm{TM}} = 1 - \frac{5}{4\pi\widetilde{\Lambda}^2}\left(a_{2,\mathrm{mod}} + b_{2,\mathrm{mod}}\right) = 1 - \frac{5}{4\pi\widetilde{\Lambda}^2}\left(\frac{a_2}{1 - \mathrm{i}a_2 C_{\mathrm{QQ}}} + \frac{b_2}{1 - \mathrm{i}b_2 C_{\mathrm{QQ}}}\right),$$

$$r_{\mathrm{TE}} = -r_{\mathrm{TM}} = \frac{5}{4\pi\widetilde{\Lambda}^2}\left(a_{2,\mathrm{mod}} - b_{2,\mathrm{mod}}\right) = \frac{5}{4\pi\widetilde{\Lambda}^2}\left(\frac{a_2}{1 - \mathrm{i}a_2 C_{\mathrm{QQ}}} - \frac{b_2}{1 - \mathrm{i}b_2 C_{\mathrm{QQ}}}\right),$$

$$(5.11)$$

where a_2 (b_2) is the electric (magnetic) quadrupolar Mie coefficients of the isolated spheres, $a_{2,\mathrm{mod}}$ ($b_{2,\mathrm{mod}}$) is the modulated electric (magnetic) quadrupolar Mie coefficients of the sphere inside the lattice (cf. Eq. 4.64-4.67), C_{QQ} is the quadrupole-quadrupole lattice coupling, and $\widetilde{\Lambda}$ is the normalized periodicity of the square/hexagonal lattice. Similar to the previous section, we only consider the TE response and, for simplicity, we denote them as t and r.

Effective Mie angles

Following a similar procedure as the previous section, the transmission and reflection for a periodic arrangement of non-absorbing and isotropic quadrupolar meta-atoms, modeled by the quadrupolar Mie angles θ_{E2} and θ_{M2}, can be written as:

$$
\begin{aligned}
t &= 1 - \frac{5}{4\pi\widetilde{\lambda}^2}\left(\frac{1}{1 - \mathrm{i}\tan\theta_{\mathrm{E2}} - \mathrm{i}C_{\mathrm{QQ}}} + \frac{1}{1 - \mathrm{i}\tan\theta_{\mathrm{M2}} - \mathrm{i}C_{\mathrm{QQ}}}\right) \qquad (5.12) \\
&= 1 - \cos\theta_{\mathrm{E2,eff}}\exp\left(\mathrm{i}\theta_{\mathrm{E2,eff}}\right) - \cos\theta_{\mathrm{M2,eff}}\exp\left(\mathrm{i}\theta_{\mathrm{M2,eff}}\right), \\
r &= \frac{5}{4\pi\widetilde{\lambda}^2}\left(\frac{1}{1 - \mathrm{i}\tan\theta_{\mathrm{E2}} - \mathrm{i}C_{\mathrm{QQ}}} - \frac{1}{1 - \mathrm{i}\tan\theta_{\mathrm{M2}} - \mathrm{i}C_{\mathrm{QQ}}}\right) \qquad (5.13) \\
&= \cos\theta_{\mathrm{E2,eff}}\exp\left(\mathrm{i}\theta_{\mathrm{E2,eff}}\right) - \cos\theta_{\mathrm{M2,eff}}\exp\left(\mathrm{i}\theta_{\mathrm{M2,eff}}\right),
\end{aligned}
$$
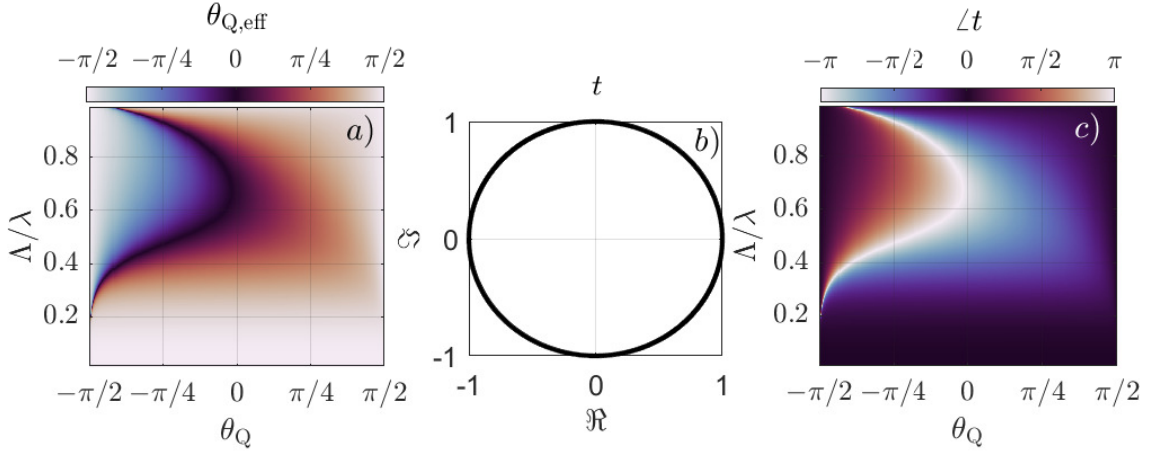
Figure 5.3: **Quadrupolar Huygens' metasurface:** a) The effective quadrupolar Mie angle as a function of the isolated quadrupolar Mie angle and the normalized periodicity of the lattice. b) The complex transmission coefficient of a quadrupolar metasurface when the effective quadrupolar Mie coefficient is swap through the whole accessible space. The transmittance is always unity. c) The phase angle of the transmission of a dual quadrupolar Huygens' metasurface (Eq. 5.16), as a function of the quadrupolar Mie angle and the normalized periodicity. Note that $a_2 = b_2$.

where $\theta_{\text{E2,eff}}$ ($\theta_{\text{M2,eff}}$) is the *effective electric (magnetic) quadrupolar Mie angle*, defined as:

$$\tan \theta_{\text{E2,eff}} = 4\pi \widetilde{\Lambda}^2 \left[\frac{\tan \theta_{\text{E2}} + \Re(C_{\text{QQ}})}{5} \right], \tag{5.14}$$

$$\tan \theta_{\text{M2,eff}} = 4\pi \widetilde{\Lambda}^2 \left[\frac{\tan \theta_{\text{M2}} + \Re(C_{\text{QQ}})}{5} \right]. \tag{5.15}$$

In Fig. 5.3a, we have plotted the general effective (electric or magnetic) quadrupolar Mie angle $\theta_{\text{Q,eff}}$, as a function of the isolated (electric or magnetic) quadrupolar Mie angle θ_{Q} and the periodicity of the 2D lattice.

Quadrupolar Huygens' metasurfaces

In case the quadrupolar electric and magnetic Mie coefficients are equal, i.e., $\theta_{\text{E2}} = \theta_{\text{M2}} = \theta_{\text{Q}}$, the transmission and reflection coefficients are derived as:

$$t = 1 - 2\cos\theta_{\text{Q,eff}} \exp\left(i\theta_{\text{Q,eff}}\right), \qquad r = 0. \tag{5.16}$$

Figure 5.3b shows the complex transmission and Fig. 5.3c shows the phase angle of the transmission through a quadrupolar Huygens' metasurface as a function of the Mie angle and the normalized periodicity. Compared with the dipolar Huygens' metasurface, the strong coupling region, i.e., where the phase shift is strongest ($|\angle t| > \pi/2$), falls in the larger periodicity region. This shows that the quadrupolar interactions are most substantial at slightly larger periods.

In the next section, we explore scenarios in which both dipolar and quadrupolar parts exist, and, hence, a richer response is expected.

5.3 Dipolar-quadrupolar metasurfaces

Only cases with no coupling among different multipole moments were considered in the previous sections. As a result, the scattered optical field was only coming from moments modulated by the lattice couplings. As discussed in Chapter 4, in a periodic lattice decorated with isotropic meta-atoms illuminated with a normally incident plane wave, the electric (magnetic) dipole moments are coupled to the magnetic (electric) quadrupole moments. This coupling provides a more complicated but richer optical response that we will explore in the following sections.

Assuming a square-periodic arrangement of isotropic dipolar-quadrupolar meta-atoms, using Eq. 4.39 and 4.40, the zeroth-order transmission and reflection for normally incident TE and TM excitation are derived as:

$$t_{\text{TE}} = t_{\text{TM}} = 1 - \frac{1}{4\pi\widetilde{\Lambda}^2}\left(3a_{1,\text{mod}}^{b_2} + 3b_{1,\text{mod}}^{a_2} + 5a_{2,\text{mod}}^{b_1} + 5b_{2,\text{mod}}^{a_1}\right), \quad (5.17)$$

$$r_{\text{TE}} = -r_{\text{TM}} = \frac{-1}{4\pi\widetilde{\Lambda}^2}\left(3a_{1,\text{mod}}^{b_2} - 3b_{1,\text{mod}}^{a_2} - 5a_{2,\text{mod}}^{b_1} + 5b_{2,\text{mod}}^{a_1}\right), \quad (5.18)$$

where $a_{1,\text{mod}}^{b_2}/b_{1,\text{mod}}^{a_2}$ ($a_{2,\text{mod}}^{b_1}/b_{2,\text{mod}}^{a_1}$) is the coupled and modulated electric/magnetic dipolar (quadrupolar) Mie coefficient (cf. Eq. 4.56-4.59). For dual meta-atoms, i.e., $a_1 = b_1, a_2 = b_2$, the reflection is zero and the transmission ($t = t_{\text{TE}} = t_{\text{TM}}$) is:

$$t = 1 - \frac{2}{4\pi\widetilde{\Lambda}^2}\left(\frac{3a_{1,\text{mod}} + 5a_{2,\text{mod}} + 2\sqrt{15}C_{\text{dQ}}a_{1,\text{mod}}a_{2,\text{mod}}}{1 + C_{\text{dQ}}^2 a_{2,\text{mod}}a_{1,\text{mod}}}\right). \quad (5.19)$$

The equation above shows a more complex response. The following section explores the phase-shift coverage that Huygens' metasurfaces can provide while maintaining the unity transmittance.

5.4 Phase-shift coverage

Non-absorbing Huygens' metasurfaces provide unity transmittance while simultaneously allowing control over the transmission phase angle. This feature makes Huygens' metasurfaces a promising candidate for holograms, for which a high transmittance efficiency and complete control over the phase-shift of the transmitted field is required. This section explores the accessible transmission phase angle in different Huygens' metasurfaces.

Dipolar Huygens' metasurfaces, i.e., metasurfaces with equally excited dipolar electric and magnetic Mie coefficients, cover 2π phase shift in transmission by tuning the wavelength through the whole resonance (cf. Fig. 5.2a). To show this more clearly, in Fig. 5.4, we have simulated a dipolar Huygens' metasurface made from meta-atoms characterized by a Lorentzian dispersion profile (cf. Eq. 3.59-3.60). The amplitude and phase angle of the modeled dipolar Mie coefficient $a_1 = b_1 = a_{\text{d}}$ are shown in Fig. 5.4a. In Fig. 5.4b, the real and imaginary parts of the transmission are plotted, and in Fig. 5.4c, the amplitude and phase angle of the transmission as a function of the operating wavelength are shown. The figure shows that complete phase-shift coverage of 2π is reached while the unity transmittance is preserved.
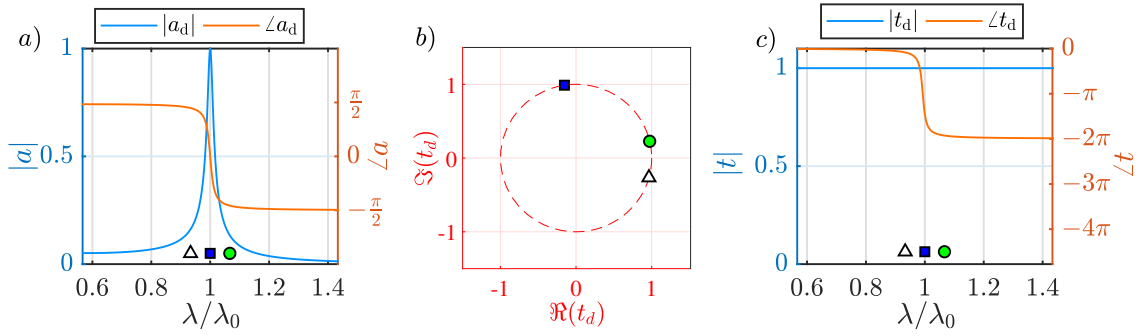
Figure 5.4: **Phase-shift coverage of a dipolar Huygens' metasurface [31]:** a) The amplitude and phase angle of a dipolar Mie coefficient $a_1 = b_1 = a_d$ modeled with a Lorentzian dispersion (cf. Eq. 3.55-3.56). b) The zeroth-order complex transmission t_d, c) its phase angle $\arg(t_d)$, and amplitude $|t_d|$ through a square-periodic sub-wavelength arrangement of the dual dipoles ($a_1 = b_1 = a_d$) as a function of the wavelength. The periodicity is 800 nm. The colored markers correspond to specific wavelengths, as can be seen from a) and c). The parameters for the Lorentzian model are: $\lambda_0 = \lambda_{0d} = 1500$ nm, $\alpha_{0d} = 8 \times 10^9$ m^3/s^2 (cf. Eq. 3.59-3.60). Adapted from Ref. [31] with permission from De Gruyter.

One step further, we study the higher-order multipoles in Huygens' metasurfaces and include the quadrupolar Mie coefficients into the equations. If a periodic arrangement of dual dipolar-quadrupolar meta-atoms is assumed, i.e. $a_1 = b_1 = a_d$, $a_2 = b_2 = a_Q$, the complex transmission t_{d+Q} as a function of the wavelength will be a double winding circle around the origin $0 + 0i$, covering an overall 4π phase shift through the four resonances. This feature is explored in Fig. 5.5 in which we have modeled the dipolar and quadrupolar Mie coefficients with a Lorentzian dispersion and have calculated the transmission.

However, metasurface-based holograms are not operated at various but a fixed wavelength. In other words, we want to have complete control over the local phase shift of the impinging wavefront at a specifically given wavelength. Therefore, the phase-shift coverage is possible by tuning the lattice constant of the arrangement. Each pixel of the metasurface should provide a different phase angle required for the hologram. Although these pixels have a finite dimension, here, we focus on infinitely periodic metasurfaces. In the next chapter, the question of finite metasurfaces is addressed. For now, it is enough to consider that for large enough pixels, we can approximate the response of a finite pixel to the response of an infinitely periodic metasurface.

To explore the phase-shift coverage of Huygens' metasurfaces with a lattice constant tuning, we have initially considered a metasurface made from meta-atoms at resonance, i.e., $a_1 = b_1 = 1$ for the dipolar case and $a_1 = b_1 = a_2 = b_2 = 1$ for the dipolar-quadrupolar case. In Fig. 5.6, we have calculated the transmission as a function of the normalized periodicity. It should be mentioned that the size of the meta-atom determines the lower limit of the periodicity. Here, to have a more realistic result, we have limited the normalized periodicity to a lower limit of $\Lambda_{\min} = 0.33\lambda$. We assume that a denser arrangement is not plausible due to the spatial extent of the meta-atoms.
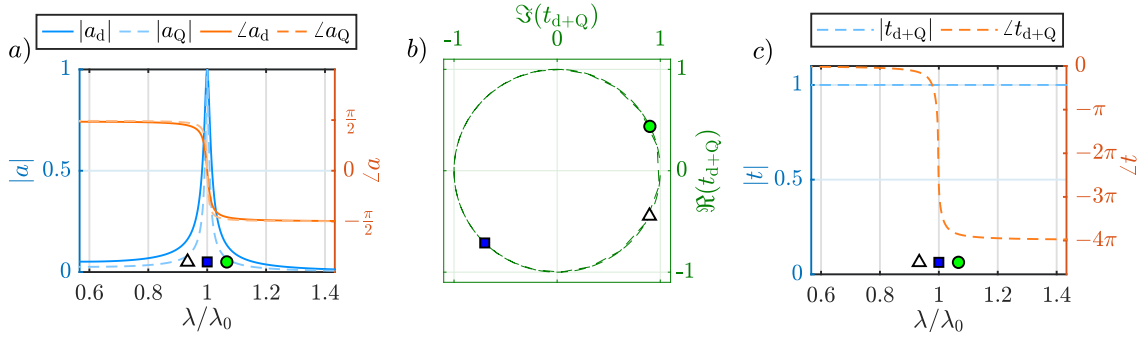
Figure 5.5: **Phase-shift coverage of a dipolar-quadrupolar Huygens' metasurface [31]:** a) The amplitude and phase angle of dual dipolar and dual quadrupolar Mie coefficients ($a_1 = b_1 = a_d$, $a_2 = b_2 = a_Q$) correspondingly modeled with a Lorentzian dispersion (cf. Eq. 3.55-3.58). b) The zeroth-order complex transmission t_{d+Q}, c) its phase angle $\arg(t_{d+Q})$, and amplitude $|t_{d+Q}|$ through a square-periodic sub-wavelength arrangement of the dual dipolar-quadrupolar Lorentzian meta-atoms as a function of the wavelength. The periodicity is 800 nm. The colored markers correspond to specific wavelengths, as can be seen from a) and c). The parameters for the Lorentzian model are: $\lambda_0 = \lambda_{0d} = \lambda_{0q} = 1500$ nm, $\alpha_{0q} = 10\alpha_{0d} = 8 \times 10^{10}$ m^3/s^2. Adapted from Ref. [31] with permission from De Gruyter.
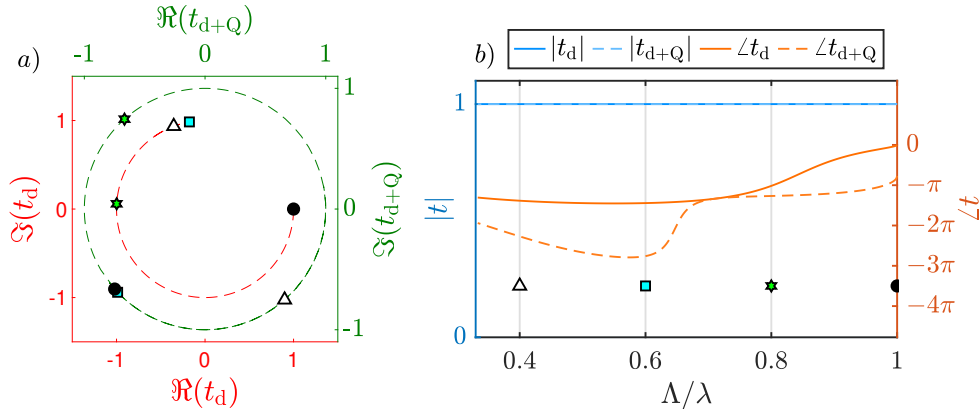
Figure 5.6: **Huygens' metasurfaces with different periodicities [31]:** a) The zeroth-order complex transmission, b) its phase angle, and amplitude through a square-array periodic sub-wavelength arrangement of dual dipolar (t_d) and dual dipolar-quadrupolar (t_{d+Q}) meta-atoms (cf. Fig. 5.5a) at their individual resonance wavelengths (i.e., $a_1 = b_1 = 1$ for t_d and $a_1 = a_2 = b_1 = b_2 = 1$ for t_{d+Q}) as a function of the normalized lattice constant. The colored markers correspond to a specific normalized lattice constant, as can be seen from b). Adapted from Ref. [31] with permission from De Gruyter.
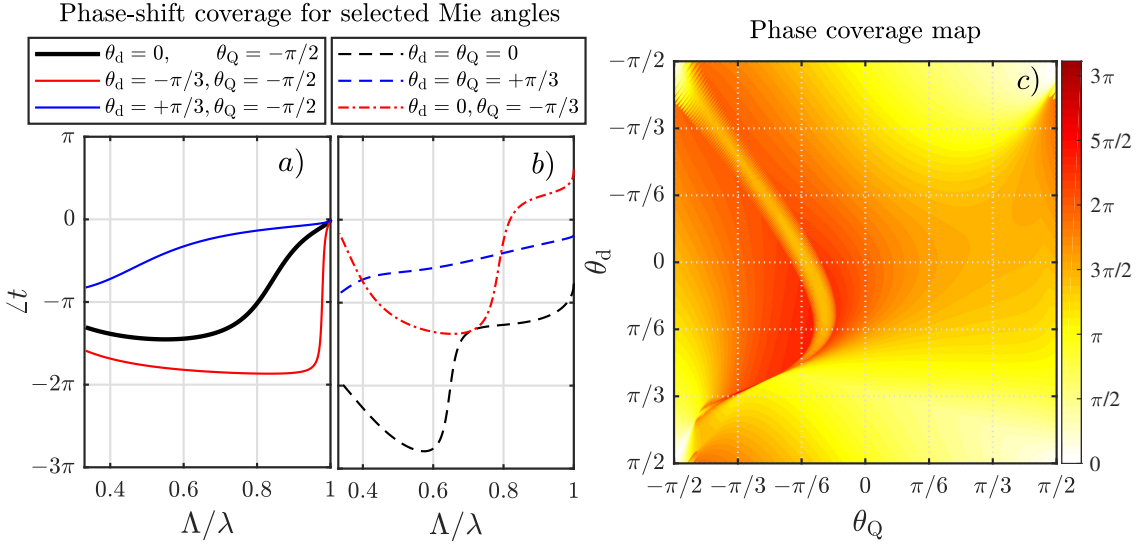
Figure 5.7: **Metasurface phase-shift coverage and the Mie coefficients [31]:** a) The phase shift achieved in a metasurface made from different combinations of dual Mie coefficient angles for dipolar and b) dipolar-quadrupolar meta-atoms as a function of the normalized lattice constant $\Lambda/\lambda \in [0.33, 1]$. c) The phase-shift coverage achieved in a metasurface by all combinations of dual Mie coefficient angles for dipolar-quadrupolar meta-atoms. The maximum phase-shift coverage is a sharp strip around $\theta_\mathrm{d} = -\theta_\mathrm{Q} = 50^o$. The simulations are done in free space at a wavelength of 1500 nm, but the results are only dependent on Λ/λ and are valid for any wavelength. Adapted from Ref. [31] with permission from De Gruyter.

As evident from Fig. 5.6, by tuning the lattice constant, the dipolar Huygens' metasurface does not provide a complete 2π phase-shift coverage. It can be shown that the maximum phase-shift coverage for a dipolar Huygens' metasurface is $3\pi/2$ [31]. On the other hand, from Fig. 5.6, we can observe that exploiting the quadrupolar resonances in the meta-atoms along with the dipolar resonances helps to cover the whole phase-shift range of 2π. However, the resonances' simultaneous existence with different ratios remains an open question, and we want to address it next.

To systematically search through all possible scenarios and go beyond the resonance condition assumed previously, we utilize the Mie angle method. To do so, in the first step, we model the dipolar and quadrupolar Mie coefficients with the dipolar ($\theta_\mathrm{d} = \theta_\mathrm{E1} = \theta_\mathrm{M1}$) and quadrupolar ($\theta_\mathrm{Q} = \theta_\mathrm{E2} = \theta_\mathrm{M2}$) Mie angles, respectively. In the next step, we simulate the transmission of a metasurface made from these meta-atoms with a periodicity range of $\Lambda/\lambda = [0.33, 1]$. For each Mie angle pair ($\theta_\mathrm{d}, \theta_\mathrm{Q}$), we identify the largest phase-shift coverage. Figure 5.7c shows the full phase-shift coverage map for all the Mie coefficient pair values. Figures 5.7a-b show the phase shift of the transmission for a few selected Mie angles. The maximum phase-shift coverage is a sharp strip around $\theta_\mathrm{d} = -\theta_\mathrm{Q} = 50^o$ and is above 3π, which is well beyond the required 2π coverage. As evident from the figure, there is a large area in which the desired 2π phase-shift coverage is reached. Therefore, a meta-atom satisfying any of the desirable Mie coefficient pairs can provide the complete phase-shift coverage in a metasurface made from the meta-atom.

In Ref. [31], exploiting the particle swarm optimization method, we have designed a core-shell sphere that provides the complete 2π phase-shift coverage in the meta-
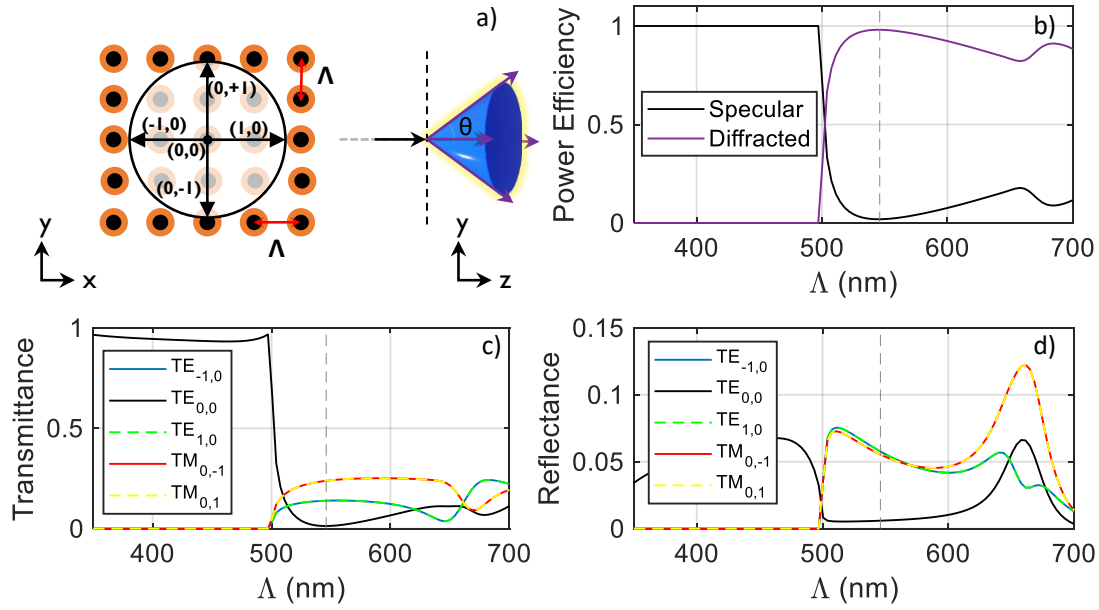
Figure 5.8: **Fully diffractive metagrating [75]:** a) A square array of core-shell spheres ($r_1 = 0.34\lambda$, $r_2 = (0.34 + 0.06)\lambda$, $n_1 = 1.86$, $n_2 = 1.43$) illuminated with a TE plane wave diffracts all the light to the first diffraction orders at a wavelength of $\lambda = 500\,\mathrm{nm}$. b) The normalized specular and diffracted power of the lattice as a function of the periodicity Λ. c) The transmittance and d) reflectance of the zeroth-order and diffracting modes of the lattice. The dashed line shows the periodicity where diffractions to $\theta = 64^o$ occur.

surface by tuning the periodicity. Furthermore, in the same reference, inspired by the core-shell results, we have designed a disk-ring meta-atom that provides full phase-shift coverage. For more technical discussions, the reader is motivated to read the article.

Here, it is worth noting that high transmittance non-resonant and non-Huygens' metasurfaces that can provide full phase-shift coverage are possible. In these metasurfaces, non-identical meta-atoms can be used [83, 84, 236–239]. Here, our focus is on resonant polarization-insensitive Huygens' metasurfaces made from identical isotropic meta-atoms.

In summary, we have utilized the analytical equations for the transmission and reflection of metasurfaces to explore the phase-shift coverage of Huygens' metasurfaces. Huygens' metasurfaces provide unity transmittance and zero reflection and, hence, are very suited for high-efficiency holography. In Ref. [31], we have explored how the added phase-shift coverage, enabled by higher-order meta-atoms, can improve the quality of hologram images. In the next section, we explore dipolar-quadrupolar metasurfaces that have a periodicity longer than the wavelength.

5.5 Metagratings

This section provides rigorous analytical expressions for the diffraction of light from metasurfaces and metagratings at normal incidence. A metagrating has wavelength-scale periodicities and can diffract light beyond the zeroth-order modes. Here, we

restrict ourselves, for brevity, to isotropic meta-atoms up to a quadrupolar order approximation. As an example, with the provided analytical expressions, we identify a metagrating that perfectly cancels the zeroth-order transmission and diffracts all the light to the four first-order diffractions.

The meta-atoms are assumed to be sufficiently described as an assortment of electric and magnetic dipoles or quadrupoles represented by their Mie coefficients a_1, a_2, b_1, b_2. From Eq. 4.39 and 4.40, reflection and transmission coefficients are derived as a function of the Mie coefficients of the individual nanoparticles and the lattice coupling matrix as:

$$t_{\mathrm{TE}_{0,0} \to \mathrm{TE}_{n_1,n_2}} = 1 - \frac{\cos\phi}{4\pi\widetilde{\Lambda}^2}\left(\frac{3a_{1,\mathrm{eff}}}{\cos\theta} + 3b_{1,\mathrm{eff}} + 5a_{2,\mathrm{eff}} + \frac{5\cos 2\theta b_{2,\mathrm{eff}}}{\cos\theta}\right), (5.20)$$

$$t_{\mathrm{TE}_{0,0} \to \mathrm{TM}_{n_1,n_2}} = \frac{\sin\phi}{4\pi\widetilde{\Lambda}^2}\left(3a_{1,\mathrm{eff}} + \frac{3b_{1,\mathrm{eff}}}{\cos\theta} + \frac{5\cos 2\theta a_{2,\mathrm{eff}}}{\cos\theta} + 5b_{2,\mathrm{eff}}\right), \quad (5.21)$$

$$t_{\mathrm{TM}_{0,0} \to \mathrm{TE}_{n_1,n_2}} = \frac{-\sin\phi}{4\pi\widetilde{\Lambda}^2}\left(\frac{3a_{1,\mathrm{eff}}}{\cos\theta} + 3b_{1,\mathrm{eff}} + 5a_{2,\mathrm{eff}} + \frac{5\cos 2\theta b_{2,\mathrm{eff}}}{\cos\theta}\right), \quad (5.22)$$

$$t_{\mathrm{TM}_{0,0} \to \mathrm{TM}_{n_1,n_2}} = 1 - \frac{\cos\phi}{4\pi\widetilde{\Lambda}^2}\left(3a_{1,\mathrm{eff}} + \frac{3b_{1,\mathrm{eff}}}{\cos\theta} + \frac{5\cos 2\theta a_{2,\mathrm{eff}}}{\cos\theta} + 5b_{2,\mathrm{eff}}\right), (5.23)$$

$$r_{\mathrm{TE}_{0,0} \to \mathrm{TE}_{n_1,n_2}} = \frac{\cos\phi}{4\pi\widetilde{\Lambda}^2}\left(\frac{3a_{1,\mathrm{eff}}}{\cos\theta} + 3b_{1,\mathrm{eff}} + 5a_{2,\mathrm{eff}} + \frac{5\cos 2\theta b_{2,\mathrm{eff}}}{\cos\theta}\right), \quad (5.24)$$

$$r_{\mathrm{TE}_{0,0} \to \mathrm{TM}_{n_1,n_2}} = \frac{\sin\phi}{4\pi\widetilde{\Lambda}^2}\left(3a_{1,\mathrm{eff}} + \frac{3b_{1,\mathrm{eff}}}{\cos\theta} + \frac{5\cos 2\theta a_{2,\mathrm{eff}}}{\cos\theta} + 5b_{2,\mathrm{eff}}\right), \quad (5.25)$$

$$r_{\mathrm{TM}_{0,0} \to \mathrm{TE}_{n_1,n_2}} = \frac{-\sin\phi}{4\pi\widetilde{\Lambda}^2}\left(\frac{3a_{1,\mathrm{eff}}}{\cos\theta} + 3b_{1,\mathrm{eff}} + 5a_{2,\mathrm{eff}} + \frac{5\cos 2\theta b_{2,\mathrm{eff}}}{\cos\theta}\right), \quad (5.26)$$

$$r_{\mathrm{TM}_{0,0} \to \mathrm{TM}_{n_1,n_2}} = \frac{\cos\phi}{4\pi\widetilde{\Lambda}^2}\left(3a_{1,\mathrm{eff}} + \frac{3b_{1,\mathrm{eff}}}{\cos\theta} + \frac{5\cos 2\theta a_{2,\mathrm{eff}}}{\cos\theta} + 5b_{2,\mathrm{eff}}\right), \quad (5.27)$$

where the effective Mie coefficients are calculated according to Eq. 4.56-4.59. Note that the angles θ and ϕ are the scattering angles of the propagating diffraction orders, derived from Eq. 4.38. Moreover, here, we only consider propagating modes, and evanescent field scattering is not considered.

The availability of analytical expressions is key to design metasurfaces with optical properties on demand. Here, we demonstrate the applicability by designing a metagrating that diffracts light only into $\theta=64^o$ degrees in the four possible directions (azimuth angles $\phi = 0^o, 90^o, 180^o, 270^o$ degrees) (cf. Fig. 5.8a). For each of the four branches, two different polarizations are possible, TE and TM. However, due to the isotropy of the constituents and lattice symmetry, some modes are zero. Here, we have assumed a TE polarized plane wave excitation at normal incidence.

As presented through the general expressions in Eq. 4.38, the diffraction angles (θ, ϕ) are uniquely determined by the diffraction order (n_1, n_2). Moreover, we want no other propagating modes except the first diffraction orders, i.e., $|n_1| + |n_2| = 1$. These two requirements set the required normalized periodicity to $\lambda/\Lambda = 1.12$. Next, using the expressions for the amplitudes of the diffraction orders and the Mie angle method [59], we systematically search through all possible Mie coefficients for regimes where the zeroth-order transmission is zero at the given periodicity. After identifying a set of Mie coefficients that cancels the zeroth-order transmission, we use
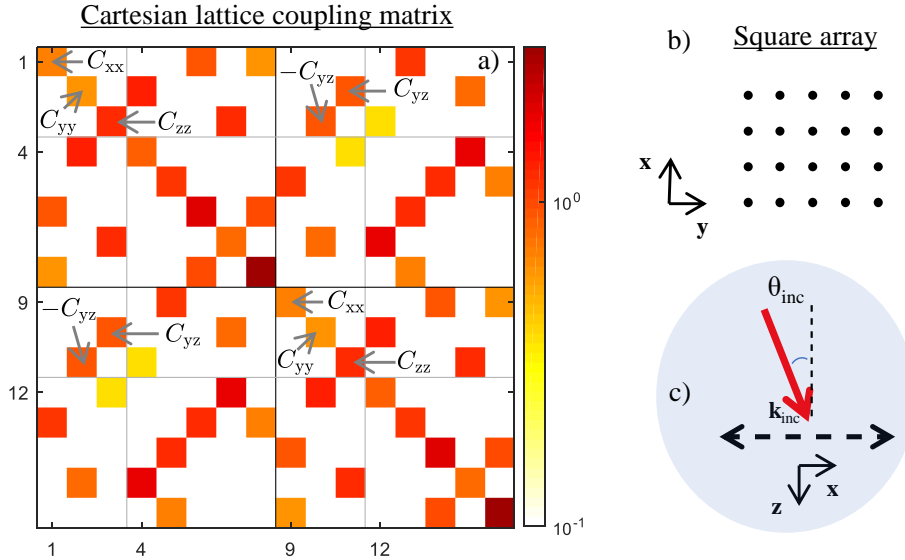
Figure 5.9: **Cartesian coupling matrix under oblique incidence [75]:** a) The Cartesian coupling matrix amplitude for a b) square array with a normalized periodicity of $\Lambda/\lambda = 0.5$, c) under oblique incidence ($\theta_{inc} = \pi/6, \phi_{inc} = 0$), up to a quadrupolar approximation. The relevant matrix entries for a metasurface made from dipolar isotropic meta-atoms are the parallel C_{xx} and C_{yy}, the perpendicular C_{zz}, and the oblique C_{yz} couplings. They are marked in the figure.

a particle swarm optimization method to find details of a core-shell sphere, namely dimensions and material parameters, that provide the required Mie coefficients.

In Fig. 5.8a, the outcomes from the design process are illustrated. Figure 5.8b shows that at the chosen periodicity $\Lambda = 1.12\lambda = 556\,\mathrm{nm}$, most of the power is diffracted, while Fig. 5.8c and d show the transmittance and reflectance of the individual modes. The reflectance and transmittance can be expressed as a function of reflection and transmission coefficients, respectively, as:

$$T = |t|^2 \frac{|\cos\theta|}{|\cos\theta_{inc}|}, \quad R = |r|^2 \frac{|\cos\theta|}{|\cos\theta_{inc}|}, \tag{5.28}$$

where for our case $\theta = 64^\circ$ and $\theta_{inc} = 0^\circ$. It is evident from the figure that the zeroth-order transmission and the zeroth-order reflection are successfully suppressed. Moreover, the reflected diffracted modes are much smaller than the transmitted ones.

Having the analytical equations at hand, different desired scattering scenarios can be explored. Our aim here was to provide a simple example for the diffraction of dipolar-quadrupolar metasurfaces. In the next section, we address the optical response of metasurfaces under oblique incidence.

5.6 Metasurfaces under oblique incidence

This section provides simplified equations for the zeroth-order transmission and reflection of a metasurface made from isotropic dipolar meta-atoms illuminated obliquely with a plane wave. In particular, dipolar Huygens' metasurfaces under oblique angles are explored. In the end, we also address the Brewster angle for single resonance metasurfaces.
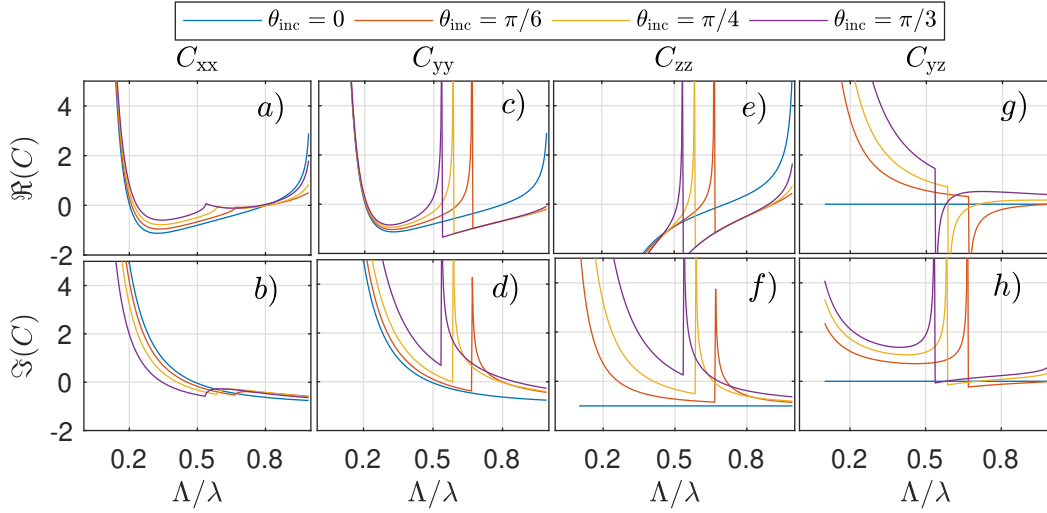
Figure 5.10: **The relevant Cartesian coupling matrix entries under oblique incidence:** a,c,e,g) The real and b,d,f,h) imaginary parts of the relevant lattice coupling matrix entries for a metasurface made from dipolar isotropic meta-atoms, as a function of the normalized periodicity Λ/λ, for few selected incident angles θ_{inc}. In all the figures $\phi_{\mathrm{inc}} = 0$. The relevant matrix entries for a metasurface made from dipolar isotropic meta-atoms are the parallel C_{xx} and C_{yy}, the perpendicular C_{zz}, and the oblique C_{yz} couplings.

The TE and TM plane-wave excitation for an oblique incidence are defined as:

$$\mathbf{E}_{\mathrm{TM}}^{\mathrm{inc}} = \begin{bmatrix} E_x \\ E_y \\ E_z \end{bmatrix} = E_0 \begin{bmatrix} \cos\theta_{\mathrm{inc}} \\ 0 \\ -\sin\theta_{\mathrm{inc}} \end{bmatrix} \mathrm{e}^{\mathrm{i}(k_x^{\mathrm{inc}}x + k_z^{\mathrm{inc}}z)}, \tag{5.29a}$$

$$\mathbf{E}_{\mathrm{TE}}^{\mathrm{inc}} = \begin{bmatrix} E_x \\ E_y \\ E_z \end{bmatrix} = E_0 \begin{bmatrix} 0 \\ 1 \\ 0 \end{bmatrix} \mathrm{e}^{\mathrm{i}(k_x^{\mathrm{inc}}x + k_z^{\mathrm{inc}}z)}, \tag{5.29b}$$

where $k_x^{\mathrm{inc}} = k\sin\theta_{\mathrm{inc}}$ and $k_z^{\mathrm{inc}} = k\cos\theta_{\mathrm{inc}}$ are the x and z component of the impinging wavevector. Under oblique incidence, there are less symmetry-protected zeros in the lattice coupling matrix, and, hence, there are more novel interference patterns to be explored. Figure. 5.9 shows the Cartesian lattice coupling matrix. The relevant dipolar coefficients are also identified and marked.

Assuming a square-periodic arrangement of dipolar Mie meta-atoms, using Eq. 4.39 and 4.40, the transmission and reflection for an obliquely incident TE and TM excitation are derived as:

$$t_{\mathrm{TE}} = 1 - \frac{3}{4\pi\widetilde{\Lambda}^2|\cos\theta_{\mathrm{inc}}|}\left(b_{1,\mathrm{mod.xx}}\cos\theta_{\mathrm{inc}}^2 + a_{1,\mathrm{mod.yy}}^{\overset{b_{zz}}{\frown}} + b_{1,\mathrm{mod.zz}}^{\overset{a_{yy}}{\frown}}\sin\theta_{\mathrm{inc}}^2\right), \tag{5.30}$$

$$t_{\mathrm{TM}} = 1 - \frac{3}{4\pi\widetilde{\Lambda}^2|\cos\theta_{\mathrm{inc}}|}\left(a_{1,\mathrm{mod.xx}}\cos\theta_{\mathrm{inc}}^2 + b_{1,\mathrm{mod.yy}}^{\overset{a_{zz}}{\frown}} + a_{1,\mathrm{mod.zz}}^{\overset{b_{yy}}{\frown}}\sin\theta_{\mathrm{inc}}^2\right), \tag{5.31}$$

$$r_{\mathrm{TE}} = \frac{3}{4\pi\widetilde{\Lambda}^2|\cos\theta_{\mathrm{inc}}|}\left(b_{1,\mathrm{mod.xx}}\cos\theta_{\mathrm{inc}}^2 - a_{1,\mathrm{mod.yy}}^{\overset{b_{zz}}{\frown}} - b_{1,\mathrm{mod.zz}}^{\overset{a_{yy}}{\frown}}\sin\theta_{\mathrm{inc}}^2\right), \tag{5.32}$$

$$r_{\mathrm{TM}} = \frac{3}{4\pi\widetilde{\Lambda}^2|\cos\theta_{\mathrm{inc}}|}\left(a_{1,\mathrm{mod.xx}}\cos\theta_{\mathrm{inc}}^2 - b_{1,\mathrm{mod.yy}}^{\overset{a_{zz}}{\frown}} - a_{1,\mathrm{mod.zz}}^{\overset{b_{yy}}{\frown}}\sin\theta_{\mathrm{inc}}^2\right), \tag{5.33}$$

where the terms in the parentheses are the effective dipolar Mie coefficients of the meta-atoms. These effective components depend on (a) the modulation of the elements with the coupling coefficients C_{xx}, C_{yy}, and C_{zz} and (b) the coupling with other multipole moments through the C_{yz} coefficient. The ⌣ shows the coupled parameters, and the coupling term is written inside the circle. Electric (magnetic) dipole moments are coupled to magnetic (electric) dipole moments. The *effective Mie coefficients* are expressed as:

$$\frac{1}{a_{1,\text{eff.yy}}} \;=\; \frac{1}{\overset{\frown}{\underset{a_{1,\text{mod.yy}}}{b_{zz}}}} = \frac{1 - C_{yz}^2 b_{1,\text{mod.zz}} a_{1,\text{mod.yy}}}{a_{1,\text{mod.yy}}\left(1 - C_{yz} b_{1,\text{mod.zz}} \sin\theta_{\text{inc}}\right)}, \tag{5.34}$$

$$\frac{1}{b_{1,\text{eff.yy}}} \;=\; \frac{1}{\overset{\frown}{\underset{b_{1,\text{mod.yy}}}{a_{zz}}}} = \frac{1 - C_{yz}^2 b_{1,\text{mod.yy}} a_{1,\text{mod.zz}}}{b_{1,\text{mod.yy}}\left(1 - C_{yz} a_{1,\text{mod.zz}} \sin\theta_{\text{inc}}\right)}, \tag{5.35}$$

$$\frac{1}{a_{1,\text{eff.zz}}} \;=\; \frac{1}{\overset{\frown}{\underset{a_{1,\text{mod.zz}}}{b_{yy}}}} = \frac{1 - C_{yz}^2 b_{1,\text{mod.yy}} a_{1,\text{mod.zz}}}{a_{1,\text{mod.zz}}\left(1 - C_{yz} \csc\theta_{\text{inc}} b_{1,\text{mod.yy}}\right)}, \tag{5.36}$$

$$\frac{1}{b_{1,\text{eff.zz}}} \;=\; \frac{1}{\overset{\frown}{\underset{b_{1,\text{mod.zz}}}{a_{yy}}}} = \frac{1 - C_{yz}^2 b_{1,\text{mod.zz}} a_{1,\text{mod.yy}}}{b_{1,\text{mod.zz}}\left(1 - C_{yz} \csc\theta_{\text{inc}} a_{1,\text{mod.yy}}\right)}, \tag{5.37}$$

and the *modulated Mie coefficients* are:

$$\frac{1}{b_{1,\text{mod.xx}}} = \frac{1}{b_1} - iC_{xx} \quad , \quad \frac{1}{b_{1,\text{mod.zz}}} = \frac{1}{b_1} - iC_{zz}, \tag{5.38}$$

$$\frac{1}{b_{1,\text{mod.yy}}} = \frac{1}{b_1} - iC_{yy} \quad , \quad \frac{1}{a_{1,\text{mod.xx}}} = \frac{1}{a_1} - iC_{xx}, \tag{5.39}$$

$$\frac{1}{a_{1,\text{mod.yy}}} = \frac{1}{a_1} - iC_{yy} \quad , \quad \frac{1}{a_{1,\text{mod.zz}}} = \frac{1}{a_1} - iC_{zz}. \tag{5.40}$$

Note that in the above equations, without losing generality, we have assumed $\phi_{\text{inc}} = 0$. The real and imaginary parts of the relevant lattice coupling coefficients as a function of the normalized periodicity, for a few selected incident angles, are shown in Fig. 5.10. The imaginary parts of the lattice couplings can be determined following a similar approach for the normal case in Chapter. 4. There might be very sharp features near a diffraction point that might not have been captured in the figures. Here, we focus our analysis on the zeroth-order transmission and reflection before the onset of diffraction orders.

5.6.1 Huygens' metasurface under oblique incidence

In this subsection, we assume equal electric and magnetic Mie coefficients (i.e., $a_1 = b_1 = a$) and explore the optical response of a subwavelength dipolar Huygens' metasurface. From Eq. 4.39 and 4.40, the transmission and reflection can be simplified as:

$$t_{\text{TE}} = t_{\text{Tm}} = 1 - \frac{3}{4\pi\widetilde{\Lambda}^2|\cos\theta_{\text{inc}}|}\left(a_{\text{mod.xx}}\cos\theta_{\text{inc}}^2 + \overset{\frown}{a_{\text{mod.yy}}^{a_{zz}}} + \overset{\frown}{a_{\text{mod.zz}}^{a_{yy}}}\sin\theta_{\text{inc}}^2\right), \tag{5.41}$$

$$r_{\text{TM}} = r_{\text{TM}} = \frac{3}{4\pi\widetilde{\Lambda}^2|\cos\theta_{\text{inc}}|}\left(a_{\text{mod.xx}}\cos\theta_{\text{inc}}^2 - \overset{\frown}{a_{\text{mod.yy}}^{a_{zz}}} - \overset{\frown}{a_{\text{mod.zz}}^{a_{yy}}}\sin\theta_{\text{inc}}^2\right). \tag{5.42}$$
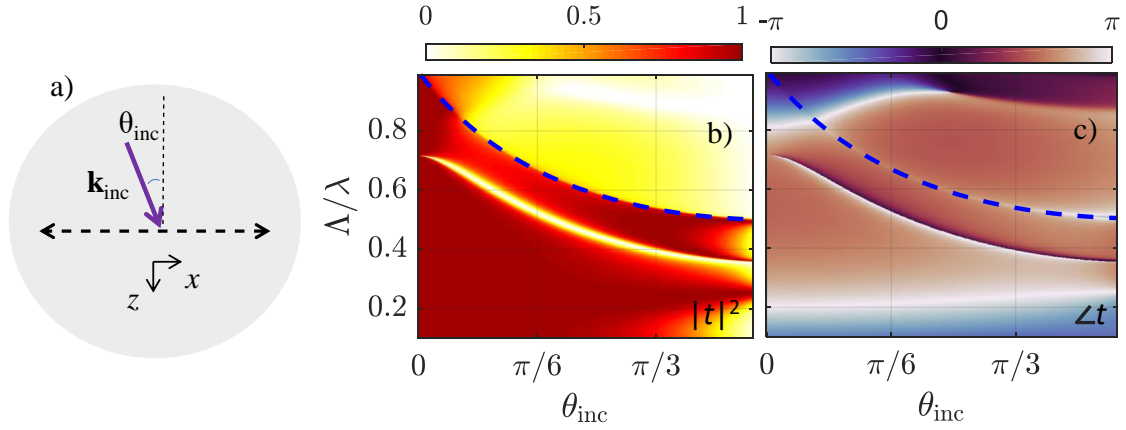
Figure 5.11: **Obliquely illuminated Huygens' metasurfaces [75]:** a) A Huygens' metasurface under TE polarized oblique plane wave incidence θ_{inc} in the z-x plane (i.e., $\phi_{inc} = 0$). b) The transmittance and c) phase angle of the zeroth-order transmission coefficient of a Huygens' metasurface as a function of the incident angle θ_{inc} and the normalized periodicity Λ/λ. The metasurface is made from meta-atoms with $a = a_1 = b_1 = 1$. The dashed blue line indicates the onset of diffraction orders. Note that for a Huygens' metasurface, the TE and TM excitations are equivalent.

Two points can be directly inferred from the above equations: 1) The TE and TM response is the same for a Huygens' metasurface, and 2) unlike the normal incidence case, under oblique incidence, the reflection is not necessarily zero.

In Fig. 5.11, we have simulated the transmission of a dipolar Huygens' metasurface made from resonant Mie meta-atoms (i.e., $a = a_1 = b_1 = 1$) illuminated with a TE polarized obliquely incident plane wave. Although the metasurface is made from dual meta-atoms and is dual itself, the backscattering does not vanish anymore. This is due to the broken discrete rotational symmetry. Indeed, as evident from Fig. 5.11b, if the incidence is only slightly tilted at a normalized periodicity of 0.71, a sharp resonance appears in the transmittance of the metasurface. This resonance can be traced back to the destructive interference of the in-plane and out-of-plane induced moments. The metasurface still preserves the helicity of the scattered light. However, the first Kerker condition is not necessarily satisfied.

Another feature explored is the phase-shift coverage of the dipolar Huygens' metasurfaces under oblique incidence. For those currently chosen Mie coefficient values ($a_1 = b_1 = 1$), it is apparent from the results in Fig. 5.11c, that for small oblique incidence (i.e., $\theta_{inc} < \pi/6$), the broad phase-shift coverage range (i.e., $\Delta(\angle t) > \pi$) falls, primarily, into the regime for which the metasurface is diffracting, and, hence, the transmission is suppressed. Therefore, a careful analysis of the complex interference relations is needed for better phase-shift coverage with high transmittance under oblique incidence. The equations provided in this section give the analytical tools required for such investigation. They can be exploited to design Huygens' metasurfaces for specific applications, avoiding certain undesired operation points.

5.6.2   Brewster angle

Polarization is a crucial property of light and its control is a fundamental necessity for wave modulation [240–242]. The Brewster angle is the illumination angle at
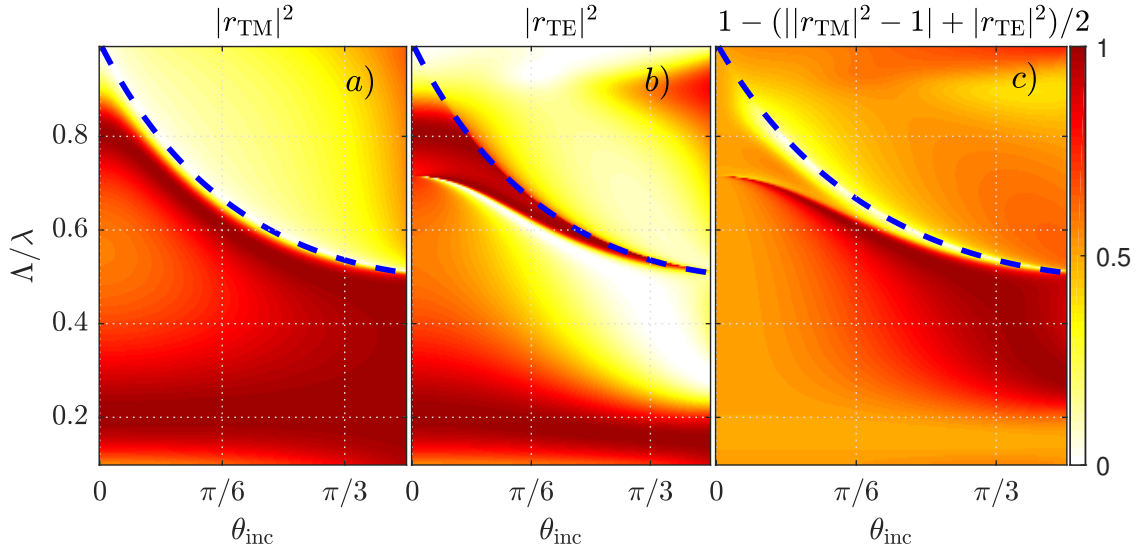
Figure 5.12: **Oblique reflection of periodic resonant magnetic dipoles:** a) Zeroth-order reflection from a square-array periodic arrangement of resonant magnetic dipoles ($b_1 = 1$) under a TE and b) TM obliquely incident plane wave illumination as a function of the incident angle θ_{inc} ($\phi_{\text{inc}} = 0$) and the normalized periodicity Λ/λ. c) The Brewster angle efficiency of the metasurface.

which the reflection for either TM or TE polarization vanishes and helps separate the two polarizations. In this subsection, we explore the possibility of finding the Brewster angle for a metasurface made from meta-atoms sustaining only a single resonance. Although in Ref. [240], the Brewster angle is realized when a certain ratio of the electric and magnetic dipole moment strength holds, here, we show that even a single resonance is enough to realize zero-reflection for either of the polarizations. We assume a metasurface consisting of only isotropic magnetic dipolar scatterers with vanishing other Mie coefficients, i.e., $a_{j>0} = b_{j>1} = 0$. Magnetic dipoles constitute the lowest-energy resonance sustained by homogeneous high-refractive-index spheres and are easier to achieve. From Eq. 5.30-5.33, the reflection coefficients for such a metasurface are derived as:

$$r_{\text{TE}} = \frac{3}{4\pi \widetilde{\Lambda}^2 |\cos \theta_{\text{inc}}|} \left(b_{1,\text{mod.xx}} \cos \theta_{\text{inc}}^2 - b_{1,\text{mod.zz}} \sin \theta_{\text{inc}}^2 \right), \quad (5.43)$$

$$r_{\text{TM}} = \frac{3}{4\pi \widetilde{\Lambda}^2 |\cos \theta_{\text{inc}}|} \left(-b_{1,\text{mod.yy}} \right). \quad (5.44)$$

In Fig. 5.12, we have calculated the reflection from a metasurface made from meta-atoms with $b_1 = 1, a_{n>0} = b_{n>1} = 0$. As evident from the figure, in the non-diffracting region, r_{TE} can be suppressed for a wide incident angle region, while r_{TM} can simultaneously stay near unity.

To determine all possible Brewster angles, we utilize the Mie angle method. To have zero TE reflection, i.e., $r_{\text{TE}} = 0$, the following equation needs to be solved:

$$b_{1,\text{mod.xx}} \cos \theta_{\text{inc}}^2 = b_{1,\text{mod.zz}} \sin \theta_{\text{inc}}^2, \quad (5.45)$$

$$\frac{\cos \theta_{\text{inc}}^2}{1 - \mathrm{i} \tan \theta_{\text{M1}} - \mathrm{i} C_{\text{xx}}} = \frac{\sin \theta_{\text{inc}}^2}{1 - \mathrm{i} \tan \theta_{\text{d}} - \mathrm{i} C_{\text{zz}}}, \quad (5.46)$$
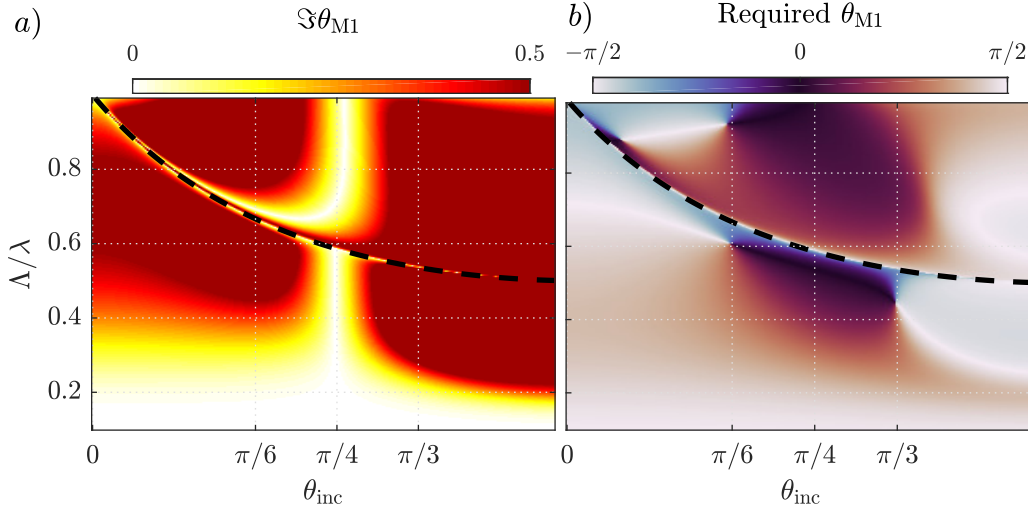
Figure 5.13: **Required Mie angle for Brewster angle realization:** a) The imaginary and b) real part of the magnetic Mie angle derived from Eq. 5.47 as a function of the incident angle θ_{inc} ($\phi_{\mathrm{inc}} = 0$) and the normalized periodicity Λ/λ.

and the magnetic dipolar Mie angle $\tan\theta_{\mathrm{M1}}$ can be derived as:

$$\tan\theta_{\mathrm{M1}} = \sin\theta_{\mathrm{inc}}^2 C_{\mathrm{xx}} - \cos\theta_{\mathrm{inc}}^2 C_{\mathrm{zz}} + \mathrm{i}\cos 2\theta_{\mathrm{inc}}. \tag{5.47}$$

To have a valid Mie angle, the expression on the right needs to be real-valued, i.e., $\Im\theta_{\mathrm{M1}} = 0$. In Fig. 5.13b, we have plotted the derived $\Re\theta_{\mathrm{M1}}$ required to make the above equation zero. In Fig. 5.13a the imaginary part of the derived Mie angle is plotted. The results in part b are valid when the imaginary part is zero. As evident from Fig. 5.13a, there is a broad region in which the imaginary part if zero, and, hence, the Brewster angle is realizable. Interestingly, around an incident angle $\theta_{\mathrm{inc}} = \pi/4$, there is a wide periodicity range into which the imaginary part of the magnetic dipolar Mie angle is zero. In the following, we only consider $\theta_{\mathrm{inc}} = \pi/4$.

At an incident angle of 45° degrees, Eq. 5.46 becomes independent of the Mie angle, and the requirement for a Brewster angle realization reduces to:

$$C_{\mathrm{xx}}\left(\theta_{\mathrm{inc}} = \pi/4, \phi_{\mathrm{inc}} = 0, \widetilde{\Lambda}\right) = C_{\mathrm{zz}}\left(\theta_{\mathrm{inc}} = \pi/4, \phi_{\mathrm{inc}} = 0, \widetilde{\Lambda}\right), \tag{5.48}$$

where, for clarity, we have shown the arguments in the parenthesis. The only degree of freedom to solve the above equation is the lattice constant. Tuning the lattice constants, we find out that for a Brewster angle of 45° degrees, the required lattice constant is:

$$\frac{\Lambda_{\theta_{\mathrm{B}}=\pi/4}}{\lambda} = 0.5352, \tag{5.49}$$

which is smaller than the dimension where the first diffraction order appears for this incidence angle (i.e., $\widetilde{\Lambda} = 0.58$) and, hence, the result is valid.

Therefore, a metasurface at a normalized periodicity of 0.5352 suppresses the reflection for TE polarization as far as the spheres are small enough compared to the operational wavelength to be described with a magnetic dipole moment only. The reflected amplitude for the other polarization can be determined via Eq. 5.44 by the strength of the effective magnetic Mie coefficient. A similar Brewster angle can be

derived to suppress reflection for the TM polarization, i.e., the s-polarization, with a metasurface made from electric dipolar particles at the same normalized periodicity point of operation.

In summary, in this section, we have explored the optical response of metasurfaces with dipolar and isotropic meta-atoms under oblique illuminations. In particular, dipolar Huygens' metasurfaces were investigated. Furthermore, we have analyzed the realization of Brewster angle in single resonance metasurfaces.

To summarize the chapter, we have provided analytical closed-form equations for the optical scattering of metasurfaces made from isotropic meta-atoms illuminated by a plane wave excitation. Our analytical equations go beyond the expressions available in the literature and describe zeroth-order and propagating diffraction modes and the response of obliquely incident metasurfaces. In particular, we have extensively explored Huygens' metasurfaces.

Moreover, the analytical tools provide in-depth insights into the physics of the metasurfaces. We have discussed different interconnected concepts like zero backscattering, Kerker conditions, duality symmetry, helicity preservation, etc., through multiple examples. In addition, we have shown the power of analytical tools to design practical metasurfaces for specific applications.

In the next chapter, we study the effect of positional disorder on the optical response of metasurfaces.

6. Disordered Metasurfaces

This section explores the optical response of disordered metasurfaces made from identical, dual, non-absorbing, and dipolar meat-atoms illuminated at resonance with a normally incident plane wave. The optical response includes the zeroth-order transmission and reflection, the induced effective dipole moments, and the directional *scatterance*. We use the term scatterance, i.e., the capacity to scatter, as a hypernym for *transmittance* and *reflectance* to general directions and as a unification of the half-spaces [38]. The specific assumptions held facilitates a systematic study of disordered metasurfaces.

The disorder that we refer to in this chapter is limited to *positional disorder* in the arrangement of meta-atoms. Moreover, the position of the meta-atoms considered are time-independent.

In the first section, we introduce statistical measures such as *configurational entropy*, *structure factor*, and *pair correlation function* for disordered arrangements and study different *point processes*. A 2D spatial point process, as used here, is a stochastic algorithm that realizes a disorder model, i.e., a *point configuration*, as a set of *events* (i.e., points) on the 2D surface. In statistics, the term event is used instead of a point so that arbitrary points in the space are not confused with the position of the actual points [243]. However, here, we use the term meta-atom, as point-like scatterers, instead of an event as it perfectly matches our setup.

In section 6.2, we introduce several disorder models and study their statistical characteristics. In section 6.3, the zeroth-order reflection from finite-size periodic metasurfaces as compared to the infinitely periodic metasurfaces are studied. We identify suitable parameters for reliable simulation of scatterance from a disordered metasurface.

Section 6.4 explores the zeroth-order transmission and reflection from disordered arrangements and the induced effective moments in the meta-atoms. In particular, we discuss an intriguing phenomenon in disordered arrangements, i.e., a *disorder-induced phase transition* that occurs at a critical disorder. At this point of operation, the zeroth-order reflection and transmission vanish and redistributes light from specular directions across all diffuse directions.

Light diffusion is explored in the last section, where we calculate the directional scatterance of different disordered metasurfaces and identify regimes where smooth and gloss-free diffusion is achievable.

The content of this chapter is based on our works in Ref. [38, 101].

6.1   Statistical measures

A periodic point configuration, i.e., a crystal, can be fully described by its base vectors. However, a disordered arrangement or point configuration needs an infinite number of positions to be fully characterized. Saving an infinite number of locations does not sound logical. For this reason, we use statistical parameters to statistically represent or characterize disordered arrangements [93].

An ensemble of disordered meta-atoms can be statistically characterized by a probability density function for each meta-atom. These functions determine the probability of finding other meta-atoms in the neighborhood of each meta-atom. In our analysis, we consider statistically homogenous ensembles, in which, statistically, the average density of meta-atoms per unit area is equal. In other words, the ensemble is statistically translation invariant. This assumption allows us to define correlation functions that depend only on the relative positions. The pair correlation function, which only considers the relative distance of two particles, is the most prominent measure for a disordered system. As we will show, the pair correlation function contains direct observation evidence about the atomic arrangement in condensed matter [93]. The statistical homogeneity does not imply equal optical response of meta-atoms when illuminated with an electromagnetic wave. However, it provides an excellent qualitative description of the optical scattering from a disordered arrangement.

In the following subsection, we assume the equal response of meta-atoms in disordered meta-atoms to derive the structure factor of a point configuration. Later, we also introduce configurational entropy as another statistical measure to characterize disordered arrangements.

6.1.1   Structure factor and pair correlation function

We consider an aggregate of N radiating meta-atoms arranged on a surface embedded in a homogenous and non-absorbing medium characterized by a wavenumber k. The meta-atoms are located at $\mathbf{R}_n = (x_n, y_n, z_n)$, where $n = 1, 2, ..., N$. The average particle density is $\rho = N/A$, where A is the extent of the ensemble. In the far-field, the vector spherical harmonics behave like spherical waves [48]. As a result, the far-field scattering of such an ensemble can be written as a sum over the scattering of all the meta-atoms (cf. Eq. 2.67):

$$\mathbf{E}\left(\mathbf{r}, \omega\right) \approx \sum_{n=1}^{N} \frac{\boldsymbol{f}_{\text{eff},n}\left(\theta, \phi, \omega\right)}{\mathbf{k}_n\left(\omega\right) \cdot \left(\mathbf{r} - \mathbf{R}_n\right)} e^{\mathbf{i}\mathbf{k}_n(\omega)\cdot(\mathbf{r}-\mathbf{R}_n)}, \qquad (6.1)$$

where $\mathbf{k}_n = k\hat{\mathbf{R}}_{\mathbf{r}-\mathbf{R}_n}$ is the wavevector pointing from meta-atom n to the collection point $\mathbf{r}$, and $\boldsymbol{f}_{\text{eff},n}\left(\theta, \phi, \omega\right)$ is the effective form factor for meta-atom n, describing the angular optical scattering of the meta-atom inside the lattice (cf. Eq. 2.67).

In the following, we assume that the meta-atoms are identical, and that the scattering is so weak that the effective response is equal to the isolated response, i.e. $\boldsymbol{f}_{\text{eff},n}(\mathbf{r},\omega) = \boldsymbol{f}(\theta,\phi,,\omega)$. This vanishing coupling regime is known as the *Born approximation*. For very large distances $r \to \infty$, we can further assume that $\mathbf{k}_n(\omega) \approx k(\omega)\hat{\mathbf{r}}$ and $\mathbf{k}_n(\omega) \cdot (\mathbf{r} - \mathbf{R}_n) \approx k(\omega) r$. Therefore, the far-field radiation under Born approximation can be written as:

$$\mathbf{E}(\mathbf{r},\omega) = \frac{\boldsymbol{f}(\theta,\phi,\omega)}{k(\omega)r} \sum_{n=1}^{N} e^{i\mathbf{k}(\omega)\cdot(\mathbf{r}-\mathbf{R}_n)}. \tag{6.2}$$

From Eq. 6.2, the far-field intensity of the ensemble can be expressed as:

$$I(\mathbf{r},\omega) = \frac{\mathbf{E}(\mathbf{r},\omega)\cdot\mathbf{E}^*(\mathbf{r},\omega)}{2Z(\omega)} = \frac{|\boldsymbol{f}(\theta,\phi,\omega)|^2}{2Z(\omega)} \sum_{n=1}^{N} e^{i\mathbf{k}(\omega)\cdot(\mathbf{r}-\mathbf{R}_n)} \sum_{n'=1}^{N} e^{-i\mathbf{k}(\omega)\cdot(\mathbf{r}-\mathbf{R}_{n'})}$$

$$= \frac{|\boldsymbol{f}(\theta,\phi,\omega)|^2}{2Z(\omega)} \sum_{n=1}^{N}\sum_{n'=1}^{N} e^{i\mathbf{k}(\omega)\cdot(\mathbf{R}_{n'}-\mathbf{R}_n)}. \tag{6.3}$$

From the above equation, we can see that the intensity is related to the sum involving the relative distance between the meta-atoms of the arrangement. The relative distance vector lies entirely in the x-y plane. Therefore, we can remove the perpendicular part of the wavevector and write:

$$I(\mathbf{r},\omega) = \frac{|f(\theta,\phi,\omega)|^2}{2Z(\omega)} \sum_{n=1}^{N}\sum_{n'=1}^{N} e^{-i2\pi\boldsymbol{\xi}(\omega)\cdot\mathbf{R}_{nn'}}, \tag{6.4}$$

where $2\pi\boldsymbol{\xi}(\omega) = \mathbf{k}_\|(\omega) = \mathbf{k}(\omega) - \mathbf{k}(\omega)\cdot\hat{\mathbf{z}}$ is the wavevector in the plane of the metasurface, and $\mathbf{R}_{nn'} = \mathbf{R}_n - \mathbf{R}_{n'}$ is the relative distance vector between a meta-atom pair. $\boldsymbol{\xi}(\omega)$ is the spatial frequency vector and is used to differentiate it from the optical wavevector.

The pattern above can also be experimentally observed and is directly linked to the pair-correlations of the ensemble. Therefore, it is straightforward to define a normalized parameter, called the *structure factor*, as:

$$S(\boldsymbol{\xi}) = \frac{1}{N} \sum_{n=1}^{N}\sum_{n'=1}^{N} e^{-i2\pi\boldsymbol{\xi}(\omega)\cdot\mathbf{R}_{nn'}} - \delta(\boldsymbol{\xi}), \tag{6.5}$$

where we have removed the point at the origin for a better interpretation.

Therefore, we can conclude that the intensity pattern of a disordered ensemble under the Born approximation, except the zeroth-order, is related to the structure factor times the form factor squared. The pair correlations directly determine the intensity pattern of an ensemble. In the following, we will define a series of parameters that we will use in the thesis. For a detailed discussion, refer to Ref. [38],

From the structure factor, the two-dimensional *pair correlation function* $g(\mathbf{r})$ of the ensemble can be expressed via Fourier transformations [244]:

$$g(\mathbf{r}) = 1 + \frac{1}{\rho} \int_{\mathbb{R}^2} [S(\boldsymbol{\xi}) - 1]\, e^{i2\pi\boldsymbol{\xi}\cdot\mathbf{r}} \mathrm{d}\boldsymbol{\xi}, \tag{6.6}$$

and, subsequently, the structure factor can be derived from the pair correlation function as:

$$S(\boldsymbol{\xi}) = 1 + \rho \int_{\mathbb{R}^2} [g(\mathbf{r}) - 1]\, e^{-\mathrm{i}2\pi\boldsymbol{\xi}\cdot\mathbf{r}} \mathrm{d}\mathbf{r}. \tag{6.7}$$

Lastly, the radial pair correlation function $g(r)$ and the radial structure factor $S(\xi)$ are the azimuthal averages of $g(\mathbf{r})$ and $S(\boldsymbol{\xi})$ and are defined as follows:

$$g(r) = \frac{1}{2\pi} \int_{-\pi}^{\pi} g(r\cos\phi\,\hat{\mathbf{x}} + r\sin\phi\,\hat{\mathbf{y}})\, \mathrm{d}\phi, \tag{6.8}$$

$$S(\xi) = \frac{1}{2\pi} \int_{-\pi}^{\pi} S(\xi\cos\phi\,\hat{\mathbf{x}} + \xi\sin\phi\,\hat{\mathbf{y}})\, \mathrm{d}\phi. \tag{6.9}$$

The pair correlation function reveals many properties of the ensemble. The distance beyond which the pair correlation function approximates to unity is defined as the range of local order [93]. Therefore, as long as the pair correlation function shows rippled patterns, the range of local order is longer. For periodic or ordered structures, this range tends to infinity, denoting long-range order. On the other extreme, for gasses, there are no ripples in their pair correlation function, showing the lack of any range of local order in gaseous environments. Liquids fall somewhere between gasses and crystals; They only show short-range order, and their correlation functions tend to unity beyond this range.

Furthermore, the *coordination number* of an ensemble is defined as the integral of the pair correlation function up to the first peak. This number denotes the overall first nearest neighbors of the meta-atoms [93].

6.1.2   Entropy

Another statistical measure that we calculate is the normalized *configurational entropy* of the local meta-atom density. In the calculation of these disorder metrics, we assumed circular bins centered around each meta-atom. For the calculation, we systematically alter the bin size, and, each time, the number of meta-atoms within the bin is counted. From these counts, the disorder metric is calculated. The normalized configurational entropy is defined as [93, 100]:

$$S\left(\widetilde{N}\right) = \frac{-1}{\log K\left(\widetilde{N}\right)} \sum_{n=1}^{N} p(n)\log[p(n)], \tag{6.10}$$

where $\widetilde{N}$ is the average number of meta-atoms counted inside the $K(\widetilde{N})$ circular bins of equal radius for all the N meta-atoms. For each bin radius, we exclude the meta-atoms on the edges where the circular bin comprising them exceeds the extent of the metasurface. $p(n)$ is the probability of having n meta-atoms in the bins. It is defined as $p(n) = \mathrm{count}(n)/K(\widetilde{N})$, with $\mathrm{count}(n)$ being the number of counts for n meta-atoms in the $K(\widetilde{N})$ bins considered for each bin radius. If the meta-atoms are ordered, i.e., the same number of meta-atoms falls into all the bins, irrespective of the bin size, then, the configurational entropy is zero for all $\widetilde{N}$.

Here, I want to acknowledge David Dams for suggesting configurational entropy as a measure for characterizing disordered arrangements. The following section introduces multiple disorder models and analyzes them with the measures developed in this section.
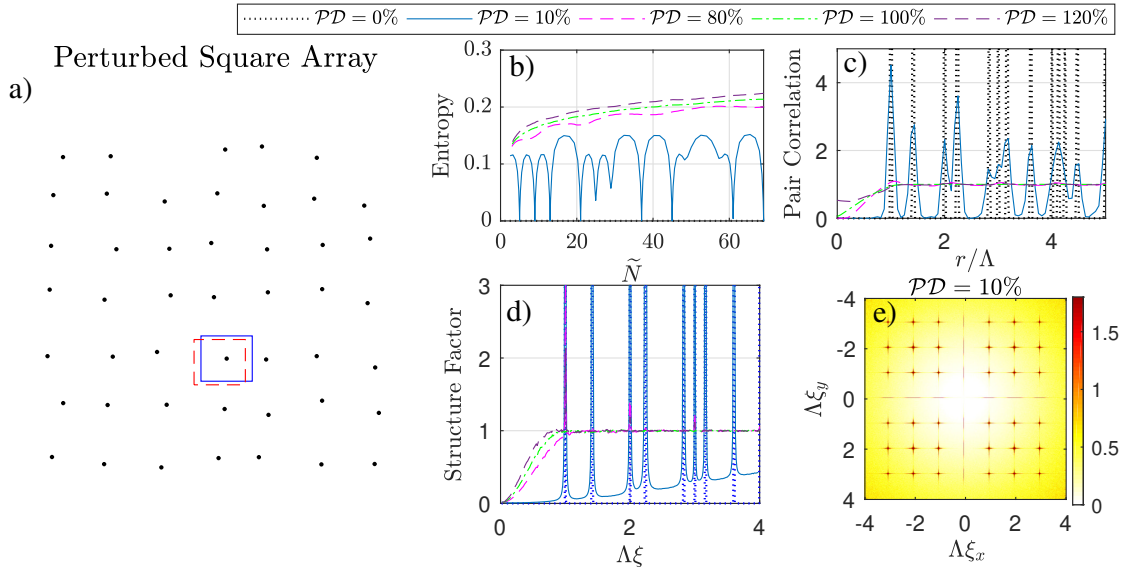
Figure 6.1: **Perturbed disorder:** a) A portion of a perturbed disorder point configuration for a positional disorder degree of $\mathcal{PD} = 30\%$. b) The configurational entropy as a function of the average meta-atom number $\widetilde{N}$, c) radial pair correlation as a function of the normalized pair distance r/Λ, and d) radial structure factor as a function of the normalized spatial frequency $\Lambda\xi$ for perturbed square arrays with 0%, 10%, 80%, 100% and 120% of positional disorder. e) The structure factor as a function of the normalized spatial frequency along x-axis $\Lambda\xi_x$ and y-axis $\Lambda\xi_y$ for a positional disorder degree of $\mathcal{PD} = 10\%$.

6.2 Models for the point configuration of 2D arrangements

This section introduces different types of disorder and analyzes each in light of the defined statistical measures.

For a reliable calculation of the statistical measures, a large enough number of meta-atoms needs to be considered. Here, for the entropy calculation, we have considered roughly 100×100 meta-atoms, while for the calculation of the pair correlation and structure factor, we have considered roughly 500×500 meta-atoms. For faster and smoother results for the latter, the ensemble is broken down to windows of 100×100 meta-atoms. These numbers of meta-atoms are enough to produce satisfying convergent and reliable results.

6.2.1 Perturbed disorder

The first intuitive introduction of disorder to an ordered system is to perturb its meta-atoms' location randomly. A perturbed 2D lattice is a point process in 2D obtained by displacing the meta-atoms of a lattice by a stochastic rule [245]. We start from a square-array periodic 2D lattice with a periodicity Λ. Centered at each lattice point, we define a square area with side lengths of $\Delta r = \mathcal{PD} \times \Lambda$ and a uniform independent probability density function, from which we draw the perturbed meta-atom coordinates. The aforementioned equation implicitly defines the degree of positional disorder as $\mathcal{PD} \in [0, 100]\%$. Therefore, we refer to this disorder type as *perturbed disorder* and measure its disorder strength by $\mathcal{PD}$. This type of positional

disorder is used very frequently in modeling disorder in optics [66, 101, 140, 246, 247], and is also called the *uniformly randomized lattice* [245] or *shuffled lattice.*

Figure 6.1a shows a portion of a point configuration for the perturbed disorder for a positional disorder degree $\mathcal{PD} = 30\%$. In Fig. 6.1, we have plotted the entropy, as well as the pair correlation function and the structure factor.

For a lattice with vanishing perturbation (dotted black line in Fig. 6.1b-d), i.e., for a periodic square array, as expected, the entropy is zero everywhere (cf. Fig. 6.1b). A configurational entropy of zero means that there are no variations in the number of points that fall into a circle centered at an arbitrary meta-atom of the lattice. The radial pair correlation function in Fig. 6.1c shows delta peaks in the radial distances where the lattice is formed, i.e., $r = [1, \sqrt{2}, 2, \sqrt{5}, ...]\Lambda$. The structure factor in Fig. 6.1d also shows delta peaks at the spatial frequencies $\xi = [1, \sqrt{2}, 2, \sqrt{5}, ...]/\Lambda$. Note that the structure factor is zero at $\xi = 0$. In other words, a periodic lattice, as expected, has a hyperuniform order [248].

When the disorder degree increases, the patterns for the statistical parameters gradually alter the shape. For $\mathcal{PD} = 10\%$ (solid blue line in Fig. 6.1b-d), the entropy is nonzero for most meta-atom count averages. However, there are still locations in the graph where entropy is zero. In pair correlation function and structure factor, the delta points of the periodic case slightly broaden for $\mathcal{PD} = 10\%$. However, the lattice diffraction pattern is still dominant, as also evident from Fig. 6.1e. Interestingly, the lattice trace, even after strong disorder degrees, persists. This is evident in Fig. 6.1d, where at a normalized spatial frequency $\Lambda\xi = 1$, a peak is observed, except for the critical point of $\mathcal{PD} = 100\%$ where the lattice trace is fully cloaked, as also reported in Ref. [245]. Another interesting finding is that independent of the disorder degree, the system stays hyperuniform. These two observations are consistent with the findings of other references [245, 247].

6.2.2 Defected disorder

Another type of disorder that we explore is the defective disorder in which we randomly remove $\mathcal{DD}\%$ of the meta-atoms from a square array lattice, where $\mathcal{DD} \in [0, 100]\%$. In other words, the perfect ordered lattice has defects and, hence, we call it *defected* disorder. This point process is also called *quasi-random* in the literature [249]. In an extreme case, if $\mathcal{DD} = 100\%$, no meta-atom is left in the configuration.

In Fig. 6.2, we have shown the statistical characteristics of the defected disorder. A disorder degree $\mathcal{DD} = 0\%$ is a square-array periodic lattice and is precisely the same as $\mathcal{PD} = 0\%$ discussed in the previous subsection. By increasing the degree of disorder, the entropy increases (cf. Fig. 6.2b). The structure factor shows that the defected disorder, unlike the perturbed disorder, is not hyperuniform anymore. Moreover, the trace of the lattice denoted as delta peaks in the location of the lattice points persists, even when an intense disorder is enforced. For both perturbed and defected disorder, the radial pair correlations function denotes an extended range of order.

6.2.3 Poisson's disorder

A spatial Poisson point process randomly places meta-atoms on a dedicated surface. The number of meta-atoms is determined by the *seed density* $\breve{\lambda}$. The Poisson point
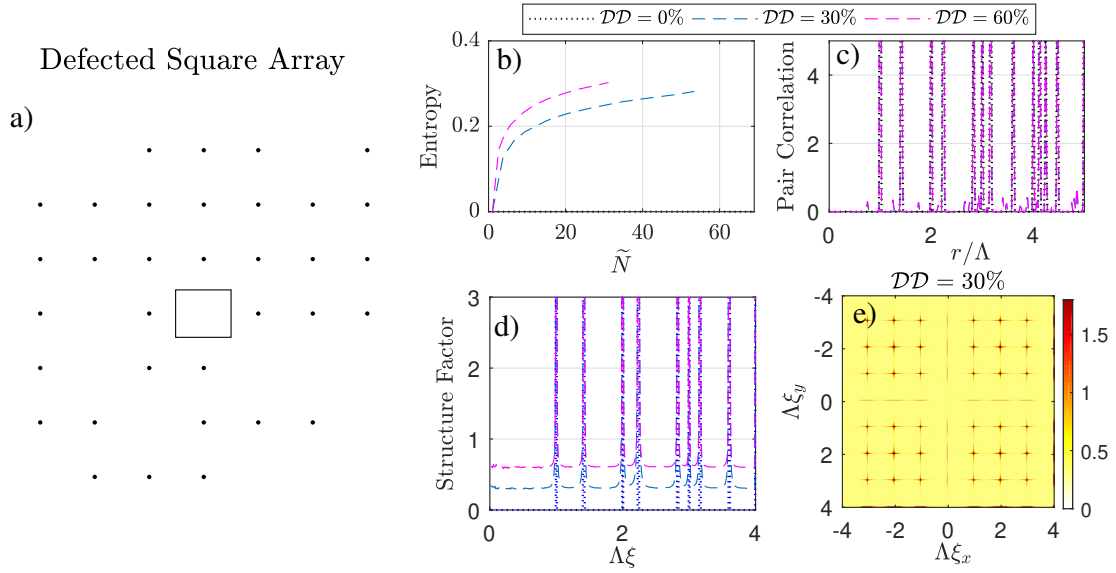
Figure 6.2: **Defected disorder:** a) A portion of a defected disorder point configuration for a positional disorder degree of $\mathcal{DD} = 30\%$. b) The configurational entropy as a function of the average meta-atom number $\widetilde{N}$, c) radial pair correlation as a function of the normalized pair distance r/Λ, and d) radial structure factor as a function of the normalized spatial frequency $\Lambda\xi$ for defected square arrays with 0%, 30%, and 60% of positional disorder. e) The structure factor as a function of the normalized spatial frequency along x-axis $\Lambda\xi_x$ and y-axis $\Lambda\xi_y$ for a positional disorder degree of $\mathcal{DD} = 30\%$.

process is sometimes called the *completely random process* [243]. Prime examples of Poisson distribution are atoms inside gasses that are completely randomly placed. Here, we refer to the spatial Poisson point configuration as *Poisson's disorder*. The terminology comes from the fact that in a Poisson's point configuration, the possibility of finding n meta-atoms in a region with an area A is determined by the Poisson distribution:

$$P[N(A) = n] = \frac{\breve{\lambda}A^n}{n!}e^{-\breve{\lambda}A}. \tag{6.11}$$

Figure 6.3 shows the statistical characteristics of a spatial Poisson's point configuration. As compared to the perturbed and defected disorder, Poisson's disorder shows higher entropy. The distinct feature of a Poisson disorder is its monotonous pair correlation and structure factor. The range of local order is zero, and the system is not hyperuniform. This point configuration is mainly used as a reference for our calculations. As we seek to maintain the same density of meta-atoms in all the arrangements, we always set the seed density to $\breve{\lambda} = 1/\Lambda^2$, where Λ is the periodicity of a periodic lattice that we compare with.

In Poisson's disorder, a meta-atoms' neighbor can be located anywhere, with no lower limit on the distance between them. This characteristic is not possible to hold for realistic metasurfaces as the nanoparticles have some spatial extent. Therefore, one needs to enforce a lower limit to the distance in between meta-atoms. In the following subsection, we explore such point processes.
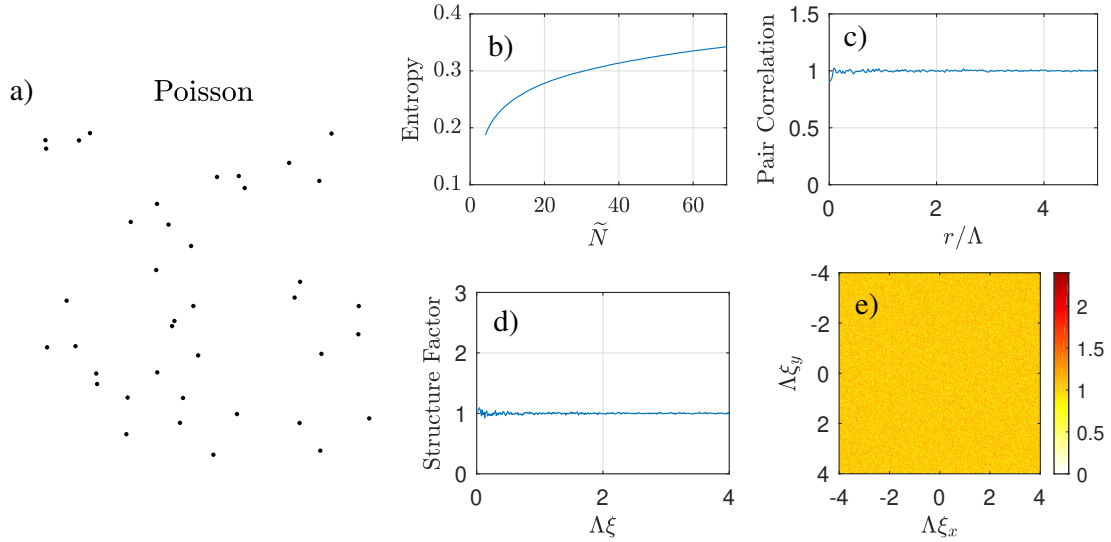
Figure 6.3: **Poisson's disorder:** a) A portion of a Poisson's disorder with a seed density $\breve{\lambda} = 1/\Lambda^2$. b) The configurational entropy as a function of the average meta-atom number $\widetilde{N}$, c) radial pair correlation as a function of the normalized pair distance r/Λ, and d) radial structure factor as a function of the normalized spatial frequency $\Lambda\xi$ for Poisson's disorder. e) The structure factor as a function of the normalized spatial frequency along x-axis $\Lambda\xi_x$ and y-axis $\Lambda\xi_y$ for Poisson's disorder.

6.2.4 Matérn III disorder

This subsection introduces two-point processes that start by a Poisson's distribution and then enforce a deletion process as a function of the meta-atoms' pair distances. These two-point process are called the *Matérn type-III hard-core* and *soft-core* disorder. In short, we refer to them as *Matérn III disorder*. The Matérn model employs a deletion probability function $F(r)$ to a Poisson's point configuration with a seed density $\breve{\lambda}$, where $1 - F(r)$ dictates how probable it is to find a meta-atom within the distance r of another meta-atom [101, 250]. We parametrized the deletion probability such that $F(r)$ decreases linearly within the range of $r \in [\alpha, \beta]$:

$$F(r; \alpha, \beta) = \begin{cases} 1 & 0 \le r < \alpha \\ \frac{\beta-r}{\beta-\alpha} & \alpha \le r < \beta \\ 0 & \beta \le r \end{cases}. \tag{6.12}$$

We label the resulting meta-atom distribution as "Matérn type-III soft-core" when $\beta > \alpha$, and as "Matérn type-III hard-core" when $\beta = \alpha$. α denotes a hard-core radius in which meta-atoms are strictly not found within that radius, and β is the soft-core radius, where some particles might be found between β and α radii, determined by the stochastic process.

As discussed before, the seed density of Poisson's point process is set to $\breve{\lambda} = 1/\Lambda^2$. However, since the deletion process removes meta-atoms, we might end up with a point configuration that is less dense as desired. Therefore, for the Matérn III disorder, we always start with a slightly higher density to approximately get the same density as a periodic lattice with a lattice constant Λ.
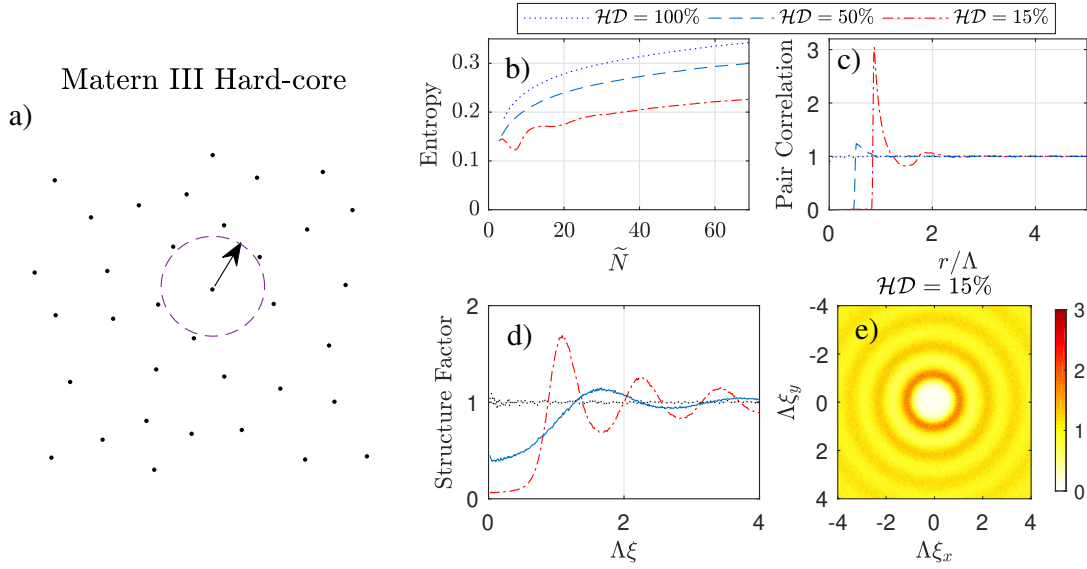
Figure 6.4: **Matérn type-III hard-core disorder:** a) A portion of a Matérn III hard-core disorder with a seed density $\breve{\lambda} = 1/\Lambda^2$ and disorder degree $\mathcal{HD} = 15\%$. b) The configurational entropy as a function of the average meta-atom number $\widetilde{N}$, c) radial pair correlation as a function of the normalized pair distance r/Λ, and d) radial structure factor as a function of the normalized spatial frequency $\Lambda\xi$ for Matérn III hard-core disorder with 100%, 50%, and 15% of positional disorder. e) The structure factor as a function of the normalized spatial frequency along x-axis $\Lambda\xi_x$ and y-axis $\Lambda\xi_y$ for Matérn III hard-core disorder with 15% of positional disorder.

Hard-core and soft-core radii cannot exceed the periodicity Λ, and the periodicity can be set as an upper limit. Therefore, we can define the disorder degree for the Matérn III hard-core as $\mathcal{HD} = 1 - \alpha/\Lambda = 1 - \beta/\Lambda$. For the Matérn III soft-core, we always set $\beta = \Lambda$ and, hence, we can define the disorder degree in this point process as $\mathcal{SHD} = 1 - \alpha/\Lambda$. Clearly, for Poisson's disorder, where no hard-core radius exists, the disorder degree is $\mathcal{HD} = 1 - (\alpha = 0)/\Lambda = 100\%$.

Figure 6.4 shows the statistical characteristics of a Matérn III hard-core point configuration. For reference, we have also included the Poisson disorder, i.e., when $\mathcal{HD} = 100\%$. Compared to the Poisson disorder, the entropy of the configurations with a slightly lower degree of disorder is consistently lower. On the other hand, the enforced hard-core has resulted in some ripples in the radial structure factor, showing a local range order level.

Interestingly, as observed in Fig. 6.4d, for lower degrees of disorder such as $\mathcal{HD} = 15\%$, the system is very close to a hyperuniform arrangement. For this reason, we may call these arrangements "uniform" [38]. The structure factor, in Fig. 6.4e, shows a striking difference when compared to the Poison disorder and the perturbed and defected disorder. Unlike the perturbed and defected disorder, no delta-point-like peaks are observed, but unlike the Poisson disorder, the ripples clearly show some order in the system. These ripples denote correlated behavior and hence signals local range order. While Poisson's disorder behaves like gasses, Matérn III disorder behaves more like liquids.

Figure 6.5 shows the statistical characteristics of a Matérn III soft-core point configuration. The results are very similar to the hard-core type. Although comparing
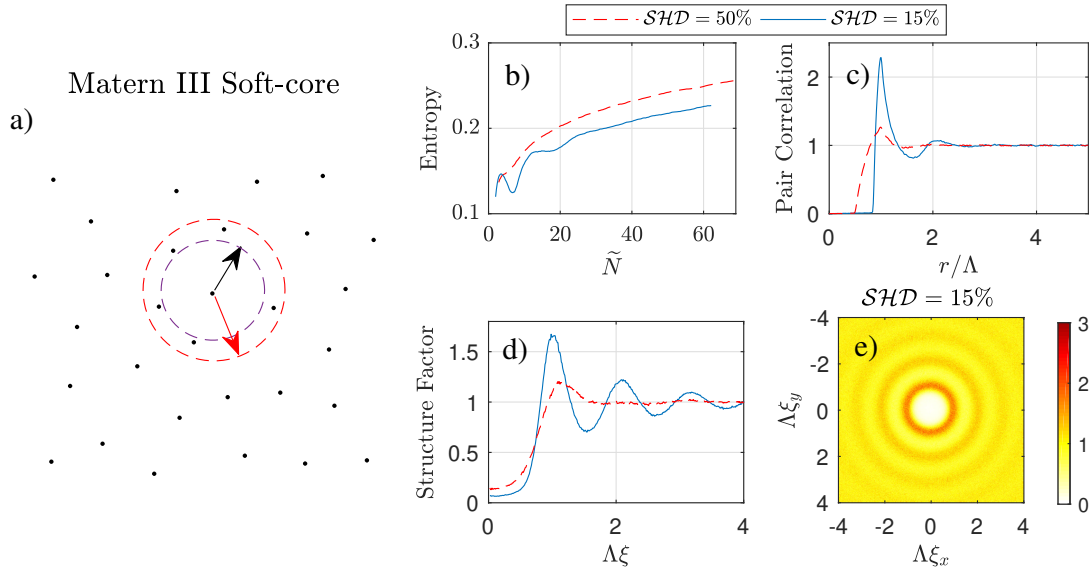
Figure 6.5: **Matérn type-III soft-core disorder:** a) A portion of a Matérn III soft-core disorder with a seed density $\breve{\lambda} = 1/\Lambda^2$ and disorder degree $\mathcal{SHD} = 15\%$. b) The configurational entropy as a function of the average meta-atom number $\widetilde{N}$, c) radial pair correlation as a function of the normalized pair distance r/Λ, and d) radial structure factor as a function of the normalized spatial frequency $\Lambda\xi$ for Matérn III soft-core disorder with 50%, and 15% of positional disorder. e) The structure factor as a function of the normalized spatial frequency along x-axis $\Lambda\xi_x$ and y-axis $\Lambda\xi_y$ for Matérn III soft-core disorder with 15% of positional disorder.

the entropy measures in Fig. 6.4b and Fig. 6.5b, the soft-core type appears slightly less disordered. Due to this similarity, we only use the Matérn III soft-core point configuration in the remainder of the thesis.

Note that realizing a disorder degree of 0% in Matérn III point configurations is a numerical challenge, as the point process is based on a post-process deletion algorithm, and choosing radically large α and β results in a very dilute arrangement that are not directly comparable to the other disordered arrangement.

6.2.5 Hyperuniform disorder

In this subsection, we study a few designed hyperuniform point configurations. These point configurations are designed by Dennis Arslan [156], and, here, after discussing their statistical measures, their optical response is measured and compared.

A hyperuniform or super homogenous point configurations are defined as the arrangements in which the structure factor tends to zero at vanishing spatial frequencies, i.e., $S(\xi \to 0) = 0$. In other words, the macroscopic variance of the density of the medium is completely suppressed at very large length scales [244]. The vanishing structure factor might be interpreted as a universal "hidden" order in hyperuniform point processes at large length scales.

Periodic arrangements are trivial examples of ordered hyperuniform point configurations. Aperiodic ordered arrangements, like quasicrystals, are other examples of hyperuniform point configurations [244]. In quasicrystals, unlike periodic lattices,
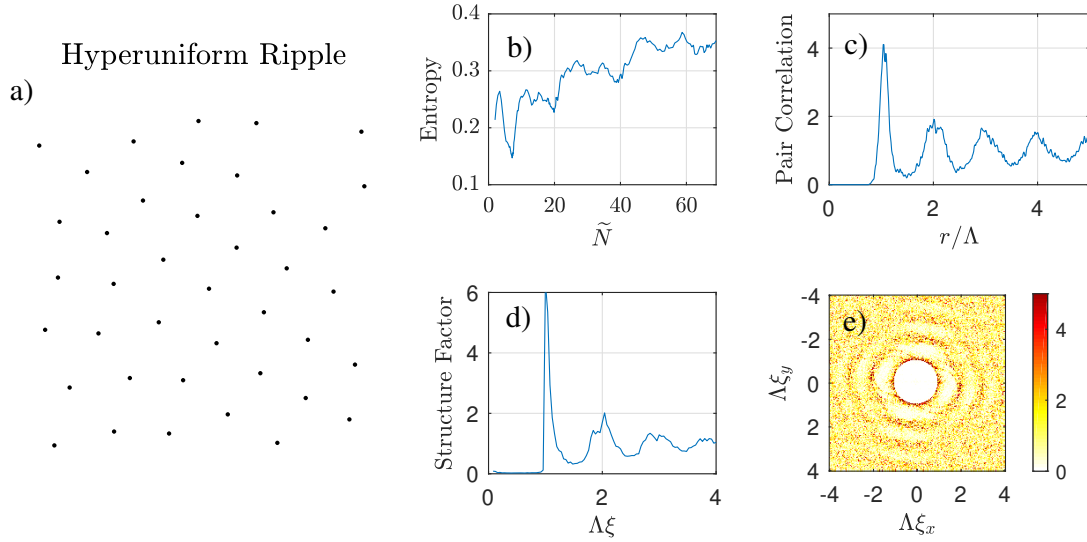
Figure 6.6: **"Hyperuniform ripple" disorder:** a) A portion of a "hyperuniform ripple" disorder with an enforced minimum pair distance of 0.71Λ. b) The configurational entropy as a function of the average meta-atom number $\widetilde{N}$, c) radial pair correlation as a function of the normalized pair distance r/Λ, and d) radial structure factor as a function of the normalized spatial frequency $\Lambda\xi$ for "hyperuniform ripple" disorder. e) The structure factor as a function of the normalized spatial frequency along x-axis $\Lambda\xi_x$ and y-axis $\Lambda\xi_y$ for "hyperuniform ripple" disorder. The point configuration is called ripple due to the extended ripples in the radial pair correlation.

there is no translational symmetry. However, sharp Bragg spots in the structure factor show long-range order in these patterns.

Another class of hyperuniform arrangements are *stealthy* hyperuniform arrangements, in which the structure factor remains zero for an extended spatial frequency range, i.e., $S(\xi < \xi_{\max}) = 0$ [244, 251]. Such arrangements are called stealthy, as the optical scattering from an arrangement of identical meta-atoms that have no coupling, i.e., under Born approximation, vanishes for an extended angular region. Note that for resonant metasurfaces, this phenomenon is not necessarily observed anymore.

In this subsection, we analyze three hyperuniform point configurations. Two are stealthy hyperuniform configurations: One has an extended range of local order (labeled *hyperuniform ripple*), and the other one has an enforced minimum range of local order (labeled *hyperuniform flat*). Then, the remaining one is non-stealthy with a cubic rise of the structure factor from the origin, i.e., $\lim_{\xi\to 0} S(\xi) \approx \xi^3$ (labeled *hyperuniform cubic*). In all these point processes, a hard-core of $r = 0.71\Lambda$ is enforced. We use the value 0.71 as we can directly compare it with metasurfaces made from actual nanocylinder that we have investigated in previous works [38, 101].

Figure 6.6 shows the statistical measures for the "hyperuniform ripple" point configuration. The point configuration in Fig. 6.6a, visually, shows a high degree of order. When looking at the radial pair correlation function, unlike the Poisson and Matérn III disorder, an extended ripple pattern is observed up to the maximum observation
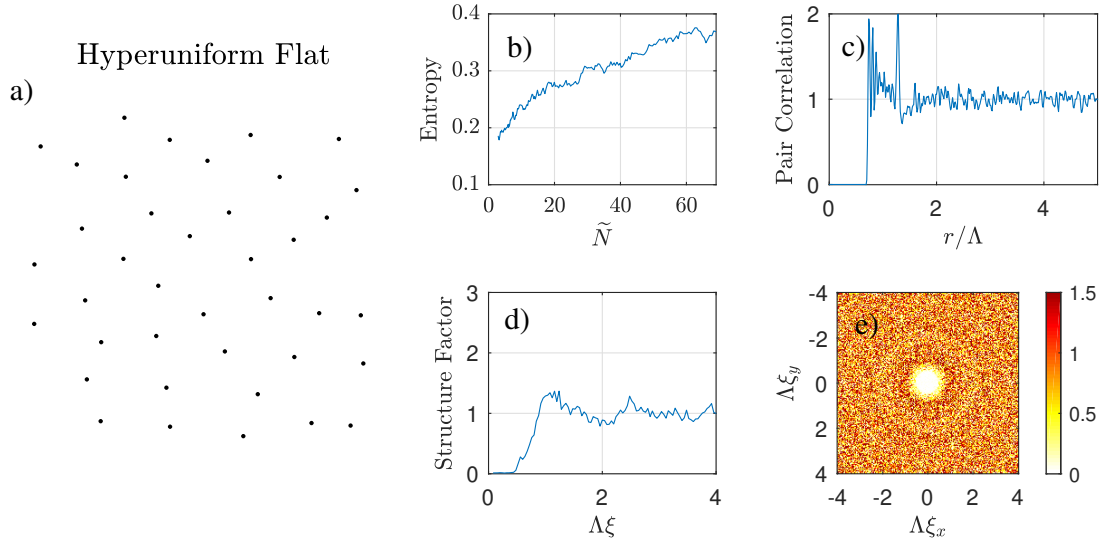
Figure 6.7: **"Hyperuniform flat" disorder:** a) A portion of a "hyperuniform flat" disorder with an enforced minimum pair distance of 0.71Λ. b) The configurational entropy as a function of the average meta-atom number $\widetilde{N}$, c) radial pair correlation as a function of the normalized pair distance r/Λ, and d) radial structure factor as a function of the normalized spatial frequency $\Lambda\xi$ for "hyperuniform flat" disorder. e) The structure factor as a function of the normalized spatial frequency along x-axis $\Lambda\xi_x$ and y-axis $\Lambda\xi_y$ for "hyperuniform flat" disorder. The point configuration is called flat due to the relatively flat radial pair correlation after the first peak.

point $r = 5\Lambda$. This extended ripple pattern shows the long-range order of the configuration. Interestingly, though, the entropy, in Fig. 6.6b, is as high as the Poisson disorder. This counterintuitive observation shows that the entropy measure cannot always be a reliable measure of order. The structure factor shows sharp Bragg peaks reminiscent of quasicrystals. Moreover, we can observe that the arrangement is a stealthy hyperuniform point configuration.

 Figure 6.7 shows the statistical measures for the "hyperuniform flat" point configuration. The enforced flat radial pair correlation function (hence, the name) shows a very short-range local order in the system. The structure factor also shows a very flat response beyond the stealthy spatial frequency.

 Figure 6.8 shows the statistical measures for the "hyperuniform cubic" point configuration. Besides the non-stealthy behavior observed in the radial structure factor and a slightly longer local-range order, the statistical parameters are similar to "hyperuniform flat."

 In summary, in this section, we have introduced some practical statistical measures to characterized disordered arrangements. Then, we have introduced multiple disorder point processes and have disused their properties using the developed statistical measures. So far, we have only focused on the arrangements of disordered arrangements. From the next section, we start calculating the optical transmission and reflection from disordered arrangements. In the next section, we introduce an approach to calculate the transmission and reflection and in Section 6.4 and 6.6, we analyze the optical scattering from the introduced disordered arrangement.
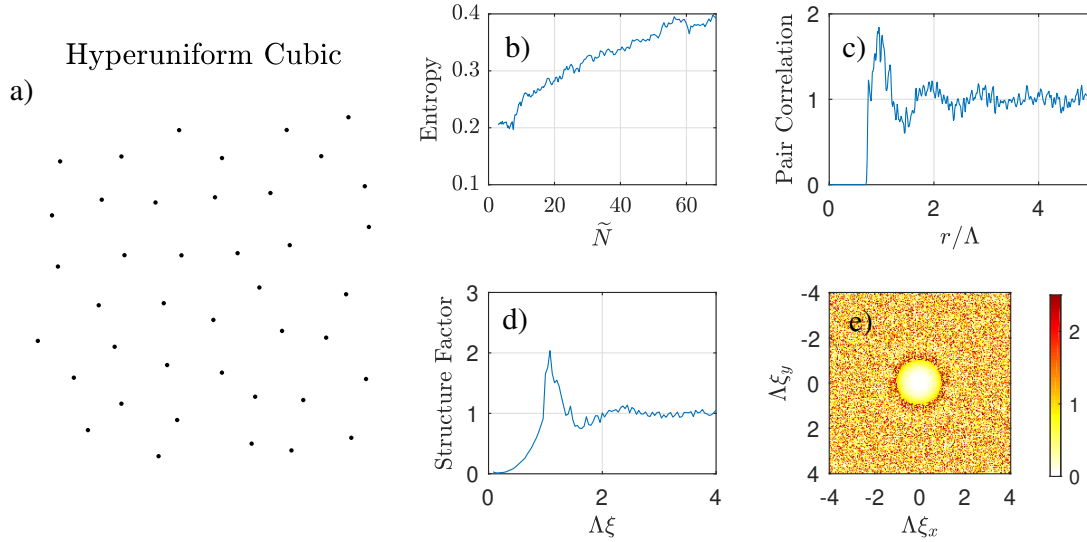
Figure 6.8: **"Hyperuniform cubic" disorder:** a) A portion of a "hyperuniform cubic" disorder with an enforced minimum pair distance of 0.71Λ. b) The configurational entropy as a function of the average meta-atom number $\widetilde{N}$, c) radial pair correlation as a function of the normalized pair distance r/Λ, and d) radial structure factor as a function of the normalized spatial frequency $\Lambda\xi$ for "hyperuniform cubic" disorder. e) The structure factor as a function of the normalized spatial frequency along x-axis $\Lambda\xi_x$ and y-axis $\Lambda\xi_y$ for "hyperuniform cubic" disorder. The point configuration is called cubic because of the cubic rise, i.e., $\lim_{\xi\to 0} S(\xi) \approx \xi^3$, of the radial structure factor from the origin.

6.3 Optical response of finite arrangements

In this section, we establish an approach to reliably measure the zeroth-order transmission and reflection from finite arrangements. The numerical approach to calculate the optical scattering from a disordered metasurface is documented in Section 4.1. The question now is to calculate transmission and reflection from the optical scattering information that we can compare to the results of an actual experiment.

In the optical experiments that are assumed here, the fabricated metasurfaces are illuminated by a collimated laser beam. Although the laser beam can be modeled with a Gaussian beam, the beam width and the collecting field aperture by the detector are such that we can assume a plane wave excitation that illuminates an extensive area of the metasurface. In the optical simulations, we tend to follow an approach similar to the experiment, i.e., we simulate a finite metasurface with a plane wave excitation and collect the scattered field in an aperture that is smaller than the spatial extent of the metasurface. The edge effects are a source of deviations. The borders of the collection grid should be distant enough from the edges, and, on the other side, a large enough number of meta-atoms need to be illuminated so that the response is representative of the whole metasurface. Moreover, the larger the number of meta-atoms is, the more computationally expensive the simulations become. The collection grid size, the number of samples, and the distance of the collection grid to the metasurface are all parameters that need to be determined. In this section, we seek to provide an estimate for these parameters.
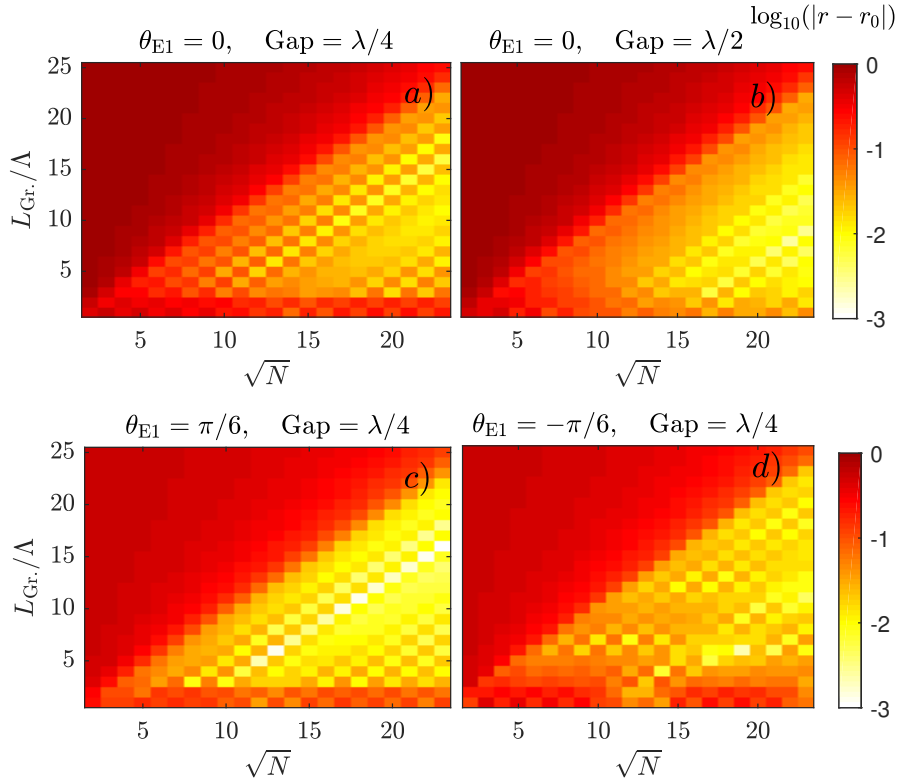
Figure 6.9: **Reflection from finite and infinite periodic metasurfaces:** The logarithmic deviation from the zeroth-order reflection of a finite periodic metasurface r, made from isotropic meta-atoms with a single electric dipole a-b) at resonance (i.e., $a_1 = 1, a_{j>1} = b_{j>0} = 0$), or c-d) slightly off-resonance, as compared to the reflection from an infinitely periodic metasurface r_0 of the same meta-atoms. The results are plotted as a function of the square root of the number of meta-atoms and the normalized square-box collection grid length $L_{\text{Gr.}}$. The collection grid is placed parallel to the metasurface at a distance Gap. The number of samples collected from the collection grid is three points per wavelength.

To provide a reliable upper limit estimate for the extent of the metasurface and the spatial extent of the collection grid, we use periodic but finite metasurfaces. A periodic but finite metasurface should have the same zeroth-order transmission and reflection as an infinite metasurface at a specific limit where the number of meta-atoms is large enough. From Chapter 4, we already know the transmission and reflection of a single-resonance infinitely periodic metasurface. Therefore, we can analyze the optical response and compare it with the finite structures with different parameters. For the comparison, here, we use a metasurface made from electric dipoles with a lattice constant of $\Lambda/\lambda = 0.8$. We use reflection data so that the effect of the incident field in the forward direction is not affecting our results.

Figures 6.9a-b, shows the logarithmic deviation that we get from the reflection of a finite periodic metasurface made from isotropic meta-atoms with a single electric dipole resonance (i.e., $a_1 = 1, a_{j>1} = b_{j>0} = 0$) as compared to the reflection from an infinitely periodic metasurface of the same meta-atoms. The results are plotted as a function of the square root of the number of particles N, and the normalized square-box collection grid length $L_{\text{Gr.}}$ placed parallel to the metasurface at a distance Gap. Zeroth-order reflection is the average of the sampled electric field
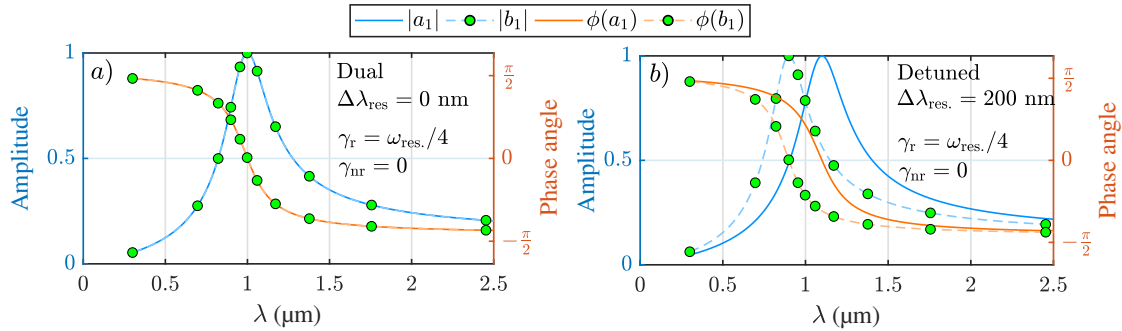
Figure 6.10: **Dual and detuned Lorentzian dipoles:** Amplitude and phase angle spectra of dipolar Mie coefficients. The amplitude and phase angle spectra of the electric (a1) and magnetic (b1) dipolar Mie coefficients with Lorentzian line shape for (a) dual and (b) detuned meta-atoms.

values on the collection grid. The number of samples collected from the collection grid is three points per wavelength, which is sufficiently large for the zeroth-order response. Figures 6.9c-d show the same analysis with meta-atoms that are slightly off-resonance. Clearly, at the resonance, the deviation will be more substantial and should be considered the worst-case scenario. Although closer gaps between the metasurface and the collection grid may result in more accurate results with fewer particles, evanescent fields will require more sampling points. This can become even more critical when we consider quadrupolar and higher-order meta-atoms. Therefore, in the following, we consider a gap distance of half a wavelength.

In the following sections, we use the insights from this section to calculate the zeroth-order and diffusive modes of the disordered metasurfaces.

6.4 Zeroth-order transmission and reflection from disordered metasurfaces

In this section, we calculate the zeroth-order transmission and reflection from the disorder types that we have introduced in Section. 6.2. Furthermore, the effective moments induced in the meta-atoms of the disordered metasurfaces are simulated.

The meta-atoms considered in this section are dipolar and are modeled with a non-absorbing Lorentzian profile (cf. Eq. 3.61). The Lorentzian profile is shown for the electric and magnetic dipoles in Fig. 6.10. The linewidth for both dipoles is the same. The electric and magnetic dipoles can have a detuning in their resonance position or no detuning, i.e., be dual. Higher-order multipole moments are not considered. In this section, we only consider dual meta-atoms, but in the following section, detuned meta-atoms are also investigated for a complete understanding of the effect of the disorder.

For the simulations ahead, we have considered 17×17 meta-atoms and have sampled the scattered electric field at a distance of half a wavelength, i.e., $Gap = \lambda/2$. The sampling grid box has a side length of 6Λ, and we have sampled the electric field with three points per wavelength. Apart from calculating transmission coefficient and its phase angle and amplitude, we also calculate a *diffuse scatterance*, which measures the ratio of power that is neither reflected nor transmitted in specular

directions. The specular response refers to the zeroth-order forward and backward scattering directions. As the meta-atoms do not have any absorption, the diffuse scatterance can be written as [38]:

$$Q^{\mathrm{D}} = 1 - |t|^2 - |r|^2, \tag{6.13}$$

where t and r are the zeroth-order transmission and reflection coefficients, respectively. In our simulations, we have mostly considered lattices with a meta-atom density of $1/\Lambda^2$. For a periodic lattice with such density, the resonance of the lattice coincides with the resonance of the isolated meta-atom. With this configuration, we can observe disorder-induced resonance shifts in the optical response of the lattice.

Furthermore, we have also calculated the normalized effective induced dipole moments of the meta-atoms, and their standard deviations at resonance, for the central 25 meta-atoms. The central meta-atoms are chosen such that edge effects are avoided. The normalization factor for the electric (magnetic) dipoles is the maximum induced electric (magnetic) moment for an isolated meta-atom. We have calculated these upper limits in Section 4.4. In the following figures, we denote these maximum normalizing values as $p_0 = p_{\mathrm{max}}$ and $m_0 = m_{\mathrm{max}}$. The derived effective moments provide meaningful insights into the microscopic effects of the positional disorder, as compared to a periodic structure. For a periodic square array lattice of dipolar meta-atoms with a periodicity $\Lambda/\lambda = 0.8$, the normalized effective electric and magnetic dipoles at resonance (i.e., $a_1 = b_1 = 1$) are equal to:

$$\frac{|p_{\mathrm{eff}}|}{p_0} = \frac{\mathrm{i}\, a_1}{1 - \mathrm{i}\, a_1 C_{\mathrm{dd}}\,(0.8)} = 2.68, \tag{6.14}$$

$$\frac{|m_{\mathrm{eff}}|}{m_0} = \frac{\mathrm{i}\, b_1}{1 - \mathrm{i}\, b_1 C_{\mathrm{dd}}\,(0.8)} = 2.68. \tag{6.15}$$

Figure 6.11 shows the simulation results for the optical response of disordered point configurations decorated with dual dipolar meta-atoms. The red cross marked line in Fig. 6.11a,e,i,m,q, show the response for a finite periodic square array. The results are very similar to an infinitely periodic metasurface (cf. Fig. 5.2); The transmittance is unity for the full resonance spectrum (cf. Fig. 6.11a), and the phase angle of transmission span a region of 2π with a *normal dispersion* (cf. Fig. 6.11b), i.e., decreasing phase angle with increasing wavelength. The normalized effective dipole moments are also very similar to the results in Eq. 6.14-6.15 (cf. Fig. 6.11q). There is, however, an anomaly in the response of a finite periodic array near the resonance wavelength. At around a wavelength of $\lambda = 1050\,\mathrm{nm}$, there is a ripple in the transmission amplitude data, and it goes above unity (cf. Fig. 6.11i). This point of operation is due to the finiteness of the metasurface and is traced back to surface waves. Changing the size of the metasurface changes the wavelength at which this phenomenon occurs. It should be emphasized that this does not violate energy conservation and is merely the result of the specific approach that we follow when calculating transmission and reflection. If we extend our grid size to fully contain the metasurface, the transmittance does not cross unity; however, the edge effects come into play that we do not want to capture. Therefore, we can ignore those points in the finite periodic array and continue the current approach.
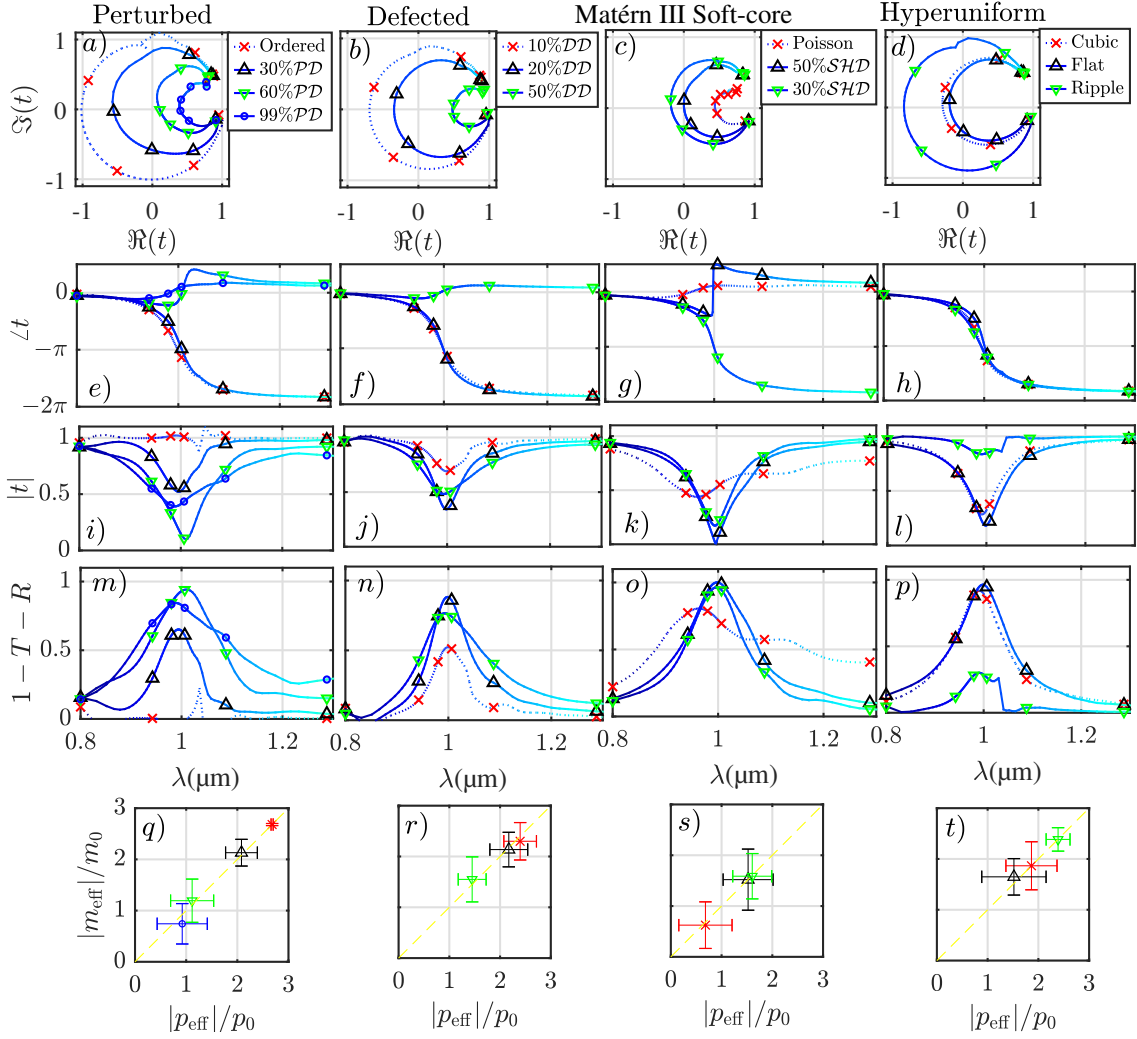
Figure 6.11: **Dual dipolar metasurfaces with disordered arrangements:** a-d) The zeroth-order transmission coefficient, e-h) phase angle of transmission, i-l) transmission amplitude, m-p) diffuse scatterance, and q-t) normalized resonant effective electric and magnetic dipole moments of a,e,i,m,q) perturbed, b,f,j,n,r) defected, c,g,k,o,s) Poisson's and Matérn type-III soft-core, and d,h,l,p,t) three hyperuniform disorder arrangements as a function of the wavelength. The point configurations are decorated with dual dipole moments that are modeled with a Lorentzian dipole (cf. Fig. 6.10a) and are illuminated with a plane wave at normal incidence. A periodicity $\Lambda = 800\,\text{nm}$ is considered for the perturbed array and the defected disorder. For the other arrangements, a density of $1/\Lambda^2$ is considered. Rainbow colors encode the wavelengths. The line markers encode the degree of positional disorder. For the simulation of the transmission, 17×17 meta-atoms are considered. The collection grid length is $L_{\text{Gr.}} = 6\Lambda$, located at a $Gap = \lambda/2$ parallel to the metasurface. The effective moments are calculated at the resonance wavelength for the 25 central meta-atoms.

Figures 6.11a,e,i,m,q show the optical response for perturbed arrays. An interesting feature that is evident from Fig. 6.11a is the shrinking of the trace of the transmission coefficient in the complex plane by increasing disorder degree $\mathcal{PD}$. In Fig. 6.11i, the shrinkage in the complex trace is manifested in the amplitude spectrum as an initial drop, and, then, a final rise of the transmittance after a *critical disorder*.

The phase angle data in Fig. 6.11e shows an intriguing phenomenon when the disorder degree crosses the critical disorder; The dispersion of the phase angle changes from normal to anomalous dispersion. Near the point of critical disorder, i.e., $\mathcal{PD} \approx 60\%$, the diffuse scatterance (Fig. 6.11m) reaches near unity at resonance. At this point of operation, the scattered power is neither absorbed nor transferred to specular directions but diffused to all non-specular directions. We will discuss the optical diffusion of disordered metasurfaces in the last section.

Figure 6.11q, shows the normalized effective moments. It is evident from the figure that although perturbed disorder decreases the amplitude of the effective moments consistently with an increasing disorder, the electric and magnetic moments preserve their equality. This phenomenon is consistently observed for the other disorder types (cf. Fig. 6.11q-t). It shows that a uniform positional disorder statistically affects the electric and magnetic dipole moments in the same way. Another exciting feature is that the deviation of the moments increases by increasing disorder.

Figures 6.11b,f,j,n,r show the optical response for defected arrays. The results are very similar to the perturbed array. For strong disorder, a spectral shift in the resonance wavelength is evident from Fig. 6.11j,n. This resonance shift is also evident in all the other disordered types for strong disorder degrees. For instance, for Poisson's disorder (Fig. 6.11k,o), a significant spectral shift is observed.

The *optical strength of disorder*, i.e., the disorder that is scanned by optical wave excitations, can be expressed as the shrinkage of the transmission coefficient in the complex plane. This shrinkage is also consistent with the decreasing of the induced effective moments. With this measure, we can also estimate the degree of disorder for the three hyperuniform point configurations. While, as expected, the "hyperuniform ripple" point configuration shows a high degree of order, the other two arrangements are more disordered (cf. Fig. 6.11d).

An interesting observation in all the disorder types is the persistence of the phase angle to changes before the critical disorder, i.e., the phase angle is topologically protected before the critical disorder. In Fig. 6.11e-g, it is evident that the phase angle hardly changes before reaching the critical disorder.

In summary, we have analyzed the zeroth-order transmission and reflection from multiple dual dipolar and disordered metasurfaces illuminated with a normal plane wave incidence. In the next section, we focus more on the critical point of disorder.

6.5 Disorder-induced phase transitions

In the previous section, we have observed that, at a critical disorder, the zeroth-order transmittance goes to zero, and the dispersion of the phase angle for the transmission coefficient sharply changes from normal to anomalous dispersion. We refer to this sharp phenomenon as a *disorder-induced phase transition* and generalize it to meta-atoms with detuned dipolar meta-atoms. The content of this section is based on our work in Ref. [101].

Phase transitions are ubiquitous. The intriguing feature is that an incremental change to a given system in one of the control parameters does not just cause an incremental change in the emerging properties of the system but, a qualitatively different behavior at particular points of operation is observed. There are multiple
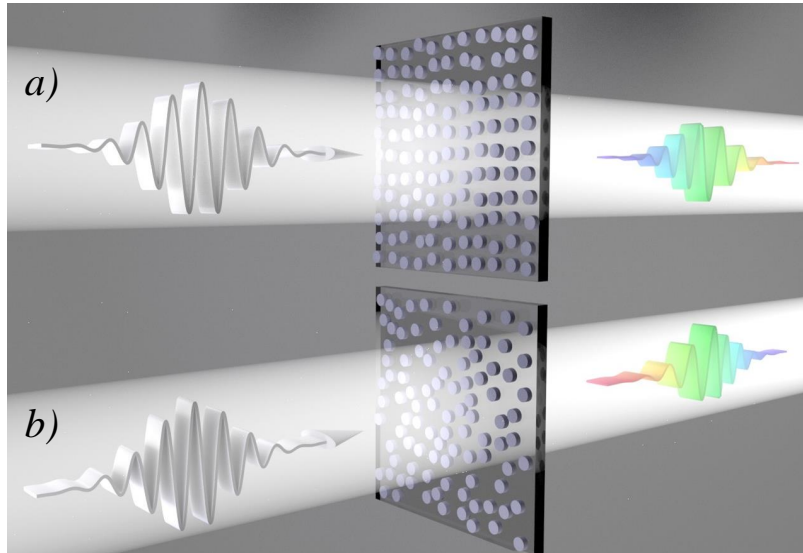
Figure 6.12: **Artistic impression of the disordered-induced phase transition:** A disorder-induced phase transition in the phase angle of the transmission coefficient that changes from a) normal to b) anomalous dispersion above a critical threshold in the positional disorder. An artistic impression of this effect illustrating how normal or anomalous dispersion in the phase angle leads to a positive or negative chirp of a transform-limited excitation pulse, respectively. The figure has been plotted in collaboration with Dennis Arslan.

examples in solid-state physics, where phase transitions in material properties have been observed at, e.g., a critical pressure or a critical temperature [252, 253]. Numerous photonic devices derive their functionalities from such phase transitions in the material properties [254–256]. Phase transitions have also been investigated in the field of nanophotonics. A notable example is the change from an elliptical to a hyperbolic dispersion relation for certain strongly anisotropic metamaterials at a critical wavelength [257, 258]. Other examples are the change from a metamaterial to a photonic crystal [259], the change from a real to a complex-valued spectrum at the spontaneous breakdown of the $\mathcal{PT}$ symmetry of a given optical potential [260, 261], or the change from a topological trivial to a topologically non-trivial band structure of a photonic material for specific geometrical deformations [262].

Disorder-induced phase transitions have possibly attracted the largest share of attention. For instance, they have been detrimental in the investigation of photonic band gaps [263]. Disorder is not just a nuisance [264, 265], but rather it can be a valuable resource with a new additional degree of freedom on which we can capitalize to tailor the flow of light [246, 266, 267].

Our focus, here, is the disorder-induced phase transitions in the phase angle of the transmission coefficient of a Huygens' metasurface. As we will show in the following section, this fundamental feature can be used to design novel phase-manipulating optical devices, e.g., diffusers. Figure 6.12 shows an artistic impression of the disordered-induced phase transition. A change in the dispersion of the transmission phase angle from normal to anomalous dispersion can lead to a positive and negative chirp in the transmitted transform-limited excitation pulse from the metasurface, respectively.
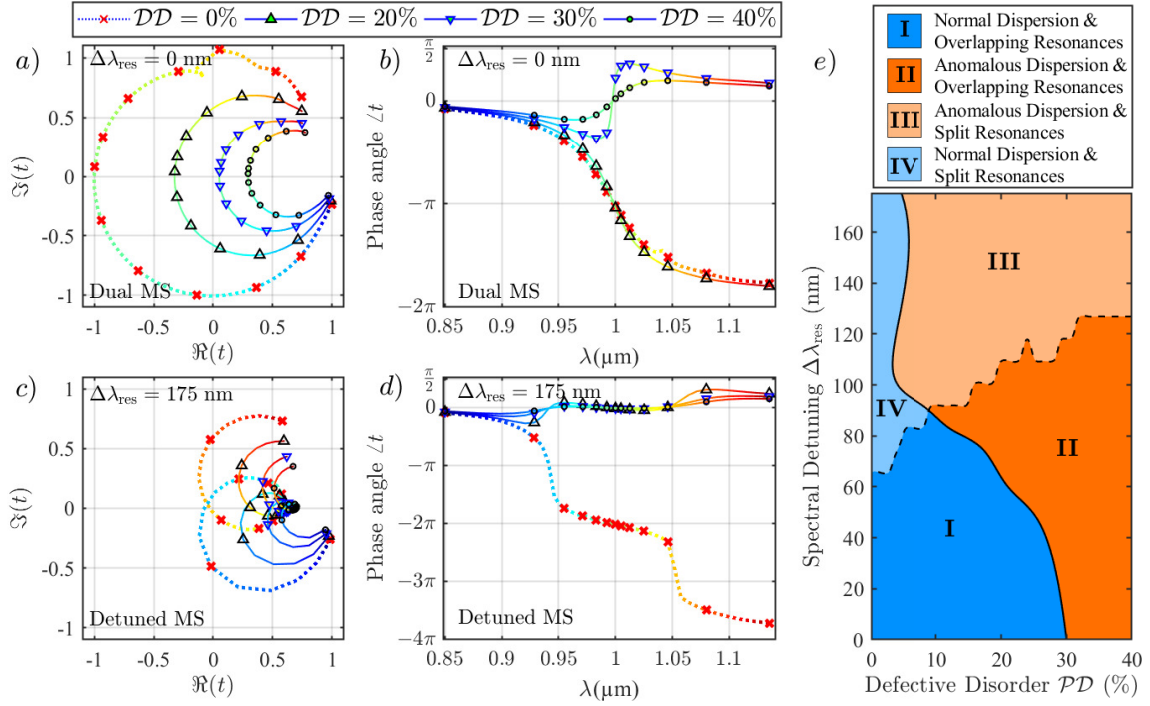
Figure 6.13: **Disorder-induced phase transitions:** a) The zeroth-order transmission coefficient $t(\lambda)$ of dual and c) detuned metasurfaces. b,d) Spectra of the phase angle $\angle t(\lambda)$ of $t(\lambda)$ as a function of the wavelength. Each metasurface consists of 17×17 non-absorbing dual meta-atoms that are modeled with a Lorentzian profile (cf. Fig. 6.10). The reference metasurface ($\mathcal{DD} = 0\%$) is a square array with lattice constant $\Lambda = 800$ nm. Rainbow colors encode the wavelength. The degree of positional disorder $\mathcal{DD} = 0, 20, 30, 40\%$ is encoded by the line markers. e) Phase diagram as a function of the positional disorder $\mathcal{DD}$ and spectral detuning $\Delta\lambda_{\mathrm{res}}$. For the simulation of the transmission, 17×17 meta-atoms are considered. The collection grid length is 6Λ, and it is located at a $Gap = \lambda/2$ parallel to the metasurface.

For the investigation of phase transitions, unlike Ref. [101] that we have studied perturbed arrays, we investigate defected disorder. The setup is the same as the previous section. Here, we have systematically tuned the disorder degree $\mathcal{DD}$ and the spectral detuning that is defined in Fig. 6.10b.

For a zero-detuning (cf. Fig. 6.13a,b), i.e., dual dipoles, as also observed in the previous section, beyond a critical disorder, the normal dispersion of the phase angle changes to an anomalous dispersion. For the defected disorder, this occurs at a critical disorder degree $\mathcal{DD} \approx 30\%$. The underlying physics can be revealed by inspecting the dispersive behavior of $t(\lambda)$ in the complex plane, as shown in Fig. 6.10a. As the positional disorder is increased, the path traced out by $t(\lambda)$ contracts towards a point t_{con} well within the positive real half-space. For slight positional disorder, the path circles the origin of the complex plane clockwise. For considerable positional disorder, the path does not circle the origin anymore, i.e., at a vanishing imaginary part of $t(\lambda)$, and the real part is always positive. We take this from now on as one objective criterion to classify our phase state. We distinguish between phase states in where the phase angle shows normal and anomalous dispersion, respectively. At the critical threshold, $|t(\lambda)|$ undergoes a root, i.e., the path passes precisely through the origin, and $\angle t(\lambda)$ abruptly changes from normal to anomalous

dispersion. A further increase in the positional disorder only further contracts the path, and $\angle t(\lambda)$ continues to exhibit anomalous dispersion. With that, we observe a sharp transition from normal to anomalous dispersion at a critical threshold for the positional disorder.

Next, we analyze the effect of detuned meta-atoms in the emerging optical response of disordered metasurfaces. For large spectral detuning of 175 nm and vanishing positional disorder, the two resonances are distinguishable from each other in the $\angle t(\lambda)$ spectrum, as can be seen in Fig. 6.13d. In Fig. 6.13c, the two resonances manifest in the complex plane as a crunode, which is a point where the path of $t(\lambda)$ is intersecting itself and thereby forming a loop. Note that for an infinite periodic arrangement, unlike the unwrapped 4π phase shift coverage that we observe for the detuned metasurface, only a 2π will be observed. The difference is that for an infinitely periodic arrangement, the transmission path intersects itself at exactly $t = 0$. However, for the finite arrangement, this intersecting point occurs at a slightly different location in the complex plane, resulting in a more considerable phase shift coverage.

As the positional disorder is increased from 0% to 40%, the path contracts again towards a point on the real axis, and the crunode vanishes at a critical threshold for the positional disorder. Above this critical threshold, the two resonances cannot be distinguished and appear as a single resonance. Hence, for large spectral detuning, we observe a sharp transition from a state with spectrally split resonances to a state with spectrally overlapping resonances at a critical threshold for the positional disorder.

In summary, we observed disorder-induced phase transitions in two distinct properties of the $\angle t(\lambda)$ spectrum: On the one hand, the dispersion switches from a state with *Normal Dispersion* (ND) to a state with *Anomalous Dispersion* (AD), and on the other hand, the apparent number of resonances switches between a state with *Split Resonances* (SR) to a state with *Overlapping Resonances* (OR). In the complex plane, we distinguish between ND and AD whether the path of $t(\lambda)$ circles the origin or not, and between SR and OR whether the path possesses a crunode or not, respectively. Consequently, four distinct phase states can be identified: *I* (ND & OR), *II* (AD & OR), *III* (AD & SR), and *IV* (ND & SR).

The phase diagram in Fig. 6.13e visualizes our findings that were obtained from a systematic analysis of wide ranges of positional disorder $\mathcal{DD} = 0, \dots, 40\%$ and spectral detuning $\Delta\lambda_{\mathrm{res}} = 0, \dots, 175$ nm. Note that the phase state boundaries are smoothed for easier interpretation. For a detailed discussion, refer to the supplementary material of Ref. [101]. Comparing the results of the perturbed array and the defected array shows striking similarities. This similarity denotes the universality of the disorder-induced phase transitions that are defined here.

In the following section, we study the angular optical scattering of dual disordered metasurfaces, especially at the points of phase transitions.

6.6 Directional scatterance of disordered metasurfaces

In this section, we investigate the optical diffusion of disordered metasurface when illuminated at normal incidence. Optical diffusion, here, refers to non-specular transmitted and reflected light that does not go to the zeroth-order transmission and

reflection. Disordered metasurfaces constitute an auspicious material platform for the diffusion of light [88, 91, 268]. The previous two sections show that the diffuse scatterance reaches unity at a critical disorder. This intriguing point of operation linked to a phase transition in the phase angle of the transmission coefficient is worth exploring further.

In the first part, we develop a set of equations to describe the optical scattering of a disordered metasurface. Later, we focus on characterizing the angular scatterance of disordered metasurface with dual dipole moments at resonance. The content of this section is partly based on our work in Ref. [38].

Plane wave description of directional scatterance

In Section 2.2, we have shown that we can write any electromagnetic field as a sum of plane waves. This section uses this basis to calculate the optical scattering of disordered metasurfaces into arbitrary angles. The detailed derivations can be found in Ref. [38, 156]. Assuming a normally incident plane wave illuminating a metasurface that is placed on the x-y plane, the directional scatterance as a function of the expanding plane wave amplitudes is:

$$Q_\Omega(\mathbf{k}) = \frac{1}{I_0} \frac{\mathrm{d}I(\theta,\phi)}{|\cos(\theta)|\,\mathrm{d}\Omega} = k_0^2 \frac{\left|b_\mathbf{k}^{\mathrm{TE}}(\mathbf{k})\right|^2 + \left|b_\mathbf{k}^{\mathrm{TM}}(\mathbf{k})\right|^2}{(2\pi)^2 \left|\hat{\mathbf{k}}\right| \cdot \hat{\mathbf{z}}}, \tag{6.16}$$

where A is the collection grid area, and I_0 is the intensity of an arbitrarily-polarized plane wave that illuminates the metasurface, respectively. Q_Ω can be interpreted as the fraction of the incident intensity that is scattered along (θ,ϕ) into a projected unit solid angle Ω. The scatterance to a certain polar angle, i.e, *polar scatterance* Q_θ is defined as:

$$Q_\theta(\theta) = \frac{\mathrm{d}Q(\theta)}{\mathrm{d}\theta} = \int_{-\pi}^{\pi} Q_\Omega(\theta,\phi) \sin(\theta) \left|\cos(\theta)\right| \mathrm{d}\phi. \tag{6.17}$$

and the *sectorial scatterance* $Q(\theta)$ is formulated as:

$$Q(\theta) = \int_0^\theta \int_{-\pi}^{+\pi} Q_\Omega(\theta',\phi)\, \mathrm{d}\theta' \mathrm{d}\phi + |t|^2 \delta_{\theta,0} + |r|^2 \delta_{\theta,\pi}, \tag{6.18}$$

which represents the fraction of the incident intensity that is scattered into a spherical sector with a half-angle of $\theta \in [0,\pi]$. r and t are the zeroth-order reflection and transmission.

In the following, we use these new parameters to characterize the optical response from disordered metasurfaces.

Ideal scatterers

To have a reference to compare the optical diffusion of disordered metasurfaces, here, we use a Hertzian dipole and a Lambertian surface. The directional and sectorial scatterance of a Lambertian surface (L) and a Hertzian dipole (H) may be written as [38]:

$$Q_\Omega^{\mathrm{L}}(\theta,\phi) = \frac{1}{2\pi}, \quad Q_\Omega^{\mathrm{H}}(\theta,\phi) = \frac{3}{4\pi} \left|\cos(\theta)\right|, \tag{6.19}$$
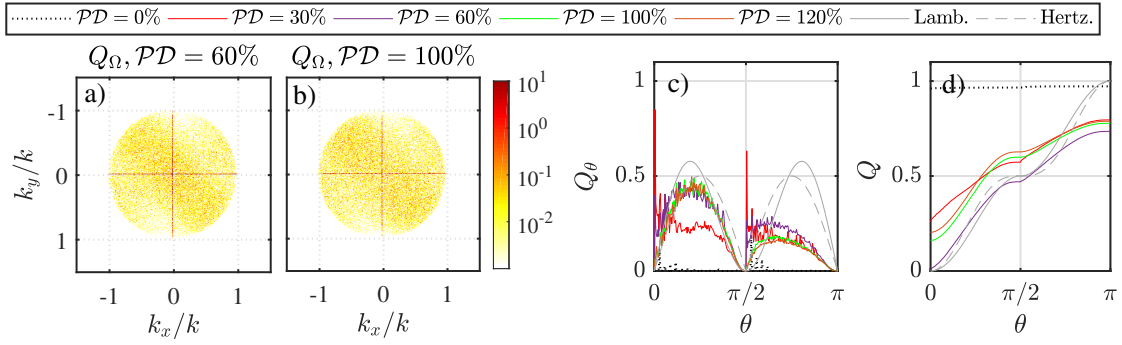
Figure 6.14: **Perturbed array scatterance:** a-b) The directional Q_Ω, c) polar Q_θ, and d) sectorial Q scatterance of a perturbed metasurface made from isotropic, dual, and dipolar meta-atoms at resonance illuminated with a plane wave at normal incidence for different degrees of positional disorder $\mathcal{PD}$. c-d) The polar and sectorial scatterance of a Hertzian dipole (gray dotted line) and a Lambertian surface (gray line) is plotted for reference.
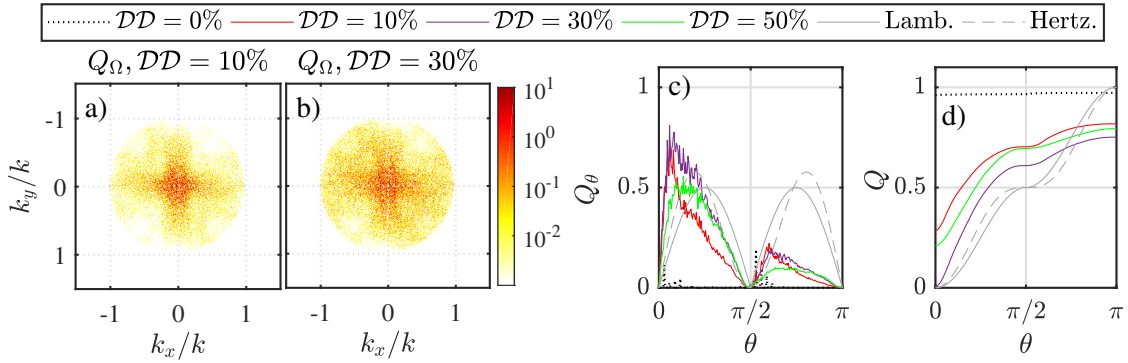
Figure 6.15: **Defected array scatterance:** a-b) The directional Q_Ω, c) polar Q_θ, and d) sectorial Q scatterance of a defected metasurface made from isotropic, dual, and dipolar meta-atoms at resonance illuminated with a plane wave at normal incidence for different degrees of positional disorder $\mathcal{DD}$. c-d) The polar and sectorial scatterance of a Hertzian dipole (gray dotted line) and a Lambertian surface (gray line) is plotted for reference.

$$Q^{\mathrm{L}}(\theta) = \begin{cases} \frac{1}{2}\sin^2(\theta) & \theta \leq \frac{\pi}{2} \\ 1 - \frac{1}{2}\sin^2(\theta) & \theta > \frac{\pi}{2} \end{cases}, \quad Q^{\mathrm{H}}(\theta) = \frac{1 - \cos^3(\theta)}{2}, \qquad (6.20)$$

where we have assumed a normalized power distribution. Moreover, for the Lambertian surface, we have assumed symmetric forward and backward scattering. The polar and sectorial scatterance of the Hertzian dipole and the Lambertian surface is plotted in Fig. 6.14c-d.

Optical diffusion of dual metasurfaces

Here, we simulate the optical diffusion of dipolar metasurfaces made from dual and isotropic meta-atoms at resonance (i.e., $a_1 = b_1 = 1$, $a_{j>1} = b_{j>1} = 0$) that are illuminated with a plane wave at normal incidence. We consider perturbed, defected, Poisson, Matérn III soft-core, and the three hyperuniform arrangements that we have introduced in Section 6.2.
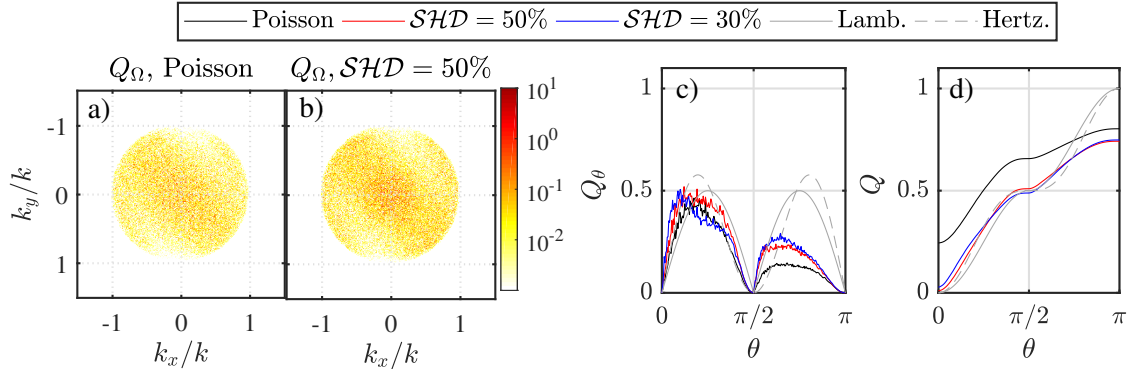
Figure 6.16: **The Poisson and Matérn III metasurface scatterance:** a-b) The directional Q_Ω, c) polar Q_θ, and d) sectorial Q scatterance of a disordered metasurface made from isotropic, dual, and dipolar meta-atoms at resonance that is illuminated with a normal plane wave incidence for the Poisson and Matérn type-III soft-core disorder with positional disorder degree $\mathcal{SHD}$. c-d) The polar and sectorial scatterance of a Hertzian dipole (gray dotted line) and a Lambertian surface (gray line) is plotted for reference.

To ensure a satisfying spectral resolution in the directional scatterance, we need a huge area for the collection grid of at least $(120\ \mu m)^2$. We used a cut-and-stitch approach since such large metasurfaces are computationally expensive to simulate in one run. In particular, we split the total metasurface into smaller, overlapping patches and simulated each patch separately. The overlaps were chosen such that the sample areas of all patches can directly be stitched together. Each of the simulations contains 17×17 metaatoms. The collection grid has a length of 10Λ and is placed at a distance $Gap = \lambda/4$ parallel to the metasurface. We have chosen a closer distance to capture high scattering angles.

Figure 6.14 shows the results for the perturbed array. We have also included the polar and sectorial scatterance of the Hertzian dipole and the Lambertian surface for comparison. For finite periodic arrays, the results are as expected; The polar scatterance is zero (except for some numerical defects), and the sectorial scatterance is almost unity, right from $\theta = 0$. These observations emphasize no diffusion, and most of the power is transferred to the zeroth-order transmittance.

Increasing positional disorder, the scatterance increases, and the starting point of the sectorial scatterance (the transmittance) decrease. At the critical disorder $\mathcal{PD} \approx 60\%$ (cf. Fig. 6.11), the sectorial scatterance at the origin tends to zero, i.e., $Q(0) = 0$. At the point of critical disorder, the sectorial and the polar scatterance in the forward direction share a large similarity to the Hertzian dipole. It should be noted that although the sectorial scatterance at $\theta = \pi$ should be unity, we see that, for most disordered metasurfaces, we do not reach it. This "missing power" is mostly going into very high angles. In other words, the diffusion performance can be assumed better than the graphs indicate. Note that for more accurate results, even more meta-atoms and larger grids are required.

In the backward direction, the scatterance is much weaker. Part of this can be traced back to the duality symmetry of the meta-atoms that can suppress the reflection not only to the zeroth-order but also relatively decrease the reflection to the
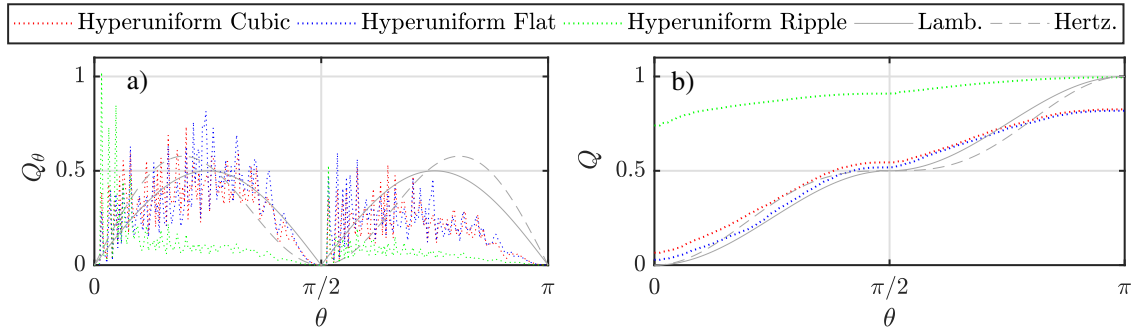
Figure 6.17: **Hyperuniform metasurface scatterance:** a-b) The directional Q_Ω, c) polar Q_θ, and d) sectorial Q scatterance of a hyperuniform metasurface made from resonant, isotropic, dual, and dipolar meta-atoms at resonance illuminated with a plane wave at normal incidence for three different hyperuniform arrangements: ripple, flat and cubic. c-d) The polar and sectorial scatterance of a Hertzian dipole (gray dotted line) and a Lambertian surface (gray line) is plotted for reference.

other angles. Beyond the critical disorder, the transmittance is no longer zero, and the scatterance deviates from the Hertzian dipole.

Figures 6.15 show the scatterance results for a defected metasurface. The trends in the results are similar to the perturbed array. As we have previously shown (cf. Fig. 6.2), defected arrays are not hyperuniform. Despite this, strong diffusion is evident from Fig. 6.15c-d for a critical disorder $\mathcal{DD} = 30\%$. However, judged from Fig. 6.15c, the large-angle scatterance is much weaker compared to the perturbed array (Fig. 6.14c).

Figure 6.16 shows the scatterance results for metasurfaces with the Poisson and the Matérn type-III soft-core point configurations. Matérn metasurfaces show strong diffusion and Hertzian-like scatterance. In Ref. [38], we have designed, fabricated, and characterized a metasurface made from silicon nanocylinders embedded in silica that is arranged with a Matérn type-III soft-core point configuration. The experimental results confirm our theoretical observations.

The optical disorder strength of Poisson's disorder is beyond the critical disorder, and, hence, the zeroth-order transmittance is not zero. This prevents a smooth diffusive response.

Finally, we want to analyze the three hyperuniform point configurations. For these arrangements, the design process did not allow for a large number of meta-atoms. The designed point configuration consisted of 625 meta-atoms. Therefore, high-resolution directional scatterance was not possible. As a result, we have only shown the polar and sectorial scatterance (cf. Fig. 6.17).

As expected, the "hyperuniform ripple" behaves like an ordered metasurface and shows minimal diffusion. On the other hand, "hyperuniform flat" shows strong similarities with a Lambertian surface. Note that the "hyperuniform flat" arrangement was also close to the point of critical disorder (Fig. 6.11). The "hyperuniform cubic" also shows smooth diffusion; however, it performs a little worse than "hyperuniform flat".

In Ref. [38], we have also studied disordered Huygens' metasurfaces under oblique incidence. Our results showed that the large diffuse scatterance also persists for

oblique angles. Therefore, we can conclude this section by reiterating that smooth gloss-free optical diffusion is achievable with multiple disorder models, given the right critical disorder is met. The critical disorder is not always easy to reach in actual metasurfaces. For instance, in Ref. [38], due to the spatial extent of the nanocylinders, the maximum achievable degree of disorder for a perturbed array was $\mathcal{PD} = 27\%$.

In summary, this chapter extensively studied the optical response of disordered metasurfaces made from identical, isotropic, and dipolar meta-atoms. Simultaneous study of the optical response and the statistical measures enabled the direct comparison of the two. Furthermore, we have discovered an exciting physical phenomenon for these disordered arrangements at a critical disorder. Moreover, we have analyzed the directional scatterance and the optical diffusion of dual dipolar metasurfaces at resonance with multiple disordered arrangements. The results show the potential for metasurfaces to realize ultrathin perfect optical diffusers with a near-Lambertian scattering profile.

Our results were limited to dipolar meta-atoms. We envision that incorporating higher-order meta-atoms can further improve metasurfaces' directional scatterance near the point of critical disorder.

7. Summary & Outlook

Research into metasurfaces in the past decade has proved the capability of these ultra-thin surfaces to replace bulky conventional optical components and shape a miniaturized future. The flat interface and compatibility with the mature field of nanofabrication are two crucial factors to drive metasurface research ahead.

In the doctoral thesis at hand, we have followed a step-by-step approach to analyze the optical scattering from a metasurface made from arbitrarily arranged identical meta-atoms. In Chapters 3 and 4, we have provided a comprehensive and unifying multipolar theory to analyze isolated and periodic array of meta-atoms, respectively.

We have developed a minimal model for an isotropic meta-atom, as the building blocks of the metasurfaces, that can capture the Mie coefficients of spherical objects, whether homogenous, core-multishell, or colloidal, with only two degrees of freedom per multipole moment. Considering non-absorbing meta-atoms, as is the case in this thesis, the response of a spherical particle can be modeled with a single real angle per multipole moment. We have shown, through multiple examples, that this model facilitates the understanding of the underlying physics of light-matter interactions and empowers design in nanophotonics. Although the model is limited to spherical particles, the insights are easily extended to other geometries [31, 38, 101].

The optical response of meta-atoms is best described in the vector spherical harmonics basis. The spherical basis is most suited for a single scatterer from a geometry point of view. This basis was developed more than 100 years and is the standard [58]. On the other hand, for surfaces, macroscopic equations, e.g., Fresnel equations, are more suitably expressed in the Cartesian coordinates. This thesis shows that linking the two coordinates can bring about accurate, symmetric, and easy expressions. In Chapter 4, we have linked the spherical response of the meta-atoms to the macroscopic Cartesian response of the metasurfaces. We have shown through multiple examples that the analytical expressions can help design metasurfaces with desired functionalities (cf. Chapter 5). Examples addressed in the thesis are full phase-shift coverage of higher-order Huygens' metasurfaces, fully diffracting metagratings, enhancement of magnetic dipole moments inside a lattice, meta-atom-independent polarization filters, etc.

In Chapter 6, we have extensively studied disordered metasurfaces. The Born approximation that relates the directional scatterance of a metasurface to its structure

factor is valid in the absence of optical interaction between the meta-atoms, i.e., when the meta-atoms are too far apart, or the interaction is diminished due to absorption (e.g., in plasmonic metasurfaces). In the thesis, our focus was primarily on resonant non-absorbing meta-atoms placed on a subwavelength arrangement. These meta-atoms strongly interact, and, as we have shown, the induced effective moments are different from the response of the isolated meta-atoms when no coupling is considered. Despite this limitation, the structure factor, along with its Fourier counterpart, the pair correlation function, provides solid insights into the disordered point configurations. And indeed, the optical response of metasurfaces can be qualitatively correlated with the statistical measures.

Using the analytical methods, we have revealed intriguing features of disordered metasurfaces where the zeroth-order transmission and reflection from a dual dipolar metasurface at resonance vanishes at a critical disorder. At this point, that we linked to a disorder-induced phase transition, a slight change in the disorder degree of the meta-atoms abruptly changes the normal dispersion of the transmission phase angle to an anomalous dispersion. We have shown that, at the point of the phase transition, the radiation strength of the electric and magnetic dipole are statistically equal. However, the induced effective moments simultaneously weaken, leading to a drop in the transmission. At this critical disorder, the light is neither reflected nor transmitted, somewhat diffused to all directions. This optical diffusion is the topic of the last part of the thesis, in which we have extensively investigated the directional scatterance of dual dipolar metasurfaces with multiple disordered arrangements. We have shown that many disordered point processes can reach the point of critical disorder irrespective of their structure factor. Finally, we have identified multiple designs suited for a smooth optical diffusion. Based on the insights, in Ref. [38], we have designed, fabricated, and characterized a perfect optical diffuser.

Throughout the thesis, we have assumed a homogenous embedding medium for the metasurfaces. Although this might seem like a hurdle in photonics design, in multiple experiments, through matching simulation results [38, 101], we have shown that embedding the nanoparticles in a material that has a refractive index comparable to the substrate will have no detrimental effect on the validity of the homogenous medium assumption. Nevertheless, including a substrate in the analytical equations increases design opportunities and is a future research direction.

Furthermore, we have only considered identical meta-atoms with identical orientations. Recently, the research into the *bound states in the continuum* [269] and *optically-induced antiferromagnetic order* [270] have shown a huge potential for novel applications in metasurfaces made from multiple meta-atoms or made from meta-atoms with different orientations. Developing analytical expressions for such metasurfaces in another outlook of the current thesis.

The ultra-thin metasurfaces enable fabrications of multilayer of metasurfaces [271]. A solid analytical tool that enables the investigation of such structures would boost the metasurface capabilities and is subject to future research.

Moreover, most of the analysis of the thesis was based on spherical meta-atoms. The general equations provided can be the basis for exploring other types of meta-atoms, e.g., anisotropic, bianisotropic, and chiral meta-atoms. We envision that exploiting the provided equations enables many novel optical applications.

Bibliography

[1] B. Cui (Ed.), "Recent advances in nanofabrication techniques and applications," 2011.

[2] A. B. Frazier, R. O. Warrington, and C. Friedrich, "The miniaturization technologies: Past, present, and future," *IEEE Trans. Ind. Electron.*, vol. 42, no. 5, pp. 423–430, 1995.

[3] F. Capasso, "The future and promise of flat optics: A personal perspective," *Nanophotonics*, vol. 7, no. 6, pp. 953–957, 2018.

[4] N. Yu and F. Capasso, "Flat optics with designer metasurfaces," *Nat. Mater.*, vol. 13, no. 2, pp. 139–150, 2014.

[5] S. Chen, W. Liu, Z. Li, H. Cheng, and J. Tian, "Metasurface-empowered optical multiplexing and multifunction," *Adv. Mater.*, vol. 32, no. 3, p. 1 805 912, 2019.

[6] R. Dezert, P. Richetti, and A. Baron, "Complete multipolar description of reflection and transmission across a metasurface for perfect absorption of light," *Opt. Express*, vol. 27, no. 19, pp. 26 317–26 330, 2019.

[7] O. Quevedo-Teruel *et al.*, "Roadmap on metasurfaces," *J Opt .*, vol. 21, no. 7, p. 073 002, 2019.

[8] H. K. Shamkhi *et al.*, "Transverse scattering and generalized kerker effects in all-dielectric Mie-resonant metaoptics," *Phys. Rev. Lett.*, vol. 122, no. 19, p. 193 905, 2019.

[9] R. Ahmed *et al.*, "Tunable fano-resonant metasurfaces on a disposable plastic-template for multimodal and multiplex biosensing," *Adv. Mater.*, vol. 32, no. 19, p. 1 907 160, 2020.

[10] E. Karimi, S. A. Schulz, I. D. Leon, H. Qassim, J. Upham, and R. W. Boyd, "Generating optical orbital angular momentum at visible wavelengths using a plasmonic metasurface," *Light: Sci. Appl.*, vol. 3, no. 5, e167, 2014.

[11] H.-T. Chen, A. J. Taylor, and N. Yu, "A review of metasurfaces: Physics and applications," *Rep. Prog. Phys.*, vol. 79, no. 7, p. 076 401, 2016.

[12] Y. Bao, J. Ni, and C.-W. Qiu, "A minimalist single-layer metasurface for arbitrary and full control of vector vortex beams," *Adv. Mater.*, vol. 32, no. 6, p. 1 905 659, 2019.

[13] X. Ni, A. V. Kildishev, and V. M. Shalaev, "Metasurface holograms for visible light," *Nat. Commun.*, vol. 4, p. 2807, 2013.

[14] L. Huang, S. Zhang, and T. Zentgraf, "Metasurface holography: From fundamentals to applications," *Nanophotonics*, vol. 7, no. 6, pp. 1169–1190, 2018.

[15] V. E. Babicheva and A. B. Evlyukhin, "Metasurfaces with electric quadrupole and magnetic dipole resonant coupling," *ACS Photonics*, vol. 5, no. 5, pp. 2022–2033, 2018.

[16] E. Plum *et al.*, "Metamaterial with negative index due to chirality," *Phys. Rev. B*, vol. 79, no. 3, p. 035 407, 2009.

[17] D. R. Smith, J. B. Pendry, and M. C. Wiltshire, "Metamaterials and negative refractive index," *Science*, vol. 305, no. 5685, pp. 788–792, 2004.

[18] N. Engheta and R. W. Ziolkowski, *Metamaterials: physics and engineering explorations*. John Wiley & Sons, 2006.

[19] C. Pfeiffer and A. Grbic, "Metamaterial Huygens' surfaces: Tailoring wave fronts with reflectionless sheets," *Phys. Rev. Lett.*, vol. 110, no. 19, p. 197 401, 2013.

[20] G. Yoon, T. Tanaka, T. Zentgraf, and J. Rho, "Recent progress on metasurfaces: Applications and fabrication," *J. Phys. D Appl. Phys.*, vol. 54, no. 38, p. 383 002, 2021.

[21] P. Genevet, F. Capasso, F. Aieta, M. Khorasaninejad, and R. Devlin, "Recent advances in planar optics: From plasmonic to dielectric metasurfaces," *Optica*, vol. 4, no. 1, pp. 139–152, 2017.

[22] P. Lalanne and P. Chavel, "Metalenses at visible wavelengths: Past, present, perspectives," *Laser Photonics Rev.*, vol. 11, no. 3, p. 1 600 295, 2017.

[23] W. T. Chen and F. Capasso, "Will flat optics appear in everyday life anytime soon?" *Appl. Phys. Lett.*, vol. 118, no. 10, p. 100 503, 2021.

[24] N. I. Landy, S. Sajuyigbe, J. J. Mock, D. R. Smith, and W. J. Padilla, "Perfect metamaterial absorber," *Phys. Rev. Lett.*, vol. 100, no. 20, p. 207 402, 2008.

[25] R. Alaee, M. Albooyeh, and C. Rockstuhl, "Theory of metasurface based perfect absorbers," *J. Phys. D Appl. Phys.*, vol. 50, no. 50, p. 503 002, 2017.

[26] R. Zhao, L. Zhang, J. Zhou, T. Koschny, and C. Soukoulis, "Conjugated gammadion chiral metamaterial with uniaxial optical activity and negative refractive index," *Phys. Rev. B*, vol. 83, no. 3, p. 035 105, 2011.

[27] T. Kodera, D. L. Sounas, and C. Caloz, "Artificial faraday rotation using a ring metamaterial structure without static magnetic field," *Appl. Phys. Lett.*, vol. 99, no. 3, p. 031 114, 2011.

[28] P. Genevet and F. Capasso, "Holographic optical metasurfaces: A review of current progress," *Rep. Prog. Phys.*, vol. 78, no. 2, p. 024 401, 2015.

[29] K. E. Chong *et al.*, "Polarization-independent silicon metadevices for efficient optical wavefront control," *Nano Lett.*, vol. 15, no. 8, pp. 5369–5374, 2015.

[30] F. Zhou, Y. Liu, and W. Cai, "Plasmonic holographic imaging with V-shaped nanoantenna array.," *Opt. Express*, vol. 21, no. 4, pp. 4348–4354, 2013.

[31] A. Rahimzadegan *et al.*, "Beyond dipolar Huygens' metasurfaces for full-phase coverage and unity transmittance," *Nanophotonics*, vol. 9, pp. 75–82, 1 2019.

[32] A. Arbabi, Y. Horie, M. Bagheri, and A. Faraon, "Dielectric metasurfaces for complete control of phase and polarization with subwavelength spatial resolution and high transmission," *Nat. Nanotechnol.*, vol. 10, no. 11, p. 937, 2015.

[33] M. Khorasaninejad *et al.*, "Achromatic metasurface lens at telecommunication wavelengths," *Nano Lett.*, vol. 15, no. 8, pp. 5358–5362, 2015.

[34] D. Lin, P. Fan, E. Hasman, and M. L. Brongersma, "Dielectric gradient metasurface optical elements," *Science*, vol. 345, no. 6194, pp. 298–302, 2014.

[35] P. R. West *et al.*, "All-dielectric subwavelength metasurface focusing lens," *Opt. Express*, vol. 22, no. 21, pp. 26 212–26 221, 2014.

[36] M. Khorasaninejad, W. Zhu, and K. Crozier, "Efficient polarization beam splitter pixels based on a dielectric metasurface," *Optica*, vol. 2, no. 4, pp. 376–382, 2015.

[37] M. Jang *et al.*, "Wavefront shaping with disorder-engineered metasurfaces," *Nat. Photonics*, vol. 12, no. 2, pp. 84–90, 2018.

[38] D. Arslan *et al.*, "Toward perfect optical diffusers: Dielectric Huygens' metasurfaces with critical positional disorder," *Adv. Mat.*, vol. 34, no. 5, p. 2 105 868, 2022.

[39] J. Siegel, A. Y. Wang, S. G. Menabde, M. A. Kats, M. S. Jang, and V. W. Brar, "Self-stabilizing laser sails based on optical metasurfaces," *ACS Photonics*, vol. 6, no. 8, pp. 2032–2040, 2019.

[40] N. Gieseler, A. Rahimzadegan, and C. Rockstuhl, "Self-stabilizing curved metasurfaces as a sail for light-propelled spacecrafts," *Opt. Express*, vol. 29, no. 14, pp. 21 562–21 575, 2021.

[41] A. Tittl *et al.*, "Imaging-based molecular barcoding with pixelated dielectric metasurfaces," *Science*, vol. 360, no. 6393, pp. 1105–1109, 2018.

[42] P. Lin *et al.*, "Coherent raman scattering imaging with a near-infrared achromatic metalens," *APL Photonics*, vol. 6, no. 9, p. 096 107, 2021.

[43] E. Mohammadi, A. Tittl, K. L. Tsakmakidis, T. Raziman, and A. G. Curto, "Dual nanoresonators for ultrasensitive chiral detection," *ACS photonics*, vol. 8, no. 6, pp. 1754–1762, 2021.

[44] T. Stav *et al.*, "Quantum entanglement of the spin and orbital angular momentum of photons using metamaterials," *Science*, vol. 361, no. 6407, pp. 1101–1104, 2018.

[45] K. Wang *et al.*, "Quantum metasurface for multiphoton interference and state reconstruction," *Science*, vol. 361, no. 6407, pp. 1104–1108, 2018.

[46] Y.-l. Xu, "Electromagnetic scattering by an aggregate of spheres," *Appl. Opt.*, vol. 34, no. 21, p. 4573, 1995.

[47] S. Mühlig, C. Menzel, C. Rockstuhl, and F. Lederer, "Multipole analysis of meta-atoms," *Metamaterials*, vol. 5, no. 2, pp. 64–73, 2011.

[48] M. I. Mishchenko, L. D. Travis, and A. A. Lacis, *Scattering, absorption, and emission of light by small particles*. Cambridge university, 2002.

[49] D. A. Powell, "Interference between the modes of an all-dielectric meta-atom," *Phys. Rev. Appl.*, vol. 7, no. 3, p. 034 006, 2017.

[50] F. Bernal Arango, T. Coenen, and A. F. Koenderink, "Underpinning hybridization intuition for complex nanoantennas by magnetoelectric quadrupolar polarizability retrieval," *ACS Photonics*, vol. 1, no. 5, pp. 444–453, 2014.

[51] J. Mun, S. So, J. Jang, and J. Rho, "Describing meta-atoms using the exact higher-order polarizability tensors," *ACS Photonics*, vol. 7, no. 5, pp. 1153–1162, 2020.

[52] V. S. Asadchy, I. A. Faniayeu, Y. Ra'di, and S. A. Tretyakov, "Determining polarizability tensors for an arbitrary small electromagnetic scatterer," *Photonics Nanostructures: Fundam. Appl.*, vol. 12, no. 4, pp. 298–304, 2014.

[53] X.-X. Liu, Y. Zhao, and A. Alù, "Polarizability tensor retrieval for subwavelength particles of arbitrary shape," *IEEE Trans. Antennas Propag.*, vol. 64, no. 6, pp. 2301–2310, 2016.

[54] T. D. Karamanos and N. V. Kantartzis, "Full polarizability matrix extraction formulas for electrically small particles via reflection/transmission coefficients," *Prog. Electromagn. Res. B*, vol. 82, pp. 93–114, 2018.

[55] M. Fruhnert, I. Fernandez-Corbaton, V. Yannopapas, and C. Rockstuhl, "Computing the t-matrix of a scattering object with multiple plane wave illuminations," *Beilstein J. Nanotechnol.*, vol. 8, no. 1, pp. 614–626, 2017.

[56] G. Demésy, J.-C. Auger, and B. Stout, "Scattering matrix of arbitrarily shaped objects: Combining finite elements and vector partial waves," *J. Opt. Soc. Am. A*, vol. 35, no. 8, pp. 1401–1409, 2018.

[57] X. G. Santiago, M. Hammerschmidt, S. Burger, C. Rockstuhl, I. Fernandez-Corbaton, and L. Zschiedrich, "Decomposition of scattered electromagnetic fields into vector spherical wave functions on surfaces with general shapes," *Phys. Rev. B*, vol. 99, no. 4, p. 045 406, 2019.

[58] G. Mie, "Beiträge zur optik trüber medien, speziell kolloidaler metallösungen," *Ann. Phys.*, vol. 330, no. 3, pp. 377–445, 1908.

[59] A. Rahimzadegan, R. Alaee, C. Rockstuhl, and R. W. Boyd, "Minimalist Mie coefficient model," *Opt. Express*, vol. 28, no. 11, pp. 16 511–16 525, 2020.

[60] A. Rahimzadegan, M. Fruhnert, R. Alaee, I. Fernandez-Corbaton, and C. Rockstuhl, "Optical force and torque on dipolar dual chiral particles," *Phys. Rev. B*, vol. 94, no. 12, p. 125 123, 2016.

[61] R. Alaee, M. Albooyeh, A. Rahimzadegan, M. S. Mirmoosa, Y. S. Kivshar, and C. Rockstuhl, "All-dielectric reciprocal bianisotropic nanoparticles," *Phys. Rev. B*, vol. 92, no. 24, p. 245 130, 2015.

[62] S. Tretyakov, *Analytical Modeling in Applied Electromagnetics*. Artech House, 2003.

[63] P. A. Belov and C. R. Simovski, "Homogenization of electromagnetic crystals formed by uniaxial resonant scatterers," *Phys. Rev. E*, vol. 72, no. 2, p. 026 615, 2005.

[64] A. I. Dimitriadis, D. L. Sounas, N. V. Kantartzis, C. Caloz, and T. D. Tsiboukis, "Surface susceptibility bianisotropic matrix model for periodic metasurfaces of uniaxially mono-anisotropic scatterers under oblique te-wave incidence," *IEEE Trans. Antennas Propag.*, vol. 60, no. 12, pp. 5753–5767, 2012.

[65] A. I. Dimitriadis, N. V. Kantartzis, T. D. Tsiboukis, and C. Hafner, "Generalized non-local surface susceptibility model and fresnel coefficients for the characterization of periodic metafilms with bianisotropic scatterers," *J. Comput. Phys.*, vol. 281, pp. 251–268, 2015.

[66] M. Albooyeh *et al.*, "Resonant metasurfaces at oblique incidence: Interplay of order and disorder," *Sci. Rep.*, vol. 4, p. 4484, 2014.

[67] S. S. Kruk *et al.*, "Polarization properties of optical metasurfaces of different symmetries," *Phys. Rev. B*, vol. 91, no. 19, p. 195 401, 2015.

[68] V. E. Babicheva and A. B. Evlyukhin, "Analytical model of resonant electromagnetic dipole-quadrupole coupling in nanoparticle arrays," *Phys. Rev. B*, vol. 99, no. 19, p. 195 444, 2019.

[69] V. E. Babicheva and A. B. Evlyukhin, "Multipole lattice effects in high refractive index metasurfaces," *J. Appl. Phys.*, vol. 129, no. 4, p. 040 902, 2021.

[70] D. Beutel, A. Groner, C. Rockstuhl, and I. Fernandez-Corbaton, "Efficient simulation of biperiodic, layered structures based on the t-matrix method," *J. Opt. Soc. Am. B*, vol. 38, no. 6, pp. 1782–1791, 2021.

[71] A. Modinos, "Scattering of electromagnetic waves by a plane of spheres-formalism," *Physica A: Statistical Mechanics and its Applications*, vol. 141, no. 2-3, pp. 575–588, 1987.

[72] N. Stefanou, V. Yannopapas, and A. Modinos, "Multem 2: A new version of the program for transmission and band-structure calculations of photonic crystals," *Comput. Phys. Commun.*, vol. 132, no. 1-2, pp. 189–196, 2000.

[73] P. P. Ewald, "Die berechnung optischer und elektrostatischer gitterpotentiale," *Ann. Phys.*, vol. 369, no. 3, pp. 253–287, 1921.

[74] A. Popov and V. Popov, "Calculation of lattice sums of general type," *J. Math. Chem.*, vol. 58, no. 10, pp. 2399–2414, 2020.

[75] A. Rahimzadegan *et al.*, "A comprehensive multipolar theory for periodic metasurfaces," *Adv. Opt. Mater.*, vol. 10, no. 10, p. 2 102 059, 2022.

[76] I. Staude and J. Schilling, "Metamaterial-inspired silicon nanophotonics," *Nat. Photonics*, vol. 11, no. 5, pp. 274–284, 2017.

[77] M. Decker *et al.*, "High-efficiency dielectric Huygens' surfaces," *Adv. Opt. Mater.*, vol. 3, no. 6, pp. 813–820, 2015.

[78] A. I. Kuznetsov, A. E. Miroshnichenko, M. L. Brongersma, Y. S. Kivshar, and B. Luk'yanchuk, "Optically resonant dielectric nanostructures," *Science*, vol. 354, no. 6314, aag2472, 2016.

[79] S. M. Kamali, E. Arbabi, A. Arbabi, and A. Faraon, "A review of dielectric optical metasurfaces for wavefront control," *Nanophotonics*, vol. 7, no. 6, pp. 1041–1068, 2018.

[80] M. Chen, M. Kim, A. M. Wong, and G. V. Eleftheriades, "Huygens' meta-surfaces from microwaves to optics: A review," *Nanophotonics*, vol. 7, no. 6, pp. 1207–1231, 2018.

[81] S. Liu *et al.*, "Huygens' metasurfaces enabled by magnetic dipole resonance tuning in split dielectric nanoresonators," *Nano Lett.*, vol. 17, no. 7, pp. 4297–4303, 2017.

[82] S. Jahani and Z. Jacob, "All-dielectric metamaterials," *Nat. Nanotechnol.*, vol. 11, no. 1, pp. 23–36, 2016.

[83] M. I. Shalaev, J. Sun, A. Tsukernik, A. Pandey, K. Nikolskiy, and N. M. Litchinitser, "High-efficiency all-dielectric metasurfaces for ultracompact beam manipulation in transmission mode," *Nano Lett.*, vol. 15, no. 9, pp. 6261–6266, 2015.

[84] Y. F. Yu, A. Y. Zhu, R. Paniagua-Domínguez, Y. H. Fu, B. Luk'yanchuk, and A. I. Kuznetsov, "High-transmission dielectric metasurface with 2π phase control at visible wavelengths," *Laser Photonics Rev.*, vol. 9, no. 4, pp. 412–418, 2015.

[85] I. Staude *et al.*, "Tailoring directional scattering through magnetic and electric resonances in subwavelength silicon nanodisks," *ACS Nano*, vol. 7, no. 9, pp. 7824–7832, 2013.

[86] X. Chen and P. Yao, "Huygens' metasurface made of core-shell spherical nanoparticles," in *Metamaterials, Metadevices, and Metasystems 2018*, International Society for Optics and Photonics, vol. 10719, 2018, p. 1 071 907.

[87] M. Schirber, "Nobel prize: Complexity from atoms to atmospheres," *Physics*, vol. 14, p. 141, 2021.

[88] D. S. Wiersma, "Disordered photonics," *Nat. Photonics*, vol. 7, no. 3, pp. 188–196, 2013.

[89] M. Segev, Y. Silberberg, and D. N. Christodoulides, "Anderson localization of light," *Nat. Photonics*, vol. 7, no. 3, pp. 197–204, 2013.

[90] I. M. Vellekoop, A. Lagendijk, and A. P. Mosk, "Exploiting disorder for perfect focusing," *Nat. Photonics*, vol. 4, no. 5, pp. 320–322, 2010.

[91] M. Jang *et al.*, "Wavefront shaping with disorder-engineered metasurfaces," *Nat. Photonics*, vol. 12, no. 2, pp. 84–90, 2018.

[92] P. Moitra, B. a. Slovick, Z. Gang Yu, S. Krishnamurthy, and J. Valentine, "Experimental demonstration of a broadband all-dielectric metamaterial perfect reflector," *Appl. Phys. Lett.*, vol. 104, no. 17, p. 171 102, 2014.

[93] J. M. Ziman *et al.*, *Models of disorder: the theoretical physics of homogeneously disordered systems*. CUP Archive, 1979.

[94] W. Steurer, "Twenty years of structure research on quasicrystals. part i. pentagonal, octagonal, decagonal and dodecagonal quasicrystals," *Z. Kristallogr. Cryst. Mater.*, vol. 219, no. 7, pp. 391–446, 2004.

[95] S. Torquato and F. H. Stillinger, "Jammed hard-particle packings: From kepler to bernal and beyond," *Rev. Mod. Phys.*, vol. 82, no. 3, pp. 2633–2672, 2010.

[96] S. Torquato and F. H. Stillinger, "Local density fluctuations, hyperuniformity, and order metrics," *Phys. Rev. E*, vol. 68, no. 4, p. 041 113, 2003.

[97] G. Zhang, F. H. Stillinger, and S. Torquato, "The perfect glass paradigm: Disordered hyperuniform glasses down to absolute zero," *Sci. Rep.*, vol. 6, no. 1, p. 36 963, 2016.

[98] E. C. Oğuz, J. E. S. Socolar, P. J. Steinhardt, and S. Torquato, "Hyperuniformity of quasicrystals," *Phys. Rev. B*, vol. 95, no. 5, p. 054 119, 2017.

[99] R. A. DiStasio, G. Zhang, F. H. Stillinger, and S. Torquato, "Rational design of stealthy hyperuniform two-phase media with tunable order," *Phys. Rev. E*, vol. 97, no. 2, p. 023 311, 2018.

[100] C. Kittel and H. Kroemer, *Thermal Physics*. Freeman, 1980.

[101] A. Rahimzadegan *et al.*, "Disorder-induced phase transitions in the transmission of dielectric metasurfaces," *Phys. Rev. Lett.*, vol. 122, no. 1, p. 015 702, 2019.

[102] K. Lee *et al.*, "Simultaneously enhanced device efficiency, stabilized chromaticity of organic light emitting diodes with lambertian emission characteristic by random convex lenses," *Nanotechnology*, vol. 27, no. 7, p. 075 202, 2016.

[103] Y. Y. Kim *et al.*, "Novel microlens arrays with embedded al_2o_3 nanoparticles for enhancing efficiency and stability of flexible polymer light-emitting diodes," *RSC Adv.*, vol. 6, no. 70, pp. 65 450–65 458, 2016.

[104] A. Egel and U. Lemmer, "Dipole emission in stratified media with multiple spherical scatterers: Enhanced outcoupling from OLEDs," *J. Quant. Spectrosc. Radiat. Transf.*, vol. 148, pp. 165–176, 2014.

[105] M. A. Golub *et al.*, "Compressed sensing snapshot spectral imaging by a regular digital camera with an added optical diffuser," *Appl. Opt.*, vol. 55, no. 3, pp. 432–443, 2016.

[106] H. Yilmaz, E. G. van Putten, J. Bertolotti, A. Lagendijk, W. L. Vos, and A. P. Mosk, "Speckle correlation resolution enhancement of wide-field fluorescence imaging," *Optica*, vol. 2, no. 5, p. 424, 2015.

[107] J. Bertolotti, E. G. van Putten, C. Blum, A. Lagendijk, W. L. Vos, and A. P. Mosk, "Non-invasive imaging through opaque scattering layers," *Nature*, vol. 491, no. 7423, pp. 232–234, 2012.

[108] G. Kim, "A PMMA composite as an optical diffuser in a liquid crystal display backlighting unit (BLU)," *Eur. Polym. J.*, vol. 41, no. 8, pp. 1729–1737, 2005.

[109] Z. Cai, J. Chen, G. Pedrini, W. Osten, X. Liu, and X. Peng, "Lensless light-field imaging through diffuser encoding," *Light: Sci. Appl.*, vol. 9, no. 1, p. 143, 2020.

[110] L. Lu, J. Sun, J. Zhang, Y. Fan, Q. Chen, and C. Zuo, "Quantitative phase imaging camera with a weak diffuser," *Front. Phys.*, vol. 7, p. 77, 2019.

[111] R. A. Hoover and R. G. Hoover, "Light diffuser for optical microscopes replacing condenser with opal glass to produce near-koehler illumination," U.S. Patent US6963445B2, 2003.

[112]   N. Antipa *et al.*, "DiffuserCam: Lensless single-exposure 3d imaging," *Optica*, vol. 5, no. 1, pp. 1–9, 2018.

[113]   P. Song *et al.*, "Super-resolution microscopy via ptychographic structured modulation of a diffuser," *Opt. Lett.*, vol. 44, no. 15, p. 3645, 2019.

[114]   W. Yang *et al.*, "All-dielectric metasurface for high-performance structural color," *Nat. Commun.*, vol. 11, no. 1864, 2020.

[115]   T. H. Zhao, G. Jacucci, X. Chen, D.-P. Song, S. Vignolini, and R. M. Parker, "Angular-independent photonic pigments via the controlled micellization of amphiphilic bottlebrush block copolymers," *Adv. Mater.*, vol. 32, no. 47, p. 2 002 681, 2020.

[116]   A. K. González-Alcalde and A. Reyes-Coronado, "Large angle-independent structural colors based on all-dielectric random metasurfaces," *Opt. Commun.*, vol. 475, p. 126 289, 2020.

[117]   S. K. Sahoo, D. Tang, and C. Dang, "Single-shot multispectral imaging with a monochromatic camera," *Optica*, vol. 4, no. 10, p. 1209, 2017.

[118]   R. French, S. Gigan, and O. L. Muskens, "Speckle-based hyperspectral imaging combining multiple scattering and compressive sensing in nanowire mats," *Opt. Lett.*, vol. 42, no. 9, p. 1820, 2017.

[119]   K. Monakhova, K. Yanny, N. Aggarwal, and L. Waller, "Spectral Diffuser-Cam: Lensless snapshot hyperspectral imaging with a spectral filter array," *Optica*, vol. 7, no. 10, pp. 1298–1307, 2020.

[120]   Z. Fang *et al.*, "Novel nanostructured paper with ultrahigh transparency and ultrahigh haze for solar cells," *Nano Lett.*, vol. 14, no. 2, pp. 765–773, 2014.

[121]   W. Wu, N. G. Tassi, H. Zhu, Z. Fang, and L. Hu, "Nanocellulose-based translucent diffuser for optoelectronic device applications with dramatic improvement of light coupling," *ACS Appl. Mater. Interfaces*, vol. 7, no. 48, pp. 26 860–26 864, 2015.

[122]   T. G. Deepak, G. S. Anjusree, S. Thomas, T. A. Arun, S. V. Nair, and A. S. Nair, "A review on materials for light scattering in dye-sensitized solar cells," *RSC Adv.*, vol. 4, no. 34, pp. 17 615–17 638, 2014.

[123]   H. Butt *et al.*, "Electrically tunable scattering from devitrite-liquid crystal hybrid devices," *Adv. Opt. Mater.*, vol. 5, no. 1, p. 1 600 414, 2016.

[124]   R. Schittny, A. Niemeyer, F. Mayer, A. Naber, M. Kadic, and M. Wegener, "Invisibility cloaking in light-scattering media," *Laser Photonic Rev.*, vol. 10, no. 3, pp. 382–408, 2016.

[125]   A. P. Mosk, A. Lagendijk, G. Lerosey, and M. Fink, "Controlling waves in space and time for imaging and focusing in complex media," *Nat. Photonics*, vol. 6, no. 5, pp. 283–292, 2012.

[126]   A. Colombo, F. Tassone, F. Santolini, N. Contiello, A. Gambirasio, and R. Simonutti, "Nanoparticle-doped large area PMMA plates with controlled optical diffusion," *J. Mater. Chem. C*, vol. 1, no. 16, pp. 2927–2934, 2013.

[127]   S. M. Mahpeykar *et al.*, "Cellulose nanocrystal: Polymer hybrid optical diffusers for index-matching-free light management in optoelectronic devices," *Adv. Opt. Mater.*, vol. 5, no. 21, p. 1 700 430, 2017.

[128] M. S. Toivonen *et al.*, "Anomalous-diffusion-assisted brightness in white cellulose nanofibril membranes," *Adv. Mater.*, vol. 30, no. 16, p. 1 704 050, 2018.

[129] T. Alqurashi and H. Butt, "Highly flexible, stretchable, and tunable optical diffusers with mechanically switchable wettability surfaces," *ACS Cent. Sci.*, vol. 5, no. 6, pp. 1002–1009, 2019.

[130] F. Lin, L. Zhu, and S. Yang, "Effective optical diffuser based on interfacial hydrogen-bonding polymer complexation," *ACS Appl. Polym. Mater.*, vol. 2, no. 9, pp. 3805–3812, 2020.

[131] T. Ohzono, K. Suzuki, T. Yamaguchi, and N. Fukuda, "Tunable optical diffuser based on deformable wrinkles," *Adv. Opt. Mater.*, vol. 1, no. 5, pp. 374–380, 2013.

[132] S. M. Mahpeykar *et al.*, "Stretchable hexagonal diffraction gratings as optical diffusers for in situ tunable broadband photon management," *Adv. Opt. Mater.*, vol. 4, no. 7, pp. 1106–1114, 2016.

[133] S.-I. Chang, J.-B. Yoon, H. Kim, J.-J. Kim, B.-K. Lee, and D. H. Shin, "Microlens array diffuser for a light-emitting diode backlight system," *Opt. Lett.*, vol. 31, no. 20, p. 3016, 2006.

[134] S. Wadle, D. Wuest, J. Cantalupo, and R. S. Lakes, "Holographic diffusers," *Opt. Eng*, vol. 33, no. 1, pp. 213–218, 1994.

[135] C. Gu, J. Hong, J.-R. Lien, and F. Dai, "Diffraction properties of volume holographic diffusers," *J. Opt. Soc. Am. A*, vol. 13, no. 8, pp. 1704–1711, 1996.

[136] S. I. Kim, Y. S. Choi, Y. N. Ham, C. Y. Park, and J. M. Kim, "Holographic diffuser by use of a silver halide sensitized gelatin process," *Appl. Opt.*, vol. 42, no. 14, pp. 2482–2491, 2003.

[137] R. Pawluczyk, "Holographic diffusers," in *Photopolymers and Applications in Holography, Optical Data Storage, Optical Sensors, and Interconnects*, R. A. Lessard, Ed., SPIE, 1994.

[138] S. S. Kruk *et al.*, "Optical metamaterials with quasicrystalline symmetry: Symmetry-induced optical isotropy," *Phys. Rev. B*, vol. 88, no. 20, p. 201 404, 2013.

[139] M. Castro-Lopez, M. Gaio, S. Sellers, G. Gkantzounis, M. Florescu, and R. Sapienza, "Reciprocal space engineering with hyperuniform gold disordered surfaces," *APL Photonics*, vol. 2, no. 6, p. 061 302, 2017.

[140] F. Sterl, E. Herkert, S. Both, T. Weiss, and H. Giessen, "Shaping the color and angular appearance of plasmonic metasurfaces with tailored disorder," *ACS Nano*, vol. 15, no. 6, pp. 10 318–10 327, 2021.

[141] G. Osnabrugge, R. Horstmeyer, I. N. Papadopoulos, B. Judkewitz, and I. M. Vellekoop, "Generalized optical memory effect," *Optica*, vol. 4, no. 8, p. 886, 2017.

[142] M. Odeh, M. Dupré, K. Kim, and B. Kanté, "Optical response of jammed rectangular nanostructures," *Nanophotonics*, vol. 10, no. 1, pp. 705–711, 2020.

[143] E. Maguid, I. Yulevich, M. Yannai, V. Kleiner, M. L. Brongersma, and E. Hasman, "Multifunctional interleaved geometric-phase dielectric metasurfaces," *Light: Sci. Appl.*, vol. 6, no. 8, e17027, 2017.

[144] S. Fasold *et al.*, "Disorder-enabled pure chirality in bilayer plasmonic metasurfaces," *ACS Photonics*, vol. 5, no. 5, pp. 1773–1778, 2018.

[145] A. Rahimzadegan, C. Rockstuhl, and I. Fernandez-Corbaton, "Core-shell particles as building blocks for systems with high duality symmetry," *Phys. Rev. Appl.*, vol. 9, no. 5, p. 054 051, 2018.

[146] J. D. Jackson, *Classical electrodynamics*. American Association of Physics Teachers, 1999.

[147] A. Zangwill, *Modern Electrodynamics*. Cambridge University, 2013.

[148] T. G. Mackay and A. Lakhtakia, *Electromagnetic anisotropy and bianisotropy: a field guide*. World Scientific, 2010.

[149] A. Serdyukov, I. Semchenko, S. Tretyakov, and A. Sihvola, *Electromagnetics of Bianisotropic Particles*. Gordon and Breach Science Publichers, 2001.

[150] E. Hebestreit, "Multipole Analysis of Optical Nano-Structures," Ph.D. dissertation, Friedrich-Schiller-Universität Jena Multipole, 2013.

[151] J. A. Stratton, *Electromagnetic theory*. John Wiley & Sons, 2007.

[152] F. Frezza, F. Mangini, and N. Tedeschi, "Introduction to electromagnetic scattering: Tutorial," *J. Opt. Soc. Am. A*, vol. 35, no. 1, pp. 163–173, 2018.

[153] I. Fernandez-Corbaton, S. Nanz, R. Alaee, and C. Rockstuhl, "Exact dipolar moments of a localized electric current distribution," *Opt. Express*, vol. 23, no. 26, pp. 33 044–33 064, 2015.

[154] S. Nanz, "Toroidal Moments and Their Properties," M.S. thesis, Karlsruhe Institute of Technology (KIT), 2015.

[155] Encyclopedia of Mathematics, *Fourier method <accessed 01 october 2021.>*

[156] D. Arslan, "Positional disorder in Huygens' metasurfaces," Ph.D. dissertation, Friedrich-Schiller-Universität Jena, 2022 (Expected).

[157] C. F. Bohren and D. R. Huffman, *Absorption and Scattering of Light by Small Particles*. John Wiley & Sons, 2008.

[158] I. Fernandez-Corbaton, X. Zambrana-Puyalto, and G. Molina-Terriza, "Helicity and angular momentum: A symmetry-based framework for the study of light-matter interactions," *Phys. Rev. A*, vol. 86, no. 4, pp. 1–14, 2012.

[159] I. Fernandez-Corbaton, "Helicity and Duality Symmetry in Light Matter Interactions: Theory and Applications," Ph.D. dissertation, Macquarie University, 2014. eprint: arXiv:1407.4432.

[160] W.-K. Tung, *Group Theory in Physics*. World Scientific, 1985.

[161] X. Zambrana-Puyalto, X. Vidal, M. L. Juan, and G. Molina-Terriza, "Dual and anti-dual modes in dielectric spheres," *Opt. Express*, vol. 21, no. 15, pp. 17 520–17 530, 2013.

[162] A. Rahimzadegan, R. Alaee, I. Fernandez-Corbaton, and C. Rockstuhl, "Fundamental limits of optical force and torque," *Phys. Rev. B*, vol. 95, no. 3, p. 035 106, 2017.

[163] A. Rahimzadegan, "Optical force and torque on bianisotropic metamolecules," M.S. thesis, Karlsruher Institut für Technologie (KIT), 2016.

[164] P. Waterman, "Matrix formulation of electromagnetic scattering," *Proc. IEEE*, vol. 53, no. 8, pp. 805–812, 1965.

[165] M. Born and E. Wolf, *Principles of Optics: Electromagnetic Theory of Propagation, Interference and Diffraction of Light*. Elsevier, 2013.

[166] M. Kerker, *The scattering of light and other electromagnetic radiation: physical chemistry: a series of monographs*. Academic press, 2013, vol. 16.

[167] T. Wriedt, "Mie theory: A review," in *The Mie Theory*, Springer, 2012, pp. 53–71.

[168] M. I. Mishchenko, L. D. Travis, and D. W. Mackowski, "T-matrix computations of light scattering by nonspherical particles: A review," *J. Quant. Spectrosc. Radiat. Transf.*, vol. 55, no. 5, pp. 535–575, 1996.

[169] A. Moroz, "A recursive transfer-matrix solution for a dipole radiating inside and outside a stratified sphere," *Ann. Phys.*, vol. 315, no. 2, pp. 352–418, 2005.

[170] R. Alaee, C. Rockstuhl, and I. Fernandez-Corbaton, "An electromagnetic multipole expansion beyond the long-wavelength approximation," *Optics Communications*, vol. 407, pp. 17–21, 2018.

[171] E. A. Gurvitz, K. S. Ladutenko, P. A. Dergachev, A. B. Evlyukhin, A. E. Miroshnichenko, and A. S. Shalin, "The high-order toroidal moments and anapole states in all-dielectric photonics," *Laser Photonics Rev.*, vol. 13, no. 5, p. 1 800 266, 2019.

[172] A. Alù and N. Engheta, "Guided propagation along quadrupolar chains of plasmonic nanoparticles," *Phys. Rev. B*, vol. 79, no. 23, p. 235 412, 2009.

[173] E. Mobini, A. Rahimzadegan, C. Rockstuhl, and R. Alaee, "Theory of optical forces on small particles by multiple plane waves," *J. Appl. Phys.*, vol. 124, no. 17, p. 173 102, 2018.

[174] C. D. H. Chisholm, *Group Theoretical Techniques in Quantum Chemistry*. New York: Academic Press, 1976.

[175] R. Dezert, P. Richetti, and A. Baron, "Isotropic Huygens dipoles and multipoles with colloidal particles," *Phys. Rev. B*, vol. 96, no. 18, p. 180 201, 2017.

[176] I. Fernandez-Corbaton, M. Fruhnert, and C. Rockstuhl, "Objects of maximum electromagnetic chirality," *Phys. Rev. X*, vol. 6, p. 031 013, 3 2016.

[177] M. I. Abdelrahman, C. Rockstuhl, and I. Fernandez-Corbaton, "Broadband suppression of backscattering at optical frequencies using low permittivity dielectric spheres," *Sci. Rep.*, vol. 7, no. 1, p. 14 762, 2017.

[178] I. Fernandez-Corbaton, M. Fruhnert, and C. Rockstuhl, "Dual and chiral objects for optical activity in general scattering directions," *ACS Photonics*, vol. 2, no. 3, pp. 376–384, 2015.

[179] P. B. Johnson and R.-W. Christy, "Optical constants of the noble metals," *Phys. Rev. B*, vol. 6, no. 12, p. 4370, 1972.

[180] I. H. Malitson, "Interspecimen comparison of the refractive index of fused silica," *J. Opt. Soc. Am.*, vol. 55, no. 10, pp. 1205–1209, 1965.

[181] L. Novotny and B. Hecht, *Principles of Nano-Optics.* Cambridge university, 2012.

[182] J. E. Sipe and J. V. Kranendonk, "Macroscopic electromagnetic theory of resonant dielectrics," *Phys. Rev. A*, vol. 9, no. 5, pp. 1806–1822, 1974.

[183] K. D. Bonin and V. V. Kresin, *Electric-dipole polarizabilities of atoms, molecules, and clusters.* World Scientific, 1997.

[184] P. Lambropoulos and D. Petrosyan, *Fundamentals of quantum optics and quantum information.* Springer, 2007, vol. 23.

[185] V. Cachorro and L. Salcedo, "New improvements for Mie scattering calculations," *J. Electromagn. Waves Appl.*, vol. 5, no. 9, pp. 913–926, 1991.

[186] D. Tzarouchis and A. Sihvola, "Light scattering by a dielectric sphere: Perspectives on the Mie resonances," *Appl. Sci.*, vol. 8, no. 2, p. 184, 2018.

[187] M. Alam and Y. Massoud, "A closed-form analytical model for single nanoshells," *IEEE Trans Nanotechnol*, vol. 5, no. 3, pp. 265–272, 2006.

[188] J. Shen, "Algorithm of numerical calculation on Lorentz Mie theory," *PIERS Online*, vol. 1, no. 6, pp. 691–694, 2005.

[189] H. C. Hulst and H. C. van de Hulst, *Light scattering by small particles.* Courier Corporation, 1981.

[190] J. A. Adam, "Scattering of electromagnetic plane waves in radially inhomogeneous media: Ray theory, exact solutions and connections with potential scattering theory," in *Light Scattering Reviews 9*, Springer, 2015, pp. 101–132.

[191] W. T. Grandy Jr and W. T. Grandy, *Scattering of waves from large spheres.* Cambridge University, 2005.

[192] R. G. Newton, *Scattering theory of waves and particles.* Springer Science & Business Media, 2013.

[193] R. Gómez-Medina, P. San José, A. García-Martín, M. Lester, M. Nieto-Vesperinas, and J. Sáenz, "Resonant radiation pressure on neutral particles in a waveguide," *Phys. Rev. Lett.*, vol. 86, no. 19, p. 4275, 2001.

[194] A. García-Etxarri *et al.*, "Strong magnetic response of submicron silicon particles in the infrared," *Opt. Express*, vol. 19, no. 6, pp. 4815–4826, 2011.

[195] Z. Ruan and S. Fan, "Design of subwavelength superscattering nanospheres," *App. Phys. Lett.*, vol. 98, no. 4, pp. 2013–2016, 2011.

[196] C. F. Bohren, "Recurrence relations for the Mie scattering coefficients," *J. Opt. Soc. Am. A*, vol. 4, no. 3, pp. 612–613, 1987.

[197] S. Tretyakov, "Maximizing absorption and scattering by dipole particles," *Plasmonics*, vol. 9, no. 4, pp. 935–944, 2014.

[198] R. Alaee, M. Albooyeh, and C. Rockstuhl, "Theory of metasurface based perfect absorbers," *J. Phys. D Appl. Phys.*, vol. 50, no. 50, p. 503 002, 2017.

[199] B. Hopkins, W. Liu, A. E. Miroshnichenko, and Y. S. Kivshar, "Optically isotropic responses induced by discrete rotational symmetry of nanoparticle clusters," *Nanoscale*, vol. 5, no. 14, pp. 6395–6403, 2013.

[200] D. W. Mackowski, "Calculation of total cross sections of multiple-sphere clusters," *J. Opt. Soc. Am. A*, vol. 11, no. 11, pp. 2851–2861, 1994.

[201] D. W. Mackowski and M. I. Mishchenko, "Calculation of the t matrix and the scattering matrix for ensembles of spheres," *J. Opt. Soc. Am. A*, vol. 13, no. 11, pp. 2266–2278, 1996.

[202] R. Alaee, C. Rockstuhl, and I. Fernandez-Corbaton, "Exact multipolar decompositions with applications in nanophotonics," *Adv. Opt. Mater.*, vol. 7, no. 1, p. 1 800 783, 2019.

[203] M. Z. Alam, I. De Leon, and R. W. Boyd, "Large optical nonlinearity of indium tin oxide in its epsilon-near-zero region," *Science*, vol. 352, no. 6287, pp. 795–797, 2016.

[204] K. Y. Lee and M. A. El-Sharkawi, *Modern heuristic optimization techniques: theory and applications to power systems.* John Wiley & Sons, 2008, vol. 39.

[205] A. Rahimzadegan, R. Alaee, T. D. Karamanos, R. W. Boyd, and C. Rockstuhl, "Colossal enhancement of the magnetic dipole moment by exploiting lattice coupling in metasurfaces," *J. Opt. Soc. Am. B*, vol. 38, no. 9, pp. C217–C224, 2021.

[206] K. M. McPeak *et al.*, "Plasmonic films can easily be better: Rules and recipes," *ACS Photonics*, vol. 2, no. 3, pp. 326–333, 2015.

[207] L. D. Landau and E. M. Lifshitz, *Electrodynamics of Continous Media*, 2nd ed. Pergamon Press, 1984, vol. 8.

[208] M. Hentschel, M. Schäferling, T. Weiss, N. Liu, and H. Giessen, "Three-dimensional chiral plasmonic oligomers," *Nano Lett.*, vol. 12, no. 5, pp. 2542–2547, 2012.

[209] J. Kaschke and M. Wegener, "Optical and infrared helical metamaterials," *Nanophotonics*, vol. 5, no. 38, 2016.

[210] J. K. Gansel, M. Wegener, S. Burger, and S. Linden, "Gold helix photonic metamaterials: A numerical parameter study," *Opt. Express*, vol. 18, no. 2, pp. 1059–1069, 2010.

[211] M. Decker, M. Klein, M. Wegener, and S. Linden, "Circular dichroism of planar chiral magnetic metamaterials," *Opt. Lett.*, vol. 32, no. 7, pp. 856–858, 2007.

[212] S. Lobanov *et al.*, "Controlling circular polarization of light emitted by quantum dots using chiral photonic crystal slabs," *Phys. Rev. B*, vol. 92, no. 20, p. 205 309, 2015.

[213] G. Von Freymann *et al.*, "Three-dimensional nanostructures for photonics," *Adv. Funct. Mater.*, vol. 20, no. 7, pp. 1038–1052, 2010.

[214] K. Hannam, D. A. Powell, I. V. Shadrivov, and Y. S. Kivshar, "Broadband chiral metamaterials with large optical activity," *Phys. Rev. B*, vol. 89, no. 12, p. 125 105, 2014.

[215] R. Zhao, T. Koschny, and C. M. Soukoulis, "Chiral metamaterials: Retrieval of the effective parameters with and without substrate," *Opt. Express*, vol. 18, no. 14, pp. 14 553–14 567, 2010.

[216]   R. Zhao, J. Zhou, T. Koschny, E. N. Economou, and C. M. Soukoulis, "Repulsive casimir force in chiral metamaterials," *Phys. Rev. Lett.*, vol. 103, no. 10, p. 103 602, 2009.

[217]   A. Guijarro and M. Yus, *The Origin of Chirality in the Molecules of Life: A Revision from Awareness to the Current Theories and Perspectives of this Unsolved Problem.* Royal Society of Chemistry, 2008.

[218]   G. Gübitz and M. G. Schmid, "Chiral separation principles in chromatographic and electromigration techniques," *Mol. Biotechnol.*, vol. 32, no. 2, pp. 159–179, 2006.

[219]   R. Alaee, "Optical nanoantennas and their use as perfect absorbers," Ph.D. dissertation, Karlsruher Institut für Technologie (KIT), 2015.

[220]   L. Tsang, J. A. Kong, and R. T. Shin, *Theory of Microwave Remote Sensing (Wiley Series in Remote Sensing and Image Processing).* Wiley-Interscience, 1985.

[221]   Y.-L. Xu, "Efficient evaluation of vector translation coefficients in multiparticle light-scattering theories," *J. Comput. Phys.*, vol. 139, no. 1, pp. 137–165, 1998.

[222]   E. P. Wigner, "On the matrices which reduce the kronecker products of representations of sr groups," in *The Collected Works of Eugene Paul Wigner*, Springer, 1993, pp. 608–654.

[223]   A. Messiah, "Clebsch-gordan (c.-g.) coefficients and'3j'symbols," *Appendix CI in Quantum Mechanics*, vol. 2, pp. 1054–1060, 1962.

[224]   K. Kambe, "Theory of low-energy electron diffraction," *Z. Naturforsch. A*, vol. 22, no. 3, pp. 322–330, 1967.

[225]   D. Beutel, "Electromagnetic Scattering from Periodic Arrays of Dielectrics and Molecules," M.S. thesis, Karlsruhe Institute of Technology (KIT), 2019.

[226]   G. Achim, "Analysing diffraction from periodically arranged scatterers while considering their T-Matrix," M.S. thesis, Karlsruhe Institute of Technology (KIT), 2018.

[227]   T. Antonakakis *et al.*, *Gratings: Theory and numeric applications.* AMU,(PUP), CNRS, ECM, 2014.

[228]   R. J. Bettles, S. A. Gardiner, and C. S. Adams, "Enhanced optical cross-section via collective coupling of atomic dipoles in a 2d array," *Phys. Rev. Lett.*, vol. 116, no. 10, p. 103 602, 2016.

[229]   E. Shahmoon, D. S. Wild, M. D. Lukin, and S. F. Yelin, "Cooperative resonances in light scattering from two-dimensional atomic arrays," *Phys. Rev. Lett.*, vol. 118, no. 11, p. 113 601, 2017.

[230]   M. Kerker, D.-S. Wang, and C. Giles, "Electromagnetic scattering by magnetic spheres," *J. Opt. Soc. Am.*, vol. 73, no. 6, pp. 765–767, 1983.

[231]   A. Alù and N. Engheta, "How does zero forward-scattering in magnetodielectric nanoparticles comply with the optical theorem?" *J. Nanophotonics*, vol. 4, no. 1, p. 041 590, 2010.

[232] R. Alaee, R. Filter, D. Lehr, F. Lederer, and C. Rockstuhl, "A generalized Kerker condition for highly directive nanoantennas," *Opt. Lett.*, vol. 40, no. 11, pp. 2645–2648, 2015.

[233] M. Nieto-Vesperinas, R. Gomez-Medina, and J. Saenz, "Angle-suppressed scattering and optical forces on submicrometer dielectric particles," *J. Opt. Soc. Am. A*, vol. 28, no. 1, pp. 54–60, 2011.

[234] I. Fernandez-Corbaton, "Forward and backward helicity scattering coefficients for systems with discrete rotational symmetry," *Opt. Express*, vol. 21, no. 24, p. 29 885, 2013.

[235] X. Zambrana-Puyalto, I. Fernandez-Corbaton, M. Juan, X. Vidal, and G. Molina-Terriza, "Duality symmetry and kerker conditions," *Opt. Lett.*, vol. 38, no. 11, pp. 1857–1859, 2013.

[236] M. Khorasaninejad, W. T. Chen, R. C. Devlin, J. Oh, A. Y. Zhu, and F. Capasso, "Metalenses at visible wavelengths: Diffraction-limited focusing and subwavelength resolution imaging," *Science*, vol. 352, no. 6290, pp. 1190–1194, 2016.

[237] C. Jin *et al.*, "Dielectric metasurfaces for distance measurements and three-dimensional imaging," *Advanced Photonics*, vol. 1, no. 3, p. 036 001, 2019.

[238] L. Wang *et al.*, "Grayscale transparent metasurface holograms," *Optica*, vol. 3, no. 12, pp. 1504–1505, 2016.

[239] A. J. Ollanik, J. A. Smith, M. J. Belue, and M. D. Escarra, "High-efficiency all-dielectric Huygens metasurfaces from the ultraviolet to the infrared," *ACS Photonics*, vol. 5, no. 4, pp. 1351–1358, 2018.

[240] R. Paniagua-Domínguez *et al.*, "Generalized brewster effect in dielectric metasurfaces," *Nat. Commun.*, vol. 7, no. 1, p. 10 362, 2016.

[241] S. Yin and J. Qi, "Metagrating-enabled brewster's angle for arbitrary polarized electromagnetic waves and its manipulation," *Opt. Express*, vol. 27, no. 13, pp. 18 113–18 122, 2019.

[242] C. Wang, Z. Zhu, W. Cui, Y. Yang, L. Ran, and D. Ye, "All-angle brewster effect observed on a terahertz metasurface," *Appl. Phys. Lett.*, vol. 114, no. 19, p. 191 902, 2019.

[243] P. J. Diggle, *Statistical analysis of spatial and spatio-temporal point patterns.* CRC press, 2013.

[244] S. Torquato, "Hyperuniform states of matter," *Phys. Rep.*, vol. 745, pp. 1–95, 2018.

[245] M. A. Klatt, J. Kim, and S. Torquato, "Cloaking the underlying long-range order of randomly perturbed lattices," *Phys. Rev. E*, vol. 101, no. 3, p. 032 118, 2020.

[246] C. Helgert *et al.*, "Effective properties of amorphous metamaterials," *Phys. Rev. B*, vol. 79, no. 23, p. 233 107, 2009.

[247] A. Gabrielli, "Point processes and stochastic displacement fields," *Phys. Rev. E*, vol. 70, no. 6, p. 066 131, 2004.

[248] M. A. Klatt, J. Kim, and S. Torquato, "Cloaking the underlying long-range order of randomly perturbed lattices," *Phys. Rev. E*, vol. 101, no. 3, p. 032 118, 2020.

[249] V. I. Zakomirnyi, S. V. Karpov, H. Ågren, and I. L. Rasskazov, "Collective lattice resonances in disordered and quasi-random all-dielectric metasurfaces," *J. Opt. Soc. Am. B*, vol. 36, no. 7, E21–E29, 2019.

[250] J. Teichmann, F. Ballani, and K. G. van den Boogaart, "Generalizations of matérn's hard-core point processes," *Spat. Stat.*, vol. 3, pp. 33–53, 2013.

[251] P. M. Piechulla, B. Fuhrmann, E. Slivina, C. Rockstuhl, R. B. Wehrspohn, and A. N. Sprafke, "Tailored light scattering through hyperuniform disorder in self-organized arrays of high-index nanodisks," *Adv. Opt. Mater.*, vol. 9, no. 17, p. 2 100 186, 2021.

[252] A. V. Kolobov, P. Fons, A. I. Frenkel, A. L. Ankudinov, J. Tominaga, and T. Uruga, "Understanding the phase-change mechanism of rewritable optical media," *Nat. Mater.*, vol. 3, no. 10, pp. 703–708, 2004.

[253] A. Zylbersztejn and N. F. Mott, "Metal-insulator transition in vanadium dioxide," *Phys. Rev. B*, vol. 11, no. 11, pp. 4383–4395, 1975.

[254] M. Liu *et al.*, "Terahertz-field-induced insulator-to-metal transition in vanadium dioxide metamaterial," *Nature*, vol. 487, no. 7407, pp. 345–348, 2012.

[255] M. Wang, H. Li, D. Gao, L. Gao, J. Xu, and C.-W. Qiu, "Radiation pressure of active dispersive chiral slabs," *Opt. Express*, vol. 23, no. 13, pp. 1094–4087, 2015.

[256] B. Gholipour, J. Zhang, K. F. MacDonald, D. W. Hewak, and N. I. Zheludev, "An all-optical, non-volatile, bidirectional, phase-change meta-switch," *Adv. Mater.*, vol. 25, no. 22, pp. 3050–3054, 2013.

[257] H. N. Krishnamoorthy, Z. Jacob, E. Narimanov, I. Kretzschmar, and V. M. Menon, "Topological transitions in metamaterials," in *Conference on Lasers and Electro-Optics*, OSA, 2012, QM2E.6.

[258] I. I. Smolyaninov and E. E. Narimanov, "Metric signature transitions in optical metamaterials," *Phys. Rev. Lett.*, vol. 105, no. 6, p. 067 402, 2010.

[259] M. V. Rybin, D. S. Filonov, K. B. Samusev, P. A. Belov, Y. S. Kivshar, and M. F. Limonov, "Phase diagram for the transition from photonic crystals to dielectric metamaterials," *Nat. Commun.*, vol. 6, no. 1, p. 10 102, 2015.

[260] A. Guo *et al.*, "Observation of PT-symmetry breaking in complex optical potentials," *Phys. Rev. Lett.*, vol. 103, no. 9, p. 093 902, 2009.

[261] C. E. Rüter, K. G. Makris, R. El-Ganainy, D. N. Christodoulides, M. Segev, and D. Kip, "Observation of parity-time symmetry in optics," *Nat. Phys.*, vol. 6, no. 3, pp. 192–195, 2010.

[262] M. Verbin, O. Zilberberg, Y. E. Kraus, Y. Lahini, and Y. Silberberg, "Observation of topological phase transitions in photonic quasicrystals," *Phys. Rev. Lett.*, vol. 110, no. 7, p. 076 403, 2013.

[263] S. John, "Strong localization of photons in certain disordered dielectric superlattices," *Phys. Rev. Lett.*, vol. 58, no. 23, pp. 2486–2489, 1987.

[264] T. Baba, "Slow light in photonic crystals," *Nat. Photonics*, vol. 2, no. 8, pp. 465–473, 2008-08.

[265] E. Lidorikis, M. M. Sigalas, E. N. Economou, and C. M. Soukoulis, "Gap deformation and classical wave localization in disordered two-dimensional photonic-band-gap materials," *Phys. Rev. B*, vol. 61, no. 20, pp. 13 458–13 464, 2000.

[266] C. Helgert *et al.*, "Effects of anisotropic disorder in an optical metamaterial," *Appl. Phys. A*, vol. 103, no. 3, pp. 591–595, 2010.

[267] T. Pertsch *et al.*, "Nonlinearity and disorder in fiber arrays," *Phys. Rev. Lett.*, vol. 93, no. 5, p. 053 901, 2004.

[268] S. Yu, C.-W. Qiu, Y. Chong, S. Torquato, and N. Park, "Engineered disorder in photonics," *Nat. Rev. Mater.*, vol. 6, no. 3, pp. 226–243, 2021.

[269] C. W. Hsu, B. Zhen, A. D. Stone, J. D. Joannopoulos, and M. Soljačić, "Bound states in the continuum," *Nat. Rev. Mater.*, vol. 1, no. 9, pp. 1–13, 2016.

[270] A. E. Miroshnichenko, D. Filonov, B. Lukyanchuk, and Y. Kivshar, "Antiferromagnetic order in hybrid electromagnetic metamaterials," *New J. Phys.*, vol. 19, no. 8, p. 083 013, 2017.

[271] K. Tanaka *et al.*, "Chiral bilayer all-dielectric metasurfaces," *ACS Nano*, vol. 14, no. 11, pp. 15 926–15 935, 2020.

Acknowledgement